AN OROGRAPHIC MECHANISM FOR RAPID FRONTOGENESIS

by

Stephen Trent Garner

B.A. Yale College (1976)

SUBMITTED TO THE DEPARTMENT OF
EARTH, ATMOSPHERIC AND PLANETARY SCIENCES
IN PARTIAL FULFILLMENT OF THE REQUIREMENTS
FOR THE DEGREE OF

DOCTOR OF PHILOSOPHY

at the

MASSACHUSETTS INSTITUTE OF TECHNOLOGY

February 1986

Signature of Author _____
                    Department of Earth, Atmospheric and Planetary Sciences
                                                      November, 1985

Certified by _____
                                                      Kerry A. Emanuel
                                                      Thesis Supervisor

Accepted by _____
                                                      Theodore R. Madden
                          Chairman, Departmental Graduate Committee

AN OROGRAPHIC MECHANISM FOR RAPID FRONTOGENESIS

by

Stephen T. Garner

Submitted to the Department of
Earth, Atmospheric and Planetary Sciences
on November 7, 1985, in partial fulfillment of the requirements
for the Degree of Doctor of Philosophy in Meteorology

ABSTRACT

        Observations of the New England coastal front show that the
extraordinary temperature gradients are caused by ageostrophic wind
deformation, that is, deformation in the vertical plane. The phenomenon
is therefore an instance of rapid (non-classical) frontogenesis, a process
broadly characterized by a lack of geostrophic balance between the
temperature gradient and vertical wind shear. The primary cause of the
deformation has thus far been difficult to identify. Furthermore, the
relevance of a secondary vertical circulation comparable to that driven by
slight mass-momentum imbalance in large-scale fronts has not been
established.

        Local sea-surface heating (in itself frontogenetical) and the
surface roughness contrast at the coast have been proposed elsewhere as
the necessary catalysts for the frontal collapse. The alternative
explored in the present study is that the frontogenesis arises primarily
from an interaction between an initially balanced baroclinic flow and an
inland mountain barrier. The advantage of this purely orographic theory
is that it can be shown to be consistent with the systematic, long-term
steepening of an upwind gradient. It thus becomes a more robust mechanism
under certain environmental conditions.

        The likelihood of the orographic mechanism is investigated both
analytically and numerically. The analysis proceeds from a canonical
study of linear line-source disturbances in an unbounded, stable,
baroclinic atmosphere. The results are used to identify a plausible
feedback mechanism to account for the virtually unlimited frontogenesis
observed in nature. The feedback is found to involve a secondary response
to increased stratification in the vertical, rather than the horizontal.
By requiring upward motion in a stably-stratified flow, the barrier plays
an analogous role to the classical mechanism of horizontal wind
deformation, which requires geostrophic adjustment. The feedback is
significant only in the case of a narrow (high Rossby number) mountain
profile.

The linear analysis is suggestive, but still less than conclusive, especially in regard to the long-term consequences of a feedback. Hence, numerical simulation using a new Lagrangian technique is called upon to solve the idealized two-dimensional initial-value problem. The simulation confirms the expectation of upwind blocking and frontogenesis via the proposed mechanism, and reproduces several observable features of coastal fronts.

Comparing solutions for different mountain widths and vertical shears leads to a consistent and largely intuitive explanation for the quasi-stationary character of the observed front, and its dependence on the details of the mountain profile. The disturbed flow in the simulations becomes progressively isolated at the ground, where a strongly-stratified blocked layer develops on the windward side of the mountain. This cold pool has limiting dimensions determined by the mountain barrier, and exhibits a gradual strengthening of temperature and parallel velocity gradients. The long-term explanation thus involves the simultaneous advection of ambient absolute momentum and potential temperature, and the reduction of nonlinearity in the unblocked flow.

The analysis and numerical simulations provide a qualitative understanding of the alternative explanations for the vertical deformation, namely the coastal gradients of surface heating and roughness. The analysis suggests that the heating is potentially the stronger effect, whereas the roughness gradient produces better agreement with the observed location of the frontogenesis. The ability of the heating and friction to support the frontogenesis is readily established. The numerical experiments confirm the simple analytical conclusion that horizontal shearing deformation also enhances the orographic frontogenesis. In fact, a more robust frontal structure is predicted when the basic state contains a temperature gradient along the barrier.

Thesis supervisor: Kerry A. Emanuel
Title: Professor of Meteorology

ACKNOWLEDGEMENTS

CONTENTS

CHAPTER 1. INTRODUCTION AND BACKGROUND

The purpose here is to investigate a simple hypothesis concerning the enhancement, and especially the causation, of shallow atmospheric fronts by orography. Related studies of the barrier effect of mountain chains on existing fronts include some of the earliest synoptic analyses by the Norwegian meteorologists, and the extensive Alpine Experiment of 1982. In the interim, the theories of mountain flow and frontogenesis have developed in relative isolation. Each, it seems, has succeeded by neglecting an essential feature of the other, i.e., the baroclinicity of frontogenetical disturbances or the ageostrophy of orographic ones.

It is clear that a formal treatment of orographic frontogenesis will require a difficult synthesis. The approach in the present work is to develop insights from the existing theories and from a generalized linear analysis of line-source disturbances, and then to use numerical simulation to test the sufficiency of one of the more obvious frontogenetical mechanisms, to be spelled out in section 1.4. Both efforts will focus on obtaining and studying a system governed by a minimal set of parameters. The numerical model, in particular, will be designed to avoid additional degrees of freedom.

The chief observational reference for the study is the New England coastal front, a well-documented perennial phenomenon which is extraordinary among fronts in the atmosphere. Strong circumstantial evidence, to be reviewed in section 1.3, points to the crucial role of the frictional and thermodynamic land-sea contrast in this instance. However,

the alternative hypothesis of this paper is that the coastal mountains are part of a sufficient frontogenetical mechanism which does not require coastal geography, _per se_. Such a scenario is also supported by circumstantial evidence, but has not been emphasized by researchers.

1.1 The relationship between fronts and orography

Although the New England front forms _in situ_ within a stratified atmosphere (Bosart, 1975), an example of orographic modification of an existing frontal system provides a useful model. On the basis of surface observations in Scandinavia, Bjerknes and Solberg (1921) described the typical passage of a warm front over a mountain range. Their illustration is reproduced in Fig. 1.1, and shows some of the receding cold air becoming trapped on the windward side of the mountains. Godske et al. (1957) note that blocking of this kind is also common in Greenland and western North America.

Analytical principles allowing a physical interpretation of the illustration have for the most part become available after the time of the Scandinavian observations. For example, it is now known (Long, 1972; Baines and Davies, 1980) that the ability of an obstacle to block a layer of homogeneous fluid increases sharply as the height of the barrier approaches the fluid depth. Beyond a critical ratio of these heights, the impinging fluid lacks both the kinetic energy to lift the free surface (supercritical flow) and the potential energy to "spill" completely over the obstacle (subcritical).

Contrary to the simplified illustration, the pooled air must spread upstream to some extent in response to the stagnation pressure. If
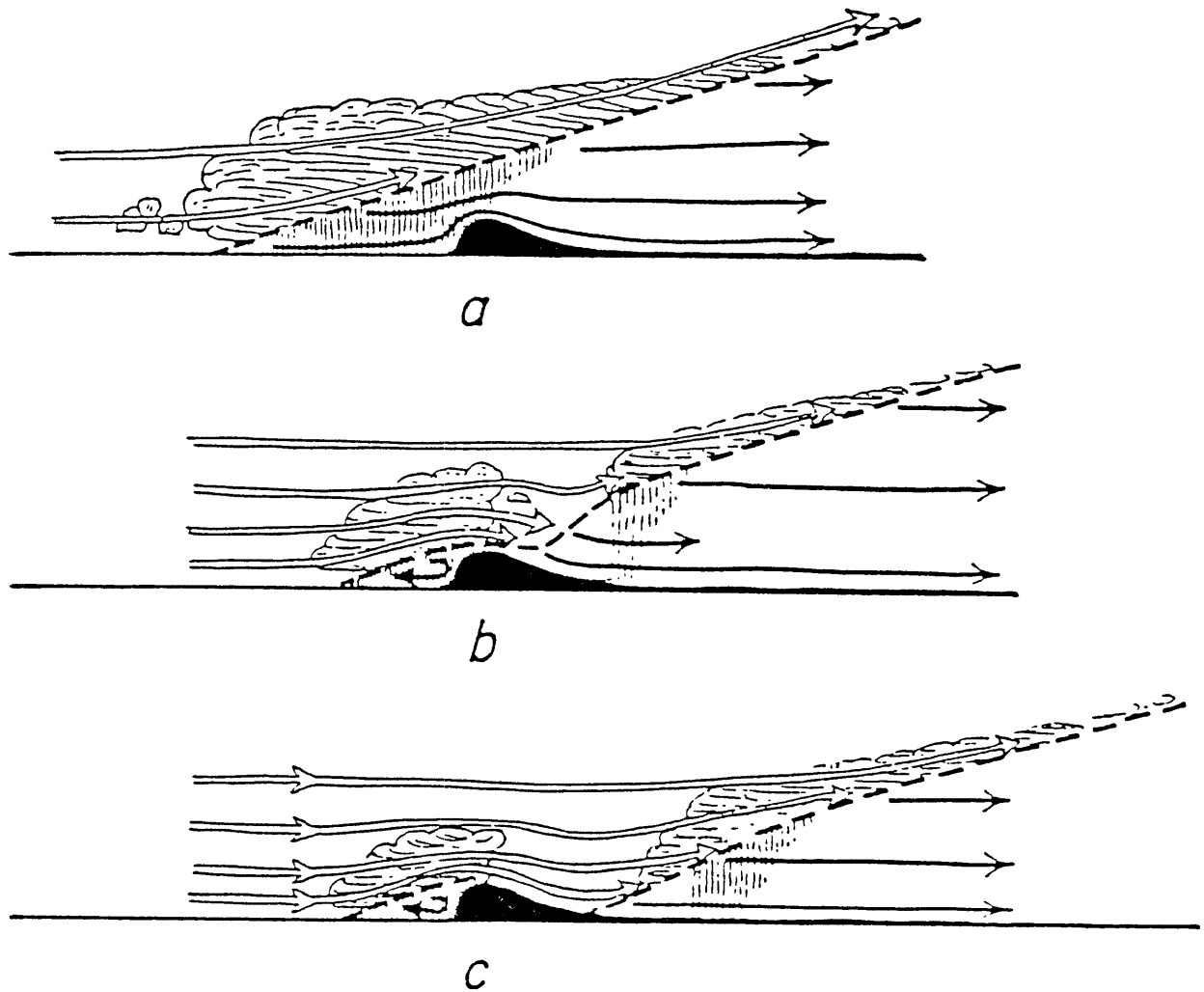
Fig. 1.1. Profile of a warm front crossing a mountain range (from Bjerknes and Solberg, 1921).

this process is rapid, the detached front should move as a density
current; otherwise it remains geostrophic, with the spreading beginning
well in advance of the separation. The distinction must be determined by
the mountain width and frontal velocity. What is unusual about the
adjustment process in this case is that the trapped air continues to move
relative to the mean flow. Hence, without dissipation or inhomogeneities
in the two air masses, there is no asymptotic shape for the density
interface in a rotating atmosphere.

Fronts moving parallel to a ridge are affected by a dynamically
similar deformation, also relevant to observations of in situ
frontogenesis. This particular variation has been documented by Bosart et
al. (1973) for the Appalachian chain, by Lilly (1980) for the Rockies, and
by Coulman et al. (1985) for the Great Dividing Range of eastern
Australia. Coulman et al. point to a further example along the Andes
range in South America. In all cases, the front on the east side of the
ridge is strengthened and accelerated relative to the west side.

The synoptic analysis in Fig. 1.2 is taken from Baines (1984) and
shows the Australian phenomenon, known as the "southerly buster" because
of its dramatic effect on the coastal cities. The nearly identical
Appalachian front has acquired the name "back-door" (Bosart et al., 1973),
and has been linked to the phenomenon of cold-air "damming" (Baker, 1970).

An explanation for the wind-side enhancement of obliquely-oriented
fronts is complicated by the contrasting surface boundary layers across
the coastal ranges. Yet, even if the smoother, and sometimes cooler, sea
surface assists the movement on the east side, the synoptic analyses
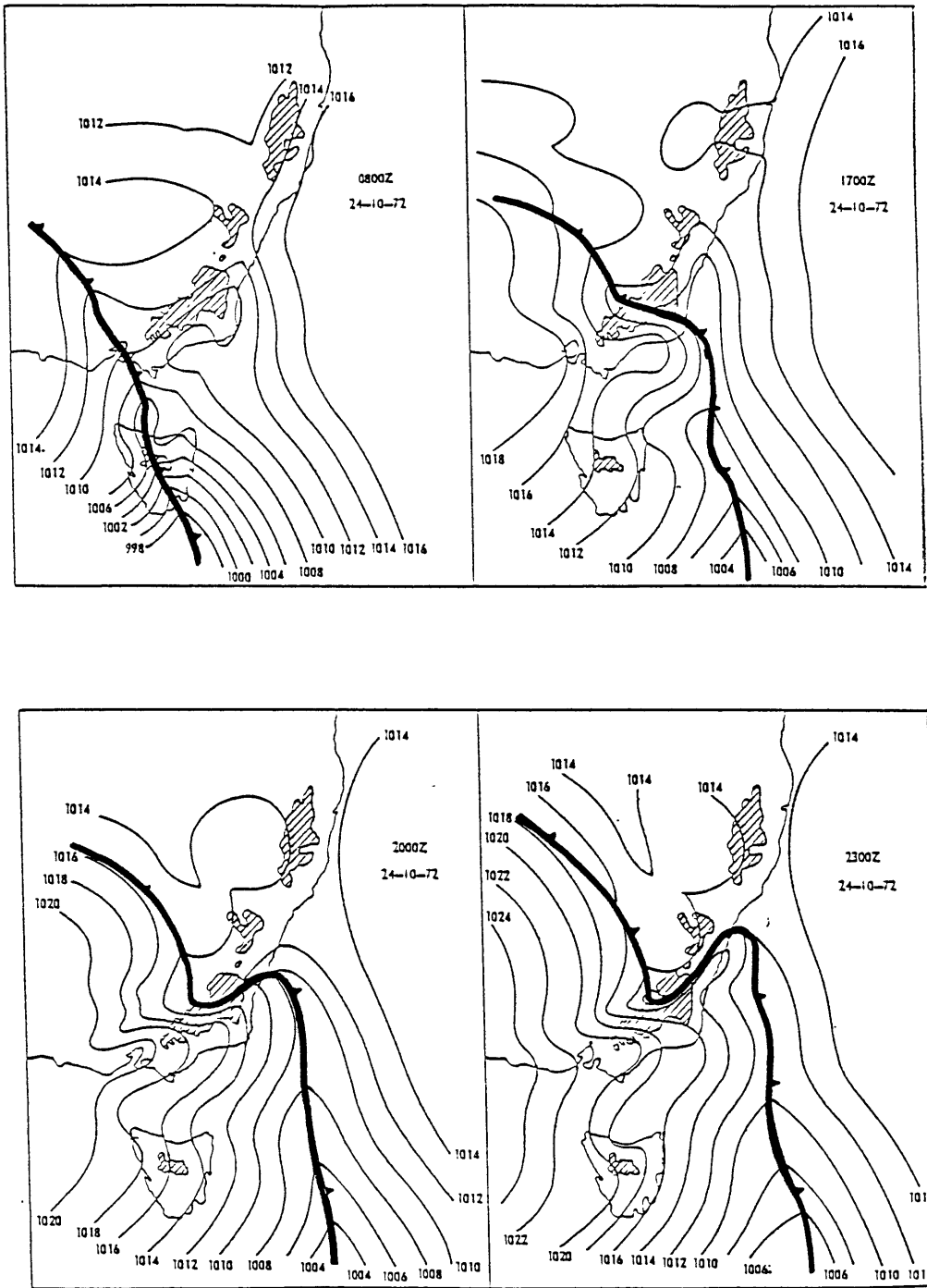clearly show the maximum deformation occurring along the mountain

Fig. 1.2. Sequence of sea-level synoptic analyses showing the development of a southerly buster on a cold front (from Baines, 1984).

barrier. Moreover, the typical antisymmetry of the deformation seen in the Australian example is consistent with the induced parallel circulation in steady quasi-geostrophic flow over a mountain ridge.

Baines (1984) also discounted the coastal contrast, and showed with a time-dependent linear model that partial blocking of the geostrophic wind behind the front would produce an ageostrophic current along the barrier in the direction of the front on the windward side, but opposite the front on the leeward side. Although his model is strictly linear, the speed at which the disturbance propagates along the ridge suggests a density current. Baines further showed that the depth of the disturbance decays away from the mountain on the scale of the Rossby deformation radius based on the mountain height.

Essentially the same structure and length scale emerge from a nonlinear analysis if it is assumed only that the deflected air conserves potential vorticity and eventually achieves geostrophic balance. (The connection between the deformation radius and the potential vorticity for nonlinear, stratified flows was described by Hoskins, 1975). The geostrophic adjustment behind back-door fronts cannot be significantly different from the inferred spreading process in the first illustration.

An indirect advantage of studying systems of homogeneous fluids is that most of the principles have analogues for continuously-stratified flows. The latter normally provide a better description of the atmosphere, but also a more difficult problem in analysis. The effort to generalize the interpretations of orographic modification of existing fronts has to contend with the basic difference between layered and stratified fluids. What distinguishes the latter is a continuous spectrum

of internal waves which not only act more efficiently to redistribute disturbance energy, but also resist the nonlinear interactions which characterize external waves in homogeneous flows (see Smith, 1977).

An effort to broaden the notions of frontal modification into ones of orographic frontogenesis will begin in the next section with a selective review of the theories of frontogenesis and stratified hydrostatic mountain flow. Inasmuch as the study refers principally to the New England coastal front, the next step is a careful review of that still unexplained phenomenon. The wealth of case studies has already eliminated much of the mystery concerning the mature character of the coastal front. The emphasis in section 1.3 will therefore be placed on identifying aspects of the initial synoptic environment and early frontogenesis. The reviews of theory and observation will be followed in section 1.4 by a description of the proposed orographic mechanism and the procedure for testing it.

1.2 Relevant aspects of frontogenesis and mountain flow theory

The time-dependent analytic models of frontogenesis rely on the classical mechanism of geostrophic wind deformation. The model of Stone (1966) assumes the quasi-geostrophic form of the two-dimensional Boussinesq system, in which ageostrophic advection is neglected. The more successful semi-geostrophic theory of Hoskins and Bretherton (1972) allows ageostrophic momentum and temperature advection, but continues to bind the ageostrophic circulation to the task of maintaining thermal wind balance. The balance assumption eliminates gravity-inertia waves, and along with them, the possibility of energy dispersion and additional ageostrophic steepening of momentum and temperature gradients.

The velocity fields in Stone's (1966) solution were sufficiently realistic to confirm the predominant role of geostrophic deformation in large-scale frontogenesis. The greatest achievement of Hoskins and Bretherton (1972) was to expose the feedback mechanism which allows frontal collapse in a finite time. In their solutions, the frontogenesis outruns the background stretching deformation because the ageostrophic velocity feeds back on the solenoidal field which generates it. Hoskins and Bretherton also obtained semi-geostrophic solutions of the Eady problem of baroclinic instability, and found that horizontal shearing deformation of the meridional temperature gradient was a less effective mechanism for frontogenesis.

It is well-known that fronts in nature, even those with planetary-scale dimensions, do not conform to the balanced or semi-balanced models near the ground (e.g., Sanders, 1955), where indeed they are often accompanied by secondary features such as gravity waves and squall lines (Plotkin, 1965). Numerical simulations by Keyser and Anthes (1982) have explained some of the discrepancy as a consequence of surface friction, while Sanders (1955) and Plotkin (1965) have also emphasized diabatic effects. Emanuel (1985) showed that the semi-geostrophic model yields more realistic vertical velocity fields when reversible latent heating is incorporated through horizontal variations in potential vorticity.

Fronts which violate the geostrophic balance assumption are not systematically weaker than classical fronts; indeed, evaporatively-driven density currents and coastal fronts are two examples which can be considerably stronger. There is a need to make a distinction between

semi-geostrophic frontogenesis and the processes which lead to fronts that are only weakly influenced by rotation. Since "ageostrophic" does not exclude the semi-balanced process, the term "rapid" frontogenesis will be used here. Part of the reason for the choice is that "slowness" compared to the background rotation period is necessary to insure semi-geostrophy (Hoskins, 1982). Although other mechanisms can be as effective in breaking the rotational constraint, the terminology is reasonable if all tend to produce characteristics of rapid frontogenesis, per se.

It is probably not possible to find a time-dependent analytic solution for rapid frontogenesis. The classical theory of density currents (e.g., Benjamin, 1968) assumes an initial discontinuity and so offers few insights for frontogenesis in a stratified flow. In fact, it would be a prodigious task to show analytically that solutions of the inviscid Boussinesq primitive equations can develop discontinuities from smooth initial conditions.

Ley and Peltier (1979) developed an analytic model for the secondary wave-like phenomena accompanying large-scale frontogenesis. However, they were obliged to treat the semi-geostrophic part of the disturbance as a small perturbation on the background deformation, so that wave motions generated by local frontal imbalance would add linearly. The separation of a disturbance into non-interacting linear and nonlinear regions is a common device when weakly-nonlinear theory is inadequate (cf. also the Lighthill, 1952, theory of jet noise). The approach is most convincing when the nature of the nonlinearity and the reason for the non-interaction are known.

A similar idea has been used speculatively for upstream influence in two-dimensional stratified barrier flow, which Pierrehumbert and Wyman (1985, hereafter PW) determined was not a weakly-nonlinear phenomenon. They suggested, on the basis of numerical simulation, that breaking lee waves could excite an upstream disturbance with linear properties still capable of significantly decelerating the fluid.

The non-interaction theory applied to mountain flow is plausible for several reasons. In the first place, the linear upstream response contains shear layers of the type observed and simulated in barrier flow. Also, because of its long horizontal scales and reduced velocities, the upstream disturbance can remain laminar and slowly-varying well beyond the ordinary threshold for nonlinearity. Finally, according to linear theory, the influence radius as a fraction of the width of the forcing (presumed to be a two-dimensional region with the same dimensions as the mountain), is apparently correlated with the degree of blocking in PW's simulations.

The simulations and analysis by PW are a major contribution to the theory of stratified, hydrostatic mountain flow, and will be summarized in chapter 5. Their study, like the classical theory, examines the dependence on the Rossby and Froude numbers characterizing the basic state. The theory can be organized according to the importance of background rotation. Rotation is unimportant if the mountain width, ℓ, is a small fraction of the inertial distance, $\lambda_I = U_0/f$ (where U_0 is the mean flow speed and f is the Coriolis frequency), i.e., if the Rossby number, $Ro = U_0/(f\ell)$ is large. In that case, all of the disturbance energy is carried vertically in buoyancy (gravity) waves of uniform vertical wavelength, $\lambda_G = U_0/N$, where N is the buoyancy frequency.

Vertical overshooting and downstream waves are absent in the hydrostatic limit.

The Froude number for stratified fluids can be defined as the ratio of the mountain height to the internal scale, λ_G, i.e., $Fr = Nh/U_0$. In the homogeneous case, it is more natural to use the undisturbed height, D, of the free surface. This leads to the definition $Fr_0 = (gD)^{1/2}/U_0$, where g is the acceleration of gravity. Steady solutions for the nonrotating stratified fluid exhibit characteristics both of supercritical homogeneous flows -- in which $Fr_0 < 1$ by definition and the pressure is high over the mountain -- and of subcritical homogeneous disturbances -- in which $Fr_0 > 1$ and the pressure is low. In the stratified case, the disturbance develops alternating regions of high and low pressure over a symmetric obstacle. The pressure and vertical velocity in steady solutions are anticorrelated with the horizontal velocity; this can be seen as the mechanism whereby energy propagates vertically but not horizontally, relative to the mountain.

Hydrostatic balance implies that the amplitude of the pressure disturbance is the product of the buoyancy perturbation and the vertical scale, i.e., $N^2 h \lambda_G = Fr\, U_0^2$. The relationship between the pressure and velocity noted above is such that the regions of maximum deceleration (where $u' = -Fr\, U_0$) coincide with the high-pressure levels over the mountain. The surface deceleration is weaker because it occurs upstream, where the vertical displacements are smaller.

It is important to recognize that the pressure cannot be neglected in energy considerations aimed at determining the location and strength of the decelerated regions. Ignoring the pressure anomaly at the mountaintop

allows the conclusion that all of the kinetic energy of the surface flow is given up to potential energy at the critical point $U_0^2/2 = N^2h^2/2$. The partial analysis then implies incorrectly that Fr = 1 is sufficient to bring the surface flow to rest at the summit, in violation of the condition that the velocity components be anticorrelated.

The linear solutions show, in fact, that the pressure along the undisturbed level of the bounding streamline first increases on approach to the mountain, but then recovers to its ambient value at the position of the peak. Further, the hydrostatic assumption requires that the vertical pressure gradient supply all of the work done against reduced gravity, whence it follows that the pressure anomaly at the summit is sufficiently negative to restore the velocity to its mean value.

This finite-amplitude interpretation of the linear results is consistent with the fully nonlinear solutions (Lilly and Klemp, 1979). The linear theory also correctly predicts that the first flow stagnation induced by symmetric or sinusoidal topography requires Fr = O(1), and occurs in the layer $\pi < z/\lambda_G < 3\pi/2$, either directly over the summit or slightly downstream. Hence surface stagnation is preceded by convective overturning, or "wave-breaking", high over the mountain.

The finite-amplitude theory in the nonrotating limit is based on Long's (1955) discovery that the fully nonlinear system reduces to a linear equation (Poisson's equation) for the streamline displacement if steady state is assumed. The "nonlinear" (strictly, transcendental) lower boundary condition for the displacement can be expanded in powers of the mountain "amplitude", Fr, to obtain a weakly-nonlinear theory (Smith, 1977).

The lowest-order analysis for the hydrostatic case predicts
wave-steepening "into the wind", i.e., such that the velocity anomalies
are enhanced at all levels over the lee slope. This effect is not
explained entirely by nonlinear momentum advection, which favors negative
anomalies; rather, it is clear that the nonlinearity increases the overall
amplitude of the pressure perturbation in the lee.

Lilly and Klemp (1979) were able to obtain fully nonlinear
solutions of the nonrotating, hydrostatic problem by using an elegant
numerical procedure. They also noted that mountain waves could be
"unsteepened" by choosing a terrain profile which mimics the linear
streamline pattern at the steepening levels over a symmetric mountain.
Much of the understanding about nonrotating flow past asymmetric mountains
is based on their analysis.

In linear, hydrostatic flow past broad mountain ridges, with Ro $\ll$
1, the Coriolis force acts on a parallel wind to balance most of the
induced streamwise pressure gradient, and waves are strongly suppressed.
In the quasi-geostrophic limit, the balance is exact and there are no
waves. Accordingly, the streamline displacement conforms to the shape of
the mountain at all vertical levels, and decays on a scale of $\lambda_{qg} = f\ell/N$
(there being no internal scales).

It follows that the hydrostatic pressure perturbation in the
quasi-geostrophic solutions has an amplitude of $N^2 h\lambda_{qg} = Ro^{-1}Fr\ U_0^2$.
As noted, the parallel wind scales with the pressure gradient, or $v/U_0 = O(Fr)$, so that the streamwise component responsible for the parallel flow
has an amplitude of $u'/U_0 = O(RoFr)$. Hence the nonlinearity of the
response is determined by RoFr, rather than Fr, when Ro is small.

Pierrehumbert (1984) has emphasized the fact that RoFr = $Nh/(f\ell)$ depends only on the nondimensional steepness of the mountain.

The circulation over a broad mountain ridge is anticyclonic because of the high pressure and geostrophic balance. Hence it is the parallel, rather than streamwise, disturbance velocity which changes sign at the summit. The streamwise component in turn reaches its maximum value at the same point. Away from the mountain, downstream as well as upstream, the normal flow is decelerated.

As in the nonrotating case, finite-amplitude solutions can be obtained analytically for broad mountains. It must be assumed that the nonlinearity preserves the geostrophy of the parallel flow, and that the fluid is horizontally uniform far upstream. Solutions for the resulting semi-geostrophic problem take into account the advection of perturbation temperature and parallel momentum by the meridional circulation. Exact analysis requires a mathematical transformation to a Lagrangian vertical coordinate (Merkine, 1975) — for example, the streamfunction.

Semi-geostrophic solutions for isolated mountains have been obtained by Pierrehumbert (1984). Because the governing equation is identical to the quasi-geostrophic case, the perturbation streamfunction is only a distortion of the linear quasi-geostrophic solution. The velocity perturbation is altered in much the same way as the relative vorticity in semi-geostrophic frontogenesis. If u'_{qg} is the quasi-geostrophic perturbation velocity, then the semi-geostrophic result is given by $1+u'_{sg}/U_0 = (1-u'_{qg}/U_0)^{-1}$.

The semi-geostrophic analysis implies that the balance assumption breaks down in the accelerated regions when RoFr is order-unity. Since

this is also the linearity condition, it seems that the semi-geostrophic

analysis is of little additional value. However, Pierrehumbert (1984)

speculated, and PW confirmed, that an important part of the solution,

namely the upstream deceleration, remains quite accurate until

wave-breaking begins around RoFr = 3.

The most interesting mountain disturbances occur in the

"mesoscale" regime, Ro ≈ 1. Under such conditions, neither the buoyancy

nor the inertial restoring force is negligible, and gravity-inertia waves

appear in the lee. The pure inertia waves are confined energetically to

the immediate boundary, and exhibit the interesting property of a

vanishing pressure perturbation. Exact nonlinear solutions exist for the

inertia waves but not for the mixed gravity-inertia disturbance.

1.3 The New England coastal front as an example of rapid frontogenesis

The first case studies of the New England front were published by

Bosart et al. (1972), who also introduced the name "coastal front". The

observations leave little doubt that the land-sea boundary layer contrast

determines much of the character of the mature front. Hence, even if the

coastal mountains are necessary to complete the process, the widely-used

term is probably not a misnomer.

Part of the evidence for a strict coastal mechanism lies in the

fact that the frequency of occurrence peaks in December, and that coastal

fronts are virtually unknown in the summer months. Of course, the summer

minimum can be attributed to the lack of a large-scale temperature

gradient, but the peak during the first of the winter months probably does

reflect the mesoscale baroclinicity imposed by the coastline. The
difference between air and sea-surface temperatures is greatest for the
region in December.

The composite synoptic analysis in Fig. 1.3 summarizes the
large-scale weather pattern. The cold anticyclone in eastern Canada is
already receding at the time of the frontogenesis, which takes place
either just offshore or on the coastal plain in southeastern New England.
The position and timing of the anticyclone are different in cases of
back-door fronts, in which the cold air first arrives along the coast in a
northeasterly flow (Bosart et al., 1973). In the coastal front cases
described by Bosart et al. (1972), Bosart (1975), and McCarthy (1977), the
cold air is well-established before the flow becomes easterly. By that
time, the period of large-scale cold advection is nearly at an end.

The distinction is further clarified by noting that coastal
frontogenesis occurs within a large-scale thermal ridge, with steadily
increasing southwesterly shear and warm advection. In place of a
southward-moving cold front and upper-level cold advection, the coastal
front environment features a lowering warm frontal inversion signalling
the approach of a warm front from the south. The inversion typically
reaches the level of 850 mb over New England by the time the surface
frontogenesis is underway.

The frontogenesis begins suddenly, in that the convergence zone
which is to become the front more than doubles in strength in the first
three hours of a typical event. The initial stage conforms to one of two
main patterns. In those reported cases in which the air-sea temperature
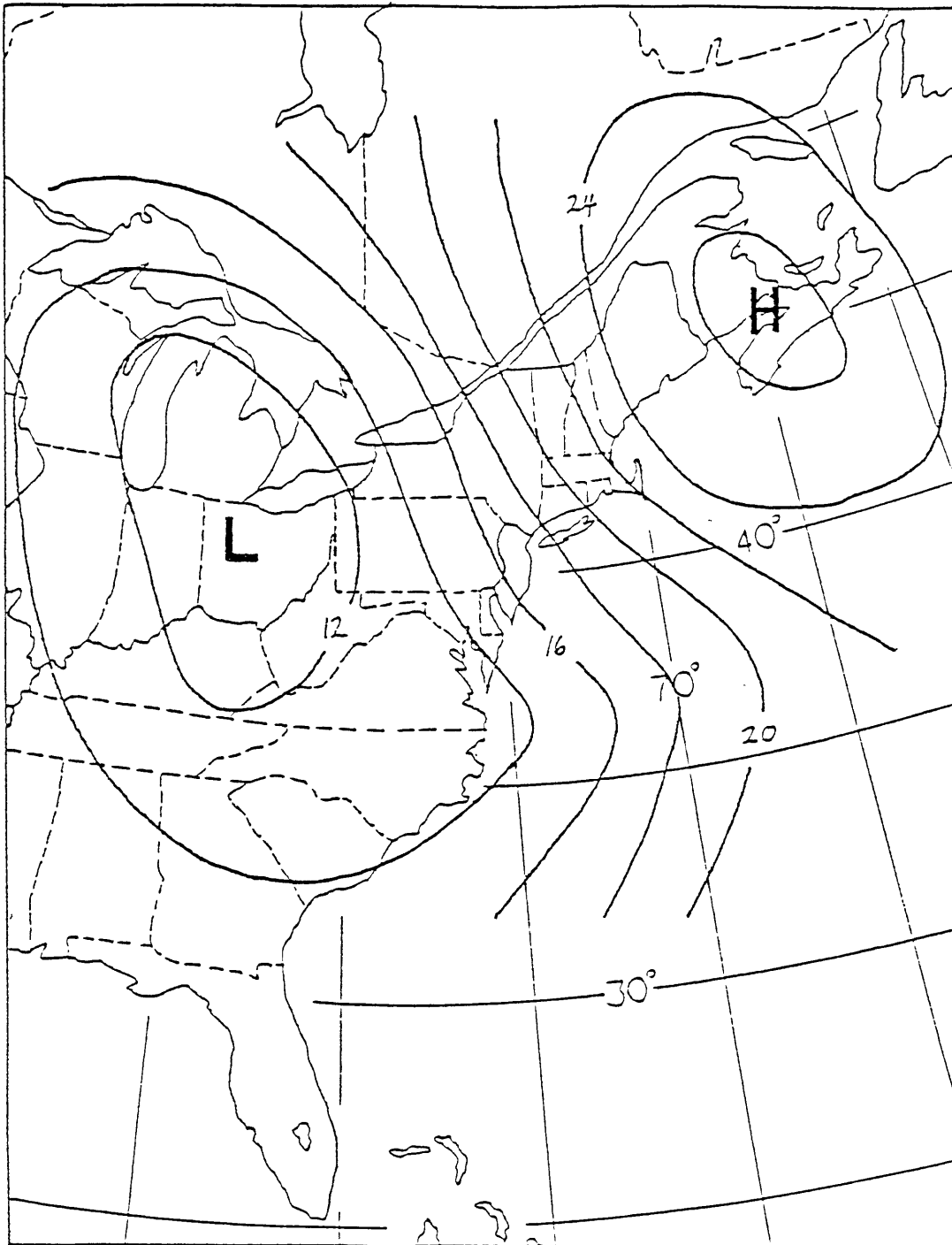contrast is largest, the coastal convergence normally precedes the

Fig. 1.3. Composite analysis of sea-level pressure at onset of coastal frontogenesis (from McCarthy, 1977).

transition of the large-scale flow from cold to warm advection, and the front conforms more closely to the shape of the coastline. It is clear in the analysis of the onset of the event of 24 December 1970, reproduced in Fig. 1.4, that the warm advection at the ground never penetrates beyond the immediate coast, except over Cape Cod. In the analysis of 4 December 1968, shown for comparison, the easterly flow reaches well inland to the high terrain. Such cases are often characterized by a period in which the most rapid warming occurs at the (higher) inland stations. In all cases, the surface flow over inland sections eventually weakens and turns into the north.

These two patterns are evidently connected with the initial strength or weakness of the pressure ridge over land, as well as that of the large-scale easterly flow. The high pressure is primarily a reflection of an extremely shallow temperature anomaly, of which no evidence exists at 850 mb (Bosart et al., 1972). To the extent that the ridge is the result of cold-air damming, its presence is initially independent of any strong frontogenesis which may ensue. However, the combination of radiative cooling over land and sensible heating over water also contributes to the hydrostatic pressure gradient. It is likely that in the more baroclinic events, the resulting land-breeze tendency is strong enough to establish the initial coastal convergence and frontogenesis.

The description of the coastal front as a land-breeze becomes inadequate soon after the appearance of the convergence zone. One reason is that the front becomes quasi-stationary over land, where the land-breeze model requires surface divergence and frontolysis. Further,
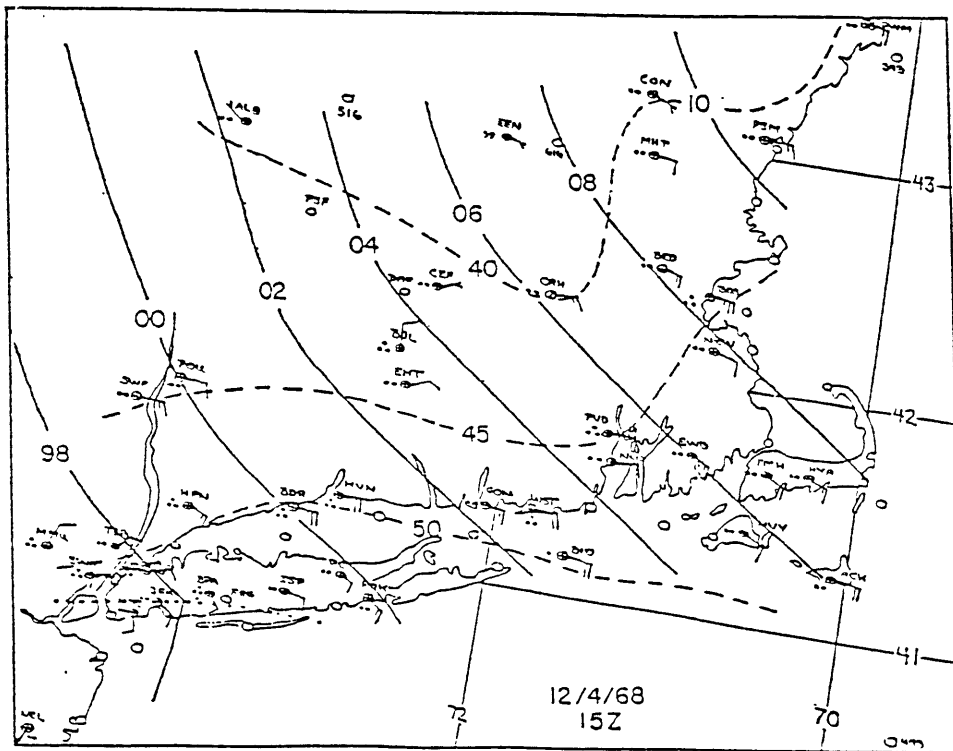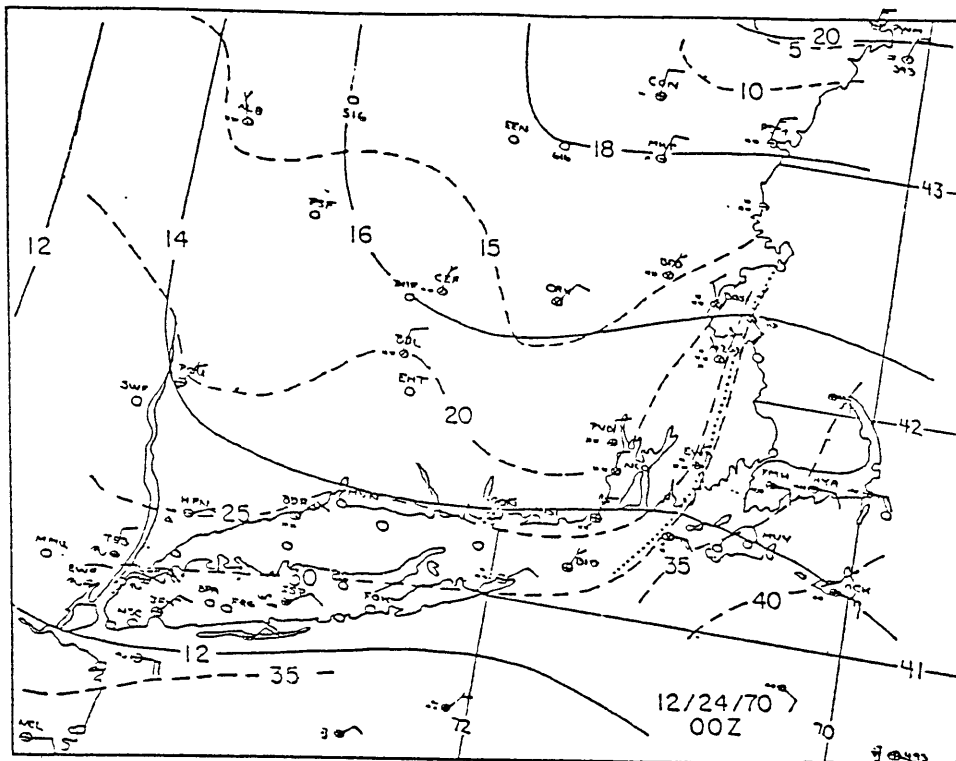
Fig. 1.4. Mesoscale synoptic analyses of two coastal front events near time of onset. The cases differ in air-sea temperature contrast and geostrophic wind speed. (From Bosart et al., 1972)

the notion of a land-breeze circulation embedded in a geostrophic onshore flow requires sudden relative cooling by the land surface as the ocean-equilibrated flow crosses the coast. With radiative effects curtailed by cloudiness, such an effect is of dubious importance.

Eliminating the land-breeze model certainly does not exclude a more fundamental solenoidal theory for coastal fronts. The latter requires only a baroclinic flow prevented through some mechanism from achieving or maintaining geostrophic balance. In some instances of frontogenesis, such as low-viscosity density currents, there is no other mechanism than the rapidity with which the density anomaly is created. Thunderstorm gust fronts provide the most familiar example. In large-scale frontogenesis, background geostrophic wind deformation is the crucial mechanism, as revealed analytically by Stone (1966) and Hoskins and Bretherton (1972).

The data analyzed by Bosart (1975) make it clear that neither of these factors is instrumental in the case of the coastal front. In the first place, there is sufficient time during the 6-12 h development of the front to reach thermal wind balance with the initial temperature gradient. Furthermore, the coastal front forms without exception in a zone of neutral or adverse geostrophic deformation.

The need to identify an ageostrophic deformation mechanism has produced speculation on the possible role of the surface friction and orography. Any diabatically-forced high pressure anomaly over land is an independent effect also worthy of consideration, particularly since a flow of 10 m/s has a stagnation pressure of only about 1 mb. The diabatic effect has been mentioned in connection with the possibility of an initial

land-breeze circulation. However, for the reasons already cited, and because the effect does not explain the failure of the cold air to respond to large-scale changes in the geostrophic wind, it is believed that <u>local</u> diabatic forcing is not necessary. This point will be argued further in chapter 5 in discussing a numerical simulation by Ballantine (1980), who concluded otherwise.

Ballantine also determined that the coastal contrast in surface roughness makes a non-essential, though positive, contribution to the frontogenesis. This conclusion is a more persuasive one simply because the frictional contribution is not as sensitive to the details of the environment. It can be shown, for example, that an Ekman-type balance using Rayleigh friction requires that the deceleration vary roughly as the square of the turning angle, with a typical angle of 20 deg corresponding to a decelaration of only about ten percent. It is known that even a low mountain barrier has the potential for a much greater effect on a statically stable flow.

Certain quantitative details of the vertical structure of the coastal front are needed to complete the review. The topography of southern New England is shown in Fig. 1.5. The east-west cross-section through the southern mountains is sufficiently complex to make it difficult to identify the characteristic vertical and horizontal distances. An average value for the height of the two ridges is about 500 m, and the horizontal scale appears to be about 100 km. However, the "half-width", or distance over which half of the relief occurs, is much shorter than 100 km.
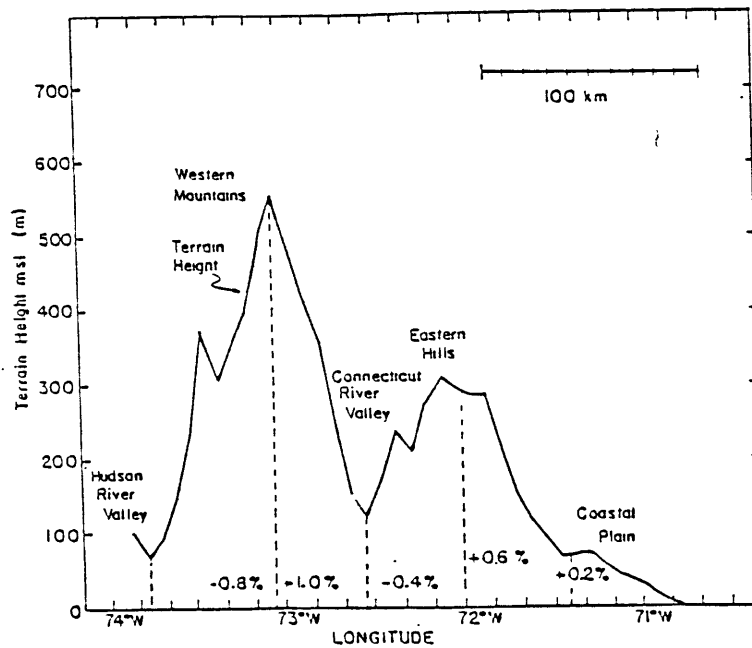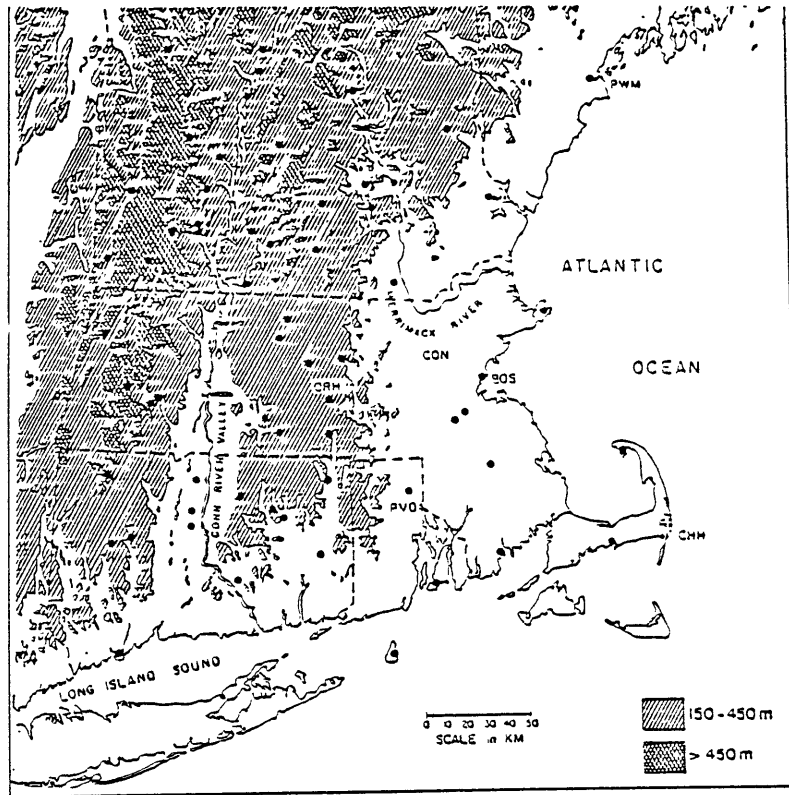
Fig. 1.5. Plan view and vertical cross-section of topography of southern New England. Cross-section is averaged over state of Massachusetts. (From Passarelli and Boehme, 1984).

McCarthy (1977) provides cross-sectional isentropic analyses for several cases during 1969-1975, based on a combination of surface observations and sounding data. Fig. 1.6 shows the strong case of 24 December 1970, also studied by Bosart et al. (1972). The cross-section spans the state of Massachusetts along roughly the same line as in the topographic cross-section in Fig. 1.5. Although soundings were available only at the endpoints, McCarthy's analyses of several other cases using additional upper air data over Boston contained no surprises. His conclusions about the shape of the isentropes over the water and along the mountain slopes are reasonable inferences in view of the obervations of ocean temperature and surface wind.

The warm-front inversion near 850 mb happens to be unusually weak in this case. Of particular interest is the stratification below 850 mb in the upstream sounding (CHH). The potential temperature plotted between 1000 mb and 850 mb determines a buoyancy frequency of about .01 s^{-1}, a low value for the troposphere. However, it may be assumed that the ambient stratification was stronger during the early frontogenesis, when the air was colder over the water. Indeed, the vertical gradient is generally larger at CHH in McCarthy's other cases, and is nearly twice as strong at ALB in the case shown. The horizontal temperature gradient evident in the slope of the 275 K isentrope is also noted. The wind profile at CHH showed a uniform southwesterly shear totalling 20 m/s between 1000 and 800 mb. Thus, the best estimate for the ambient shear is .01 s^{-1}, which, however, probably underestimates the thermal wind (and indirectly the warm advection) in the layer.
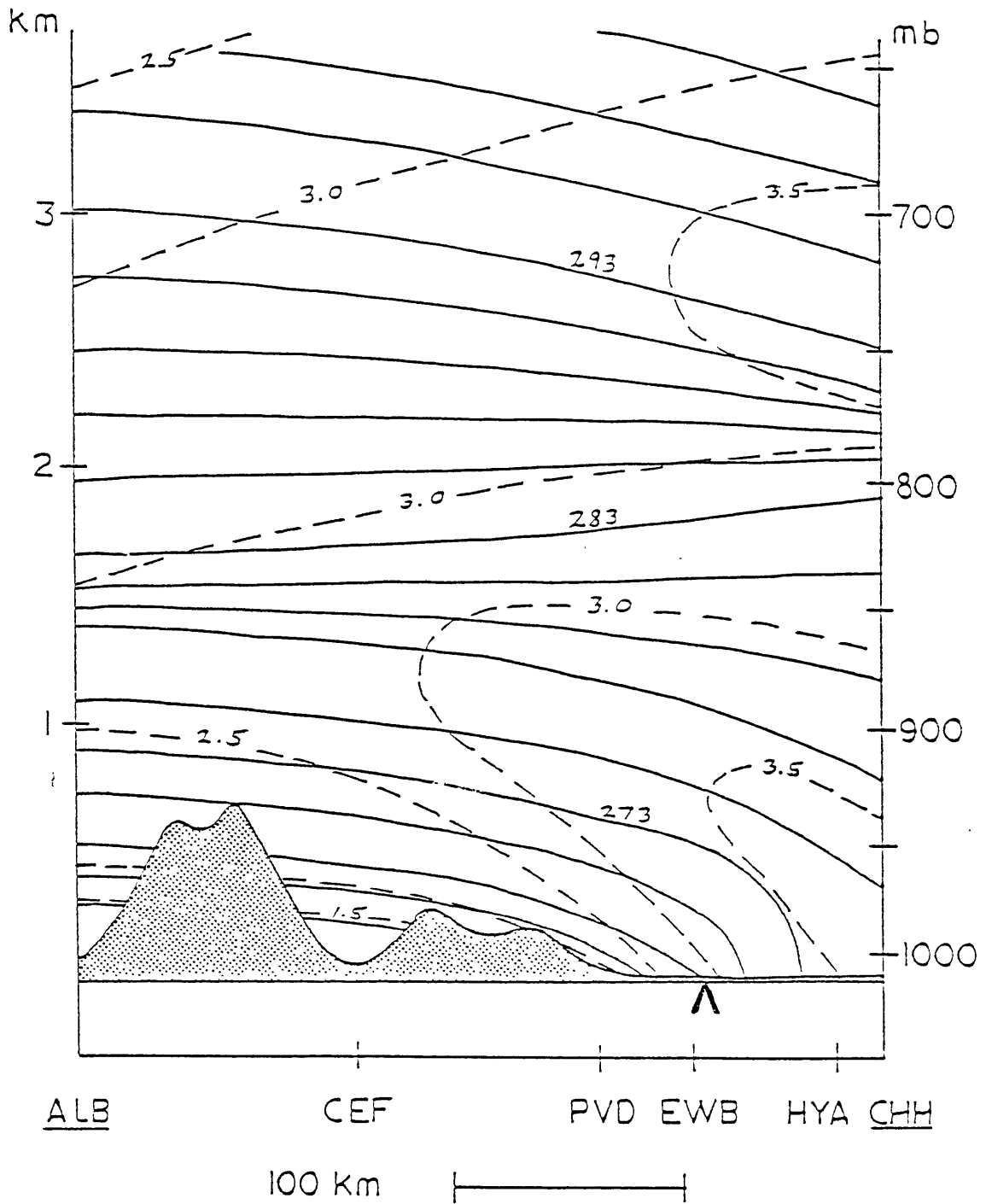
Fig. 1.6. Cross-sectional analysis of potential temperature (K) and water vapor mixing ratio (g/kg) between Chatham, MA, and Albany, NY, during coastal frontogenesis on 24 December 1970 (from McCarthy, 1977).

A far more detailed cross-section, based on aircraft observations analyzed by Neilley (1984), is shown in Fig. 1.7 in order to bring out an important point. The data were obtained along the coast of New Hampshire, where the coastal topography is steeper, and the air-sea temperature contrast stronger. Neilley (1984) has demonstrated that the front behaves essentially as a density current with relative normal flow on both sides, and an extremely subgeostrophic vertical shear of the parallel wind. The ageostrophy suggests an important, if secondary, role for local diabatic or frictional effects in determining the flow on the smallest scales of the well-developed front. For the time being, modelling these small-scale characteristics must be given a lower priority than the effort to identify the basic dynamics and dimensions of the cold-air pooling.

1.4 Proposed mechanism for rapid frontogenesis

The proposed frontogenesis mechanism is a simple extension of the blocking scenario investigated by PW. The single addition to the conditions in their study is a synoptic-scale horizontal temperature gradient. Although the focus is on a streamwise gradient, a component along the mountain barrier will also be considered, in analogy to the oblique case of frontal deformation discussed in section 1.1. Thus, it is proposed that a two-dimensional barrier under conditions of large-scale warm advection can instigate and support rapid wind-side frontogenesis, in which the maximum strength of the gradient is limited only by diffusion. It is further proposed that a component of temperature gradient parallel to the barrier can substantially strengthen and accelerate the frontogenesis through the process of horizontal shearing deformation.

POTENTIAL TEMPERATURE (C) AND WIND 1/10/83

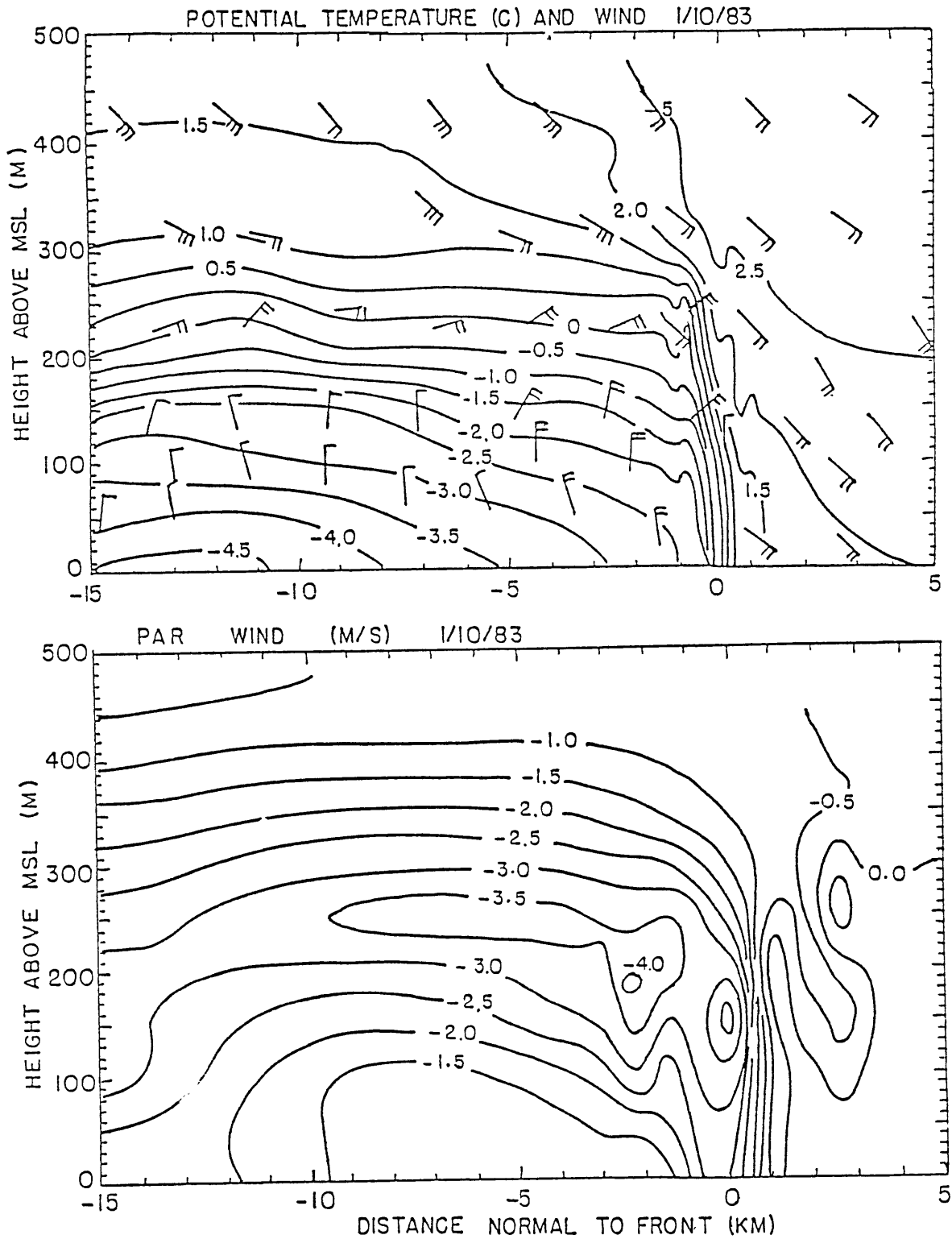PAR WIND (M/S) 1/10/83

DISTANCE NORMAL TO FRONT (KM)

Fig. 1.7. Analyzed cross-sections of aircraft-observed potential temperature and wind in mature coastal front (from Neilley, 1984).

There are fundamental differences between the classical and the hypothesized orographic mechanisms. The proposed initiating mechanism consists of a barrier-induced ageostrophic vertical circulation, which evidently cannot be distinguished analytically from the additional solenoidal circulation made possible by the horizontal gradient. In contrast, the deformation field in classical frontogensis is horizontal and independently balanced, or else (in the Eady problem) can be analyzed independently of the ageostrophic circulation because of the balance assumption. A further crucial difference is that in the classical case, fluid parcels reside in the geostrophic deformation for the duration of the frontal collapse. The residence time in the ageostrophic deformation may be quite limited.

A frontogenetical feedback mechanism missing from the barotropic simulations of PW is suggested by the Scandinavian "model" discussed in section 1.1. Namely, in the baroclinic flow, the energy needed to overstep the barrier increases in time as the static stability, and local Froude number, are modified by vertical shearing deformation of the potential temperature field. The implied feedback is positive only in the warm-advection case.

Since background rotation is a necessary feature of the baroclinic flow, a stagnant layer cannot extend indefinitely far upstream, but is limited essentially to the deformation radius. If this radius is strictly determined by the barrier height and a uniform ambient potential vorticity, it is not time-dependent. Thus, the frontogenesis is expected to occur at an upstream distance approximating the deformation radius, provided the initial Froude number and horizontal temperature gradient are large enough.

There is some reason to suspect that coastal frontogenesis depends crucially on non-uniform initial conditions. In particular, the shallow high pressure over land and the stratification discontinuity near 850 mb appear from observations to be indispensible features of the environment. The present investigation aims, however, to determine the robustness of a basic mechanism, and will leave the matter of non-uniform initial conditions largely to inference or later study. Note, however, that the generation of a meso-high by orographic means is not excluded.

It will be assumed that the development of a steady, nonlinear inviscid solution from uniform initial conditions demonstrates the insufficiency of the proposed mechanism for given parameter choices. Conversely, if such an equilibration does not take place without the help of numerical effects, a process of frontogenesis limitable only by diffusion will be inferred. In this regard, it should be known that all of PW's rotating barotropic simulations reached a quasi-steady state which contained no stagnant fluid.

Thought experiments about orographic frontogenesis require very difficult deductions about the disturbance pressure and parallel wind. A more fruitful exercise is a formal analysis of the linear response to stationary line sources in a baroclinic flow. This part of the study is carried out in chapter 2 to determine whether baroclinicity in the linear disturbance offsets or supports the possible nonlinear effect described above. Chapter 3 attempts to relate the linear analysis to physical scenarios involving smooth forcing distributions. The linear baroclinic solutions, interpreted at finite amplitude, should crudely indicate under what conditions the vertical stratification can be sufficiently enhanced to allow blocking.

Chapter 4 is devoted to describing and verifying a new grid-point model developed for rapid frontogenesis. The model simulations to test the orographic hypothesis are presented in chapter 5, along with the overall conclusions of the study. The simulations are limited to cases of moderate Froude number, in which blocking would not not occur under barotropic conditions.

CHAPTER 2.   LINEAR RESPONSES TO LINE-SOURCE FORCING

Because frontogenesis in general is a nonlinear alteration of temperature and velocity fields, it is not directly accessible through ordinary linear analysis. Strictly interpreted, the linear study in this chapter will describe only the weak reaction of a stable baroclinic flow to isolated stationary forcing. Further, since nonlinear interactions are not modelled, the nature of the forcing is necessarily ad hoc. The expectation based on the discussion in chapter 1 is that the linear solutions will illuminate the important processes in the generation of a finite-amplitude upstream response, while also resolving the disturbance into barotropic and baroclinic effects. In addition, the linear results are to be used to verify the numerical model developed later for the finite-amplitude study.

2.1 The physical model and equations

The essential features of rapid frontogenesis are captured in the two-dimensional primitive equations with constant background rotation. Applications of slab-symmetric f-plane models include stratified flow over a ridge, sea-breeze circulations, slant convection and classical frontogenesis, all of which share basic properties with rapid frontogenesis. To obtain the minimal baroclinic version of the model, it will be assumed that the flow is Boussinesq and hydrostatic, and that the basic geostrophic wind and thermal stratification are uniform, except for a constant shear in the parallel velocity component.

The first undertaking is to develop the parameter and forcing dependence for the linearized system. It will be shown that the problem is completely determined by the amplitude and shape of the forcing distribution and three dimensionless quantities: the Rossby and Froude numbers, and a third parameter measuring the baroclinicity. The dependence on the first two has been studied extensively in the case of steady topographic forcing since that particular problem was formally posed by Queney (1947). Recently, Pierrehumbert (1984) has used asymptotic analysis of the Green's function solution to investigate the barrier effect of mountain ridges. The same approach will be used here to study the special effects of baroclinicity and interior forcing.

Emphasis will be placed on describing the steady upstream response to interior and topographic forcing, and on determining the forcing strength needed to induce nonlinear effects in the near-field response. More particularly, estimates of the horizontal velocity perturbation will be sought in terms of the three flow parameters just named and the amplitude of the forcing. The baroclinic topographic problem will be covered briefly at the end of the chapter in further preparation for the discussion of blocking and frontogenesis theories in chapter 3.

The nonlinear, non-hydrostatic and time-dependent system is written, for reference, in the form

$$du/dt = fv - p_x \tag{2.1a}$$

$$dv/dt = -fu \tag{2.1b}$$

$$dw/dt = b - p_z \tag{2.1c}$$

$$db/dt = 0 \tag{2.1d}$$

$$0 = u_x + w_z, \tag{2.1e}$$

in which $d/dt \equiv \partial/\partial t + u\partial/\partial x + w\partial/\partial z$ is the parcel derivative in two dimensions, and $b \equiv g\theta/\theta_0$ is the potential buoyancy, i.e., the product of the gravitational acceleration and nondimensional potential temperature. The notation for the Coriolis parameter, pressure, velocity and independent variables is standard. The equations belong to the same Boussinesq system used by Williams (1972) and Hoskins and Bretherton (1972) for large-scale frontogenesis, and by Bennetts and Hoskins (1979) for slant convection.

Appropriate boundary conditions include no-normal-flow at the ground and energy radiation at large z or x. The basic state is to consist of linear fields of both temperature, $B = fV_z x + N^2 z$, and velocity, $(U,V) = (U_0, V_0 + V_x x + V_z z)$, with U_0, V_0, V_x, V_z and the buoyancy frequency, N, all constant. These choices are consistent with the requirements of two-dimensionality and basic-state geostrophic and hydrostatic balance. The absence of shear in the x-component of velocity can be a significant limitation of the model, and will be considered further in chapters 3 and 5.

The normalization of the equations is based on vertical and horizontal distance scales, H and L, to be specified later. The remaining scales are $N^2 H$ and $N^2 H^2$ for the perturbation buoyancy and pressure, L/U_0 for the time, and U_0, $U_0 a$ and $U_0 H/L$ for the perturbation velocity components in x, y and z, respectively. Here $a \equiv \sqrt{(1+V_x/f)}$ is the square-root of the nondimensional absolute vorticity, assumed positive. With u, v, w, b and p henceforth representing the nondimensional perturbations, and x, y, z and t the nondimensional independent variables, the linearized system is

$$R(u_t + u_x) = v - RF^2 p_x + RF_u(x,z) \qquad (2.2a)$$

$$R(v_t + v_x) = -u - RF\beta w + RF_v(x,z) \qquad (2.2b)$$

$$0 = b - p_z \qquad (2.2c)$$

$$b_t + b_x = -w - (RF)^{-1}\beta u + F_b(x,z) \qquad (2.2d)$$

$$0 = u_x + w_z. \qquad (2.2e)$$

The three parameters are defined $R = U_0/(faL)$, $F = NH/U_0$ and $\beta = V_z/(Na)$. The friction and heating, F_u, F_v and F_b, are in units of U_0^2/L, $U_0^2 a/L$ and $N^2 H U_0/L$, respectively. These forcing terms are intended to include certain "apparent" sources such as nonlinear meridional (x-z) advection and linear zonal advection of momentum or temperature. Hence the terms "friction" and "heating" are used loosely.

In the vertical momentum equation (2.2c), the neglected acceleration terms are proportional to F^{-2} and the square of the aspect ratio, H/L. If the forcing has depth and width scales of h and ℓ, and since the only alternative vertical and horizontal scales are U_0/N and U_0/f, it can be shown that H/L may only assume the values f/N, h/ℓ and products of these with $U_0/(Nh)$ and $f\ell/U_0$. Hence, the hydrostatic approximation (dw/dt = 0) adopted above is justified for all quasi-steady disturbances of interest with $h/\ell \ll 10^{-1}$ and N on the order of 10^{-2} s^{-1}.

The mathematical inhomogeneities in the problem consist of the three sources and topographical forcing. Although these introduce external length scales, the overall notation will be simplest if the internal scales, $H = U_0/N$ and $L = U_0/(fa)$ are used. The scaling is not aimed at further reducing the equations. The choices for H and L imply

that $R = F = 1$, and show that in the absence of baroclinicity and forcing, the hydrostatic equations are fundamentally parameter-free.

The parameters associated with the forcing are its nondimensional depth, $Nh/U_0 \equiv Fr$, and width, $fal/U_0 \equiv Ro^{-1}$, which have been identified as a Froude number and an inverse Rossby number, respectively. An interior source is therefore proportional to some nondimensional, order-unity distribution, $g_1(Ro\ x, Fr^{-1}z)$, which may have order-unity variations with respect to its arguments.

Steady topographical forcing is imposed at $z = 0$ by the boundary condition

$$\psi(x,0) = Fr\ g_0(Ro\ x), \qquad (2.3)$$

where $\psi = -\int^z u\,dz'$ is the nondimensional mass streamfunction, and g_0 has properties like g_1. Note that the height of the topography enters the linear problem as an amplitude, Fr, rather than an actual distance (in the sense of a wavelength or decay scale). Further information or assumptions will be needed to determine the amplitude of the interior forcing.

The baroclinic parameter, $\beta = V_z/(Na)$, is related to the Richardson number, $Ri \equiv N^2/V_z^2$, through $\beta^2 = Ri^{-1}(1+V_x/f)^{-1}$. Because Ri involves a horizontal temperature gradient in this case, the condition for neutral linear modes is that $Ri > (1+V_x/f)^{-1}$ (e.g., Bennetts and Hoskins, 1979). To eliminate free inertial instability, the Richardson number inequality and the equivalent condition $|\beta| < 1$ will be assumed throughout. Under the further assumption that $U_0 > 0$, particular attention will be given to the case $\beta < 0$, corresponding to basic-state warm advection and negative parallel shear, as this choice is relevant to the frontogenesis problem.

2.2 Dispersion properties of the neutral baroclinic modes

The time-dependent wave equation is derived by Bennetts and Hoskins (1979). Its steady-state, nondimensional form, based on (2.2a)-(2.2e), is

$$\psi_{xxzz} + \psi_{xx} - 2\beta\psi_{xz} + \psi_{zz} = 0, \qquad (2.4)$$

where the streamfunction ψ satisfies $\psi_x = w$ and $\psi_z = -u$ in accord with mass conservation. The first term in the equation is related to the advection of horizontal vorticity, $-u_z = \psi_{zz}$, and is necessary for the existence of wavy, propagating solutions. The terms ψ_{xx} and ψ_{zz} arise, respectively, from the gravitational and inertial restoring forces. In effect, these forces are modified by the advection of basic-state wind, $V(z)$, and temperature, $B(x)$, which gives rise to the baroclinic term proportional to β. A separate balance among the last three terms, which are elliptic when $|\beta| < 1$, yields a trapped response to localized forcing.

The nature of the inhomogeneities for the streamfuncton equation, and the various limiting responses, will be considered in the next section. A useful preliminary is to examine the effect of β on the free waves directly from the dispersion relation,

$$-k^2\mu^2 + k^2 - 2\beta k\mu + \mu^2 = 0, \qquad (2.5)$$

obtained by assuming normal-mode solutions, $\psi = \psi_0\exp(ikx+i\mu z)$, to (2.4). Such modal solutions are vertically evanescent for real k in the range $k^2 < 1-\beta^2$, and horizontally evanescent for real μ in the analogous interval.

A graph of the dispersion relation for the plane-wave modes is shown in Fig. 2.1 for the values $\beta = 0$ and $\beta = -0.6$. In view of the symmetry of (2.5), the graphs can be continued to $k < 0$ by reflecting the plotted curves in the origin. Changing the sign of β causes a reflection in either axis.

A salient effect of non-zero β is to allow propagating modes to exist with wavelengths longer than the barotropic vertical and horizontal cutoffs, $\lambda_C = U_0/N$ and $\lambda_I = U_0/f$, i.e., within the normally evanescent ranges $|\mu| < 1$ and $|k| < 1$. In particular, the limit point at $k = \sqrt{(1-\beta^2)} = \beta\mu$, consists of a solution with velocities exactly along the basic isentropes. The point thus represents a pure inertial oscillation with zero pressure disturbance, and will be identified henceforth as the baroclinic inertial limit. When $\beta = 0$, the isentropes are horizontal, and such a solution is no longer possible for finite μ.

The solution at $\mu = -\sqrt{(1-\beta^2)} = \beta k$ has intrinsic velocities parallel to the basic absolute momentum surfaces, $M \equiv x + \beta z = const$ (dimensionally, $M_* = U_0 aM = fx_* + V$). If M' is the "intrinsic" absolute momentum, defined by measuring x in the basic flow-relative frame, the system conserves <u>total</u> absolute momentum, $m = M' + v$. Hence the second limit, the baroclinic buoyancy limit, is a pure buoyancy oscillation with $v = 0$. When $\beta = 0$, the M-surfaces are exactly vertical and the pure buoyancy oscillations ($k \to \infty$) are not hydrostatic. However, the slope for general β, namely $\alpha_M = -(fa/N)(\partial M/\partial x)/(\partial M/\partial z) = -fa^2/V_z$, can be as small as $\pm 10^{-2}$ in strongly sheared environments. The shear thus makes possible purely buoyant, <u>hydrostatic</u> motions despite the background rotation.

μ

4

3

2

$\underset{\sim}{c}_g'$

$\beta = -0.6$

1

$\beta = 0$

1   2   3   4   5

0    $\longrightarrow k$

$\mu = r/\beta$
$k = r$

$\mu = -r$
$k = r/|\beta|$

$\beta = -0.6$

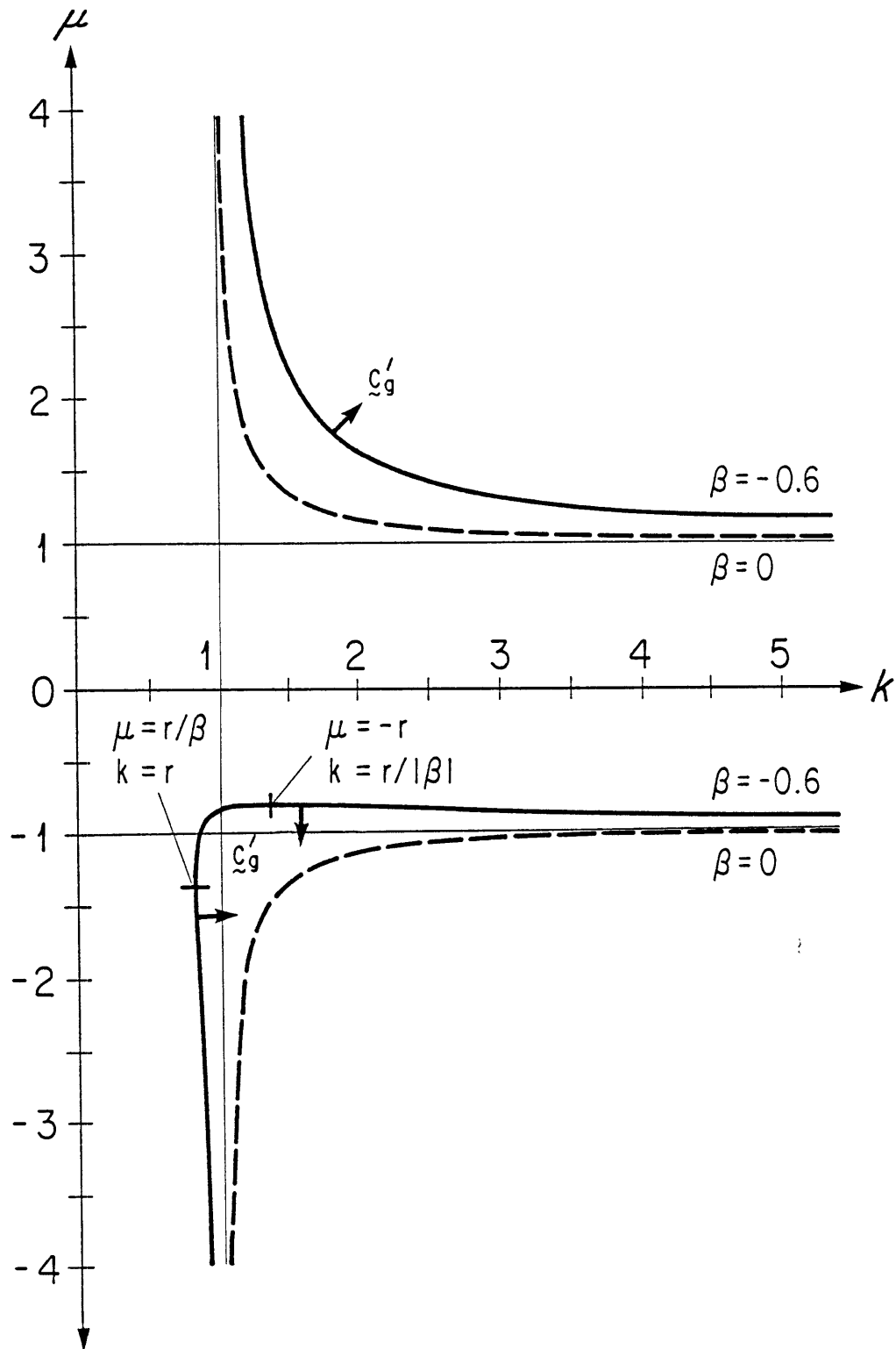$\underset{\sim}{c}_g'$

$\beta = 0$

-1

-2

-3

-4

Fig. 2.1. Dispersion relation for gravity-inertia plane waves assuming baroclinic (solid) and barotropic (dashed) basic state. Limit points $k = \sqrt{(1-\beta^2)} \equiv r$ and $\mu = -r$, and direction of group velocity, are indicated in baroclinic case.

The parameter $1-\beta^2 \equiv r^2$ is proportional to the inertial restoring force along the basic isentropes. Thus, $\omega_I = rf$ gives the dimensional frequency of free oscillations on these surfaces, and the lowest frequency possible in the neutral modes. The analogous frequency on the absolute momentum surfaces may be expressed $\omega_G = \alpha_M rN$. The parameter r^2 is also proportional to the Ertel potential vorticity, $q \equiv \partial(b,m)/\partial(x,z) = fa^2N^2r^2$, which is an individual constant in the nonlinear system. The potential vorticity is often invoked to restate the Richardson number condition cited in the previous section. That is, the linear modes are neutral if, and only if, $r \geq 0$.

The analogy between the barotropic and baroclinic pure oscillations extends to the energetic properties of the waves; that is, the group propagation at the baroclinic limit points $k = r$ and $\mu = -r$ is entirely horizontal or vertical, as in the limits $k = 1$ and $\mu = \pm 1$. This can be appreciated most easily by noting the relationship between the slope of the graph of $\mu(k)$ and the direction of group propagation. If ω' is the wave frequency in the stationary frame, then the graph in Fig. 2.1 has slope

$$dz/dx\big|_{\omega'=0} = -(\partial\omega'/\partial x)/(\partial\omega'/\partial z). \qquad (2.6)$$

Therefore the slope of the energy vector, $c_{gz}/c_{gx}' = (\partial\omega'/\partial z)/(\partial\omega'/\partial x)$, is also that of the perpendicular to the graph. Here c_{gz} and c_{gx}' denote the two components of the group velocity relative to the stationary frame.

For the most part, the group velocity for $k > 0$ is directed away from both axes (viewed as coordinate axes). However, it can be seen that

for $\beta\mu > r$, group propagation is slightly upward. Inasmuch as the phase propagation is also upward, these shallow modes have an anomalous phase tilt for gravity-inertia waves. The <u>intrinsic</u> horizontal group speed, in general $c_{gx} \equiv c_{gx}'-1 = -(\mu/k)c_{gz}$, is also found to be positive if and only if $\beta\mu > r$. The transition occurs because the correlation between the velocity and the hydrostatic pressure changes sign when the fluid motions become shallower than the basic isentropes, i.e., when upward displacement is associated with warm anomaly. (Instability is then precluded only by the inertial restoring force.) This explanation is based on the equivalence of the energy vector and the "pressure flux", whose components are pu and pw.

The other transition, at $|\beta|k = r$, coincides with a critical value of the horizontal pressure flux, pu. It can be seen that for the steeper waves, i.e., $|\beta|k > r$, the relative group speed, c_{gx}', is negative. As a consequence of the strong vertical advection of background parallel wind in these modes, v is more strongly correlated with vertical than with streamwise displacement. The Coriolis acceleration in the x-momentum equation then fails to offset the advection, and an unusually strong horizontal pressure gradient arises.

Thus, the solution at $|\beta|k = r$ resembles nonrotating hydrostatic gravity waves in having only vertical dispersion, while in the steeper waves, the pressure disturbance is strong enough that $|pu| > 1$ (in units of U_0^3) and $c_{gx}' < 0$. The baroclinic buoyancy waves have the "proper" tilt in that group propagation is upward (downward) if the corresponding M-surfaces slope to the left (right) with height. The fact that upstream propagation also requires downward propagation in a warm-advection basic

state ($\beta < 0$) will be thematic in the results to follow. Upstream-propagating modes can also be recognized as having u smaller in amplitude than the x-component of perturbation absolute momentum, u-y' (where y' is the parallel displacement), which in turn is proportional to the pressure perturbation (see Smith, 1979).

The discussion of energy propagation is a proper context for some remarks on transient waves. If $\beta = 0$, the horizontal group speed for the transients may be written without explicit reference to the frequency as

$$c'_{gx} = 1 \pm \mu^{-1}/\sqrt{(1+\mu^2/k^2)}, \qquad (2.7)$$

where the second term takes the sign of the intrinsic horizontal phase speed. In discussing mechanisms for upstream influence in a steady, nonrotating flow, Pierrehumbert and Wyman (1985) point out that sufficiently large μ^{-1} (identifiable with the Froude number) permits upstream energy propagation, as can be seen by taking $\mu/k = 0$ in (2.7). However, modes with $\mu \neq 1$ in such a system must have $k = 0$ (and are not buoyancy oscillations). Moreover, energy propagation by these so-called "columnar modes" clearly requires a horizontal spectrum of buoyancy waves near $k = 0$.

Therefore the columnar disturbance can be understood only in connection with transient or evanescent modes. In a rotating system, the frequency of the upstream transient waves must be at least O(f), since in order to get $\mu^{-1} > 1$, it is necessary to satisfy

$$(\omega'/k - 1)^2 - k^{-2} > 1, \qquad (2.8)$$

the left side being the same as μ^{-2}. Therefore, unless the relative frequency ω' <u>and</u> the horizontal scale $1/k$ are at least $O(1)$ (in units of f and U_0/f, respectively), not even the transients will carry the disturbance upstream, regardless of the vertical scale of the forcing. PW used this fact implicitly to interpret their barrier-flow simulations. They estimated the radius of upstream influence by integrating (2.7), with $\mu/k = 0$, over a time period of length $1/f$.

Another way to generalize the columnar disturbance is to associate the $k = 0$ modes with the steady, horizontally-evanescent normal modes of the rotating system. However, the connection is misleading if the steady solution significantly underestimates the amplitude of the upstream disturbance during the transient phase. It will be assumed here that rotation is important enough that the effect of the transients, with ω' and $k \gg 1$, is to produce only a small shift in the sufficient conditions for blocking. Note, however, that this assumption is incorrect in PW's infinite Rossby number simulations, in which blocking occurs despite the non-existence of steady-state upstream effects.

In the rotating barotropic case, the horizontally-evanescent modes alone determine the upstream response when the forcing consists of a distribution in z. In the baroclinic case, the analogous modes with real μ become both damped and oscillatory in x, and the damping distance no longer vanishes at the buoyancy limit, $\mu = r$. In fact, $1/\left|k\right|$ remains $O(1)$ throughout $\mu < r$ for moderate values of β, thus permitting a more significant upstream disturbance. Recall, as well, that the baroclinic plane-wave disturbance can extend a certain distance upstream because of the negative horizontal group speeds. These important upstream baroclinic effects will all appear in the Green's function analysis.

2.3 Green's function for an interior source

The foregoing energy considerations will be needed in the
construction of the Green's function solutions to the forced equation.
To establish some preliminary contact with the physical problem, consider
the form of the inhomogeneity in the streamfunction equation. Given the
sources F_u, F_v and F_b, the problem for ψ is found from (2.2a)-(2.2e)
to be

$$\pounds(\psi) = \frac{\partial}{\partial x}F_b - \frac{\partial^2}{\partial x \partial z}F_u - \frac{\partial}{\partial z}F_v , \qquad (2.9)$$

where $\pounds$ is the linear operator in (2.4). Hence, a circulation can be
driven by x-gradients in the heating or in the vertical derivative of the
streamwise friction, as well as by a vertical gradient in the cross-stream
friction.

Since it may be assumed that the friction decreases upward from
the ground, (2.9) shows that the first two sources are negative if the
strongest friction and cooling occur downstream. However, the sign of the
third source is less obvious. If the transverse friction is due to
surface stress, and the basic-state surface flow, V_0, is negligible, the
sign of F_v must be opposite that of the induced low-level flow parallel
to the forcing. Most often, this flow is toward low pressure, so that
$F_v < 0$, and the third source is also negative. The important task of
estimating the actual forcing amplitude for these and other physical
scenarios will be undertaken in the next chapter.

Because the contribution from topography is additive, (2.9) may be
solved subject to $\psi = 0$ at $z = 0$. Let the forcing consist of a

concentrated source at $x = x_0$ and $z = z_0$, i.e., $\mathcal{L}(\Psi) = \delta(x-x_0)\delta(z-z_0)$.
Then, after obtaining

$$\mu = \beta k/(1-k^2) \pm k(k^2-r^2)^{1/2}/(k^2-1) \qquad (2.10)$$

from (2.5) for the vertical wavenumber, the Green's function for all $z \geq 0$
may be written

$$\Psi = -\frac{1}{2\pi}\int_{-\infty}^{\infty}\exp\left[ik\left(x-x_0+\frac{\beta(z-z_0)}{1-k^2}\right)\right]\frac{\exp\left(i\mu_0\left|z-z_0\right|\right)-\exp\left(i\mu_0(z+z_0)\right)}{2ik(k^2-r^2)^{1/2}}dk. \quad (2.11)$$

The square-root occurring in $\mu_0(k) \equiv k(k^2-r^2)^{1/2}/(k^2-1)$ must be chosen
to satisfy a radiation condition at $z \to \infty$. For $k^2 < r^2$, $\text{Im}\{k(k^2-r^2)^{1/2}\}$
< 0 is needed for boundedness. Elsewhere μ_0 is real, and the branch
corresponding to upward energy propagation, namely $(k^2-r^2)^{1/2} > 0$, must
be used in (2.11).

The negative branch of $(k^2-r^2)^{1/2}$ is the implicit choice for the
unreflected waves (first term in the integrand) below the source, which
are obviously the result of downward group propagation. The negative
branch can be identified in Fig. 2.1 as being continuous at $k = 1$ and
containing the baroclinic buoyancy waves. If $\beta > 0$, these waves instead
have upward group velocity. It follows from these remarks and
ray-tracing theory that the baroclinic modes, with bounded μ and k, will
alter not only the symmetry of the solutions with respect to the forcing
level, but the length scales as well.

The term depending on $z+z_0$ in the Green's function integral can be
attributed mathematically to an image near $x = x_0$, $z = -z_0$. However, as
long as $\beta \neq 0$, the wave equation is non-separable and the location of the

image is wavenumber-dependent. The phase of the unreflected waves can be expressed

$$\phi^{\pm}(x,z) = k(x-x_0) + \mu^{\pm}(z-z_0) ,\qquad (2.11)$$

where $\mu^{\pm} \equiv \beta k/(1-k^2) \pm \mu_0$ is defined. The phase of the reflections can then be written more transparently as $\varphi^{+}_{ref}(x,z) = \phi^{-}(x,0) + \mu^{+}z$. If $\beta \neq 0$, then $\mu^{+} \neq -\mu^{-}$ and the angle of reflection from the lower boundary differs from the angle of incidence. Also if $\beta \neq 0$, the damped modes in $-r < k < r$ are tilted toward the ambient absolute momentum surfaces, and their image points are shifted toward the extension of the M-surface containing the source, i.e., the surface $x-x_0 + \beta(z-z_0) = 0$.

By using the radiation constraints on μ_0, the Green's function can be rewritten with a real integrand as

$$\Psi = -\frac{1}{2\pi} \int_0^r \frac{\exp\left(-\mu_{0i}\left|z-z_0\right|\right)-\exp\left(-\mu_{0i}(z+z_0)\right)}{k\sqrt{(r^2-k^2)}} \cos k\left(x-x_0+\frac{\beta(z-z_0)}{1-k^2}\right) dk$$

$$-\frac{1}{2\pi} \int_r^{\infty} \left\{ \frac{\sin\left(k(x-x_0+\frac{\beta(z-z_0)}{1-k^2})+\mu_0\left|z-z_0\right|\right)}{k\sqrt{(k^2-r^2)}} \right. \qquad (2.12)$$

$$\left. -\frac{\sin\left(k(x-x_0+\frac{\beta(z-z_0)}{1-k^2})+\mu_0(z+z_0)\right)}{k\sqrt{(k^2-r^2)}} \right\} dk,$$

where $\mu_{0i} = (1-k^2)^{-1}k\sqrt{(r^2-k^2)}$ in the first integral, and $\mu_0 = (k^2-1)^{-1}k\sqrt{(k^2-r^2)}$ in the second. For later reference, the equivalent vertical transform is given without the reflection terms as

$$\Psi = -\frac{1}{2\pi} \int_0^r \frac{\exp\left(-k_{0i}\left|x-x_0\right|\right)}{\mu\sqrt{(r^2-\mu^2)}} \cos\ \mu\left(z-z_0+\frac{\beta(x-x_0)}{1-\mu^2}\right)\ d\mu$$

$$+\frac{1}{2\pi} \int_r^1 \frac{\sin\ \left(\mu(z-z_0+\frac{\beta(x-x_0)}{1-\mu^2})-k_0\left|x-x_0\right|\right)}{\mu\sqrt{(\mu^2-r^2)}}\ d\mu \qquad (2.13)$$

$$+\frac{1+\mathrm{sgn}(x-x_0)}{2}\frac{1}{2\pi} \int_1^\infty \{ \frac{\sin\ \left(\mu(z-z_0+\frac{\beta(x-x_0)}{1-\mu^2})-k_0(x-x_0)\right)}{\mu\sqrt{(\mu^2-r^2)}}$$

$$-\frac{\sin\ \left(\mu(z-z_0+\frac{\beta(x-x_0)}{1-\mu^2})+k_0(x-x_0)\right)}{\mu\sqrt{(\mu^2-r^2)}}\ \}\ d\mu + \cdots\ ,$$

where $k_{0i} = (1-\mu^2)^{-1}\mu\sqrt{(r^2-\mu^2)}$, etc. The horizontal asymmetry of the plane-wave component is more apparent in the second formulation. Notice in particular that there is no wavy disturbance in $x < x_0$ if $r = 1$ ($\beta=0$). The vertical transform is, however, of limited use because the integral for the wave reflections is unwieldy when $\beta \neq 0$.

Both (2.12) and (2.13) can be reduced to simpler forms by applying certain near- and far-field approximations. These will be discussed separately in the next two sections. Except for the propagating part of the far-field response, all of the limiting solutions are affected by one or more of the singularities in the integrals, which therefore merit some preliminary consideration.

In an infinite domain, the simple pole in the long-wave integrals ($0 < k < r$ and $0 < \mu < r$), would produce logarithmic behavior in the streamfunction at large x and z. However, the pole is removed through the effect of a solid lower boundary, which stops the growth of Ψ outside a radius comparable to the height of the source.

There is no singularity near the source because the overall factor multiplying the integrand in (2.12) decreases as k^{-2}, rather than k^{-1}, for large k (showing the effect of vorticity advection). It is significant that the same factor becomes k^{-2} for all k when the problem is posed with f = 0. The integral then diverges because of the small wavenumbers, regardless of the boundary conditions. The implied large response in the limit of weak rotation is concealed by the scaling in (2.12), but in fact, the dimensional streamline displacement, Ψ_*/U_0, is proportional to $\lambda_I \equiv U_0/f$ in this limit.

The f = 0 singularity has an interpretation similar to that for steady flow over a two-dimensional step (e.g., Lilly and Klemp, 1979). That is, in practical applications, the assumptions of a uniform environment, zero viscosity and two-dimensional forcing often cease to apply on scales comparable to λ_I when this distance is large enough to produce an extreme response. If the assumptions do not break down before λ_I becomes very large, then indeed only a nonlinear or unsteady response is possible.

An integrable square-root singularity at k = r also affects the solution when the $O(\lambda_I)$ horizontal scales are relevant. Although the energy propagation becomes horizontal at this point in the spectrum, where the graph of $\mu(k)$ is vertical, the analysis will show that vertical dispersion due to buoyancy still affects the associated downstream wave-train. An analogous result will be found to apply to the buoyancy disturbance ($\mu \approx r$) directly above and below the source. There, the amplitude and phase of the streamfunction are controlled by horizontal dispersion induced by rotation. As already observed, this rotational

influence yields to nonlinear, three-dimensional, transient or other effects as $f \to 0$. The other limit, $N \to 0$, requires a non-hydrostatic analysis.

Finally, it is noted that the square-root singularity splits from the essential singularity at $k = 1$ when $\beta \neq 0$. The effect is to superimpose broader vertical scales on the slowly-decaying inertial wave-train, and (less significantly) to suppress the very short vertical scales on one side of the horizontal axis. Analogously, the buoyancy disturbance acquires intermediate horizontal length scales, and the rapidly-varying component is concentrated on one side of the vertical axis. The horizontal dispersion of the buoyancy disturbance, whose slowly-varying components are especially important for upstream influence, will be easier to analyze in the vertical transform (2.13).

2.4 Far-field asymptotic response

The trapped part of the far-field Green's function, valid in $(x-x_0)^2 + (z \pm z_0)^2 \gg 1$, is

$$\Psi_{qg} = - \frac{1}{2\pi} \int_0^\infty \frac{\exp[-rk|z-z_0|]-\exp[-rk(z+z_0)]}{rk} \cos k[x-x_0+\beta(z-z_0)] \, dk. \quad (2.14)$$

This limit is obtained by ignoring the short waves and letting $k \to 0$ in (2.12). The integral has the closed-form expression,

$$\Psi_{qg} = \frac{1}{4\pi r} \log \frac{[x-x_0+\beta(z-z_0)]^2 + r^2(z-z_0)^2}{[x-x_1+\beta(z+z_0)]^2 + r^2(z+z_0)^2}, \quad (2.15)$$

in which the image position $x_1 \equiv x_0 + 2\beta z_0$ is introduced to bring out the symmetry (notice that $x-x_0$ and $x-x_1$ may be interchanged with $z-z_0$ and

$z+z_0$, respectively). The logarithmic solution is recognizable as the Green's function for the three elliptic terms in (2.4), without the vorticity advection. The corresponding circulation is precisely that required to maintain geostrophic balance in the disturbed flow, whence the notation "qg" for quasi-geostrophic.

The quasi-geostrophic solution is substantially influenced by the baroclinicity. Mathematically, β induces a transformation to the non-orthogonal coordinates $X = x+\beta z$ and $Z = rz$. This system is aligned with the basic absolute momentum surfaces and stretched vertically by the factor r^{-1}. Eliassen (1962) showed that the solution implicitly includes the nonlinearity in the original y-momentum equation if the X coordinate surfaces are redefined to lie along the surfaces of <u>total</u> absolute momentum, M+v. Hence there is no formal distinction between the quasi-geostrophic and semi-geostrophic problems, except for nonlinearities in the lower boundary condition.

The Eliassen transformation is particularly useful because the boundary remains a coordinate surface. However, the <u>form</u> of the barotropic solution can also be recovered through the transformation $X' = rx$, $Z' = z+\beta x$, if the above definition for x_1 is used. It follows that an orthogonal transformation, $x' = x\pm z$, $z' = z\mp x$, also converts (2.15) to the simple logarithmic potential.

In physical space, the orthogonal transformation is a rotation through an angle $(1/2)\tan^{-1}[2\beta s/(1-s^2)] \approx \alpha_B$, where $s = fa/N \ll 1$, and $\alpha_B = fV_z/N^2$ is the slope of the basic isentropes. The fact that the quasi-geostrophic result in stretched coordinates (and with no boundary) is unbiased with respect to the buoyancy and absolute momentum surfaces

distinguishes it from the near-field solutions to be discussed in the next section.

The effect of β on the velocity can be isolated by writing (2.15) in the form

$$\Psi_0 = (1/2\pi)(\log R - \log R_{ref}), \qquad (2.16)$$

where the definitions $\Psi_0 = r\Psi_{qg}$, $R^2 = (X-X_0)^2+(Z-Z_0)^2$, and $R_{ref}^2 = (X-X_0)^2+(Z+Z_0)^2$ are used, along with $X_0 = x_0+\beta z_0$ and $Z_0 = rz_0$. Now, in terms of the derivatives $-\partial\Psi_0/\partial Z \equiv u_0$ and $\partial\Psi_0/\partial X \equiv w_0$, which give the perturbation velocity field for $\beta = 0$, the actual velocity perturbation is

$$u = u_0 - (\beta/r)w_0,$$
$$\qquad (2.17)$$
$$w = (1/r)w_0.$$

Because of the increased depth of the circulation, the amplitude of the vertical velocity is evidently increased by introducing baroclinicity of either sign. However, in the convergent regions, where $u < 0$ and $w > 0$, the horizontal deceleration is reduced if $\beta < 0$. The latter feature is a consequence of the ambient vertical shear, which provides a second source (the first being horizontal convergence) for the perturbation parallel momentum needed to balance the pressure anomaly.

Near the ground, the baroclinic effect on the amplitude of the velocity is negligible, but the changes in its distribution are not. In particular, since the maximum in $|u|$ is displaced to $x = x_0+\beta z_0$, the baroclinicity substantially favors the long-wave upstream response for moderate negative values of β. The displacement increases the opportunity for blocking because of the increased vertical shear (the β contribution

to $\partial u/\partial z$ leading to a further enhancement of the vertical stratification), and presumably also because of the increased distance between forcing and response. It remains to be seen whether the shorter waves offset or contribute to this long-wave effect closer to the forcing.

From a direct examination of Ψ_{0z}, it is learned that u varies as $(z-z_0)^{-1}$ relatively near the source $(1 \ll |z-z_0| \ll z_0)$, but decreases more rapidly, as z^{-2}, far above the source $(|z-z_0| > z_0)$ because of the lower boundary. Inside an order-unity radius from the forcing, a qualitative estimate for the long-wave contribution can be obtained by setting $\log R = 0$ in (2.16). Thus,

$$\Psi(x_0, z_0) \approx -\log(2rz_0)/(2\pi) \qquad (2.18)$$

is reasonably accurate for $z_0 > 1$, and provides a useful estimate for the quasi-geostrophic contribution to the total disturbance mass flux beneath the center of circulation. For shallow forcing, $z_0 \ll 1$, it is easy to show directly from (2.13) that the mass flux contribution from real $\mu < 1$ is bounded by $z_0^2/(2\pi r)$. The corresponding estimate for the surface velocity perturbation is $u < z_0/(2\pi r)$.

An examination of the mixed gravity-inertia wave disturbance will complete the far-field analysis. Because these waves propagate to the lee of the forcing, and are weaker than the near-field buoyancy and inertia waves, they are not expected to play a role in blocking or wave-breaking. The analysis is therefore included for completeness, and to provide a check on subsequent numerical results.

The wavy part of the far-field disturbance is approximated by the method of stationary phase, applied to the second integral in (2.12).

The approximation assumes $\left| x-x_0 \right| \gg 1$ and $\left| z-z_0 \right| \gg 1$, but not $k \ll 1$, as in the trapped far-field limit. Because the stationary-phase method is essentially a ray-tracing procedure, the remarks of section 2.2 on plane-wave energetics will be directly relevant.

Let $\alpha \equiv \left| z \pm z_0 \right| /(x-x_0)$ be the slope of the ray connecting the observation point to either the source or its (ordinary) image. Allowing α to take the sign of $x-x_0$, but not $z-z_0$, anticipates the symmetry of the wavy disturbance. The stationary-phase condition on k, referring to either of the sine terms in (2.12), is then

$$\left(1 - \beta\frac{k^2+1}{k^2-1} \left[s\surd(k^2-r^2) - \beta \right] \right) \alpha - (k^2-1)\surd(k^2-r^2) = 0, \qquad (2.19)$$

for which a positive solution, $k_s{}^2$, will be sought. Here $s \equiv (z-z_0)/\left| z \pm z_0 \right|$ takes the values ± 1 for the primary disturbance, and a fraction of ± 1 for the reflections.

The familiar physical interpretation of (2.19) is that α must be the slope of the energy (or group velocity) vector for some wavenumber. Close examination of the dispersion curves in Fig. 2.1 shows that at least one solution, from the interval $k > 1$, can be found throughout $x > 0$, and that one or two additional solutions, from $r < k < 1$ or $r < \left| \mu \right| < 1$, may also exist by virtue of the baroclinic basic state. Only the latter wavenumbers are relevant in the upstream region ($\alpha < 0$), which cannot be reached by the barotropic waves.

The stationary-phase condition for $\beta = 0$ and $\alpha > 0$ has the exact solution $k^2 = 1 + \alpha^{2/3} \equiv k_{s0}{}^2$. The first-order correction for β must then satisfy $k_{s0}k_{s1} = -(\beta s/3)(\alpha+2\alpha^{1/3})$, whence

$$k_s{}^2 - 1 = \alpha^{2/3} - \frac{2}{3}\beta s \left(\alpha + 2\alpha^{1/3}\right) + O(\beta^2), \qquad \alpha > 0. \qquad (2.20)$$

Thus if β is small, the sign of βs determines whether the local horizontal scale is lengthened or shortened by the baroclinicity. In the warm-advection case, for example, the scale is shortened above the forcing, where $\beta s < 0$.

The fact that βs is positive in regions where the propagating waves slope toward the M-surfaces suggests a physical interpretation of the baroclinic effect. Namely, when $\beta s > 0$, vertical propagation becomes significant at relatively small k because the rotational constraint can be broken while the waves are still shallow. Conversely, if $\beta s < 0$, the wave motions produce large v anomalies, and relatively steep motions are required before buoyancy effects can prevail. The modification of k_s is greatest near the vertical axis ($\alpha \gg 1$), where it will be shown that the vertical wavenumber is relatively unaffected by β (indeed this has been assumed in the above argument).

Since the basic isentropes slope in the same direction as the M-surfaces, analogous reasoning indicates that μ_s must vary with the sign of βs in the same way as k_s. For confirmation, note first that the complete phase of the far-field solution has the symmetric form $\phi_s = k_s'(x-x_0) + \mu_s'\left|z \pm z_0\right| + O(\beta^2)$, where the new (primed) wavenumbers are related by (2.10), except with β replaced by βs. From the symmetry of the dispersion relation, it can be deduced that $\mu_s'^2 - 1$ must be given by the right side of (2.20) with α replaced by $1/\alpha$. It is then readily confirmed that the actual vertical wavenumber, μ_s, for both the primary and reflected waves is increased in the region $\beta s < 0$ and reduced in $\beta s > 0$,

and that the modification is greatest near $z = \pm z_0$ $(1/\alpha \gg 1)$ and smallest near the vertical axis.

The results for k_s and μ_s together yield

$$\phi_s = \left((x-x_0)^{2/3} + |z \pm z_0|^{2/3} \right)^{3/2} \left(1 - \frac{\beta s}{\alpha^{1/3} + \alpha^{-1/3}} \right) + O(\beta^2) \qquad (2.21)$$

for the full stationary phase. The lowest-order result reduces to $\phi_s = x-x_0$ at $z = z_0$, and $\phi_s = |z \pm z_0|$ at $x = x_0$, revealing the wavenumber limits $k = 1$ and $\mu = 1$. However, the vertically- and horizontally-propagating regions are not accurately represented by the stationary-phase approximation, which has errors of order $1/(x-x_0)$ and $1/|z \pm z_0|$. The lowest-order part of ϕ_s can also be found in Queney's analysis of the corresponding mountain-wave problem (e.g., Queney, 1948).

The amplitude of the stationary-phase estimate depends on the second derivative of the phase, ϕ_{kk} (see Bender and Orszag, 1979), and for present purposes, requires a small-β expansion of the denominator in (2.12). The complete approximation to first order in β may be written

$$\Psi_{sp} = -\frac{1}{\sqrt{6\pi}} \left[\frac{\sin\left(\phi_s + \pi/4\right)}{\phi_{s0}^{1/2}} (1 + \beta A) \right.$$

$$\left. - \frac{\sin\left((\phi_s)_{ref} + \pi/4\right)}{(\phi_{s0})_{ref}^{1/2}} (1 + \beta A_{ref}) \right], \qquad (2.22)$$

where ϕ_{s0} is the lowest-order phase estimate [cf. (2.21)], and "ref" denotes the reflections. Thus, at lowest order, the amplitude of both the primary waves and the reflections is constant on the respective phase surfaces. The mountain-wave solution does not share this particular property.

The quantity

$$A = \frac{s}{3}\left(\alpha^{1/3} + \alpha^{-1/3} + \frac{3}{2}(\alpha^{1/3} + \alpha^{-1/3})^{-1}\right)$$

in (2.22) determines the amplitude correction due to β. Since A takes the sign of s, the amplitude is increased by the baroclinicity in the regions where the wavenumbers are decreased. This relationship implies that the amplitude changes in the <u>velocity</u> field are at least partially offset by the wavelength modification. Further analysis at first order shows that, with one exception, the conflict is resolved in favor of the amplitude correction. Thus, for example, $u_{sp} = -\partial\Psi_{sp}/\partial z$ is slightly <u>reduced</u> in amplitude above the forcing when $\beta < 0$. However, for large enough z_0, the correction in the reflected part of the disturbance takes the sign of the wavenumber correction.

The small-β expansion is invalid wherever the correction terms are $O(1)$. The breakdown regions, $\alpha < |\beta|^3$ and $\alpha^{-1} < \pm\beta^3$, are also the regions where multiple stationary wavenumbers may exist, specifically in the intervals $k^2 - 1 < O(\beta^2)$ and $\mu^2 - 1 < O(\beta^2)$, respectively. It is not helpful to know these wavenumbers precisely, because the formalism leading to (2.22) does not apply to a significant portion of the two regions. The reason for the failure is that the various stationary contributions overlap (higher derivatives of the phase are not negligible), or that one of the far-field assumptions, $|x-x_0| \ll 1$ and $|z \pm z_0| \ll 1$, is violated.

The near-field analysis of the next section reveals some of the anticipated focusing of wave energy by the baroclinicity, which will also be apparent in the numerically-generated solutions presented in sections 2.6 and 2.7. Part of the justification for the near-field analysis still depends on identifying the stationary wavenumbers. Hence

this section ends with a qualitative discussion of the baroclinic effect on the symmetry of the wavy disturbance. Only the primary disturbance will be mentioned, but the conclusions also apply to the reflections whenever the appropriate regions would include the physical domain, $z >$ 0. The case $\beta < 0$ is summarized in Fig. 2.2.

It is found, first of all, that the solution in $0 < -\beta(z-z_0) \ll \beta^4(x-x_0)$ on one side of the horizontal axis is affected by three stationary wavenumbers. Two of these, $k_s = 1 \pm 0(\alpha/\beta^3)$, combine to give large amplitude to the barotropic inertial disturbance, whose important feature is a strong vertical gradient. The third wavenumber occurs near the baroclinic inertial limit, $k_s \approx r$, where μ is bounded. Its existence implies a large contribution at the forcing level from the longer vertical wavelengths normally removed by buoyancy effects. On the opposite side of the forcing level, the slowly-varying inertial waves are the only stationary contribution.

Near the vertical axis in $0 < -\beta(x-x_0) \ll \beta^4(z-z_0)$ (above the source) or in $0 < \beta(x-x_0) \ll \beta^4(z_0-z)$ (below the source), the phase is stationary at $\mu_s = 1 \pm 0(\alpha^{-1}/\beta^3)$. The large horizontal gradient characterizing barotropic buoyancy waves therefore dominates both areas. When $x = x_0$ is crossed, the phase is no longer stationary for large k. Thus where $\beta(z-z_0)$ is positive (negative), the horizontal gradient is reduced on the downstream (upstream) side of $x = x_0$. On the other hand, the influence of the baroclinic buoyancy waves, with $\mu_s \approx r$, is found on both sides of $x = x_0$, but only in $\beta(z-z_0) > 0$. Here again, the importance of the stationary phase of the baroclinic waves is to focus more long-wave energy along the axis. Note that the region affected by the longer buoyancy waves is below the source if $\beta < 0$.
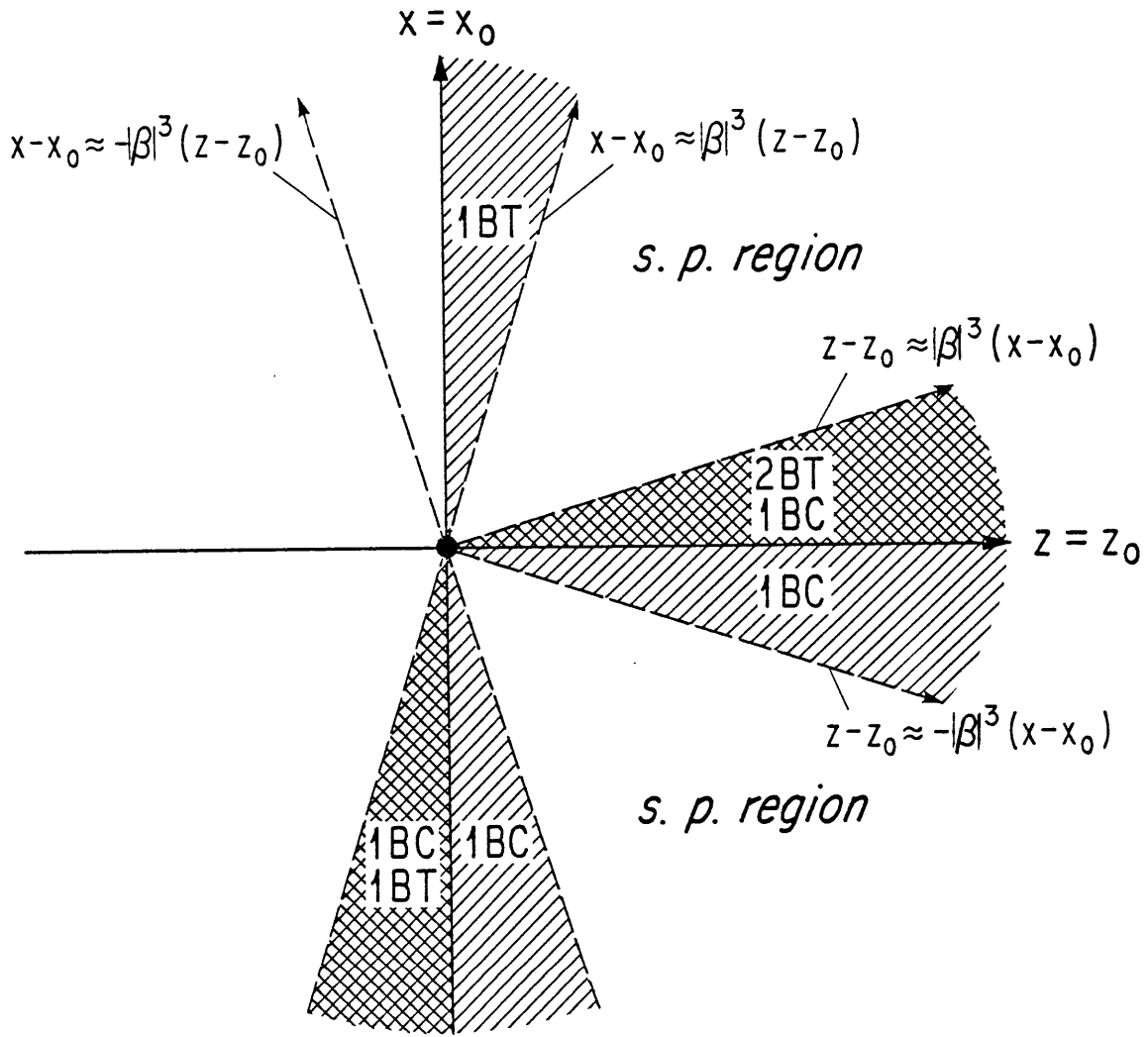
Fig. 2.2. Schematic showing type and location of propagating waves forced at (x_0, z_0), assuming baroclinic basic state ($\beta < 0$). Regions dominated by either buoyancy or rotational effects are shaded.

2.5 Near-field asymptotic response

The near-field disturbance is produced, in principle, by non-dispersive waves propagating vertically or horizontally along $x = x_0$ or $z = z_0$. However, as noted in section 2.2, a bounded near-field solution cannot be found which is entirely unaffected by dispersion from rotation or buoyancy. One of the objectives here is to describe this effect formally.

Although the approximation along each axis requires essentially the same analysis, it is clear at the outset that certain properties will distinguish the two regions. Whereas the horizontal near-field disturbance along $x = x_0$ is restricted to modes with the same tilt, the vertical near-field solution contains both upstream- and downstream-tilting modes in $x > x_0$, and is entirely excluded from $x < x_0$.

The horizontal near-field limit of (2.12), nominally valid in, $\left| x - x_0 \right| \ll 1$, is obtained by assuming $k \gg 1$ and $\mu = 1$. The result

$$\Psi_G = - \frac{1}{2\pi} \int_{k_1}^{\infty} \frac{\sin\left(k(x-x_0)+\left|z-z_0\right|\right) - \sin\left(k(x-x_0)+z+z_0\right)}{k^2} \, dk + C_G \quad (2.23)$$

determines the contribution from the gravity waves. The factor k^{-2} produces a long-wave singularity which has been discussed in section 2.2. Thus, in order that Ψ_G be bounded, an undetermined long-wave interval, $k < k_1$, has been removed from the integral and its contribution written as C_G.

The ambiguity associated with k_1 will be resolved by assuming that the long-wave contribution is independent of x, i.e., $C_G = C_G(z)$. The

relevance of k_1 is then to determine the region of validity of the x-dependent part of Ψ_G, which will be seen to shrink with increasing vertical distance from the source. With regard to the x-dependence, it is noted straight away that C_G is affected by the baroclinic gravity waves when $\beta \neq 0$. These have an intermediate horizontal scale close to the inertial distance which will not show up in the following analysis.

Before turning to the problem of estimating C_G, a closed-form expression for the barotropic gravity-wave integral will be found by assuming the second x-derivative is unaffected by the long waves. Thus, $k_1 = 0$ is assumed, in writing

$$\frac{\partial^2}{\partial x^2}\Psi_G = -\sin z_0 \, [\delta(x-x_0) \cos z - \frac{1}{\pi(x-x_0)} \sin z],\qquad(2.24)$$

in which it is understood that z and z_0 must be interchanged below the forcing. This result shows an alternation above $z = z_0$ between a symmetric and an antisymmetric horizontal structure, a characteristic of gravity waves propagating in one vertical direction.

By itself, the expression in brackets is the Green's function for mountain waves in a non-rotating flow. The interior forcing in the presence of a reflecting boundary evidently creates an interference pattern in which the symmetric component, $\delta(x-x_0)$, takes either sign at the forcing level, while the antisymmetric part at $z = z_0$ is limited to one sign or zero, as z_0 varies.

The appropriate integral of (2.24) is

$$\Psi_G = -\sin z_0 \, \left(\left|\frac{x-x_0}{2}\right| \cos z - \frac{x-x_0}{\pi} \log \left|x-x_0\right| \sin z\right) + C_G,\qquad(2.25)$$

except that z and z_0 must be interchanged in $z < z_0$. It is clear that the x-dependent part of this estimate, being unattenuated in z, is not directly affected by horizontal dispersion. When the Green's function is used in a convolution integral over distributed forcing, the x-dependence is equivalent to a double x-integral over the forcing (cosine term) or its Hilbert transform (sine term).

A procedure for obtaining the integration constant, $C_G(z)$, is suggested by an analysis used by Queney (1947) and Pierrehumbert (1984) to find the z-derivative of the streamfunction along a topographic boundary. The Green's function is first rewritten as a vertical transform (2.13), and reduced to one dimension by setting $x = x_0$. To isolate the gravity-wave contribution, the complex integration path is altered as shown in Fig. 2.3b. Thus, in the region $\beta(z-z_0) > 0$,

$$\Psi(x_0,z) = -\frac{1}{2\pi} \int_0^\infty \frac{\exp\left(-\mu_i \left|z-z_0\right|\right)}{\mu_i \sqrt{(\mu_i^2+r^2)}} \, d\mu_i$$

$$-\frac{1}{2\pi} \left(\int_r^\infty \frac{\sin \mu \left|z-z_0\right|}{\mu\sqrt{(\mu^2-r^2)}} \, d\mu + \int_r^1 \frac{\sin \mu \left|z-z_0\right|}{\mu\sqrt{(\mu^2-r^2)}} \, d\mu \right) + \cdots . \tag{2.26}$$

When the integration contour is redrawn for $\beta(z-z_0) < 0$ (the dashed contour in the right-hand diagram of Fig. 2.3b), the two plane-wave integrals are replaced by a single integral over the complementary interval $(1,\infty)$. If $\beta < 0$, this contour is also used for the omitted reflection integrals, in which $z+z_0$ replaces $\left|z-z_0\right|$.

Since the phase is stationary near the branch point at $\mu = r$, ignoring the x-dependence cannot produce a singular limit. If $\left|z-z_0\right| \gg 1$, the two plane-wave integrals can be related to the Gamma function with
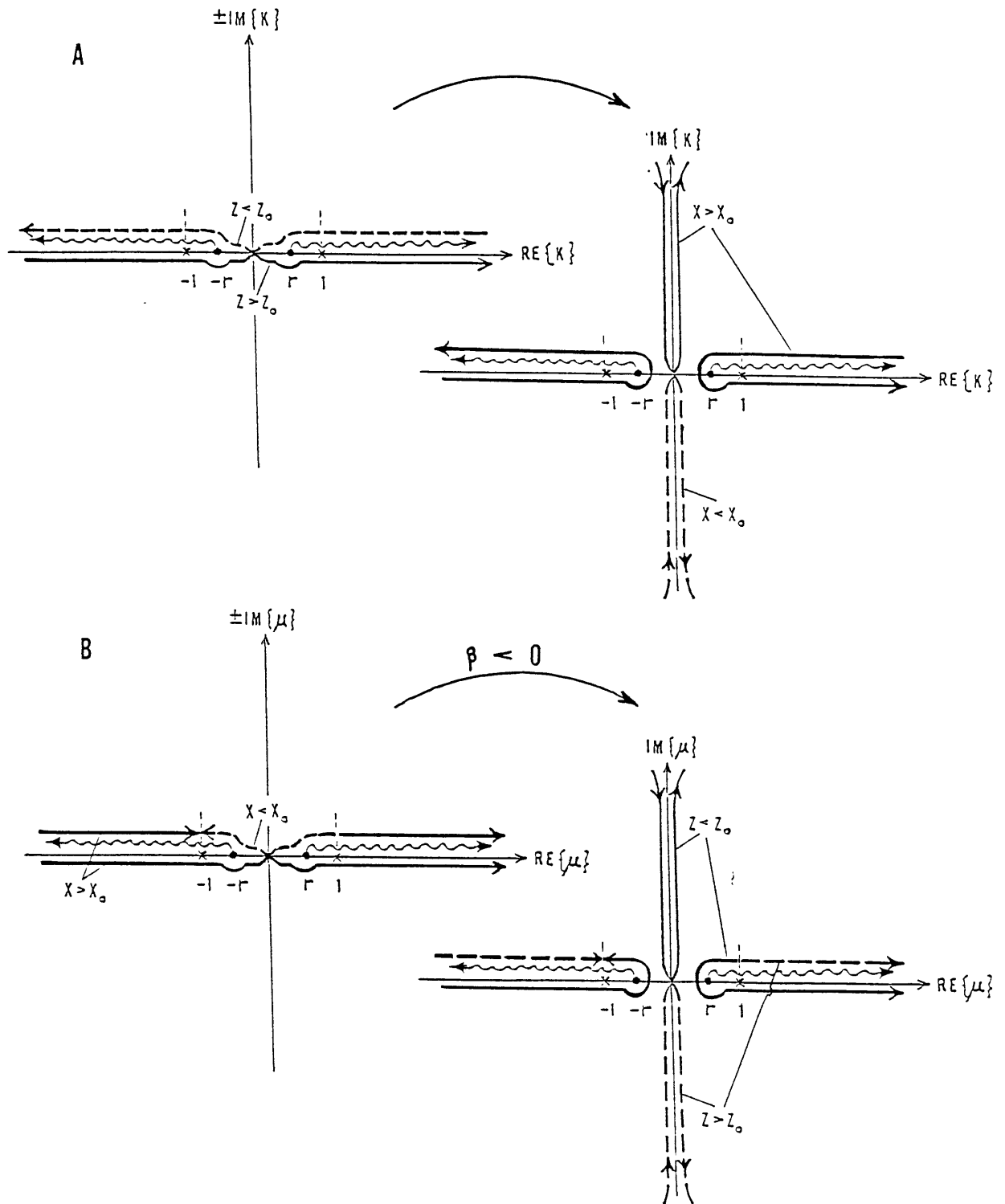
Fig. 2.3. Original and deformed complex Fourier integration paths for
(a) horizontal and (b) vertical transforms, showing branch points at k or
$\mu = \pm r$, and essential singularities at k or $\mu = \pm 1$. In left-hand
diagrams, imaginary values in upper half-plane take the sign of $z-z_0$ or
$x-x_0$ to permit unique determination of the sign of the square-root, which
is absorbed in path direction in right-hand diagrams.

parameter $1/2$ by letting $\mu = r+\epsilon$, and assuming $\epsilon \ll 1$. The integration

constant for (2.24) is determined in this way to be

$$C_G(z) = -\frac{1}{2r} \left(\frac{\sin(r|z-z_0|+\pi/4) + A_1\sin(r|z-z_0|+\phi_1)}{(2\pi r|z-z_0|)^{1/2}} \right) + \cdots. \quad (2.27)$$

The second of the two wavy integrals has been approximated by the

incomplete Gamma function, $\Gamma(z_1; 1/2)$ with $z_1 = (1-r)|z-z_0|$ serving as the

integration limit. It suffices to note that as z_1 increases, A_1 varies

from zero to unity, and ϕ_1 from zero to $\pi/4$, each with a damped

oscillation about the higher limit. Therefore if $|z-z_0| \gg 1/(1-r)$, the

contribution from the last integral in (2.26) roughly doubles the value

which obtains when $r = 1$, or when $|z-z_0|$ is small. In the same limit, the

complementary integral which applies to the region $\beta(z-z_0) > 0$, and in

some cases to the reflections, vanishes.

The vertical damping and $\pi/4$ phase shift in (2.27) are

characteristics of a dispersive wave disturbance. Nevertheless, the

result is different from the standard stationary-phase approximation,

which cannot be used near the vertical axis. The analysis succeeds in

quantifying the contribution from the baroclinic gravity waves, and in

confirming their presence below the forcing in the warm-advection case.

The contributing waves have phase surfaces close to the ambient

M-surfaces, $x + \beta z = $ const, which implies an intermediate (order-unity)

horizontal scale below the forcing for moderate negative values of β.

Since the baroclinic waves are superimposed on the barotropic gravity

waves, the analysis reveals an enhanced upstream disturbance in the near

and intermediate field in the case of basic-state warm advection.

Inside a radius $|z-z_0| \approx 1$, the special long-wave estimate (2.18)

is the best choice for the integration constant (replacing C_G), and the

nondispersive part of the remaining near-field approximation (for the

inertial disturbance, $k \approx 1$) is also additive. Thus, the three

contributions near the source come from the regions $k \ll 1$, $k \approx 1$, and $k \gg$

1 on the real k-axis.

The vertical near-field approximation involves the large-μ limit

of the Green's function expressed as a vertical transform [cf. (2.13)].

The integral vanishes in $x < x_0$, while in $x > x_0$, it is

$$\Psi_I = - \frac{1}{2\pi} \int_{\mu_1}^{\infty} \frac{\sin[\mu(z-z_0)+x-x_0] - \sin[\mu(z-z_0)-(x-x_0)]}{\mu^2} \, d\mu \; + C_I. \quad (2.28)$$

The boundary reflections of the horizontal wave-train are insignificant

for $z_0 > O(1)$, and are omitted. As expected, Ψ_I has different symmetry

properties from Ψ_G. The closed-form expression for (2.28) is simply

$$\Psi_I = \left| \frac{z-z_0}{2} \right| \sin(x-x_0) + C_I, \quad (2.29)$$

showing only even symmetry about the forcing level. The z-dependence here

corresponds to a double z-integral over an actual forcing distribution.

The remainder of the approximation for the inertial wave-train is

found by analyzing the horizontal transform (2.12) near the branch point,

and neglecting any z-dependence. Since the wave energy is less

drastically divided according to phase tilt than in the gravity waves, the

baroclinic effect (favoring either upward or downward propagation) will be

neglected.

Although the analysis is formally valid only in $x-x_0 \gg 1$, an acceptable approximation can be obtained for $x-x_0 = O(1)$ by considering higher-order terms in the expansion parameter $\varepsilon \equiv k-1 \ll 1$. The result of including terms to $O(\varepsilon^2)$ in the integrand is

$$C_I(x) = -\frac{1}{[2\pi(x-x_0)]^{1/2}} \left\{ \sin\left(x-x_0 + \frac{\pi}{4}\right) \left(1 - \frac{129/128}{(x-x_0)^2}\right) - \frac{5/8}{x-x_0} \cos\left(x-x_0 + \frac{\pi}{4}\right) \right\}.$$

(2.30)

The coefficients of the higher-order terms in $(x-x_0)^{-1}$ are products of Taylor coefficients and values of the complete Gamma function with parameters $3/2$ and $5/2$.

The higher-order terms produce a new local minimum, $C_I \approx -0.22$, near $x = x_0 + 1.5$, where the lowest-order term by itself is decreasing monotonically toward $x = x_0$. This value of C_I can be interpreted as the inertia-wave contribution to the disturbance mass flux below the center of the circulation. Inside $x-x_0 \approx 1$, C_I must be replaced by the long-wave approximation (2.18), plus the nondispersive part of Ψ_G.

Some caution is necessary in extending the near-field results to cases of distributed forcing. The problem is that the neglect of the long waves, $k < k_1$ and $\mu < \mu_1$, in estimating the derivatives of the streamfunction implies a scale selection in the direction perpendicular to the inertia and gravity wave-trains. Since the scale does not appear anywhere in the asymptotic results, it must be understood that the near-field analysis assumes an effective forcing length scale which is always the smaller of Ro^{-1} (or Fr) and $1/k_1$ (or $1/\mu_1$). (The fact that such restrictions do not apply to C_I and C_G underscores the importance of the baroclinicity.)

Thus it remains to find practical estimates for the wavenumbers k_1 and μ_1, which are at least $O(1)$. An examination of $\mu(k)$ in (2.10), with $\beta = 0$, reveals that $k_1{}^2$ must be considerably larger than the nondimensional distance $\left| z \pm z_0 \right|$ in order to justify $\mu = 1$ throughout the short-wave interval. The neglect of the long waves is therefore appropriate only in $(x-x_0)^2 \ll 1/\left| z \pm z_0 \right| < 1$, and the effective Rossby number is no _smaller_ than $O(\left| z \pm z_0 \right|^{-1/2})$. In the nonrotating limit, the corresponding dimensional radius is infinite, and the nondispersive part of Ψ_G is valid everywhere.

Similarly, the vertical near-field approximation applies in $(z-z_0)^2 \ll 1/(x-x_0) < 1$, and the effective Froude number does not exceed $O([x-x_0]^{-1/2})$. It is noted that at the limits of the near-field regions, i.e., where $(x-x_0)^2 \approx 1/\left| z \pm z_0 \right|$ or $(z-z_0)^2 \approx 1/(x-x_0)$, the nominal contributing wavenumbers, $k^2 > \left| z-z_0 \right|$ or $\mu^2 > x-x_0$, begin to overlap the stationary-phase interval around $k^2 = [(z-z_0)/(x-x_0)]^{2/3}$ or $\mu^2 = [(x-x_0)/(z-z_0)]^{2/3}$, whose contribution was found to damp with height.

2.6 Numerical evaluation of the Green's function

The alternative integration contour drawn in Fig. 2.3a best serves the purposes of numerical evaluation. The resulting asymmetric form of the horizontal transform, including the reflections, can be written

$$\Psi = -\frac{1}{\pi} \int_0^\infty \frac{\exp[-k_i(x-x_0+\frac{\beta(z-z_0)}{1+k_i^2})\text{sgn}(x-x_0)] \sin \mu_{0r}z \sin \mu_{0r}z_0}{k_i\sqrt{(k_i^2+r^2)}} dk_i$$

$$\text{(2.31)}$$

$$-\frac{1+\text{sgn}(x-x_0)}{\pi} \int_r^\infty \frac{\sin k(x-x_0+\frac{\beta(z-z_0)}{1-k^2}) \sin \mu_0 z \sin \mu_0 z_0}{k\sqrt{(k^2-r^2)}} dk \quad ,$$

where $\mu_{0r} = (k_i^2+1)k_i^{-1}\sqrt{(k_i^2+r^2)}$. This version is preferred

because numerical convergence is improved in $x < x_0$, and because there are

no singularities (except $k_i = \infty$) in the first integral.

The numerical integration of the damped modes is truncated at the

smaller of the limits $k_i = 1/(\pi\varepsilon)$ and $k_i = (\log \pi\varepsilon x')/x'$, where $x' \equiv$

$|x-x_0+\beta(z-z_0)|$. It can be seen that the absolute truncation error is then

bounded by ε, which is taken to be .01. The plane-wave integral is

truncated at $k = 30$ and, near the inertial singularity, $\mu = 30$. The

branch-point singularity is removable if $r \neq 1$.

The integration is carried out using the Romberg scheme (iterated

Simpson's Rule) on subintervals of variable length determined by the

condition that the phase of the primary and reflected waves vary by no

more than 2π. The solutions to be shown are contour plots of 1500 data

points (50 horizontal by 30 vertical). The calculation time for each

point averages about 1 sec on a PDP 11/44 computer.

Attention will be focused on two aspects of the solutions. The

first is the maximum amplitude of the streamfunction, Ψ_m, or what is the

same, the mass flux beneath the center of the circulation. The quantity

Ψ_m/z_0 is the upper bound on the vertically-averaged downstream

deceleration, and therefore measures the effectiveness of the waves in

removing disturbance energy. For comparison, note that in the absence of pressure and Coriolis effects, a nondimensional streamwise frictional forcing of unit amplitude implies $u_x = -1$, or if the friction begins at $x = 0$, $u(x=1) = -1$.

The other relevant aspect of the solutions is the baroclinic effect on the upstream deceleration, which is expected to favor blocking when $\beta < 0$ and z_0 is large. Solutions will be obtained using different forcing heights and for the three the cases $\beta = 0$ and $\beta = \pm 0.6$ ($r = 0.8$). Negative forcing will be used for the sake of physical relevance.

In the first set of solutions, shown in Fig. 2.4, the source is placed at $x_0 = 0$ and $z_0 = \pi/4$. The fact that the circulation is centered at the forcing level, rather than above or below the source, reveals the importance of the inertia waves in determining the horizontal mass flux. However, the nondispersive part of the gravity-wave contribution adds considerably to Ψ_m. Setting $x-x_0 = 1$ and $z = z_0 = \pi/4$ in (2.25) yields $\Psi_G = -0.25$, or over half of the computed value of $\Psi_m \approx -0.47$ in the barotropic solution.

On the basis of the present solution and those to follow, it appears that the result $C_I = -0.22$ obtained in section 2.4 is a good practical estimate for the inertia-wave contribution. However, it can be verified that (2.25) gives the position and amplitude of <u>subsequent</u> crests in the downstream wave train much more accurately. For smaller z_0, the amplitude is overestimated by (2.25), as the reflections begin to interfere. On the other hand, because the inertial response has little dependence on z_0 for higher forcing, the average downstream deceleration, Ψ_m/z_0, is maximal when $z_0 \approx 1$. Negative forcing at this level yields an average $u \approx -0.6$ below the source.
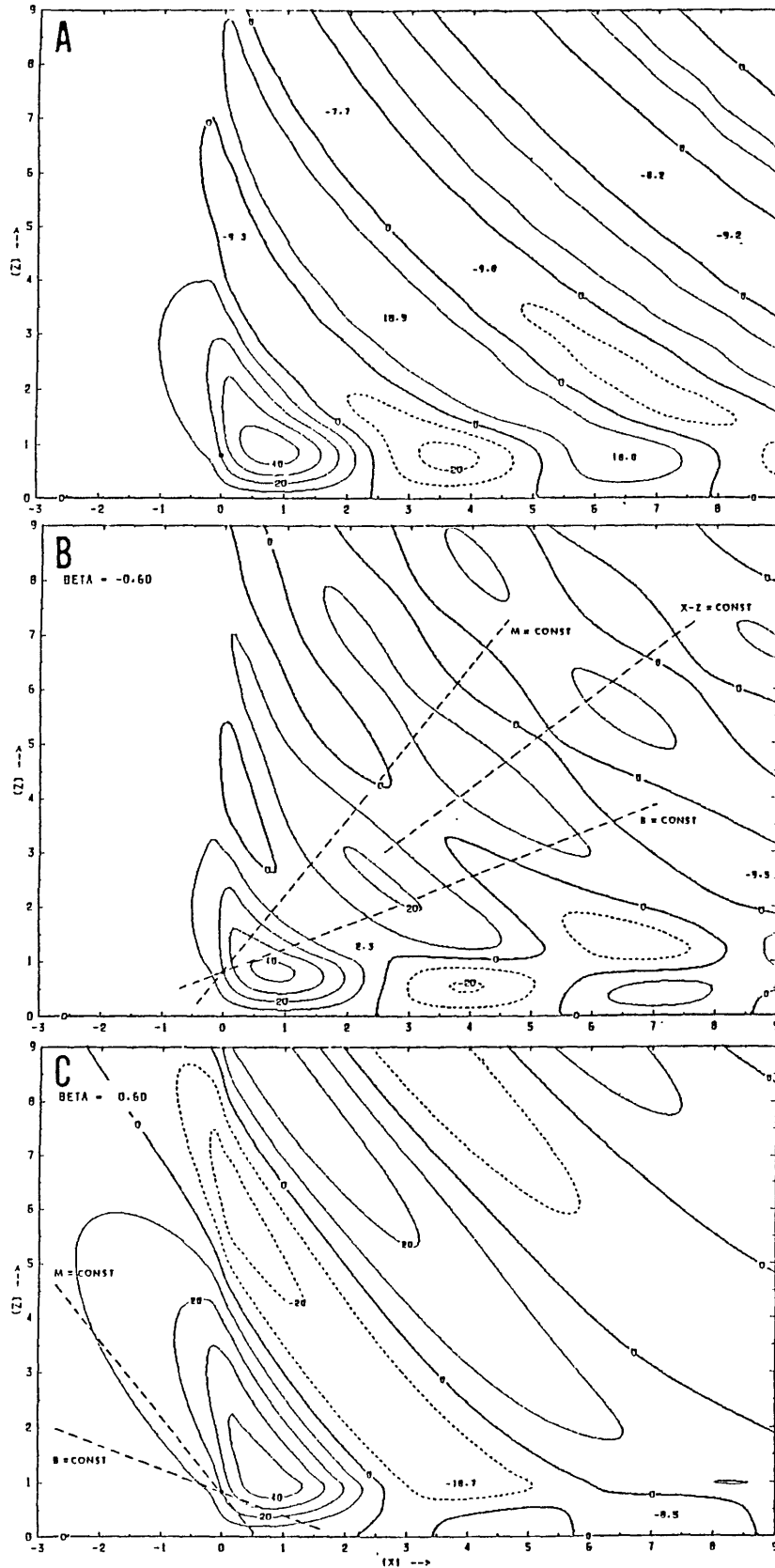
Fig. 2.4. Steady perturbation streamfunction for negative line-source forcing at $x_0 = 0$, $z_0 = \pi/4$, assuming $\beta =$ (a) 0, (b) -0.6 and (c) +0.6. Contour interval is one-tenth the forcing strength.

The absence of an upstream disturbance in the first solutions shows that the long and intermediate waves, $\mu \ll 1$ and $\mu \approx r$, are negligible for z_0 somewhat smaller than unity. The quasi-geostrophic contribution is nevertheless responsible for the obvious distortion of the phase surfaces along $x = z-z_0$ in the warm-advection case. This surface, shown in the figure as a dashed line between the basic absolute momentum and buoyancy surfaces, is the major axis of the elliptic long-wave response centered at the source. In the cold-advection solution, the same line would be the minor axis.

The baroclinic solutions show clearly the expected wavelength modification in the gravity-inertia lee waves. In further agreement with the stationary-phase analysis, there is relatively little energy above the source in the case $\beta < 0$, and a relatively large amount in the cold-advection case (recall that the baroclinic buoyancy wave energy propagates upward when $\beta > 0$). A final point of agreement with the analysis relates to the vertical gradient above and below the forcing level. Because of the deflection of the barotropic inertia waves, the strongest gradient (or phase shift) appears above the forcing in the negative-β case, and below in the positive-β case. This particular effect will be more apparent in the topographic solutions, which are free of reflections.

Putting the source at $z_0 = \pi/2$ (Fig. 2.5) allows a somewhat stronger long-wave contribution, with a noticeable upstream disturbance. The barotropic gravity-wave contribution in this case brings the circulation center nearer to the source. With $z = z_0 = \pi/2$ in (2.25), the maximum theoretical contribution is $\Psi_G \approx -1/(\pi e) = -.12$ and occurs close

PERT STREAMFUNCTION
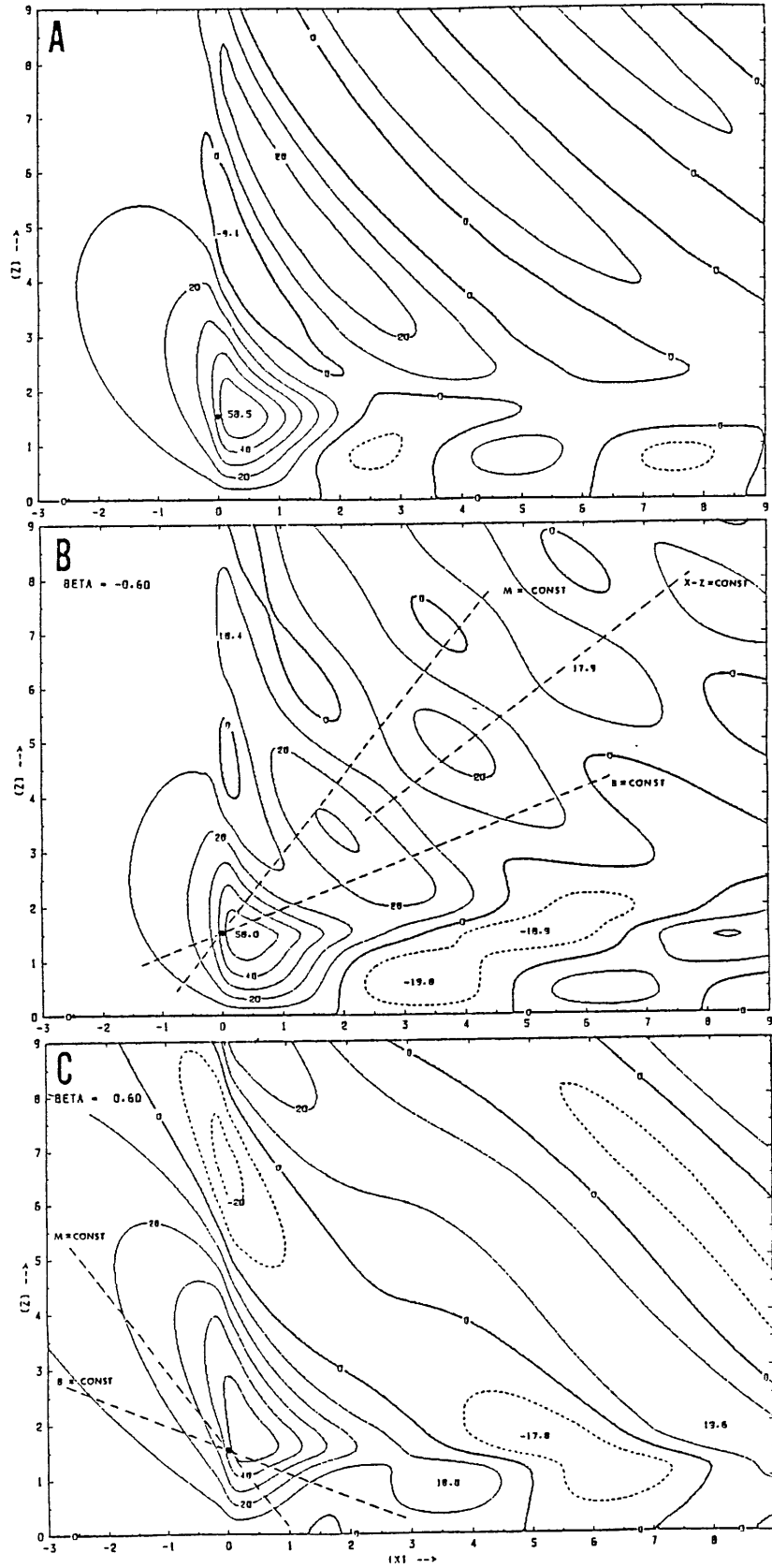
Fig. 2.5.   As in Fig. 2.4, except $z_0 = \pi/2$.

to the source at $x = 1/e = .37$. Taking $\Psi_I \approx -.22$ and $\Psi_{qg} \approx -(\log \pi)/$ $(2\pi) = -.18$ [from (2.18)] for the remaining contributions yields a surprisingly good estimate for the computed value, $\Psi_m = -.58$, in the barotropic solution. Note the striking effect produced by the separation of wave energy into pure gravity and pure inertia modes in the positive-β solution.

In the remaining solutions, a major part of the disturbance occurs upstream from the source. First, note that for the choice $z_0 = \pi$ (Fig. 2.6), the analytic estimate $\Psi_m \approx -.29$ ($k \ll 1$) $- .22$ ($k \approx 1$) $- .00$ ($k \gg$ 1) once again comes close to the computed value. The dispersive part of the buoyancy disturbance is evident for the first time in Fig. 2.6b, where $\beta = -0.6$. The crest of the buoyancy wave-train occurs, as predicted, at z $= 2.2$, where the sine argument in (2.27) hase the value $\pi/2$.

The buoyancy disturbance is significantly enhanced when $\beta < 0$ but remains rather confined to the vicinity of $x = x_0$ in Fig. 2.6. The slope of the M-surfaces, shown by the dashed line through the source, gives an indication of the horizontal scale of the baroclinic waves (the vertical scale being unity). Much of the upstream enhancement is due to the quasi-geostrophic contribution, whose major axis is also indicated.

The source in the final numerical solutions (Fig. 2.7) is placed at $z_0 = 3\pi/2$. This height is about 2.3 km when $U_0 = 10$ m/s and N = .02 s^{-1}. The solution shows that the negative shear causes a doubling of the low-level upstream deceleration as far out as $x = -3$. When $\beta < 0$, the vertical gradient of Ψ is greatest near the ground, where the downstream-propagating reflections are largely confined. Although the forcing level is somewhat high for the physical problem studied here, the

PERT STREAMFUNCTION

FR = -100.   RO = 1.00   BETA = 0.00   ERR = 1.00   KMAX = 30.0   ZF = 3.14
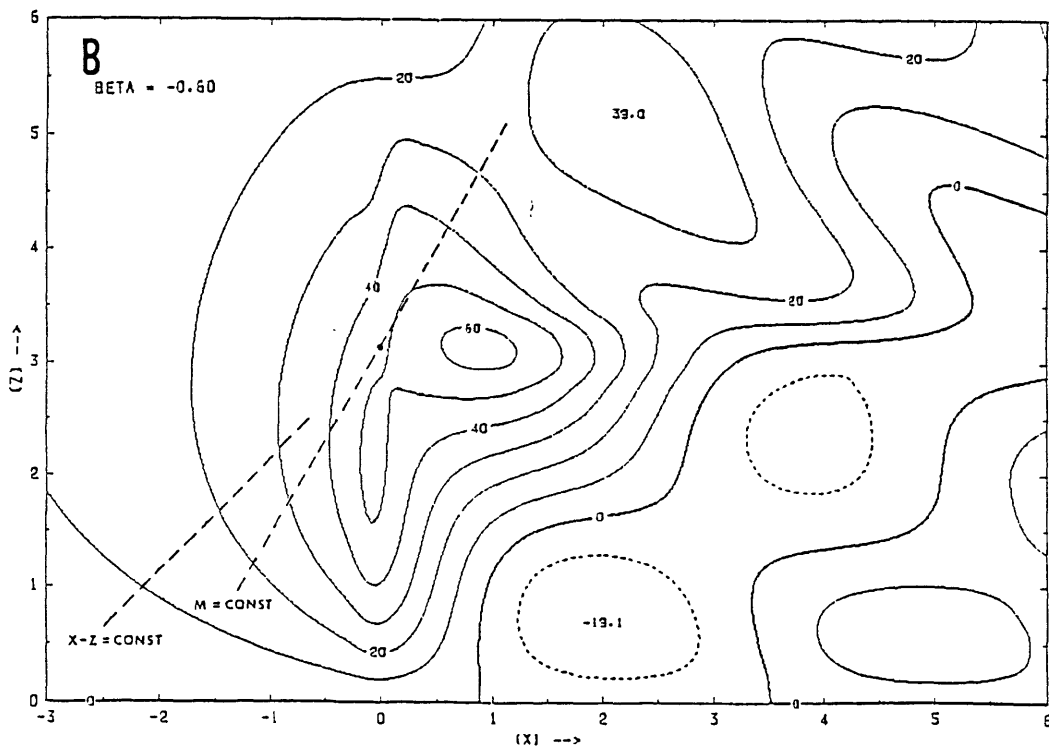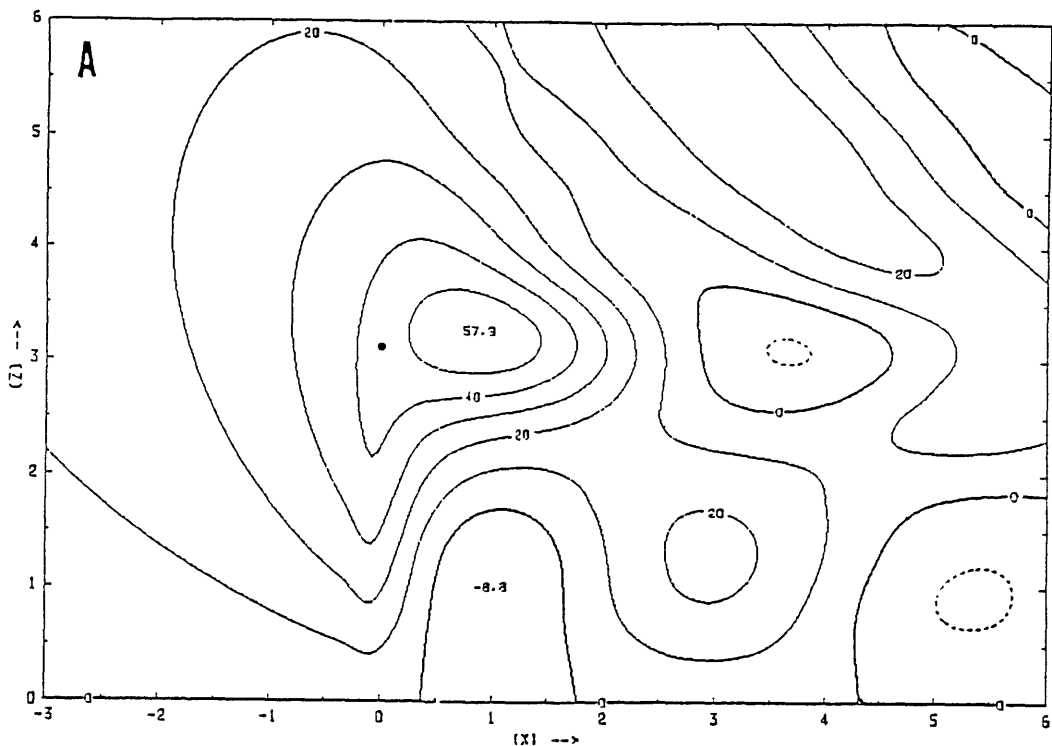
Fig. 2.6. As in Fig. 2.4, except $z_0 = \pi$, and $\beta = 0.6$ is omitted.

PERT STREAMFUNCTION

FR = -100.   RO = 1.00   BETA = 0.00   ERR = 1.00   KMAX = 30.0   ZF = 4.71
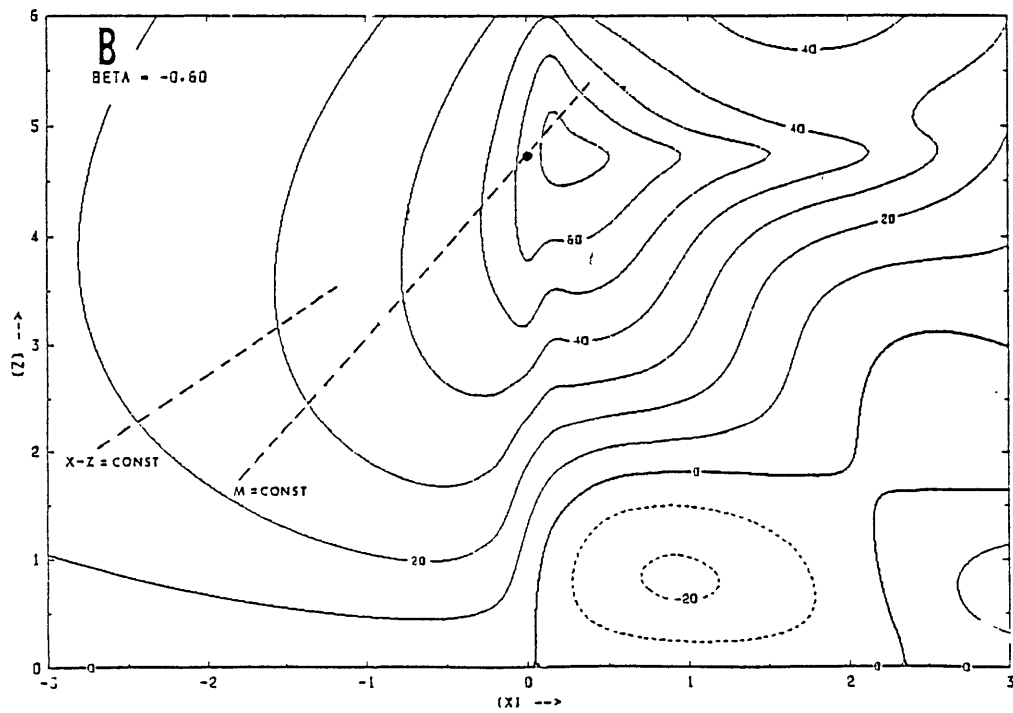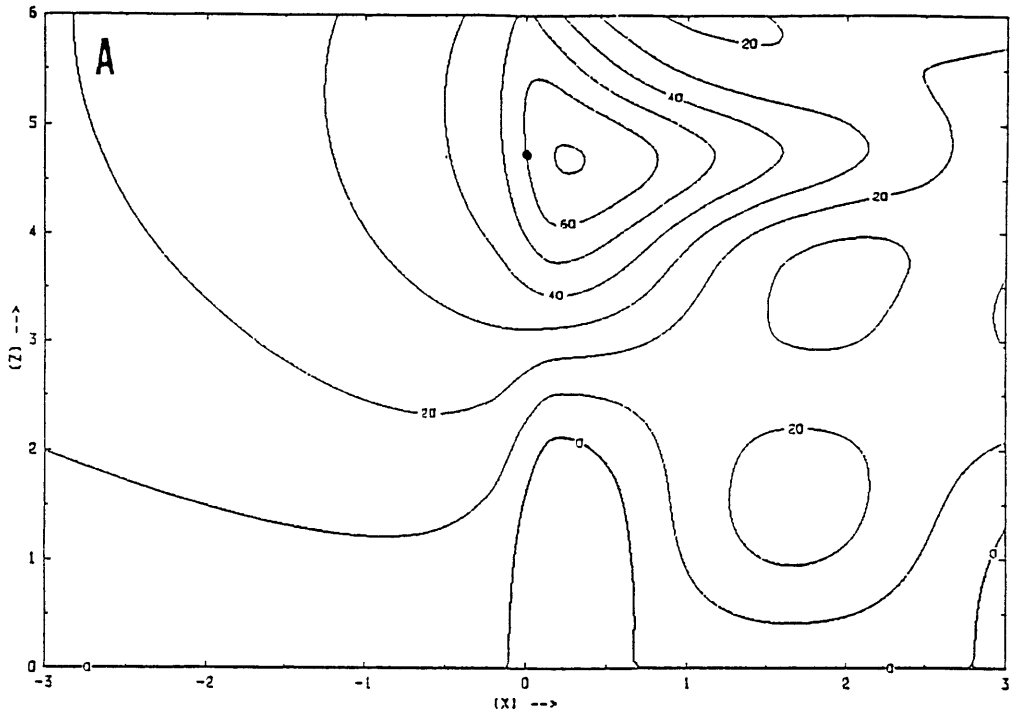
Fig. 2.7.   As in Fig. 2.4, except $z_0 = 3\pi/2$, and $\beta = 0.6$ is omitted.

potential for some baroclinic enhancement of the upstream influence is clearly established.

2.7 Baroclinic response to topographic forcing

The solution for an inhomogeneous lower boundary condition and a barotropic basic state was first obtained by Queney (1947), who also worked out certain details of the non-hydrostatic and beta-plane solutions. The one-dimensional (z = 0) Green's function has been further analyzed by Pierrehumbert (1984). Since much of the analysis required to generalize the results to baroclinic conditions has been covered in sections 2.4 and 2.5, the technical discussion of the baroclinic mountain-wave problem will be brief.

For a mountain profile $g_0 = \delta(x)$, the steady linear response expressed as a perturbation streamfunction is

$$\hat{\psi} = \frac{1}{\pi} \int_0^r \exp(-\mu_{0i}z) \cos k\left(x + \frac{\beta z}{1-k^2}\right) dk$$

$$+ \frac{1}{\pi} \int_r^\infty \cos \left[k\left(x + \frac{\beta z}{1-k^2}\right) + \mu_0 z\right] dk ,$$

(2.32)

where $\mu_{0i} = (1-k^2)^{-1}k\sqrt{(r^2-k^2)}$, $\mu_0 = (k^2-1)^{-1}k\sqrt{(k^2-r^2)}$, and $r^2 = 1-\beta^2$, as before. The horizontal transform has only the essential singularities at $k = 1$ and $k = \infty$, while the equivalent integral over μ has an additional singularity at $\mu = r$. The essential singularity at $k = \infty$, $\mu = 1$, is not integrable at $x = 0$ (directly over the mountain).

The asymmetry between k and μ is of course the result of the boundary inhomogeneity. The non-integrability of the pole, or branch point if $\beta = 0$, at $\mu = 1$ implies that the streamfunction amplitude, in

addition to its horizontal derivatives, is determined by non-dispersive buoyancy waves along x = 0, as will be seen in the formal near-field approximation.

Consider first the long-wave approximation of (2.32), which will be familiar as the quasi-geostrophic solution. The effect of β is exactly as in the response to interior forcing, namely a transformation of the coordinate variables. Thus, the long-wave limit,

$$\hat{\Psi}_{qg} = \frac{1}{\pi} \int_0^\infty \exp(-rkz) \cos k(x+\beta z) \, dk, \tag{2.33}$$

can be evaluated as

$$\hat{\Psi}_{qg} = \frac{1}{\pi} \frac{Z}{X^2+Z^2} \, , \tag{2.34}$$

with $X = x+\beta z$ and $Z = rz$. The other transformations mentioned in section 2.4 are not useful. The further limit $\Psi_{qg} \to \delta(x) = g_0$ as $z \to 0$ shows that (2.34) and the remaining contributions are not additive at small x.

The Green's function has $-\partial\Psi_{qg}/\partial z < 0$ everywhere on the boundary except at x = 0, where there is infinite acceleration. The corresponding flow over an isolated broad mountain is accelerated within roughly a half-width from the summit, and decelerated elsewhere. Thus, since w necessarily changes sign at the top, the two meridional velocity components are out of phase. The velocity can be written generally as

$$\hat{u} = r\hat{u}_0 - \beta\hat{w}_0$$

$$\hat{w} = \hat{w}_0 \, , \tag{2.35}$$

where $\hat{u}_0 = -\partial\hat{\psi}/\partial Z$ and $\hat{w}_0 = \partial\hat{\psi}/\partial X$. The amplitude of the vertical component

is of course unaffected by the baroclinicity. However, because of the phase relationship between u and w, the region of accelerated flow is shifted streamwise a distance of order $\beta\ell$. As a result of of the $1/x^2$ dependence in (2.34), the upstream deceleration is then somewhat less significant if $\beta < 0$. A physical interpretation of this effect was given in the discussion of the long-wave response to interior forcing.

The stationary-phase analysis for the far-field wavy response naturally leads to the same expression for the phase, ϕ_s, as shown in (2.21). However, the amplitude in this case depends only on the second phase derivative, ϕ_{kk}. If the definition $\alpha \equiv z/x$ is used, the estimate to first order in β can be written

$$\hat{\Psi}_{sp} = \frac{1}{\sqrt{6\pi x}} \; \frac{\cos(\phi_s + \pi/4)}{\left(\alpha^{-2/3}(1+\alpha^{-2/3})\right)^{1/4}} (1 + \beta\hat{A}). \qquad (2.36)$$

Here $\hat{A} = -(1/3)[\;(\alpha^{1/3}+\alpha^{-1/3}) - (1/2)(\alpha^{1/3}+\alpha^{-1/3})^{-1/2}\;]$ is strictly negative, contrary to the analogous result for Ψ_{sp}.

Since $\hat{A}$ has the same sign as the correction for the stationary wavenumbers k_s and μ_s [see (2.20)], the sign of β turns out to have a more important effect on the lee-wave velocity field when the forcing is topographical. Applying the forcing amplitude to the vertical velocity, rather than to higher derivatives of $\hat{\Psi}$, is also responsible for the above-mentioned short-wave singularity, and the fact that the estimate does not decay in the vertical for fixed x.

The horizontal near-field approximation contains the familiar Green's function for nonrotating mountain waves, namely,

$$\hat{\Psi}_G = \delta(x) \cos z - \frac{1}{\pi x} \sin z + \hat{C}_G . \qquad (2.37)$$

Recall from section 1.4 that the validity of the first part of the approximation is restricted to a z-dependent radius, in this case $|x| \ll z^{-1/2} < 1$.

The dispersive contribution to $\hat{\Psi}_G$, found by changing variables in (2.32) and setting $x = 0$, is infinite when $\beta = 0$. Hence the short waves completely determine the streamfunction amplitude near $x = 0$ in the barotropic case. For $\beta \neq 0$, an additional contribution from the baroclinic gravity waves appears. Since $d\mu/dk \approx \pm(\beta^2/r^2)/(\mu^2-r^2)$ near the stationary wavenumber, $\mu = r$, the contribution is found to be

$$\hat{C}_G = 2 \frac{r^2}{\beta^2} \frac{\cos(rz + \pi/4)}{\sqrt{(2\pi r z)}} , \quad \beta > 0, \qquad (2.38)$$

or $O[(1-r)^{-1}z^{-1}]$ if $\beta < 0$, where it is assumed that $z \gg 1/(1-r)$. Because of this restriction on z, the result is irrelevant for very small β.

The integration constant for the vertical near-field approximation is trivial: $\hat{C}_I = 0$. Hence the analysis of the inertial disturbance is more usefully applied to the vertical derivative of the streamfuncton. Except for an overall factor, the nondispersive part of $\partial \hat{\Psi}/\partial z$ is the same as for Ψ in (2.28). Thus,

$$\partial \hat{\Psi}_I/\partial z = z \sin x + \hat{C}_I'. \qquad (2.39)$$

An expression for $-\hat{C}_I'$ is given by Pierrehumbert (1984) as the Green's function for $u(x)$ on the boundary. Unlike C_I, this contribution has no

extremum near the forcing (mountain), so little is gained by considering a longer expansion of the integrand, $\mu(k)\exp(ikx)$, in powers of $k-1 \equiv \varepsilon \ll 1$. For reference, Pierrehumbert's result is given as

$$\hat{C}_I' = - \left(\frac{2}{\pi x}\right)^{1/2} \sin(x + \frac{\pi}{4}) \ . \qquad (2.40)$$

Close to the mountain, the vertical derivative of the horizontal near-field estimate (2.37) is additive.

It is noted once again that the near-field estimate (2.39) breaks down around $z = x^{-1/2}$. In this case, the restriction does not imply an effective value for the Froude number, which is not a length scale in the mountain-wave problem (the "forcing" excites all vertical scales). However, because of the underlying hydrostatic assumption, the physical depth of the region in which (2.39) is valid is indirectly limited by the rotation. That is, the length scale U_0/N must not become so large (via $N \to 0$) that f/N is not small. No such restriction applies to (2.37), which is valid at an arbitrarily large dimensional radius as $U_0/f \to \infty$, provided a steady state is still possible.

Some of the foregoing conclusions will be verified next by numerically evaluating certain topographic solutions. Because the actual Green's function is unbounded along $x = 0$, "bell-shaped" mountain profiles, specified by $g_0(x) = (1+x^2/\ell^2)^{-1}$, will be substituted for $\delta(x)$. The numerical approach is as follows. The Green's function, with the unbounded gravity-wave contribution formally removed, is obtained first in essentially the same way as for interior forcing. This result is integrated numerically over $g_0(x)$ to obtain the rotating part of the solution for the regular mountain. Finally, the gravity-wave contribution is calculated separately using (2.37) and added.

The mountain half-widths in Figs. 2.8 and 2.9 are $\ell = .5U_0/f$ and $\ell = U_0/f$, respectively. What is most noteworthy in both figures is the negligible, but adverse, effect of negative β on the upstream disturbance. Clearly, low-level upstream enhancement requires an elevated source when $\beta < 0$. Also in accordance with the ray-tracing analysis, the cold-advection solutions feature large-amplitude vertically-propagating disturbances which resemble solutions in the nonrotating limit.

The baroclinicity has an equally striking effect on the surface velocity within the inertial wave-train. Near $x = 3$, setting $\beta = -.6$ more than doubles the negative values of u at the ground compared to $\beta = 0$. The surface velocities at $x = 3$ in Fig. 2.8 are roughly $-0.5\ U_0$ ($\beta=0$), $-0.1\ U_0$ ($\beta>0$) and $-1.0\ U_0$ ($\beta<0$). This contrast results from the vertical deflection of the energy in the barotropic inertia-waves, as discussed in section 2.3.

Another difference between the the Ro = 1 and Ro = 2 solutions is in the strength of the trapped (quasi-geostrophic) contribution. It can be seen that the phase surfaces are most strongly affected in the case of the broader mountain, and especially if $\beta < 0$. The bias toward positive values of the streamfunction is generally due to the long waves, as expected from (2.34). It can also be verified that the far-field phase surfaces conform closely to the stationary-phase prediction: $x^{2/3} + z^{2/3} = $ const.
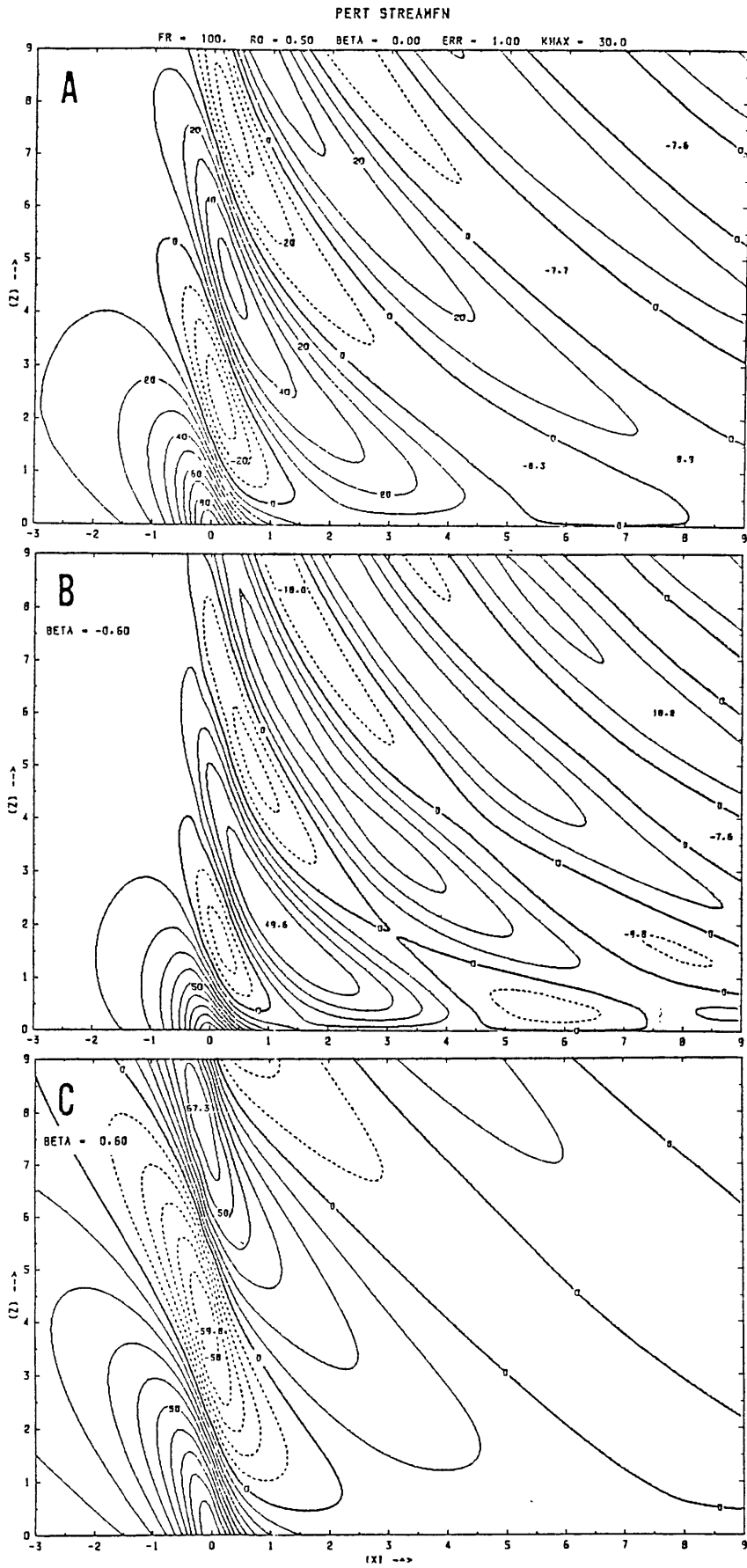
Fig. 2.8. Steady perturbation streamfunction for bell-shaped mountain ridge of width $\text{Ro}^{-1} = 1/2$, centered at $x = 0$, assuming β = (a) 0, (b) -0.6 and (c) +0.6. Contour interval is one-tenth the mountain amplitude.

STREAMFUNCTION

FR = 100.   RO = 1.00   BETA = 0.00   ERR = 1.00   KMAX = 30.0
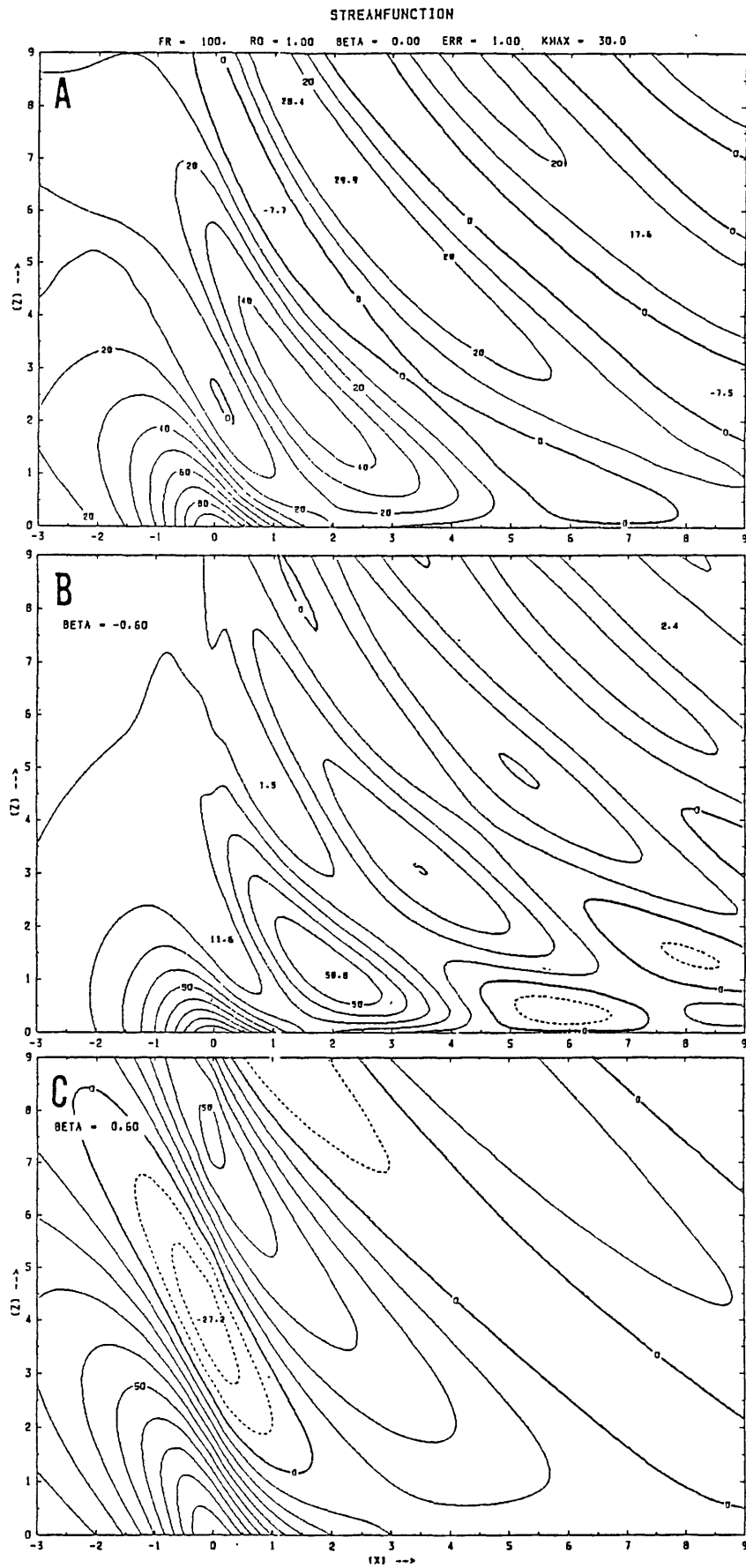
Fig. 2.9.   As in Fig. 2.8, except Ro^{-1} = 1   .

CHAPTER 3. RESPONSES TO DISTRIBUTED FORCING

The linear results of chapter 2 will be applied here to a small
number of hypothetical forcing scenarios. Many of the assumptions to be
made follow earlier attempts to model highly-nonlinear forced
disturbances. As discussed briefly in chapter 1, efforts of this kind
have typically led to good qualitative understanding without yielding
elegant or quantitative results. Thus, the goal in this chapter is only
to establish the consistency of the proposed orographic mechanism with
easily accessible details about the amplitude, dimensions and shape of
linear disturbances in a minimal environment for frontogenesis. The
alternative mechanisms involving surface friction and diabatic effects
will also be examined.

The first step in the analytic approach is to establish the role
of interior forcing, whose relevance has heretofore been inferred from
observations and numerical simulation. Under certain assumptions, the
sources written into the linear equations (2.2) may be considered to
include the nonlinear advection of momentum and temperature, as determined
by some independent (locally-valid or superimposed) disturbance.
Specifying this disturbance can be likened to making a closure hypothesis
in a theory for turbulent mixing. One approach to closing the system
(2.2) is to postulate weak nonlinearity and use a known linear, or
simplified nonlinear, topographic solution to evaluate the source terms.
The other approach is to assume the existence of highly localized regions
of turbulence capable of launching a wide spectrum of propagating waves.

Implicitly, both concepts use a non-interaction hypothesis, which considers the disturbance forced by the nonlinearity to be incapable of systematically weakening the presumed forcing. The theory of coherent, nonlinear shallow-water waves (e.g., Segur, 1973) in effect enforces non-interaction through a solvability condition. However, the same formality is not possible in cases of continuous external forcing, in which the shape and amplitude of the waves are not adjustable. Moreover, there is no significant interaction between stable, barotropic internal gravity waves. The comparison will nevertheless suggest an interpretation of the notion of "orographic adjustment" mentioned by Pierrehumbert and Wyman (1985).

3.1 The role of interior forcing in orographic adjustment theories

The wave-generation theory of upstream influence assumes further that the nonlinear conditions determining the forcing decay upstream fast enough to preserve the basic state for the secondary linear disturbance. This second hypothesis is needed in the Lighthill (1952) theory of jet noise, and is implicit in Ley and Peltier's (1979) study of wave generation through frontal collapse. PW have taken the turbulence idea somewhat beyond speculation for barrier flow by showing the coincidence of wave-breaking and upstream surges of horizontal long-wave energy. Since the resulting "columnar" disturbance is more resistant to turbulence than ordinary mountain waves, and can modify the environment without qualitatively affecting the linear propagation, the barotropic mechanism may be only weakly restricted by the localization hypothesis.

What is missing from PW's interpretation are details of the manner in which the mountain height becomes imposed on the disturbance as a length scale. They have, however, produced evidence for a type of orographic adjustment process, in which the height of the mountain is dynamically "adjusted" through the formation of a stagnant boundary layer whose depth depends linearly on h as well as λ_G. It is reasonably clear that the amplitude of the vertical streamline displacement, i.e., $z' \approx h$, can be considered a length scale of the response as soon as the laminar solution breaks down. However, since the convective patches first occur high over the mountain, at a level independent of h, the adjustment process at the ground probably depends in a complicated way on transient waves and lower boundary reflections.

If the absence of strong downslope winds in coastal front events can be taken as evidence, blocking in the baroclinic case must not be related to wave-breaking. In fact, the nonlinearities attributable to rotation and baroclinicity (notably the vertical advection of perturbation potential temperature) differ from breaking waves in two important respects. In the first place, the nonlinearity appears to be strongest at low levels near the mountain, rather than at a steepening level. As a result, the imposition of the mountain scale on the disturbance may be more direct, particularly because, as noted in chapter 1, background rotation makes it possible for an external vertical scale to determine directly the horizontal scale of the response.

In a second departure from the wave-breaking process, low-level deceleration enhances, rather than weakens, the baroclinic nonlinearity through vertical shearing deformation. Thus, a non-dissipative

two-dimensional flow appears to have no means of equilibrating the nonlinearity as the disturbance evolves. It is therefore suggested that orographic adjustment in this case is a process in which the nonlinear effects grow stronger and more concentrated in a narrow layer separating stagnant fluid below from a weakly-disturbed flow aloft.

This hypothesis is founded on the idea that an obstruction can be effectively broadened by the presence of an adjacent stagnant pool. The modified length scale is limited in theory to the deformation radius determined by the mountain height. Orographic adjustment should therefore lead to the condition $RoFr \approx 1$ relating the two limiting dimensions of the modified obstacle. Given nonlinear near-field conditions, i.e., $Fr > 1$, it follows that the adjusted flow above the obstruction has $Ro < 1$. In that case, PW's barotropic simulations imply a negligible upstream disturbance above the obstacle. Presumably, the entire adjustment process fails in a moderately-nonlinear barotropic flow because (1) upstream energy propagation is less efficient, and (2) the low-level deceleration does not produce positive feedback.

The analysis of the nonlinear apparent sources in (2.2) will require assumptions of weak nonlinearity, baroclinicity, or rotation. These do not further restrict the overall analysis, because the upstream linearity assumption already makes a complete analytic description of blocking or frontogenesis impossible. The goal is simply to establish formally a mechanism for positive feedback which is unique to the warm-advection situation. The feedback will be measured from steady solutions, under the assumption that the nonlinear processes and initial low-frequency transience only produce gradual shifts in the parameters

governing such solutions. This weak form of Long's (1955) hypothesis was identified above as a non-interaction hypothesis.

The proposed analysis is also incapable of showing how the mountain height becomes a length scale in the response. That process may be accessible by analyzing the weakly-nonlinear reaction to parameterized, flow-dependent changes in the (effective) shape of the upstream terrain. Such an analysis should first be perfected for a barotropic flow. Here, the transition to a regime in which the mountain provides a vertical forcing distribution will be assumed as part of the orographic adjustment hypothesis. That is, it is expected that the mountain height will be selected dynamically as a response scale if a positive feedback is possible.

Interpreting the forcing terms in (2.2) as apparent sources also brings in local time dependence as a forcing "mechanism". Intermittent forcing is clearly involved in the wave-breaking theory, which requires localized convective overturning, but will not be studied here in relation to baroclinic blocking. In fact, all additional terms not directly related to the horizontal temperature gradient or rotation will be ignored. The justification is that the nonlinear terms vanish identically on the right side of (2.3) when the steady, nonrotating, barotropic momentum and temperature fields are used to evalute them (see Smith, 1977).

The possible sources of upstream energy are not limited to local inertial effects. For example, the presence of a uniform temperature gradient in y and the associated x-component of thermal wind introduces several linear advection terms. In the three prediction equations, they

are $F_u = -U_1 u_x$, $F_v = -U_1 v_x$ and $F_b = -U_1 b_x - \beta_y v$, where $U_1(z)$

$= -\beta_y z$, and $\beta_y = -U_z/N = \text{const.}$

The U_1-advection will not be considered further in this chapter except to note that ray-tracing theory predicts a refraction of the propagating waves as the local Rossby number varies along the ray path (e.g., Klemp and Lilly, 1982). Suffice it to recognize that the local Rossby number for a propagating mode increases downward from an elevated source when $\beta_y > 0$, so that (1) no trapping can occur (Ro $\neq$ r) and (2) the streamwise group speed cannot change sign from negative to positive (Ro $\neq$ r/$\left|\beta\right|$).

The focus therefore will be on the apparent heat source, $F_b = -\beta_y v$, which establishes a mechanism for shearing deformation of the horizontal temperature gradient. The neglect of the U_1-advection is easier to rationalize if β_y is greatest near the ground, and if the actual vertical shear is strongly subgeostrophic, as it appears to be in nature. The effect of a critical level ($U_1 = -1$) above the source is beyond the scope of the present work.

The survey of forcing scenarios in this chapter will include a qualitative examination of friction and heating at the ground, which were discussed briefly in chapter 2. A linear relationship between F_v and v will be assumed for the transverse friction, and a step-like model of surface heating and streamwise drag will be considered. The transverse friction is of particular interest because observations of the parallel surface wind in coastal front events show a weaker "drainage" flow than might be expected with such a large ageostrophic component of streamwise velocity.

3.2 The effect of baroclinicity in the semi-geostrophic limit

Although fully nonlinear analytic solutions are not available for the topographic problem, it will be possible to treat the semi-geostrophic limit by means of a weakly-baroclinic generalization of the nonlinear barotropic solutions found by Pierrehumbert (1985). The analysis indicates an enhancement of the deceleration in the strongly nonlinear regime which is, however, probably too weak to change the transient nature of the upstream surge discovered by PW. Consequently, only narrow (Ro $\gg$ 1) mountains ridges will remain candidates for blocking in laminar flows.

It was pointed out in chapter 1 that nonlinear semi-geostrophic solutions are identical to the linear quasi-geostrophic ones except for a coordinate transformation, and that the nonlinearity only weakens the upstream deceleration and vertical shear. In appendix A, the coordinate transformation is applied in the context of a baroclinic basic state. The new vertical coordinate is the undisturbed height, ζ, in units of $fa\ell/N$, and the dependent variable, χ, is a streamfunction for the particle displacements, x' and z'.

Thus if ξ is the undisturbed (geostrophic) horizontal position in units of ℓ, $\chi(x,\zeta)$ satisfies

$$RoFr \; \chi_x = z-\zeta \equiv z'$$
$$-RoFr \; \chi_\zeta = x-\xi \equiv x',$$

(3.1)

in which x and z are also normalized by the semi-geostrophic scales, ℓ and $fa\ell/N$. According to (A.3), with Ro $\ll$ 1,

$$\chi_{xx} + \chi_{\zeta\zeta} - 2\beta\chi_{x\zeta} = -\beta RoFr \ J(\chi_x, \chi_\zeta), \qquad (3.2)$$

where the Jacobian is defined with respect to x and ζ. The variable χ has been scaled so that the lower boundary condition reads $\chi_x = g_0(x)$, with g_0 order-unity. The horizontal velocity is obtainable from χ via u+1 = $(1+z'_\zeta)^{-1} = (1-x'_x)^{-1}$. Hence positive values of x'_x correspond to accelerated flow.

Now assume weak baroclinicity such that $\left|\beta\right| < \left|\beta\right|RoFr \ll 1$, and write $\chi = \chi_0 + \beta\chi_1 + \cdots$. There is no important loss of generality in considering a bell-shaped mountain profile, $g_0(x) = (1+x^2)^{-1}$. In that case, $\chi_0 = \tan^{-1}\left(x/(1+\zeta)\right)$, and the correction satisfies

$$\nabla^2\chi_1 = \frac{RoFr + 2\left(x^2-(1+\zeta)^2\right)}{\left(x^2 + (1+\zeta)^2\right)^2}, \quad \chi_1 = 0 \text{ on } \zeta = 0, \qquad (3.3)$$

where $\nabla^2 \equiv \partial^2/\partial x^2 + \partial^2/\partial\zeta^2$. It should first be verified that when RoFr = 0, the correction produces a shift in the horizontal velocity pattern, as found in the exact linear analysis of section 2.6. In the case of negative β, the correction $\beta\chi_1$ has a negative center at an order-unity height above the summit (since $\nabla^2\chi_1 < 0$ at x = 0), and indeed the maximum surface wind is then shifted upstream, where the correction for x'_x is positive. [The reduction of u at the summit is an $0(\beta^2)$ effect which cannot be deduced from (3.3)].

When RoFr > 2, $\beta\chi_1$ becomes positive at low levels over the mountain, and the nonlinearity offsets the purely linear baroclinic effect. To obtain a conservative bound on the resulting surface displacements, note that the area integral of the nonlinear contribution to the right side of (3.3) is (4/3)RoFr. Hence, taking $z_0 = 1$ in the

long-wave analysis of (2.13) leads to $\chi_{1\zeta} < \pm(4/3)RoFr/(2\pi)$ along $\zeta = 0$, as compared with $\chi_{1\zeta} = x/(1+x^2) < \pm1/2$ in the linear solution of (3.2). It thus appears superficially that the correction is not negligible for $RoFr \gg 1$.

However, PW's simulations show that the semi-geostrophic solution, by neglecting meridional accelerations, considerably overestimates the actual displacements when $RoFr > 1$. Thus, although the breakdown of the laminar solutions for broad topography may be delayed through the reduction in lee velocity, it is reasonable to conclude that the actual nonlinear contribution to χ does not grow fast enough to change the character of the breakdown at (or beyond) $RoFr \approx 3$. The expansion assumption $|\beta|RoFr \ll 1$ strongly limits the size of β near the breakdown, but it can be tentatively assumed that the laminar solutions behave similarly for larger $|\beta| < 1$.

To give more generality to these conclusions, consider now the problem of semi-geostrophic flow over a smooth step. An analytic solution is given by $\chi_0 = (x/\pi)\tan^{-1}[x/(1+\zeta)] - [(1+\zeta)/2\pi]\log[1+x^2/(1+\zeta)^2]$, which is simply the normalized horizontal integral of the previous result. It is clear from inspection that the Jacobian of the resulting displacements, $z_0' = (RoFr/\pi)\tan^{-1}\left(x/(1+\zeta)\right)$ and $x_0' = (RoFr/2\pi)\log\left(1+x^2/(1+\zeta)^2\right)$, vanishes identically. Hence, the solution of the linear part of (3.2) includes the nonlinear effects to $O(\beta^2)$ for this terrain shape. The correction for negative β makes the low-level horizontal displacement more negative upstream, but the surface velocity is actually increased everywhere, according to (2.35) with $\beta w < 0$ and $r \approx 1$ (although the next-order correction yields decelerated flow far downstream). The more

negative upstream x' in the case of negative β implies increased surface divergence.

The smooth step thus appears to present an even weaker obstacle when the basic state is characterized by warm advection. The unboundedness of the solution for x' requires some comment, however. It is well-known that plateau topography does not permit a nontrivial steady solution in the absence of rotation, because of an excessively constrained relationship between the adverse pressure gradient and the horizontal convergence. The f-plane solution is possible because of an additional conversion of potential energy stored in the basic horizontal pressure gradient. Through this mechanism, the flow is permanently deflected toward low pressure while ascending the step.

On the other hand, the details of the parallel flow make both of the semi-geostrophic solutions unphysical at very large $\left| x \right|$. Since v is a linear combination of x' and z', the parallel velocity slowly increases to infinity as $\log \left| x \right|$ in the plateau solution, while the same growth occurs in the y-displacement (y') in the case of the isolated mountain. These are artifacts of the equally unphysical assumption that the long waves are two-dimensional, time-independent and inviscid. The solutions remain useful only to the extent that the upstream boundary condition for v and y' may be considered adjustable.

With respect only to the parallel flow and f=0 problems, the isolated mountain solution resembles the Green's function for interior sources studied in chapter 2. It is appropriate to re-emphasize an important difference between these two which pertains to the dependence on an external vertical length scale. If $\mathcal{L}_{qg}$ is the linear operator in

(3.2), the solution of $\mathfrak{L}_{qg}(\psi) = \delta(z-z_0)/(1+x^2)$, subject to $\psi = 0$ at the ground, is

$$\hat{\psi}_{qg} = -\frac{1}{4r} \log \frac{(X-X_0)^2+(|Z-Z_0|+1)^2}{(X-X_0)^2+(Z+Z_0+1)^2} , \qquad (3.4)$$

where $X = x+\beta z$ and $Z = rz$. The corresponding velocity perturbation at the ground may be expressed using the definition $\lambda \equiv Z_0+1$ as

$$\hat{u}_{qg}(x,0) = -\frac{\lambda}{(X-X_0)^2 + \lambda^2} , \qquad (3.5)$$

The perturbation is negative everywhere, and decreases as $1/x^2$ beyond $|x-x_0| \approx \lambda$. Because the details of the forcing at the boundary do not affect the response, these results are also representative of many smooth vertical distributions with depth or decay scales of z_0.

Since $z_0 = O(RoFr)$ in the semi-geostrophic solution, (3.4) and (3.5) show that z_0 takes over as the <u>horizontal</u> scale of the response below $z = z_0$ when $RoFr \gg 1$. The corresponding dimensional distance is the Rossby deformation radius, $L_D \equiv Nh/(fa)$. By contrast, the linear mountain-wave response always scales with ℓ, so that the interior forcing has a wider influence than simple topography when $RoFr = L_D/\ell$ is large. This conclusion becomes important in the next section, in which the advection of b and v by a non-semi-geostrophic meridional circulation is considered.

3.3 Apparent forcing in the near field

The momentum and temperature fields in flow over a narrow barrier produce a substantially different distribution of apparent forcing. On

reverting to the scaling of chapter 2, the nonlinearity in the y-momentum and buoyancy equations may be written $F_v = -J(\psi,v)$ and $F_b = -J(\psi,b) = -\beta J(\psi,v)$. Here, the buoyancy source has been expressed in terms of v by using the result $b = \beta v - r^2\psi$, which follows easily from the steady, homogeneous form the equations for v and b in (2.2).

The formal justification for treating the near-field nonlinear terms as sources must be based on $\psi = O(Fr) \ll 1$ or $v = O(Ro^{-1}Fr) \ll 1$, where the estimate for v follows from making a scaling change to $L = \ell$ ($R = Ro$) in (2.2b). Strictly, all but the $O(Ro^2)$ gravity-wave terms $\psi_{xx} + \psi_{xxzz} \equiv \pounds_G(\psi)$ must be considered part of the inhomogeneity in (2.7) when $Ro \gg 1$. Smith (1982) carried out the indicated large-Ro analysis formally, but his assumption that the near-field topographic solution was valid everywhere led to spurious far-field results (Pierrehumbert, 1984). The intention here is to assume, less formally, that the source terms are locally non-zero and can be evaluated from local solutions of the linear topographic problem, $\pounds(\psi) = 0$.

If such a solution is denoted by a zero subscript and inserted in the right side of (2.9), the problem for the correction, ψ_1, may be written

$$\pounds(\psi_1) = \frac{\partial}{\partial z}\Big|_M J(\psi_0,v_0), \quad \psi_1 = 0 \text{ on } z = 0, \quad (3.6)$$

where the expansion parameter (Fr or Ro^{-1}) is absorbed in ψ_1. Since the partial derivative is taken along an absolute momentum surface, it is clear that baroclinic effects are potentially quite significant. In fact, it will be assumed in the following that the partial derivative at constant x can be neglected compared to the horizontal derivative. This

simplification is justified if the mountain has finite amplitude and is considerably steeper than the M-surfaces. It is also a convenient assumption in that it allows ψ_1 to be obtained from the horizontal derivative of the solution of $\mathfrak{L}(\psi) = J(\psi_0, v_0)$, which in turn resembles the problem for the Green's function if the Jacobian is predominantly of one sign.

The y-momentum equation may be integrated to yield $v_0 = -\beta\psi_0 - \bar{u}_0$, where $\bar{u}_0 \equiv \int^x u_0 \, dx'$, and the subscript denotes the near-field topographic solution. Hence the advection of v_0 (and indirectly b_0) may be written in the form

$$J(\psi_0, v_0) = -(u_0{}^2 + w_0\bar{u}_{0z}). \qquad (3.7)$$

Both u_0 and the vorticity, u_{0z}, are $O(Fr)$. The x-integral reduces the second term by a factor of $O(Ro^{-1})$, but since the velocity components are related by $w_0/u_0 = O(Ro)$, it can be seen that both parts of the v-advection are formally of order Fr^2. The estimate for the long waves contains the additional factor $k^2 \ll 1$. Hence, the nonlinearity is indeed isolated near the mountain in the rotating topographic solution.

The Jacobian is negative upstream, then vanishes (along with u_0 and w_0) near the mountaintop, and remains small in the inertial lee-wave disturbance, where the two components of advection have opposite sign. The upstream region of negative v-advection for the case $Ro^{-1} = 0.3$ can be seen by comparing the transform solutions for ψ_0 and v_0 plotted in Fig. 3.1. In general, the vertical component of the advection dominates when Ro is large. Thus, the nonlinearity is primarily due to upward motion in a reinforced vertical stratification. The reinforcement is caused by tilting the basic horizontal temperature gradient.

PERT STREAMFN

PERT V
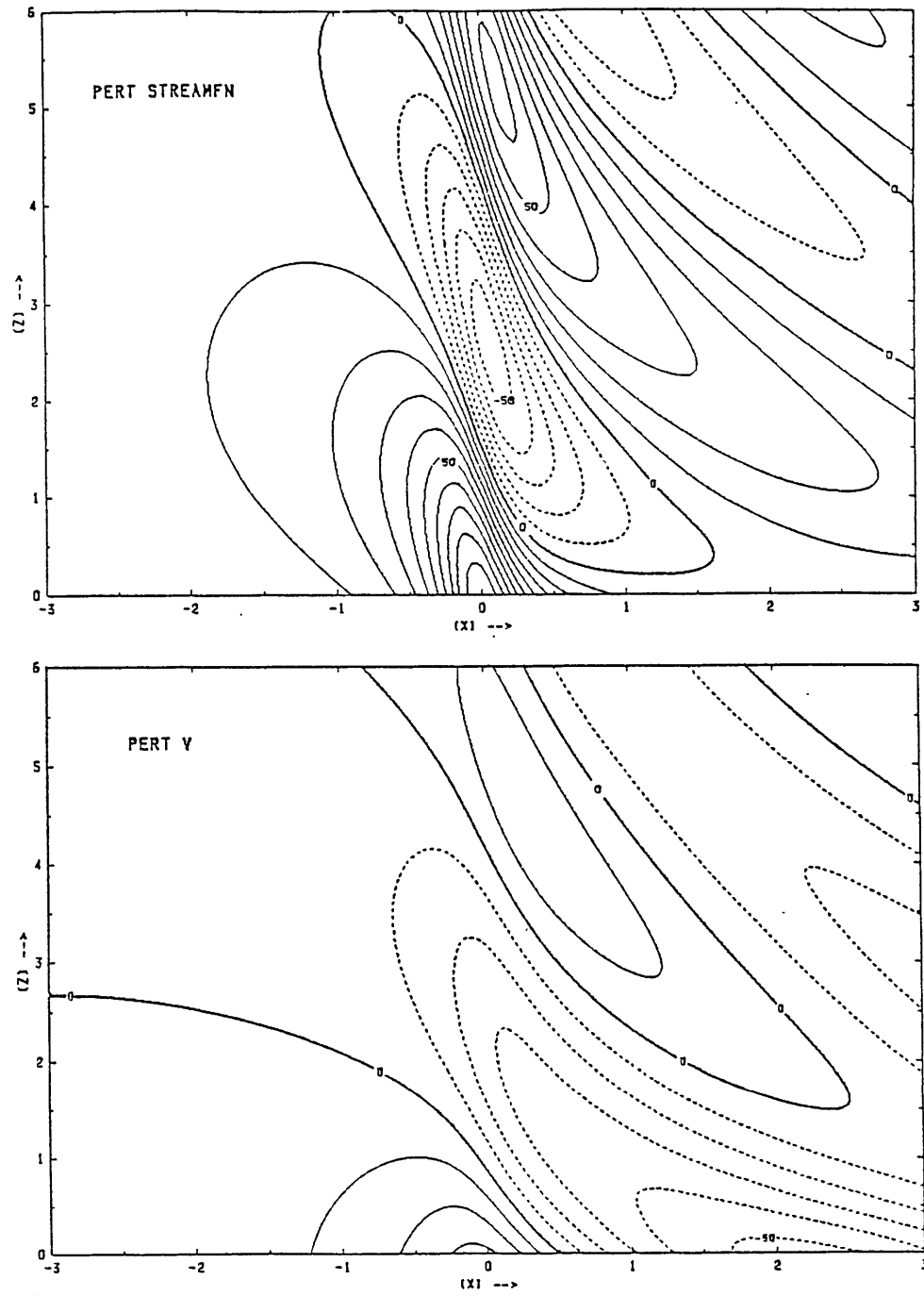
Fig. 3.1. Perturbation streamfunction and parallel wind in linear flow
past bell-shaped ridge of width Ro^{-1} = 0.3. Contour interval is
one-tenth the mountain amplitude (negative contours shown dashed).

Let it be assumed that β is negative and large enough to make the M-surfaces less steep than the mountain. Then, since the distribution peaks with negative values on the windward flank of the mountain, a positive source for ψ_1 appears near the summit, with a somewhat broader negative source of comparable strength upstream, according to (3.6). The long-wave response to such a distribution is considerably reduced by cancellation between the positive and negative regions, but this happens only outside the "semi-geostrophic" radius $\lambda = z_0+1$.

The effect is well illustrated by the x-derivative of the results (3.4) and (3.5) for a single peak. Thus, for the dipole forcing, $g_1(x) = -2x(1+x^2)^{-2}$, the surface velocity perturbation, written with semi-geostrophic variables, is

$$u_{qg} = \left| \beta \right| J_0 RoFr \, \frac{2(x-x_0)\lambda}{\left((x-x_0)^2 + \lambda^2 \right)^2}, \qquad (3.8)$$

where x_0 is now the position of the peak value, $-J_0$, of $J(\psi_0, v_0)$, and J_0 is normalized by $fa^2 U_0$. The overall factor Fr estimates the vertical integral over the forcing, while $\left| \beta \right| Ro$ arises from the horizontal derivative. The maximum deceleration is thus of order $-J_0 RoFr \lambda^{-2}$, which varies inversely with RoFr, as does the response (3.5) to forcing of one sign. However, (3.8) decays as x^{-3}, rather than x^{-2}, for large $\left| x \right|$.

The flow described by (3.8) is divergent near $x = x_0$ and convergent everywhere upstream from $x = x_0 - \lambda/\sqrt{3}$. It is clear from inspection of the Green's function solutions, e.g., Fig. 2.6, that the total response to dipole forcing will exhibit the same type of pattern. However, the horizontal length scales, as well as the amplitude dependence

on Ro, will be determined by the relative importance of the long and short waves. For moderate values of β, the baroclinic gravity waves, with $k = O(1)$, will produce roughly the same amplitude as the Green's function contribution, $C_G(z)$, except for the factors $FrRo^{-1}$ (from integrating the forcing) and $|\beta|J_0$. It will be seen that the contribution from the barotropic gravity waves, with $k \gg 1$, decreases more slowly than $1/Ro$ at large Rossby numbers. The intermediate and short waves both tend to reduce the width of the divergent region, and bring the convergence closer to the source.

The barotropic gravity-wave contribution is easiest to describe in the context of near-field topographic solutions, which requires a brief digression. Recall that the gravity wave disturbance alternates on a vertical scale of $\lambda_G = U_0/N$ between two horizontal structures. These are the mountain profile itself, $g_0(x)$, and its Hilbert transform, $G_0(x) = \pi^{-1}\int g_0(x_0)dx_0/(x_0-x)$. For the bell-shaped mountain, it happens that $G_0(x) = xg_0(x)$, whence

$$\hat{\psi}_G = Fr \left(\frac{\cos z}{1 + (Rox)^2} - \frac{Rox \sin z}{1 + (Rox)^2} \right). \tag{3.9}$$

This type of disturbance dominates the flow directly over the mountain whenever $Ro > 1$. The amplitude of the corresponding horizontal velocity perturbation is Fr, and thus does not reflect the width of the mountain as in the semi-geostrophic result.

The Hilbert transform does not exist for a smooth step; however, the divergence of the transform actually results from the long waves, which are extraneous in a near-field solution. The near-field f-plane disturbance can be seen after arranging for the unbounded long-wave

contribution to appear at $|x| = \infty$. Thus the integral of (3.9),

$$\hat{\psi}_G = Fr \left(\frac{1}{\pi} \tan^{-1}(Rox) \cos z - \frac{1}{2\pi} \log (Ro^2 x^2 + 1) \sin z \right) \qquad (3.10)$$

is accurate for the rapidly-varying disturbance near the step (in $|x| \ll 1$). The flow at the ground remains convergent throughout $x < 0$, in contrast to the semi-geostrophic result given in the previous section. Moreover, the logarithmic behavior is accurate out to $|x| = O(1)$, so that if Ro is large, the topographic step presents a particularly strong barrier to the flow.

According to (2.24), the mountain-wave structure must be multiplied by sin z, and integrated with respect to x to obtain the near-field response to the interior forcing. To highlight the small-x structure, let the horizontal distribution of $J(\psi_0, v_0)$ be represented simply as $g_1(x) = -J_0$, and its Hilbert transform as $G_1(x) = -J_0 vx$. The response below $z = z_0$ is then

$$\psi_G \approx |\beta| J_0 Fr \sin z \left(\cos z_0 - \frac{v}{2} Ro(x-x_0) \sin z_0 \right) (x-x_0). \qquad (3.11)$$

Only one integral is required because of the horizontal derivative contained in (3.6). The factor Fr is due to the vertical distribution, as in (3.8).

In general, v is proportional to the area under the graph of g_1 and the linear Taylor coefficient of g_1. The familiar choice $g_1(x) = 1/(1+x^2)$, has $v = 1$, while the Gaussian distribution with the same half-width, i.e., $g_1(x) = \exp(-x^2 \log 2)$, has $v = 2[(\log 2)/\pi]^{1/2} \approx .94$. The first derivative of the Gaussian thus produces a slightly weaker

symmetric response. This is more significant in the topographic solution, in which the Hilbert transform determines the surface velocity perturbation. The surface velocity in the case of interior forcing is

$$u_G \approx -\left|\beta\right| J_0 Fr \left(\cos z_0 - \frac{\nu}{2} Ro(x-x_0) \sin z_0\right) (x-x_0). \qquad (3.12)$$

Thus for $\pi/2 < z_0 < \pi$, the barotropic gravity waves offset the low-level divergence found close to $x = 0$ in the baroclinic gravity-wave and long-wave contributions. If a bell-shaped mountain is intended, the second term in (3.12) is an approximation of the same logarithmic structure which produced low-level convergence in (3.10), but here has an overall factor Ro^{-1}. The short wave contribution then vanishes as $\log(Ro)/Ro$ for large Rossby numbers.

Fig. 3.2 presents contour plots of the perturbation streamfunction in a baroclinic flow ($\beta = -0.6$) forced by the dipole source $g_1(x,z) = \delta(z-z_0)$ d/dx $(1+Ro^2x^2)^{-1}$. The two cases shown are for $Ro^{-1} = 0.5$ and $Ro^{-1} = 0.3$. The forcing is assigned an amplitude of -100 and centered at $x_0 = 0$, $z_0 = \pi/2$. It can be seen that the velocity perturbation contains significant upstream low-level convergence, and attains an amplitude of about $U_0/3$ at the ground just upstream from the center of the forcing. The response is somewhat weaker for the narrow distribution ($Ro^{-1} = 0.3$), for the reason just cited. Notice that the analysis also predicts an acceleration of the flow in the lee of the mountain.

PERT STREAMFN

BETA = -0.60   FR = -100.   RO = 0.50   ZF = 1.57
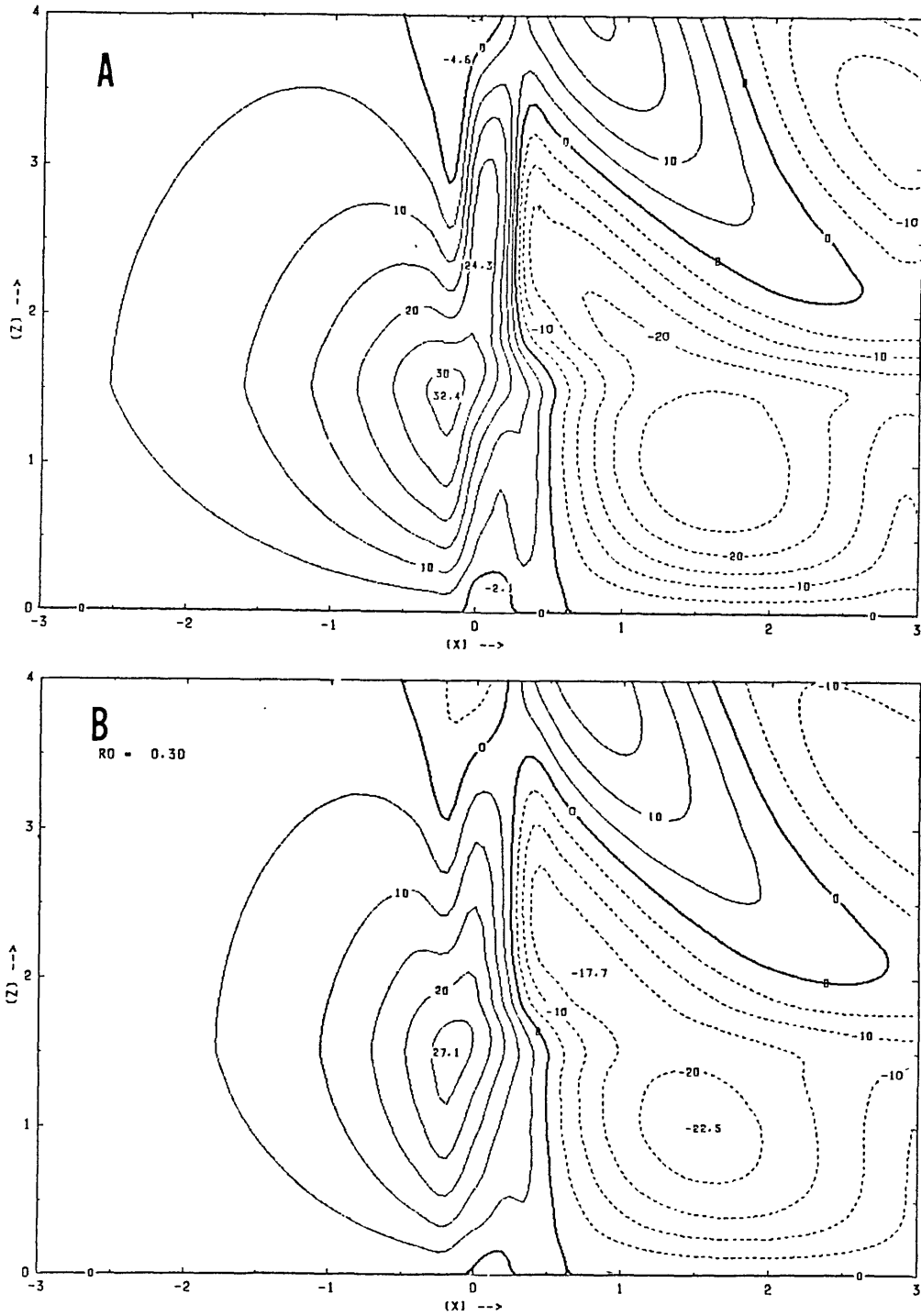
Fig. 3.2.   Perturbation streamfunction forced by dipole source defined in text, centered at $x_0 = 0$, $z_0 = \pi/2$.   Horizontal forcing scale is Ro^{-1} = (a) 0.5 and (b) 0.3, and contour interval is 1/20 of forcing strength.

3.4 Alternative mechanisms for coastal convergence

The alternative _primary_ mechanisms for convergence and frontogenesis involve sharp horizontal gradients of boundary-layer heating and friction. These can be crudely modelled by specifying the forcing as

$$F = -\tau^{-1} \frac{\text{sgn } x}{2} \exp(-z/Fr), \qquad (3.13)$$

where τ is the nondimensional time scale, in units of $1/f$, for the heating or friction, and Fr is the nondimensional boundary-layer depth for the parameterized forcing processes. Recall that the buoyancy is normalized by NU_0. Since this is not as practical as $N^2 h$ in the present context, the heating time scale will be written as $\tau_b = Fr^{-1}(f\tau_b*)$, where τ_b* is defined as the dimensional time required to heat the air by an amount $N^2 h$. The frictional time can be written simply as $\tau_u = f\tau_u*$, where τ_u* is the time needed to decelerate the mean flow to rest. These are not strictly e-folding times since (3.13) does not depend on the perturbations.

It is emphasized that the forcing times refer to the _differences_ between sea and land. If the physical problem requires it, the antisymmetric horizontal pattern in (3.13) can be changed so that F vanishes on either the upstream or downstream side of the coast, which is placed at $x = 0$. Such a change affects the variables v, p and b, but not the meridional circulation.

To further simplify, note that the vertical structure in (3.13) has a sine transform, $\int_0^\infty \exp(-z/Fr)\sin \mu z\, dz = Fr^2 \mu (1+Fr^2 \mu^2)^{-1}$, which resembles that of a concentrated source at $z = Fr$, i.e., $Fr \int \delta(z-Fr)\sin \mu z\, dz = Fr \sin(Fr\mu)$, for $Fr\mu < \pi$. Hence the response to the smooth distribution

in (3.13) is reasonably well represented by all but the rapidly-varying part of the response to a concentrated source of strength Fr at z ≈ Fr. With this simplification, the problem for both the frictional and "embedded land-breeze" disturbances is just the Green's function problem:

$\mathcal{L}(\psi) = -Fr\tau^{-1}\delta(x)\delta(z-Fr)$, where $\tau = f\tau_b*$ or $f\tau_u*$.

For quite a range of Froude numbers, the solutions of chapter 2 all indicate a maximum deceleration of the mean flow of about $U_0/2$ at the ground just downstream from a source of unit strength. Thus, a surface drag can be considered as a possible primary frontogenetical mechanism, with a direct nonlinear effect on the flow, if $\tau_u = 0(1)$, or τ_u* is on the order of 3 h. Whether this is a reasonable frictional time depends on the actual land-sea contrast, as well as the depth of the boundary layer and the efficiency of the mixing. A typical mixing coefficient of K = 5 m^2/s (Orlanski and Ross, 1977), in conjunction with a no-slip boundary condition, requires a boundary-layer depth of h = $\sqrt{(K/\tau_u*)}$ ≈ 200 m if $\tau_u = 1$. It is not likely that such a shallow frictional boundary layer could be maintained without an exceptionally strong static stability, which is also needed to keep Fr = 0(1) for such shallow forcing. Yet in reality, the ocean-heated air in the coastal front events has relatively weak static stability.

To assess the strength of the boundary-layer heating, note for example that N^2h = 6 K when N = .02 s^{-1} and h = 500 m. A heating rate of 6 K in 3 h is not impossible in nature, but clearly could occur only over water, and only during a period of large-scale cold advection. The indication, therefore, is that the coastal heating contrast may be significant briefly during the initial stages of the frontogenesis. The

same conclusion was reached tentatively in chapter 1 on the basis of the apparent connection between an early onset of coastal convergence and an especially strong land-sea thermal contrast.

The two remaining mechanisms are _secondary_ in nature, i.e., consequences of an independently forced convergence. Consider first the effect of an apparent heat source, $F_b = -\beta_y v$, made possible by a basic temperature gradient parallel to the primary forcing (note: $\beta_y = f^{-1}N^{-1}B_y$, where B_y is the dimensional buoyancy gradient). It is assumed that v is induced independently by topographic or other causes, so that the apparent heating is strictly a secondary mechanism.

The combination of β_y and a sheared horizontal flow $v(x)$ either establishes, or modifies, a streamwise component of temperature gradient, and forces a thermally direct (relative to the secondary gradient) meridional circulation. Recall that horizontal shearing deformation provides the _primary_ mechanism for frontogenesis in the nonlinear Eady problem (Hoskins and Bretherton, 1972). In general, if v varies linearly in x, the x-gradient of temperature will vary linearly in time.

In view of the homogeneous equation for v, the response to the apparent heating is governed by

$$\pounds(\psi_1) = +\beta_y u_0, \qquad\qquad (3.14)$$

where u_0 is the perturbation velocity associated with the primary disturbance. In the case of positive β_y, which is relevant to the coastal front, the equation for ψ_1 has negative sources in the decelerated regions of the main disturbance. Since such forcing creates additional low-level convergence in phase with the primary convergence, shearing deformation clearly provides a positive feedback when $\beta_y > 0$.

It can be shown that the potential vorticity of the flow is proportional to $r_1^2 \equiv 1-(\beta^2+\beta_y^2)$, which is therefore constrained to be positive. In particular, β_y is not expected to exceed unity unless the associated vertical shear is subgeostrophic. In any event, the source strength in (3.14) is $O(Fr\beta_y)$ for the topographic disturbance, or $O(Fr\tau^{-1}\beta_y)$ for the streamwise friction or diabatic forcing.

The qualitative effects of a transverse frictional stress are also within fairly easy reach. Let the forcing be given in this case by $F_v = -\tau_v^{-1}v_s(x)\exp(-z/Fr)$, where v_s is the perturbation parallel flow at the ground, and the friction time τ_v is normalized by $1/f$. The maximum in v_s coincides with the maximum upstream displacement from geostrophic position, as well as the point of zero streamwise velocity perturbation if the flow is steady. Although the linear near-field solution has $v_s = O(Ro^{-1}Fr)$, it is clear that the actual parcel displacements, and therefore v_s, can be larger than indicated by the linear results in areas where the flow verges on stagnation. Of course, the role of the y-momentum is to minimize the barrier effect and prevent stagnation, but the Coriolis force is relatively ineffective for narrow mountains, or presumably if v is reduced by friction.

Two aspects of the response to y-friction will be emphasized. First, a y-momentum sink acts more strongly on the large scales than does the heating or streamwise friction, as shown formally by the lack of an x-derivative on F_v in (2.9). Since the Coriolis effect works cumulatively with the large scales to reduce the barrier effect of an obstacle, the transverse friction can have an important positive effect on the prospects for blocking.

The second qualitative aspect of the y-friction is that the maximum surface velocity perturbation due to F_v must occur at a large fraction of the distance λ_I downstream from the primary deceleration, i.e., at the point where $u_0 = 0$. The result is a downstream shift in the zone of maximum convergence. Unlike the non-orographic primary mechanisms considered at the beginning of this section, the more complete frictional scenario thus appears to place the likely axis of frontogenesis well onshore. Only the _amplitude_ of the effect puts the frictional mechanism in doubt as the primary cause of the coastal front.

3.5 Summary and discussion of analytic results

The goal of chapters 2 and 3 has been to study the simplest physical system capable of supporting frontogenesis in a baroclinic environment, under the assumption that all imbalances are externally induced. Although the type of frontogenesis being modelled is demonstrably nonlinear and time-dependent, the approach has consisted of obtaining solutions for the steady, linear response to interior forcing.

Two arguments for the relevance of the linear approach have been given in chapters 1 and 3. First, it is known from numerical and laboratory simulations of barotropic flow past a barrier that the upstream disturbance appears suddenly, as the result of wave propagation from turbulent patches in the near field. It may be assumed that the subsequent nonlinear development of blocked flow depends primarily on the component waves which act on the upstream fluid parcels for the longest time, i.e., the steady waves. The second way in which the linear solutions are useful is in illuminating the baroclinic feedback, whose

effectiveness, it appears, can be predicted from either a weakly-nonlinear or a locally-nonlinear analysis.

The effect of baroclinicity can be reduced for analysis to the dependence on a single parameter β, which is related to the Richardson number. The two most relevant consequences for steady disturbances are easy to understand physically. These are (1) the tilting of the (quasi-balanced) long-wave response in the same direction as the B and M surfaces (the result of additional sources of perturbation b and m), and (2) the creation of a wider horizontal spectrum of vertically-propagating gravity waves (the result of reduced generation of perturbation v). In the case of basic-state warm advection ($\beta < 0$), in which the M-surfaces have the same tilt as waves with downward group propagation, the additional gravity-wave energy appears below the source and extends upstream as well as downstream.

Together, the two effects imply that the purely topographic response is weakened upstream when $\beta < 0$. Yet the orographic mechanism central to the present study assumes a basic state characterized by warm advection. Support for the orographic hypothesis therefore requires either a recognition that the linear and nonlinear processes are entirely distinct, or an assumption that nonlinear interactions can act as an elevated source of considerable depth. The second possibility has been pursued in chapter 3. In particular, the above-mentioned feedback mechanism has been emphasized, rather than attempting to model transience and turbulence (which may be unecessary anyway for frontogenesis).

To pin down the feedback mechanism, the nonlinear baroclinic effect in two Rossby number regimes has been considered. For Ro $\ll$ 1, the

semi-geostrophic solutions are valid upstream if RoFr < 3, and these implicitly take into account the barotropic nonlinearity. An additional, explicit nonlinearity due to weak basic-state warm advection offsets the linear baroclinic effect, which is known to diminish upstream influence. However, the amount of compensation in the case of bell-shaped or plateau topography is not significant until close to the point of breakdown of the laminar barotropic solution. It has thus been concluded that the feedback mechanism probably fails as long as the balance assumption applies in the near field and upstream.

The nonlinearity arising from a non-semi-geostrophic circulation (Ro $\gg$ 1) can be expressed as a quasi-horizontal derivative of the v-advection (assuming moderate β), and may be interpreted as the consequence of a locally-reinforced static stability. The linear analysis is directly relevant if the nonlinearity is localized or weak by virtue of $Ro^{-1} \ll 1$ or Fr $\ll$ 1. In view of the forcing-height dependence of the line-source response, the latter assumption does not allow as strong a feedback as when the forcing can be placed at the top of a finite-amplitude mountain. However, this distinction largely vanishes if the results are interpreted qualitatively for Fr = O(1) and Ro = O(1). Beyond this, the analysis cannot describe the long-term consequences of the feedback; however, a consistent long-term scenario was proposed in section 3.1, and will be tested by numerical simulation in chapter 5.

The analysis confirms that the sign of the apparent near-field forcing allows positive feedback through additional low-level deceleration only in the warm-advection case. The approximate strength of the forcing was obtained through a scale analysis; its further dependence on such

details as the shape of the mountain and the baroclinicity will be considered in chapter 5.

The line-source analysis produces a number of diagnostic results of relevance to alternative theories of rapid frontogenesis. The induced mass flux below the forcing can be estimated from separate asymptotic analyses of $k \ll 1$, $k \gg 1$ and $\mu \gg 1$ ($k \approx 1$), corresponding to the quasi-geostrophic, nonrotating and inertial limits. The surface velocity perturbation is largest when the forcing height is $O(U_0/N)$, which yields u $\approx U_0/2$ at a fraction of the inertial distance downstream from a source of positive unit strength.

The surface velocity estimate provides necessary conditions in order for the strict "coastal" mechanisms, consisting of heating and roughness gradients, to be considered primary causes of frontogenesis. It appears that offshore heating produces the stronger steady response, whereas the frictional mechanism has the virtue of placing the greatest surface convergence well onshore, where it is also observed during coastal front events. Both alternative mechanisms differ from the topographic mechanism in that the forcing tends to grow weaker as the flow adjusts to the heating or frictional drag. This distinction must be inferred, since the adjustment process is missing in the linear model.

Apparent heating through secondary shearing deformation of a transverse temperature gradient can be analyzed for qualitative understanding by neglecting the associated thermal wind. Positive feedback is easily demonstrated when the sign of the gradient is the same as in the New England coastal front. The relative strength of the secondary convergence equals the nondimensional gradient, $\beta_y = B_y/(fN)$, which can be as large, in nature, as the primary gradient β.

CHAPTER 4. A LAGRANGIAN NUMERICAL MODEL FOR RAPID FRONTOGENESIS

This chapter is concerned with the description and verification of a Lagrangian grid-point model developed to simulate rapid frontogenesis. The attention paid to the numerical modelling technique is thought warranted for two reasons. In the first place, the method constitutes a new way of integrating the time-dependent primitive equations for two-dimensional incompressible flow. The second reason is that the proposed model is suitable for a larger class of disturbances characterized by extreme temperature and velocity gradients but slow recirculation. The main features of the model will be summarized in the last section so that a careful reading of the entire chapter will not be necessary for continuity.

4.1 Overview of Lagrangian numerical modelling

A Lagrangian numerical method is chosen with the primary purpose of resolving temperature and velocity fields on smaller scales than any practical choice of grid spacing. Eulerian models are subject to the effects of "numerical diffusion", in which the finite-difference advection terms limit the strength of the simulated gradients. The conclusions drawn from Eulerian simulations of large-scale frontogenesis, such as those by Williams and Plotkin (1972), Orlanski and Ross (1979) and Keyser and Anthes (1982), are probably not significantly influenced by numerical diffusion. However, at scales more typical of atmospheric density currents, transient energy can exist predominantly in the form of nonlinear gravity-inertia oscillations. In such disturbances, the

interplay of wave-steepening and dispersion, which is presumably critical in rapid frontogensis, can be obscured by spurious dissipation.

It was mentioned in chapter 2 that non-hydrostatic effects are not crucial in familiar instances of rapid frontogenesis. Nevertheless, the proposed Lagrangian model makes no assumption of hydrostatic balance. Unlike Eulerian models, which gain considerable simplicity from such an assumption (e.g., R.T. Williams, 1967), the efficiency of the diagnostic step of the Lagrangian model cannot be substantially improved in this way.

Numerical models for the non-hydrostatic incompressible equations are of two main types, distinguished by the diagnostic phase of the computation. Vorticity-streamfunction models are widely preferred for two-dimensional frontogenesis simulations (e.g., Orlanski and Ross, 1979). The streamfunction is obtained at each step by solving a Poisson equation, $\nabla^2 \psi = \gamma$, in which the vorticity, γ, is predicted directly.

The alternative is based on a diagnostic equation for the pressure, essentially $\nabla^2 p = -\nabla \cdot (\underset{\sim}{w} \cdot \nabla \underset{\sim}{w})$, involving the self-advection of the meridional velocity $\underset{\sim}{w} = (u,w)$. In this case, $\underset{\sim}{w}$ is determined prognostically. Velocity-pressure models are preferred for simulating classical hydrodynamic instabilities (e.g., G. Williams, 1970), presumably because they are more amenable to scale-dependent mixing and energy conservation schemes. They are also more appropriate for three-dimensional modelling, where no mass streamfunction exists.

The model to be developed here is closely related to the vorticity-streamfunction treatment. A Lagrangian model using the alternative velocity-pressure approach has been designed and tested by

Hirt et al. (1970) for applications to homogeneous fluids with free surfaces. The present model seems preferable for rapid frontogenesis, because it better accommodates both buoyancy and topography. On the other hand, the method of Hirt et al. should be preferred for simulations of viscous and three-dimensional flows.

It is important to distinguish the fully Lagrangian treatments from the use of "markers" or pseudo-Lagrangian advection schemes. The marker-and-cell technique (e.g., Harlow and Welch, 1965) uses tracer particles to predict the position of free surfaces, and the "semi-Lagrangian" models (e.g., Bates and McDonald, 1982) in effect combine backward and forward time-steps to improve the accuracy of the advection. However, in both cases, the fields of dependent variables, including the velocity, are defined on an Eulerian grid.

A secondary motive for developing a Lagrangian model is to achieve accurate conservation of potential vorticity, a quantity which is known to play an important role in balanced frontogenesis. The importance of potential vorticity conservation has been noted in the numerical modelling work of Eliassen and Thorsteinssen (1984), who simulated mountain waves using a Lagrangian vertical coordinate.

In simple two-dimensional flows, potential vorticity conservation is the result of the conservation of potential temperature, absolute momentum and mass (Hoskins and Bretherton, 1972). In a Lagrangian model, where tracer quantities are already exactly conserved, it is therefore valuable to provide for accurate mass (i.e., volume) conservation, as well. It will be shown that volume conservation between resolved material surfaces can be achieved exactly in the spatial finite-differencing.

Preserving this important feature then becomes a guiding principle in the design of the time-differencing.

4.2 The Lagrangian equations

Hirt et al. (1970) resorted to volume integration and direct manipulation of the finite-difference equations to avoid explicitly transforming the continuous equations to Lagrangian coordinates. The explicit transformation will be shown here to provide a more familiar context in which to develop the finite-difference scheme.

As a first step, the standard dimensional vorticity-streamfunction equations are obtained from (2.1a)-(2.1e) in their inviscid, adiabatic form:

$$d\gamma/dt = b_x - fm_z \qquad (4.1a)$$

$$dm/dt = 0 \qquad (4.1b)$$

$$db/dt = 0 \qquad (4.1c)$$

$$\nabla^2 \psi = \gamma. \qquad (4.1d)$$

Here $\gamma = w_x - u_z$ is the horizontal vorticity, and $m = v + f(x - U_0 t)$ is the intrinsic absolute momentum, i.e., the part due to ageostrophic displacements in x. (The term $U_0 t$ is replaced by an integral if U is time-dependent.) In addition, the diagnostic relations, $u = -\psi_z$ and $w = \psi_x$, are needed for the advection terms ($d\gamma/dt$, dm/dt, db/dt). The lower boundary condition for the inviscid equations is simply $w = dz_s/dt$, or

$$\psi_x = -g_0'(x) \psi_z, \qquad (4.2)$$

where $g_0'(x)$ is the derivative of a height function, $g_0(x) = z_s/h$. A radiative upper boundary condition is the appropriate choice for the intended mesoscale simulations.

Now let ξ and ζ define some alternative coordinate system for the vertical plane. By assumption, the Jacobian $J(X,Z) \equiv \partial(X,Z)/\partial(\xi, \zeta)$ of the cartesian positions, X and Z, with respect to ξ and ζ is strictly positive (the upper-case letters are used to emphasize the dependence of x and z upon ξ, ζ and t). It can then be shown that the various differential operators are related by

$$\phi_x \leftrightarrow J(\phi,Z)/J(X,Z) \tag{4.3a}$$

$$\phi_z \leftrightarrow J(X,\phi)/J(X,Z) \tag{4.3b}$$

$$d\phi/dt \leftrightarrow \dot{\xi}\phi_\xi + \dot{\zeta}\phi_\zeta + \phi_t, \tag{4.3c}$$

where $\dot{\xi} \equiv d\xi/dt$ and $\dot{\zeta} \equiv d\zeta/dt$, and it is understood that each of the partial derivatives on the right side is taken with two of the independent variables ξ, ζ and t held fixed. These transformations apply even if x and z are not rectilinear.

The Lagrangian coordinates are determined by $\dot{\xi} = \dot{\zeta} = 0$, whence the prognostic equations for the flow, derived from (4.1a)-(4.1c), are

$$\Gamma_t = J(b,Z) + J(fm,X) \tag{4.4a}$$

$$m_t = 0 \tag{4.4b}$$

$$b_t = 0, \tag{4.4c}$$

with $\Gamma \equiv \gamma J(X,Z)$. The equation of mass conservation, transformed directly from (2.1e), and the definition of the vorticity, provide the two diagnostic equations,

$$J(\dot{X},Z) - J(\dot{Z},X) = 0 \qquad\qquad (4.5a)$$

$$J(\dot{X},X) + J(\dot{Z},Z) = \Gamma(\xi,\zeta), \qquad\qquad (4.5b)$$

which can be viewed as a pair of coupled, first-order, inhomogeneous equations for the velocity components,

$$X_t = \dot{X} \quad \text{and} \quad Z_t = \dot{Z}. \qquad\qquad (4.6)$$

The conservation of $J(X,Z) \equiv A(\xi,\zeta)$ implied by (4.5a) was used to write (4.4a).

Although the prognostic equations are now formally linear, the diagnostic equations for the velocity are nonlinear because of the time dependence of X and Z. This reverses the situation in the Eulerian system (4.1). In addition, the velocity equations differ from (4.1d) in being non-separable (in ξ and ζ) unless $X_\zeta = Z_\xi = 0$. The combination of these characteristics shifts the computational workload even further than usual toward the diagnostic problem, i.e., the solution of (4.5). As remarked earlier, the hydrostatic approximation, $J(\dot{Z},Z) = 0$, is not used here since it offers no important simplification.

4.3 The grid and finite-difference scheme

The numerical grid produces a pattern of adjoining quadrilateral cells with time-varying physical shapes. The most efficient scheme for "vectorized" computation is achieved by making the Lagrangian coordinate surfaces pass through pairs of <u>opposite</u> vertices in these quadrilaterals, it being assumed that the lower boundary is a coordinate surface. Thus, the vertex coordinates of the cell "centered" on (ξ_i,ζ_j) can be listed

in counterclockwise order as $(\xi_i, \zeta_j - \Delta\zeta/2)$, $(\xi_i + \Delta\xi/2, \zeta_j)$, $(\xi_i, \zeta_j + \Delta\zeta/2)$ and $(\xi_i - \Delta\xi/2, \zeta_j)$, as shown in Fig. 4.1. Note that the ζ-surfaces are chosen to follow the terrain. At the solid lower boundary, it is necessary to locate three (instead of two) vertices of each bounding quadrilateral on the boundary itself. The solid boundary thus contains, in effect, two of the ζ-surfaces, and is twice as well resolved in the horizontal as the interior surfaces.

Because $\Delta\xi$ and $\Delta\zeta$ are arbitrary increments, the Lagrangian coordinate system can be identified with the indexing scheme. In discussing the details of the finite-differencing, the dependent variables will be denoted with pairs of subscripts, as $X(\xi_i, \zeta_{j-1/2}) \equiv X_{i,j-1/2}$, for example. Where necessary, single superscripts will be used for time indexing.

The problem of mass conservation needs special attention. It is easily shown that the physical volume of a quadrilateral grid cell is <u>exactly</u> half of

$$2A_{ij} = D_\xi X_{ij} \, D_\zeta Z_{ij} - D_\zeta X_{ij} \, D_\xi Z_{ij} \equiv J_\Delta(X_{ij}, Z_{ij}), \qquad (4.7)$$

where D_ξ and D_ζ are centered difference operators, e.g., $D_\xi X_{ij} = X_{i+1/2,j} - X_{i-1/2,j}$. Differentiating (4.7) with respect to time yields $J_\Delta(\partial X_{ij}/\partial t, Z_{ij}) - J_\Delta(\partial Z_{ij}/\partial t, X_{ij}) = 2\partial A_{ij}/\partial t$. Thus if (4.5a) is satisfied with the finite-difference operator J_Δ replacing J, exact mass conservation (A_{ij} = const) is achieved without regard to the mesh size, i.e., for arbitrarily large A_{ij}.

Time-differencing errors will still be responsible for small changes in the cell volumes. However, the volume-integrated divergence
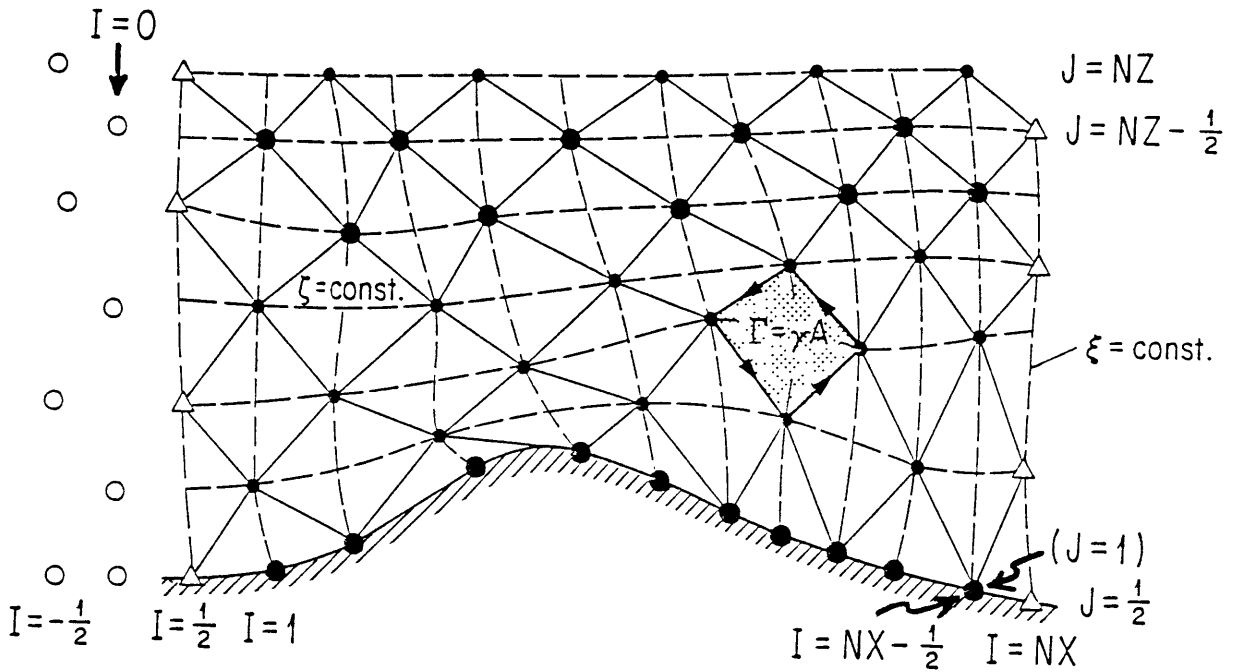
Fig. 4.1. Schematic representation of model grid. Lateral boundary condition is applied at points marked with triangles; topographic and radiation conditions apply at points indicated by large filled circles. Upstream buffer points are shown as open circles.
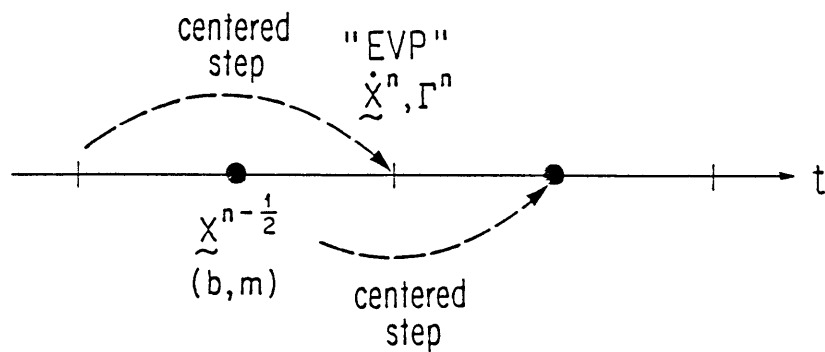
Fig. 4.2. Diagram of time-differencing scheme, showing staggering of velocities and positions. Velocities are obtained diagnostically at $t = t_n$ from vorticity (Γ^n) and positions extrapolated from $t_{n-1/2}$.

can be made to decrease as Δt^2 (where Δt is the model time step) either by
adopting a leap-frog scheme, or by including a correction term, D_{ij}, in
the finite-difference form of (4.5a). The approach involving the D_{ij}
will be used here for reasons of economy. According to this choice, the
dependent variables are staggered in time, with the vorticity and velocity
alternating with the particle positions and conservative variables, b and
m, as illustrated in Fig. 4.2. All of the time derivatives in (4.4) and
(4.6) can then be evaluated as centered differences. (The equations for b
and m may be ignored unless diabatic or mixing effects are introduced.)

The form of the divergence correction, or "apparent mass source",
D_{ij}, is obtained as (B.1) in Appendix B. The greatest complication
arises along the topographic boundary, where the grid cells cannot be
treated as quadrilaterals. Thus, (B.3) specifies an additional apparent
source required for mass conservation in the finite-difference form of
(4.5) along the boundary.

The numerical scheme can now be outlined as follows. After
initializing the dependent variables, X, Z, $\dot{X}$, $\dot{Z}$, γ, b and m, the two
vorticity sources (buoyancy and rotation) are evaluated. The vorticity is
then stepped forward according to

$$D_t \Gamma_{ij} = J_\Delta(b_{ij}, Z_{ij}) + J_\Delta(fm_{ij}, X_{ij}), \qquad (4.8)$$

which corresponds to (4.4a). Next, the divergence correction is
evaluated, and used with the vorticity as a source in the diagnostic

velocity equations,

$$J_\Delta(\dot{X}_{ij}, Z_{ij}) - J_\Delta(\dot{Z}_{ij}, X_{ij}) = D_{ij} \qquad (4.9a)$$

$$J_\Delta(\dot{X}_{ij}, X_{ij}) + J_\Delta(\dot{Z}_{ij}, Z_{ij}) = \Gamma_{ij}, \qquad (4.9b)$$

corresponding to (4.5). After these are solved for the particle velocities, the positions are stepped forward according to

$$D_t X_{ij} = \dot{X}_{ij} \qquad (4.10a)$$

$$D_t Z_{ij} = \dot{Z}_{ij} \qquad (4.10b)$$

[cf. (4.6)]. Similar equations for b and m are integrated at this time if (4.4b) and (4.4c) contain sources. The new values of X, Z, b and m determine new vorticity sources and the steps can be repeated. The diagnostic algorithm used to solve (4.9) will be discussed in the next section in connection with the boundary conditions.

The conserved quantity in (4.7a) has already been identified as the finite area element A_{ij}. It is also possible to identify the entity on the right side of (4.7b). The expanded form of this expression for the cell vorticity can be arranged as a sum over the four vertices,

$$\Gamma = 2 \sum_{k=1}^{4} V_k \, \Delta s_k, \qquad (4.11)$$

in which V_k is the velocity component in the "tangential" direction, i.e., parallel to the appropriate diagonal of the quadrilateral, and Δs_k is the average length of the two sides meeting at the k-th vertex. Hence (4.11) identifies Γ_{ij} as a finite-difference circulation integral. Interpreting the second diagnostic equation in this way provides an idea

of the model's accuracy as the cells become deformed through shearing and stretching.

4.4 Boundary conditions

Successful techniques already exist for treating both open and closed boundaries in Eulerian grid-point models. Most of these can be adapted for the Lagrangian model with only simple refinements. Indeed, the radiative boundary conditions chosen for the upper and lateral boundaries are based on principles of linear wave propagation, and are therefore simpler in the absence of explicit advection.

The greatest technical challenge is posed by the combination of stationary forcing and strong mean flow. To keep the grid centered on the forcing region (e.g., the mountain), it is necessary to add grid points continually at the upstream boundary, while removing points at the downstream boundary. However, it will be seen that extrapolating the dependent variables to the new upstream points is essentially the same process as advection, which has been largely worked out in the development of Eulerian models.

The details of the lower boundary condition will be considered first. The no-normal-flow constraint (4.2) is appropriate as one of two conditions needed to solve the velocity equations (4.5). Following a boundary grid point, the topographic slope, which is known as an analytic function of position, must be made available concurrently with the velocity and vorticity. A forward time step is therefore needed for the surface position, X_i^n (and in practice does not compromise numerical stability). Corresponding to (4.2), the lower boundary condition has the the finite-difference form

$$\dot{Z}^n_{i,1/2} - g_0{'}(X^n_{i,1/2})\; \dot{X}^n_{i,1/2} = W^n_i \;, \qquad i = 1 \text{ to } N_x, \qquad (4.12)$$

where the inhomogeneous term $W^n_i \equiv [Z^{n-1/2}_{i,1/2} - g_0(X^{n-1/2}_{i,1/2})]/\Delta t$ is

simply a hedge against the points' drifting off the boundary. Since the

boundary contains two ζ-surfaces, the subscripts $(i-1/2,1)$ also apply in

(4.12), with i taking the same integer values (see Fig. 4.1).

At the lateral boundaries, periodic conditions are the easiest to

impose. However, some form of open boundary condition is necessary for

the accurate simulation of a large-amplitude response to isolated

forcing. An adaptation of the widely-used phase advection scheme of

Orlanski (1976) will be used here. It is important to recognize that,

because the scheme assumes a non-dispersive, _linear_ disturbance, the

lateral boundaries are always capable of ruining long-term simulations

featuring nonlinear upstream (or downstream) influence.

The phase-advection boundary condition requires an estimate for

the local propagation speed c. For some predicted variable, ϕ, the

estimate is based on the formula $c = -(\partial\phi/\partial x)/(\partial\phi/\partial t)$, or in

finite-difference form (at the left boundary, $i = 1/2$, with a factor

$-2\Delta t/\Delta x$ removed),

$$c^n_j = \frac{\phi^{n-2}_{2\,1/2,j} - \phi^{n-2}_{1\,1/2,j} + \phi^{n-1}_{2\,1/2,j} - \phi^{n-1}_{1\,1/2,j}}{\phi^{n-1}_{1\,1/2,j} - \phi^{n-2}_{1\,1/2,j}}\;, \qquad j = 1 \text{ to } N_z. \qquad (4.13)$$

In the present study, the variable $\phi = \dot{Z}$ is used. A three-point filter is

applied to the c_j, which are first limited to one sign, corresponding to

outward propagation. Dependent variables at the left boundary can then be

predicted according to

$$\phi^n_{1/2,j} = \phi^{n-1}_{1/2,j} \frac{1-c_j}{1+c_j} + (\phi^{n-1}_{1 1/2,j} + \phi^n_{1 1/2,j}) \frac{c_j}{1+c_j} , \qquad (4.14)$$

which is a rearrangement of (4.13). The advection scheme is "upwind" and, following a recommendation by Klemp and Lilly (1977), semi-implicit. Similar equations are used at the right boundary ($i = N_x$, $j = 1/2$ to $N_z - 1/2$).

The phase speeds defined by (4.13) are also used to update the velocities in a buffer containing two columns ($i = -1/2$ and 0 in Fig. 4.1) reserved for the left boundary. At the end of each period $\Delta t_{buf} \equiv \Delta x/U_0$, the buffer columns become the model boundary, and the two rightmost columns of the grid are eliminated. The velocities and positions in the buffer are initialized by assuming normal derivatives of the perturbations vanish, e.g., $X_\xi = 1$. The positions are subsequently updated according to (4.10). The conservative variables are required to satisfy the zero-normal-derivative condition, e.g., $b_\xi = B_\xi$, at the moment the buffer becomes part of the domain.

At the upper boundary, an energy radiation condition is even more crucial than at the lateral boundaries for accurate simulations of mesoscale disturbances. In a stratified atmosphere, energy which is generated with frequencies exceeding the Coriolis frequency tends to disappear rapidly from the forcing region through the mechanism of vertical group propagation. Although variations in background wind and stratification, as well as nonlinear processes, can trap some of the disturbance energy at low levels, it is important that these effects be clearly distinguished from that of a reflective upper boundary.

In Eulerian models, the use of a viscous absorbing layer beneath a rigid upper boundary has been a successful method of effecting a radiative boundary condition. This approach has been used recently in mesoscale numerical studies by Orlanski and Ross (1977), Clark and Peltier (1977) and Pierrehumbert and Wyman (1985). Scale-dependent dissipation schemes are, however, considerably more difficult to implement on a Lagrangian grid, and absorbing layers in general are costly of computer resources.

Fortunately, an elegant alternative is available which is well-suited for the Lagrangian equations. The scheme is that proposed by Klemp and Durran (1983), who found it was possible to sharply reduce the generation of downward-propagating wave groups by applying principles of linear gravity waves to the information contained in a one-dimensional transform of the boundary data. The basic equation,

$$\partial u_i / \partial t = -N \sum_{I=1}^{N_x} H_{I-i} \ w_I, \qquad (4.15)$$

specifies the horizontal acceleration $(\partial u / \partial t)$ in terms of the entire distribution of vertical velocity (w) along the boundary. The weights $H_n = (1+(-1)^n)/(\pi n)$ are those of a discrete Hilbert transform, and N is the constant buoyancy frequency at the boundary.

This particular form of the basic scheme was proposed by Garner (1985) as a way of avoiding the explicit Fourier transforms and the assumption of periodic lateral boundaries which were part of the original design by Klemp and Durran (1983). Garner further showed that weak background rotational effects and a baroclinic basic state could be accommodated by including a modified Coriolis term in (4.15), and by

replacing the w_I with $w_I - \alpha_B u_I$, where $\alpha_B \equiv -B_x/B_z$ is the slope of the basic isentropes. The amplitude of a plane-wave reflection for given wavenumber vector (k, μ) is reduced by a factor of order $f \mu/(Nk)$ by the two corrections. However, as a practical matter, the correction for background thermal wind shear in large Rossby number simulations is more important than the Coriolis correction in controlling reflections.

The appropriate form of the modified Coriolis term is $(\partial u/\partial t)_f = -f(f+V_x)(x-U_0t-\xi)$, where ξ is the initial horizontal position. The finite-difference formulation of (4.15) must be semi-implicit to be consistent with the staggered time scheme, which choice is also indicated for computational stability. Best results are achieved by taking the values of $w_I - \alpha_B u_I$ from staggered positions on the two rows adjacent to the one containing the predicted u_i. The complete inhomogeneous condition to be applied to the finite-difference equations at time t_n is then

$$\dot{X}_i^n - \dot{X}_i^{n-1} = - \frac{N\Delta t}{4} \sum_{I=1}^{N_x} \sum_* (\dot{Z}_{I-1/2,j'}^{n'} + \alpha_B \dot{X}_{I-1/2,j'}^{n'})$$

$$- f^2 a^2 \Delta t \ (X_i^{n+1/2} - U_0 t - \xi_i),$$

(4.16)

where the index $j = N_z - 1/2$ is omitted and the second sum (*) is taken over $n' = n$, $n-1$ and $j' = N_z-1$, N_z. Because the lower boundary condition is applied to two ζ-surfaces, (4.16) must also be satisfied on the adjacent row, $j = N_z-1$, with $i+1/2$ and I replacing i and $I-1/2$.

The description of the basic model is now complete except for the details in the solution of the diagnostic system. The solution procedure is essentially the "error vector propagation" (EVP) method of Roache

(1976), adapted to accommodate the non-separable equations and unusual boundary conditions. The EVP method is entirely analogous to the analytical technique of combining particular and homogeneous solutions of a differential equation.

The particular solution is obtained first as follows. A set of values (e.g. from the previous step) is used as a first guess for the horizontal velocities along the lower boundary. Since the lateral boundary velocities, $\dot{X}_{1/2,1}$ and $\dot{X}_{N_X,1/2}$, are specified by (4.13) or its downstream equivalent, the set of independent guesses is a vector of length $2(N_x-1)$. The corresponding vertical velocities are found next, either from (4.15) or (at lateral boundaries) from (4.14). All terms in the expanded form of (4.9) are then known for the $j = 1$ cells, except the four which involve the velocity components at the top vertex $j = 1^1/2$ ($i = 1$ to N_x). For $i = 1$ to N_x-1, these components are obtained by solving (4.9) as a system of two linear equations in two unknowns. The downstream phase-advection prediction corresponding to (4.14) is used at the right boundary to finish off the row.

Repeating the last two steps for successive rows eventually yields values of $\dot{X}$ and $\dot{Z}$ on the top rows N_z-1 and $N_z-^1/_2$. In general, these velocities do not satisfy the upper boundary condition (4.16). Hence the final steps in the procedure are aimed at finding a homogeneous solution of (4.9), (4.12) and (4.14) which corrects the error in (4.16).

In the homogeneous form of the equations and boundary conditions, lower boundary guesses are related linearly to upper boundary errors by an "error-propagation" matrix of size $2(N_x-1)$. The matrix elements are obtained by successively solving the homogeneous problem with lower

boundary guesses consisting of all $2(N_x-1)$ unit vectors, as described by Roache (1976). Finally, the product of the inverse error matrix with the vector of upper boundary errors yields a vector containing the corrections for the first guesses along the lower boundary.

The non-iterative nature of the EVP method is an important advantage for Eulerian models. Specifically, note that the bulk of the work occurs in computing the inverse error-propagation matrix, which is a one-time calculation in a fixed-geometry model. The advantage need not be entirely lost in the Lagrangian model if the simulated nonlinear processes are slower than the linear wave motions. An economical treatment using dual time steps is discussed in the next section, along with several other model refinements.

4.5 Further refinements of the model

The heavy demand of computation time by the diagnostic calculation can be alleviated by taking advantage of a natural separation of time scales. The CFL stability condition on the time step is already somewhat relaxed because the grid-relative phase speeds in the high-frequency transients tend to be smaller in the Lagrangian frame. However, a much more important savings results from the linearizing the diagnostic equations about a state which can be updated less frequently than the model variables.

The time interval Δt_L for the updating (which entails a long matrix computation) is limited only by the time scale for the <u>nonlinear</u> processes, and can therefore exceed Δt. A comparable separation of computational time scales was used by Klemp and Wilhelmson (1978) to

handle the high-frequency acoustic waves in their compressible model of deep convection. In the present model, certain additional correction terms become necessary in the velocity equations and lower boundary condition in order to keep the time-differencing errors at $O(\Delta t^2)$, rather than $O(\Delta t_L^2)$. These are described in Appendix B.

To see the equivalence of the linearized Lagrangian system and the wave equation (2.4), consider a baroclinic basic state defined by $B = N^2 \zeta + fV_z \xi$ and $fM = f^2 a^2 \xi + fV_z \zeta$, with $X = \xi$ and $Z = \zeta$. The linearized diagnostic vorticity and divergence equations (4.9) are then

$$X'_{t\xi} - Z'_{t\zeta} = 0$$
$$-X'_{t\zeta} + Z'_{t\xi} = \Gamma, \qquad (4.17)$$

where the prime denotes a perturbation. The linearized form of the vorticity prediction equation (4.8) is

$$\Gamma_t = f^2 a^2 X'_{t\zeta} - N^2 Z'_{t\xi} + fV_z(Z'_{t\zeta} - X'_{t\xi}) . \qquad (4.18)$$

Differentiating (4.17) with respect to time, substituting for Γ_t from (4.18) and eliminating X' yields

$$Z'_{tt\zeta\zeta} - f^2 a^2 Z'_{\zeta\zeta} + 2fV_z Z'_{\xi\zeta} - N^2 Z'_{\xi\xi} = 0 \qquad (4.19)$$

for the vertical displacement, Z'. But since $\partial/\partial t$ is the parcel derivative and the flow is steady, $\partial^2/\partial t^2 = U_0^2 \partial^2/\partial \xi^2$ may be used, along with $Z' = \psi/U_0$, to obtain the dimensional form of (2.4).

The next task in refining the model is to introduce a basic-state meridional shear. This can be accomplished by setting $\dot{X} = U_0 + U_1(z)$ in

the initial and lateral boundary conditions. However, it is better to avoid the resulting systematic deformation of the grid cells by treating the sheared part of the linear horizontal advection as in an Eulerian model. If the independent variables are redefined by

$$\dot{\xi} = U_1(z) \; \xi_x \quad , \quad \dot{\zeta} = U_1(z) \; \zeta_x \; , \tag{4.20}$$

where the x-derivatives are at constant z, then only the constant part of the basic meridional velocity (U_0) appears with the perturbation velocity on the right side of (4.10), as desired.

If $f \neq 0$, the basic-state potential temperature must vary linearly in y when $U_1 \neq 0$, and y-advection terms will appear in the buoyancy equation. With the absolute momentum defined as $m = v + f(x-U_0t-U_1t)$, the prediction equations may be written

$$\gamma_t = -U_1(z) \; \gamma_x$$

$$m_t = -U_1(z) \; m_x \tag{4.21}$$

$$b_t = -U_1(z) \; b_x \; + \; fU_1'(z) \; v \; + \; Q \; ,$$

where $fU_1'(z)$ must equal the negative of the temperature gradient in y, and $Q \equiv -f(U_1 \partial V/\partial z - VU_1') = -fU_1^2 \partial(V/U_1)/\partial z$. Notice that Q vanishes identically if the basic shear is everywhere parallel to the wind in the new Lagrangian frame. The derivatives in (4.21) are evaluated using upstream differences and the formula (4.3a), except at an inflow boundary, where the advection is set to zero.

Simulations of orographic disturbances can also develop large perturbation shears capable of excessively distorting the Lagrangian

mesh. Strong horizontal divergence can be equally damaging. For this reason, the Lagrangian model is not useful in highly nonlinear situations roughly characterized by $|u-U_0| > 2U_0$. Although this constraint eliminates the kind of blocked barotropic flows simulated by Pierrehumbert and Wyman (1985), a range of moderately nonlinear baroclinic, and potentially frontogenetical, flows with $|u-U_0| \approx U_0$ are not excluded. However, these latter situations can be simulated with greater realism, and numerical stability, through a combination of parameterized subgrid-scale mixing and periodic remapping of the grid.

There are several reasons for introducing a viscosity parameterization. In the first place, it becomes necessary in order to include the effects of a surface drag. The mixing is also a purely computational stratagem in that it controls two-grid-space noise and protects the linear boundary conditions from potentially damaging large-amplitude, high-frequency motions. The unusual upstream boundary scheme used in the present model can create extraneous shear layers of the type that cannot be removed by gravity-wave propagation. They are, however, easily controlled by scale-dependent mixing. In the baroclinic simulations, an unrealistic vertical shear can develop along the lee slope of the topography in association with a film of cold air in the lowest grid points. This shear is reduced through eddy mixing of the perturbation potential temperature, as well as velocity.

Only the simplest possible scale-dependent mixing scheme will be considered here. The three prediction equations are re-written with

viscous terms as

$$\gamma_t = K \nabla^2 \gamma'$$

$$m_t = K \nabla^2 m' \qquad\qquad (4.22)$$

$$b_t = Pr^{-1} K \nabla^2 b' \ ,$$

where the prime denotes the departure from basic-state, and $\nabla_\alpha^2 \equiv$ $\alpha^{-2}\partial^2/\partial x^2 + \partial^2/\partial z^2$. The eddy-viscosity coefficient, K, the Prandtl number, Pr, and the mixing aspect ratio, α, are taken to be constant. By implication, the vertical and horizontal mixing lengths are uniform, which tends to enhance the mixing in well-resolved regions. The bias is not always realistic but can be tolerated in the pursuit of simplicity.

To begin the evaluation of the viscous terms in (4.22), fields of centered-difference first derivatives are generated using the formulae in (4.3). At the upper and lateral boundaries, the normal derivatives are set to zero. At the lower boundary, the vertical derivatives are equated with the appropriate parameterized surface fluxes, to be described next. Obtaining second derivatives of γ', m' and b' by applying (4.3) to the first derivatives is straightforward everywhere but at the lower boundary, where the mixing terms for m and b require one-sided vertical differences.

The suface flux of momentum is based on the standard formula (e.g., Ching, 1975)

$$K\left(\frac{\partial u'}{\partial z}\right)_s = C_d \left| \underset{\sim}{u}_s \right| \underset{\sim}{u}_s \ , \qquad\qquad (4.23)$$

where the horizontal velocity $\underset{\sim}{u}_s = (u'+U_0, v')_s$ is evaluated at the

ground using $v' = m - M$. If the drag coefficient is written as $C_d = Re^{-1}C_d'$, where $Re = U_0H/K$ is the Reynolds number, then C_d' must be $O(1)$ or smaller if the vertical distance H is the boundary-layer depth (taking $C_d' = 0$ imposes a free-slip condition). Orlanski and Ross's (1979) standard choice of $K = 5$ m^2/s leads to $Re^{-1} = 10^{-3}$ when $U_0 = 10$ m/s and $H = 500$ m. In all of the viscous simulations, H will be set equal to the mountain height, and $Re^{-1} = 10^{-3}$ considered an upper bound. Orlanski and Ross's choice $\alpha^{-2} = 1000$ will also be adopted consistently.

The mixing terms for the "half-cells" along the lower boundary ought not be evaluated directly because of the anomalous vertical resolution. Rather, mixing tendencies for the cell vorticity, and for values of b and m at the lower-middle vertex, are obtained from the next higher grid points, where, accordingly, the surface fluxes are defined. The vertical derivative of the vorticity (hence the vorticity flux) is evaluated as a one-sided difference at the lower boundary, taking $\gamma \approx -u_z$ from the momentum flux formula as the boundary value. The surface heat flux is specified by

$$\left(\frac{\partial b'}{\partial z}\right)_s = C_h \frac{\partial}{\partial z}b' \ , \tag{4.24}$$

where the derivative on the right is evaluated across the lowest full grid cell. There are many alternatives, but (4.24) is interesting in that it tends to restore the vertical stratification to ambient conditions. Setting $C_h = 0$ shuts off the heat flux through the boundary.

The remapping procedure consists of interpolating the model variables to more regularly-distributed physical positions. It clearly

gives up some of the advantage of the Lagrangian method by reverting temporarily to a coarser resolution in the regions of strong gradient. However, it should be appreciated that each remapping has available all of the original data points in the highly-resolved regions, and that the transport of conserved quantities across fixed locations remains more accurate than in Eulerian models with the same abundance of grid points.

The interpolation is applied to the <u>perturbation</u> fields of meridional velocity, absolute momentum, and buoyancy. The remapping algorithm is designed to leave the existing surfaces nearly intact beyond a distance of about twice the mountain height in the vertical, or about two half-widths in the horizontal. The open boundaries in particular are unaffected. The variables are first interpolated along the existing ζ-surface to more regular x-positions (which define the new ξ-surfaces), and then along the new ξ-surfaces to regular z-positions. Finally the new field of vorticity is recovered diagnostically using (4.5b) with the new velocities and positions. The actual interpolation formula uses Gaussian-weighted averages. The weights are $w_i = \exp\left(-(\Delta x_i/\Delta x)^2\right)$ for the horizontal, and $w_j = \exp\left(-4(\Delta z_j/\Delta z)^2\right)$ for the vertical interpolation, where Δx_i and Δz_j are the distances between the original and interpolated positions.

4.6 Linear test simulations

It is conventional to verify numerical models versus linear analytic solutions by choosing model parameters which guarantee an extremely weak response (e.g., Durran and Klemp, 1983). However, the Lagrangian model can be linearized more simply by excluding the

perturbation velocity from the lower boundary condition, and by omitting both the EVP updating and divergence corrections. This formal approach to removing the mountain amplitude as a parameter will be followed here.

For the linear tests, the initial distribution of physical position is specified by

$$X(\xi,\zeta) = \xi$$
$$Z(\xi,\zeta) = hg_0(\xi/\ell) \cos \frac{\pi}{2} \frac{\zeta}{\zeta_T}$$

(4.25)

where ζ_T is the upper boundary coordinate. Hence the ζ-surfaces follow the terrain shape (hg_0) at low levels, and become horizontal at the top of the model. The conservative variables are initialized as

$$b(\xi,\zeta) = N^2\zeta + fV_z\xi$$
$$m(\xi,\zeta) = fa^2\xi + V_z\zeta,$$

(4.26)

with V_z the constant ambient (upstream) shear. Since $\zeta \neq z$ according to (4.25), this initial state is not balanced near the mountain. The choice is made not only for simplicity, but actually to provide for a smoother startup. That is, (4.25) avoids a large temperature and velocity anomaly in the air pushed off the mountain.

The mean flow enters via the lower boundary condition, which specifies $\dot{Z} = U(t)hg_0'(x_g)$, with x_g the geostrophic position and $U(t)$ a function varying from zero to U_0 over a period of about one advection time across the mountain. The perturbation velocity is initially zero. Although the eddy mixing is turned off in the test simulations, a weak Rayleigh damping is applied to the vorticity to allow the lateral boundaries to be placed closer to the mountain and to be treated with an explicit (hence faster) phase-advection scheme.

The mountain profile for all but one of the test simulations is bell-shaped: $g_0(x) = 1/(1+x^2)$. The amplitude is specified by $Fr = Nh/U_0 = 1$, which has no effect on the character of the response. Plots from the first simulation in Fig. 4.3 show the time sequence in the development of steady hydrostatic mountain waves in a nonrotating flow. The conditions are established by setting $h/\ell = 0$ and $Ro^{-1} = 0$ (respectively, "AR" and "RO" in the figure heading). Because of the initial imbalance, the convergence to steady state is slightly accelerated, but on the other hand the transient disturbance is not entirely natural. The normalization of x, z and t in this and subsequent figures is observationally-oriented, i.e., based on the scales ℓ, h and ℓ/U_0. Thus, since $Fr = 1$, the theoretical vertical wavelength, $\lambda_G = 2\pi U_0/N$, is a about six model units. The positions of the boundaries in the figure are also those of the initial grid.

The scales for u' and w (perturbation $\dot{X}$ and $\dot{Z}$) are U_0 and $U_0 h/\ell$, respectively. The analytic solution [see (3.9)] therefore has $u' = O(Fr)$ and $w = O(1)$. In Figs. 4.4a and 4.4b, the model solution at $t = 40$ can be compared with the steady-state analytic solutions for u' and w. The agreement is satisfactory despite the low spatial resolution of only 2 × 36 (horizontal) × 24 (vertical) grid points covering a domain measuring $z_T = 15$ units high by $2x_L = 24$ units wide. The execution time on a (Cray) vector computer is about five seconds for the 960 time steps. The linearized version of the model is probably faster than any other designed for simulating incompressible, slab-symmetric flow on an f-plane.

The second simulation imposes the "mesoscale" condition $Ro^{-1} = 0.5$, which should give rise to both ageostrophic gravity-inertia lee waves
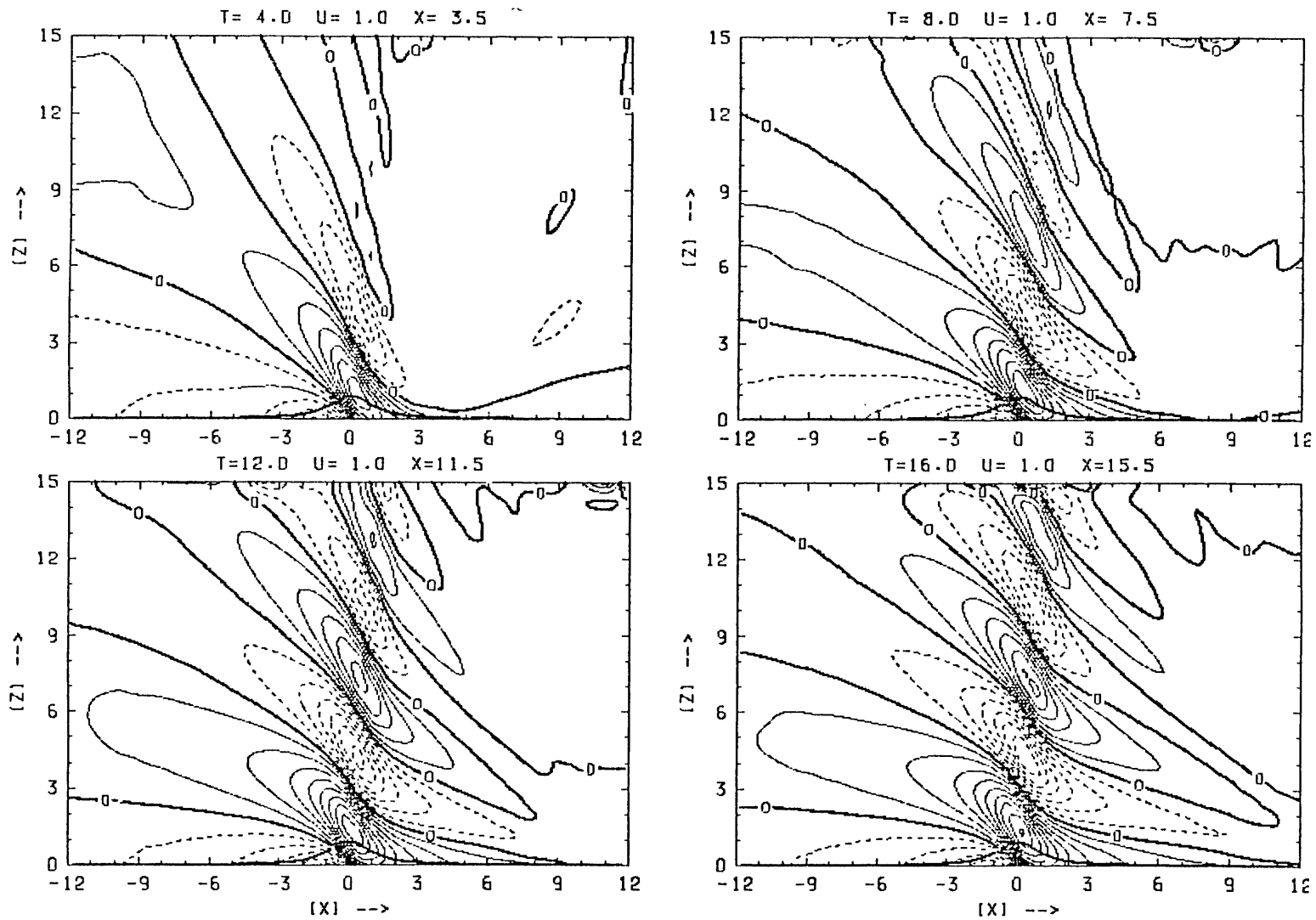
Fig. 4.3a. Time sequence of perturbation streamwise velocity, u',
in linearized model simulation of nonrotating, hydrostatic mountain
waves. Ridge profile is bell-shaped, with amplitude ten times the contour
interval. Time interval is 4 (ℓ/U_0).

1000D W LINEAR

AR = 0.00   FR = 1.00   RO = 0.00   BX = 0.00   BY = 0.00
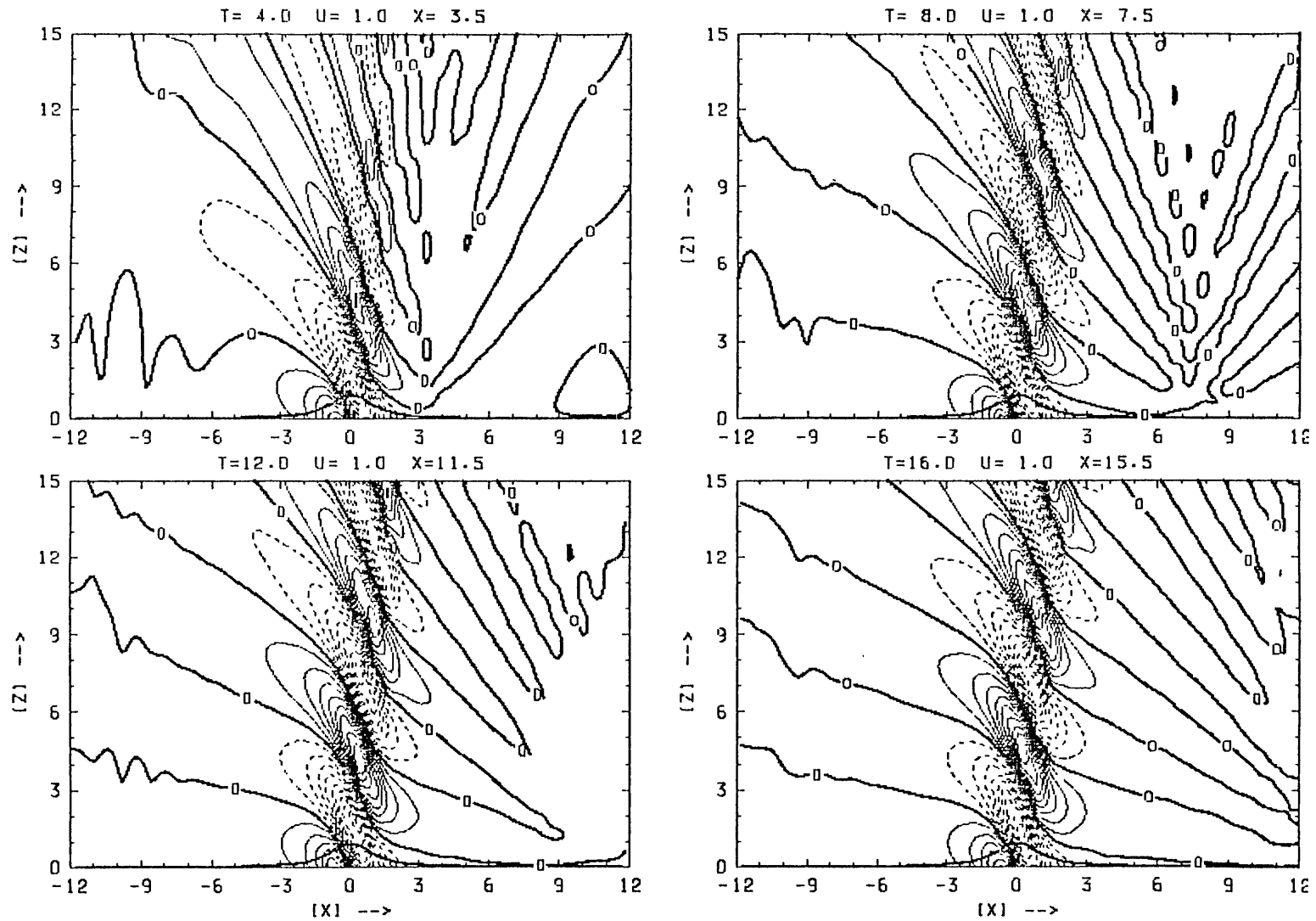
Fig. 4.3b. As in Fig. 4.3a, except model variable is w and contour interval is 0.1.

U LINEAR

AR = 0.00   FR = 1.00   RO = 0.00   BX = 0.00   BY = 0.00   T = 40.0   U = 1.0   X = 39.5

Fig. 4.4a. Comparison of nonrotating linearized model solution at t =
40 (top) with steady-state analytic solution for u'. Mountain profile and
contour interval as in Fig. 4.3.

W LINEAR

AR = 0.00   FR = 1.00   RD = 0.00   BX = 0.00   BY = 0.00   T = 40.0   U = 1.0   X = 39.5
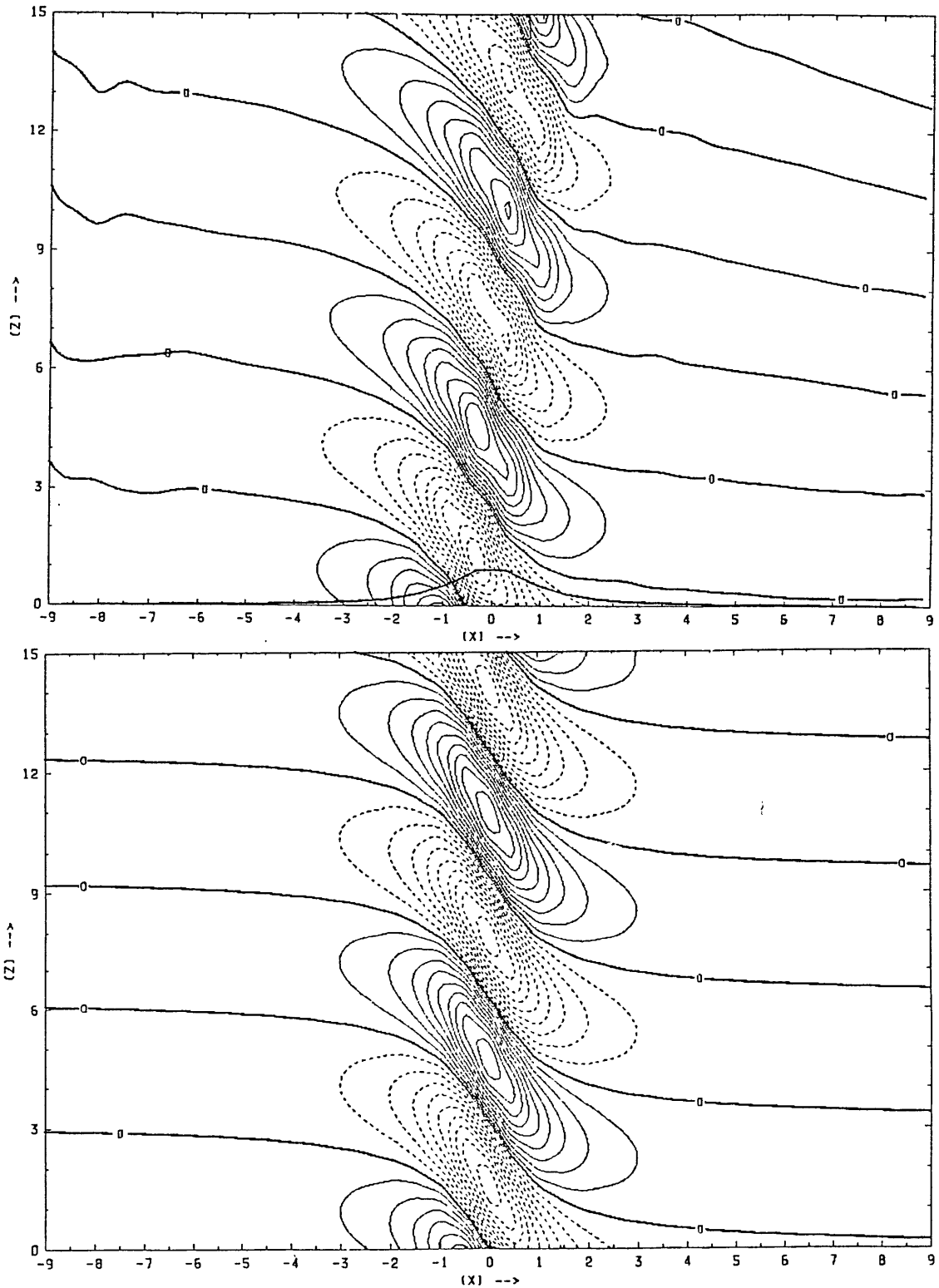
Fig. 4.4b. As in Fig. 4.4a, except model variable is w.

and a more nearly balanced upstream disturbance. These characteristics
can be seen in Fig. 4.5, which presents the time sequence for u' and v'.
Since v' is normalized by U_0, the geostrophy of the motion can be
judged from the ratio $Ro\Delta u'/(v'\Delta x)$, containing the finite-difference
derivative of u'. The basic state is made barotropic by setting $\beta \equiv$
$V_z/(Na) = 0$ ("BX" in the headers). With Ro = 2, the inertial time, 1/f,
is twice the model time unit. Hence, the inertial wave-train, having zero
intrinsic group speed, develops at the rate of about one wavelength per
twelve (4π) advection times. The inertial wavelength is $2\pi Ro = 4\pi$
half-widths.

The quasi-steady (t = 40) model solutions for u', v and w are
compared to the analytic solutions in Fig. 4.6. The "analytic" solution
for u' is obtained essentially as described in chapter 2 through numerical
quadrature of the appropriate inverse Fourier transform. However, the
solution for v' in Fig. 4.6b is the result of integrating the gridded
values of u' directly according to the linearized momentum equation. The
assumption v' = 0 at x = -6 makes this technique somewhat less accurate
than the model simulation for the long wavelengths. The vertical velocity
component in Fig. 4.6c is obtained by numerical convolution of the Green's
function for ψ with the derivative of $g_0(x)$.

The next two simulations contain a strong streamwise temperature
gradient, still with $Ro^{-1} = 0.5$. The velocity perturbation for the
warm-advection case, $\beta = -0.6$, is shown in Fig. 4.7, along with the
steady-state transform solution. The slope of the basic-state isentropes
in the figure is $\beta/(RoFr) = -3/10$, and that of the absolute momentum
surfaces is $\beta^{-1}/(RoFr) = -5/6$. The model correctly simulates the

1005B V LINEAR

AR = 0.00   FR = 1.00   RO = 0.50   BX = 0.00   BY = 0.00
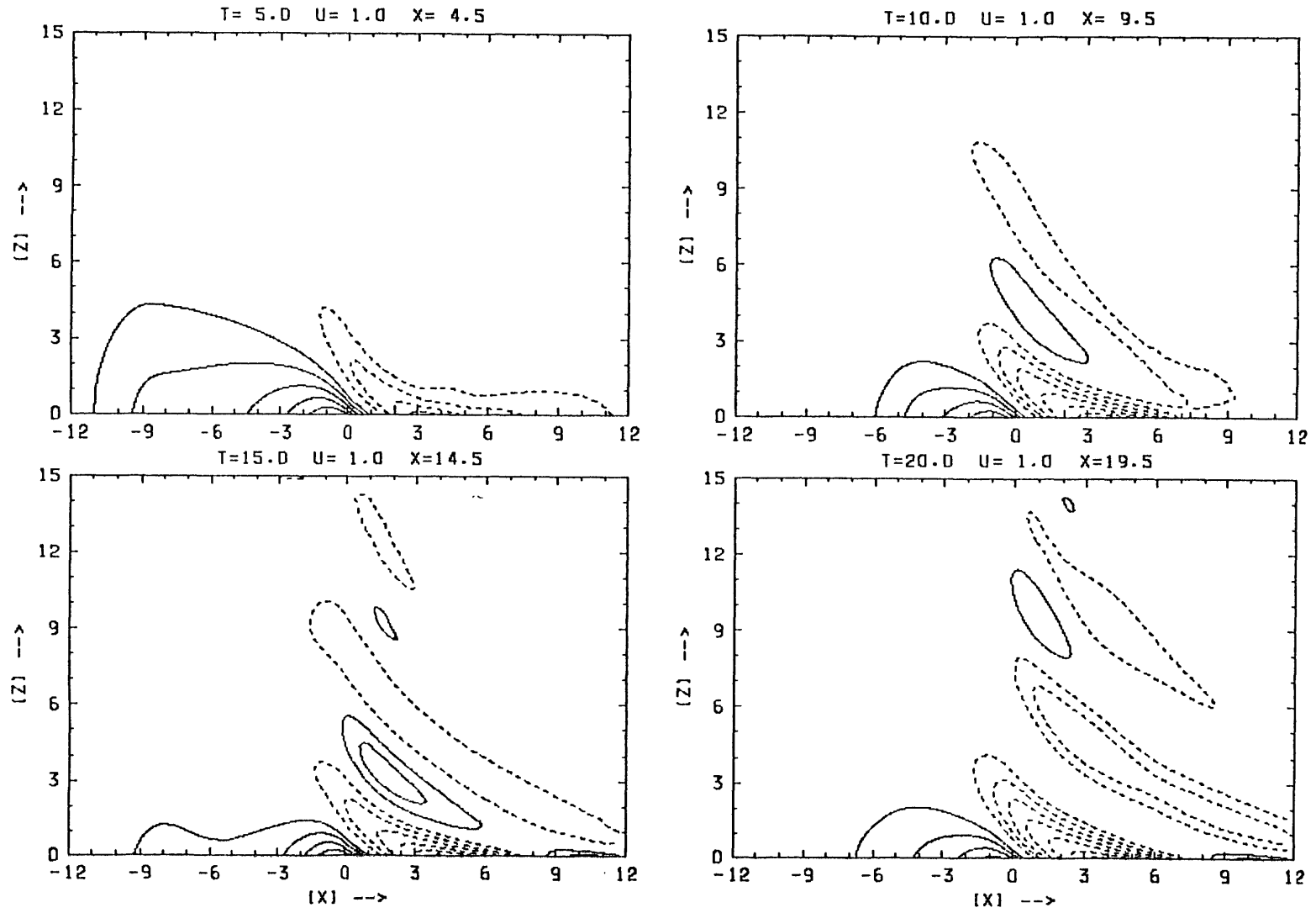
Fig. 4.5b. As in Fig. 4.3a, except model variable is v'.

AR = 0.00   FR = 1.00   RO = 0.50   BX = 0.00   BY = 0.00
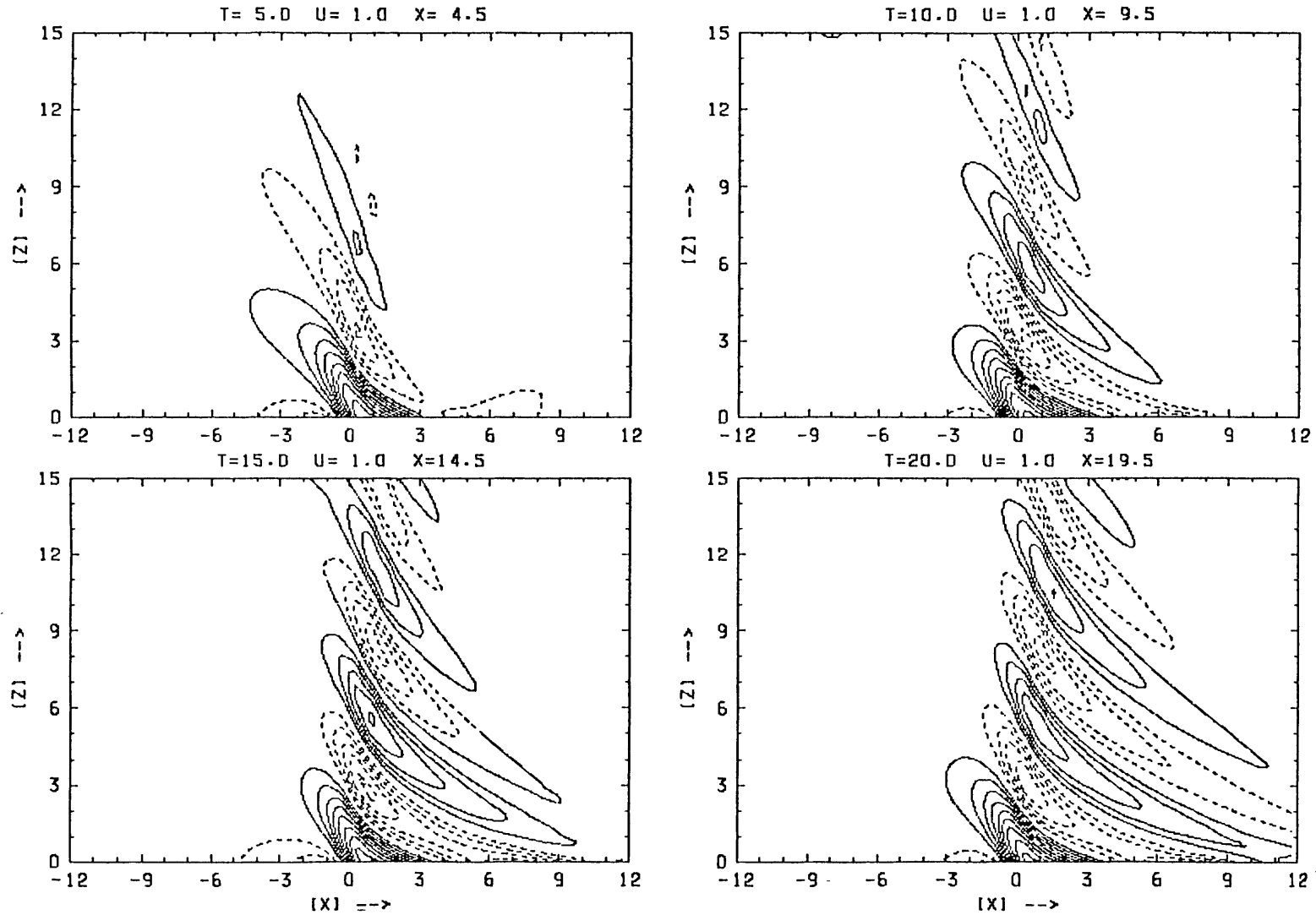
Fig. 4.5a. Time sequence of perturbation streamwise velocity, u',
in linearized model simulation of rotating, hydrostatic mountain waves.
Ridge profile is bell-shaped, with half-width Ro^{-1} = 1/2 and amplitude
ten times the contour interval. Time interval is 5 (ℓ/U_0).

AR = 0.00   FR = 1.00   RO = 0.50   BX = 0.00   BY = 0.00   T = 40.0   U = 1.0   X = 39.5
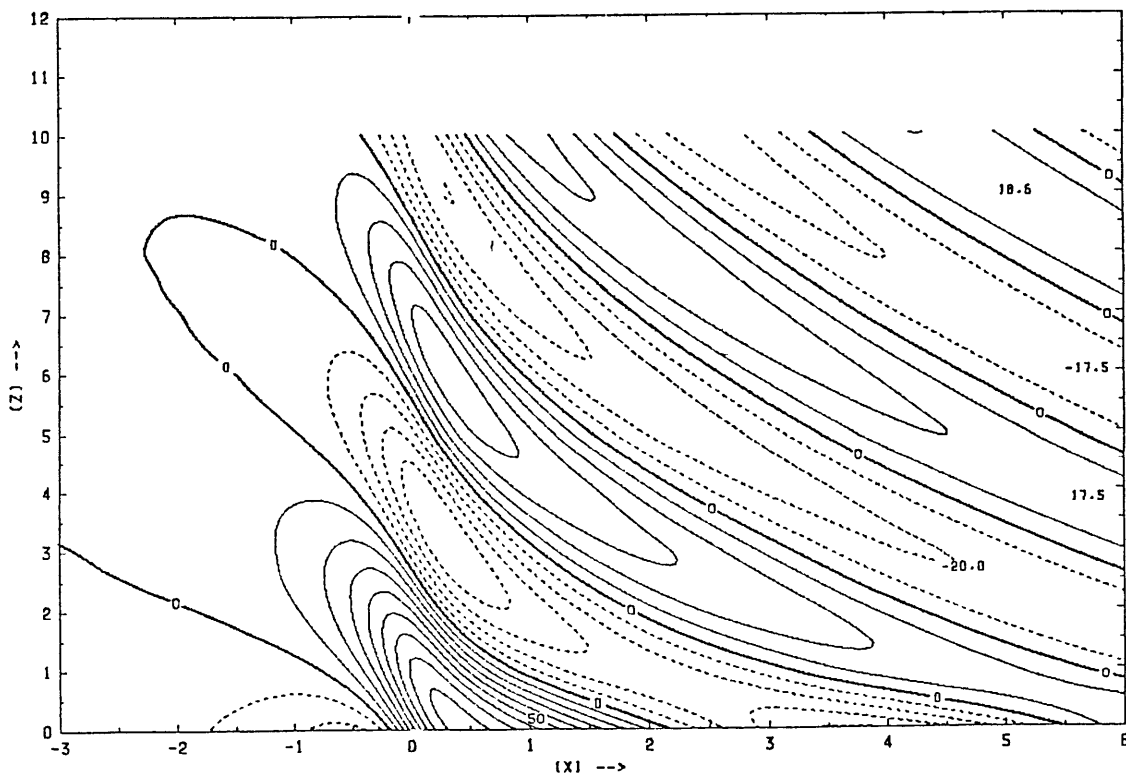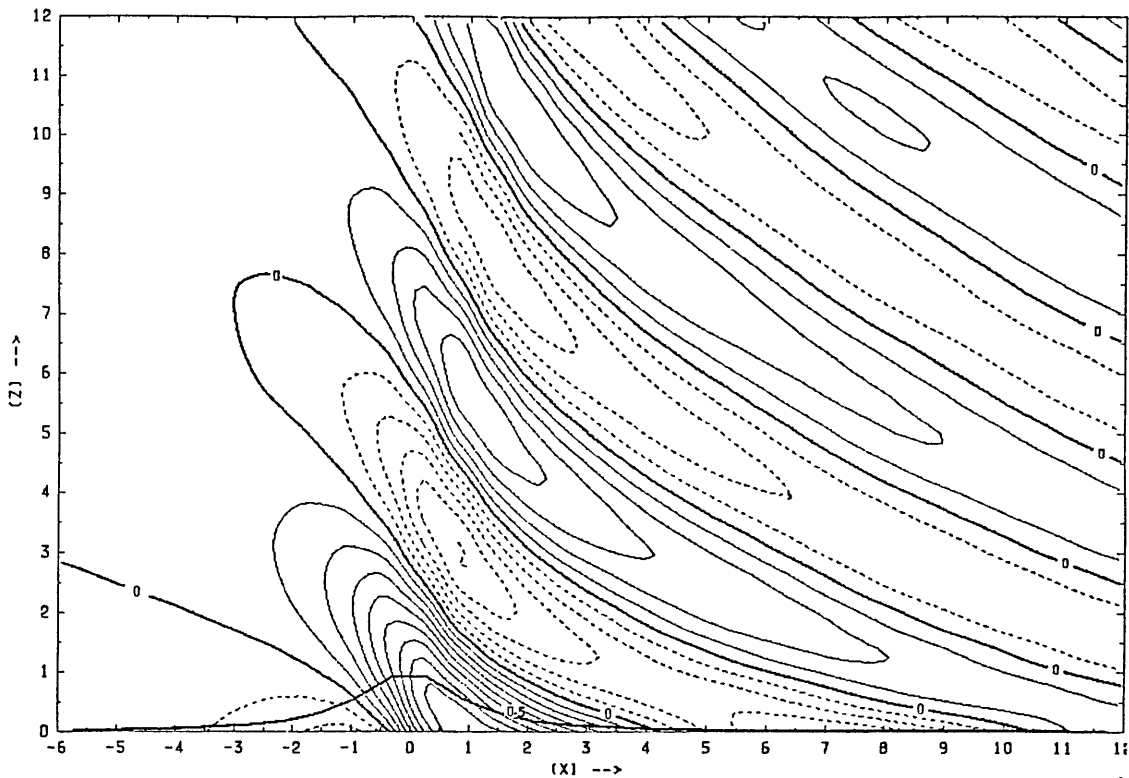
Fig. 4.6a. Comparison of linearized model solution at t = 40 (top) with steady-state analytic solution for u'. Mountain profile and contour interval as in Fig. 4.5.
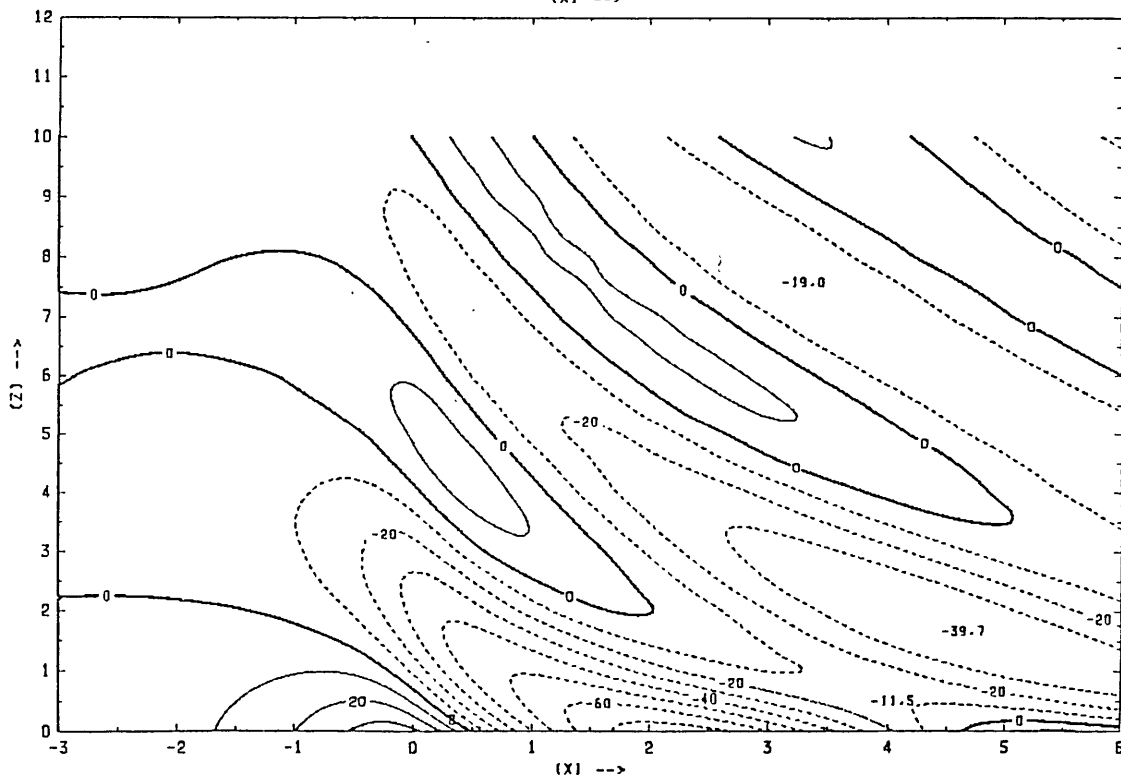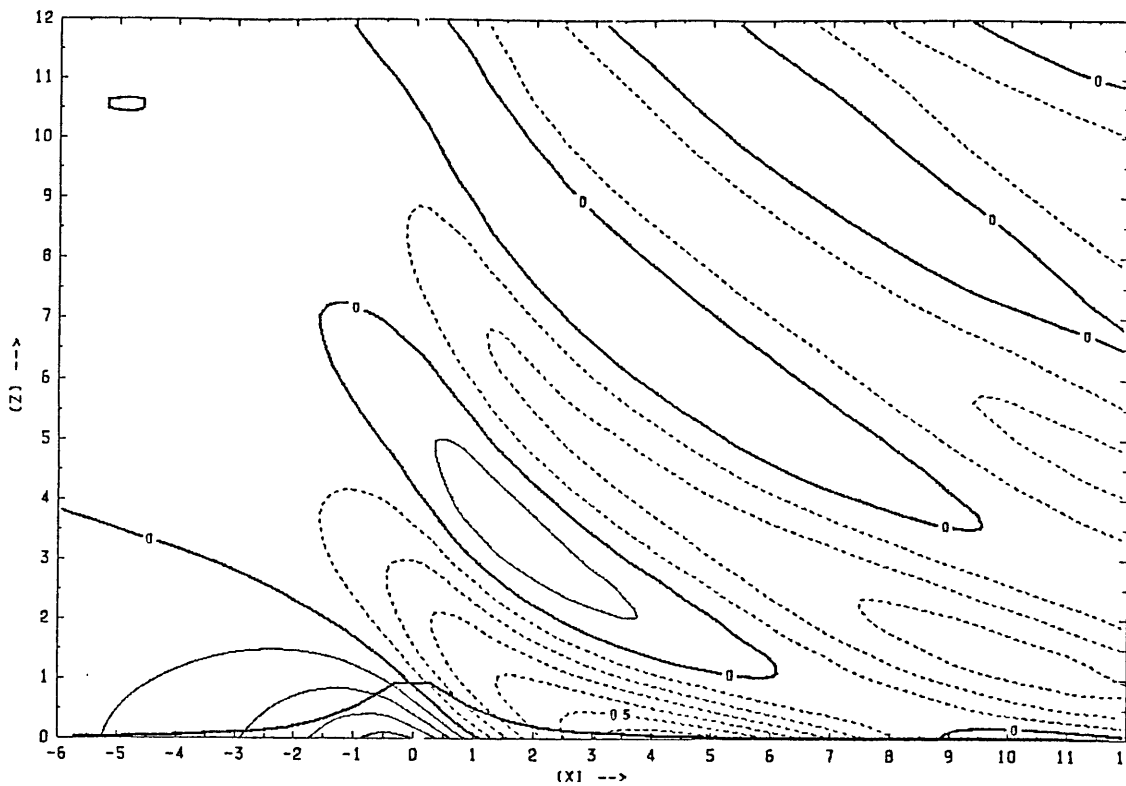
Fig. 4.6b. As in Fig. 4.6a, except model variable is v'.

1005B W LINEAR

AR = 0.00   FR = 1.00   RO = 0.50   BX = 0.00   BY = 0.00   T = 40.0   U = 1.0   X = 39.5
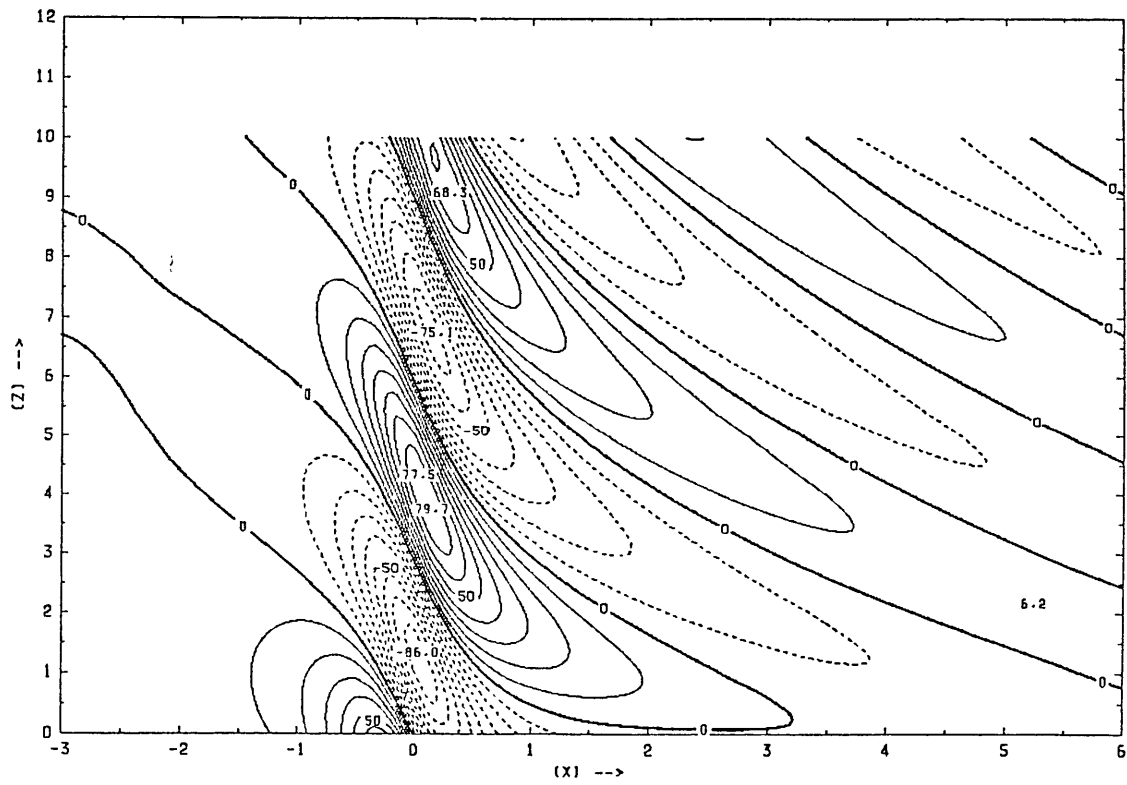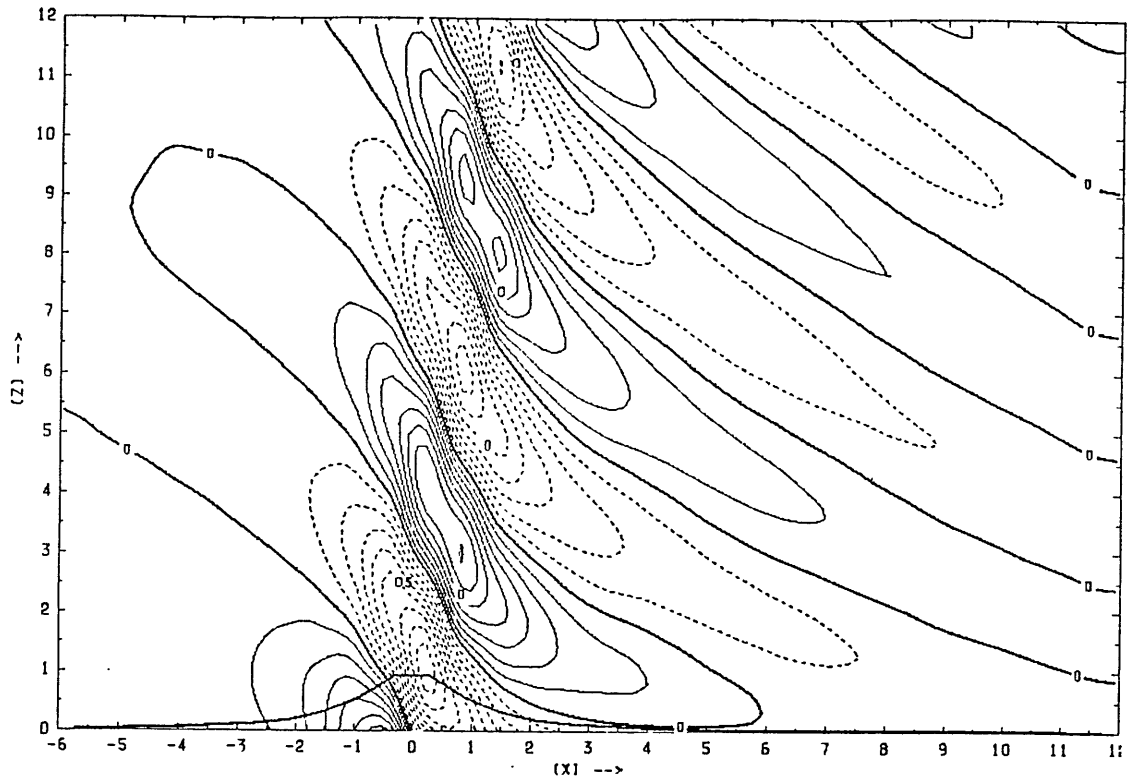
Fig. 4.6c. As in Fig. 4.6a, except model variable is w, and contour interval is 0.1.

comparative weakness of the upstream deceleration, and of the buoyancy waves over the mountain. The cold-advection case, $\beta = 0.6$, in Fig. 4.8 shows an enhancement of these same two features, as well as the weaker inertial wave train anticipated in chapter 2. The model also captures the drastic wavelength modification by β. The amplitude discrepancies in the far-field waves are the result of the weak Rayleigh damping introduced to suppress the transients as they approach the lateral boundaries.

The solution plotted in Fig. 4.9 is included primarily to test the treatment of the parallel velocity at the upstream boundary. The mountain is broadened on the lee side to produce greater upstream deceleration and larger v anomalies (see chapter 5). The particular profile is formed by joining opposite halves of two bell-shaped mountains at $x = 0$, i.e.,

$$g_0(x) = \begin{cases} (1+x^2)^{-1} & , x < 0 ; \\ (1+x^2/\ell_1^2)^{-1} & , x > 0 . \end{cases} \qquad (4.27)$$

The Rossby number will be defined by the width of the upstream ($x < 0$) portion. The broadening factor used in the simulation is $\ell_1 = 5$. Lilly and Klemp (1979) noted that a singularity appears in the nonrotating solution as $\ell_1 \to \infty$. The same "plateau singularity" was discussed in chapter 2. In the rotating case, a side-effect of the broadening is the suppresion of the far-field lee waves, whose amplitude depends on the projection of the mountain profile onto $O(\lambda_I)$ wavelengths. The asymmetric bell mountain will be used extensively in the finite-amplitude experiments of chapter 5.

Fig. 4.7. As in Fig. 4.6a, except basic state is baroclinic, β = -0.6.

1005P U LINEAR

AR = 0.00   FR = 1.00   RD = 0.50   BX = 0.60   BY = 0.02   T = 20.0   U = 1.0   X = 19.5
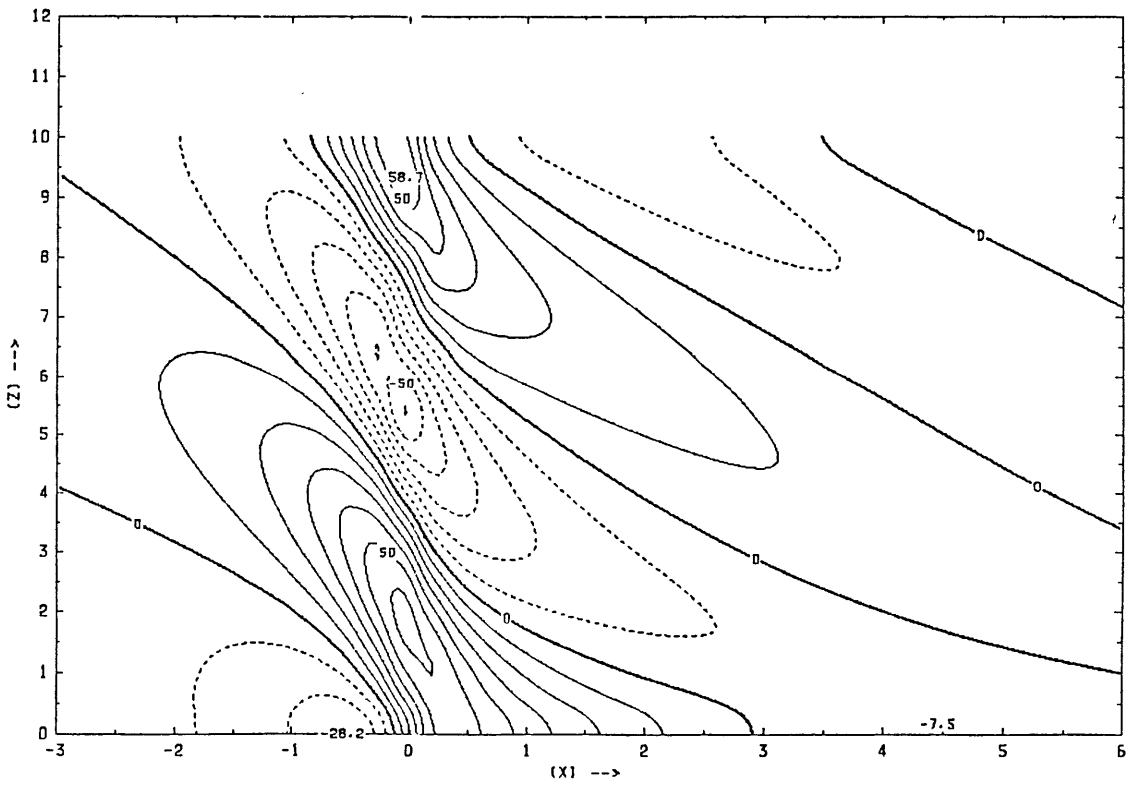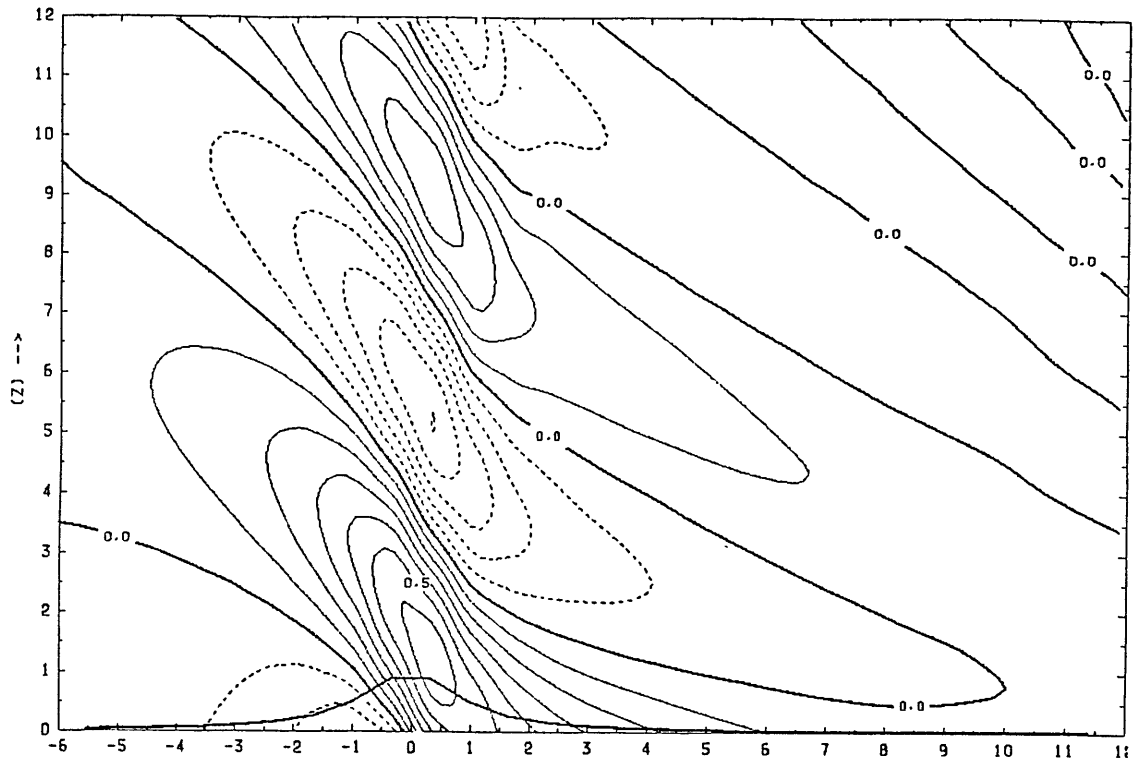
Fig. 4.8.   As in Fig. 4.6a, except basic state is baroclinic, β = +0.6.

U LINEAR (B5)

V LINEAR (B5)
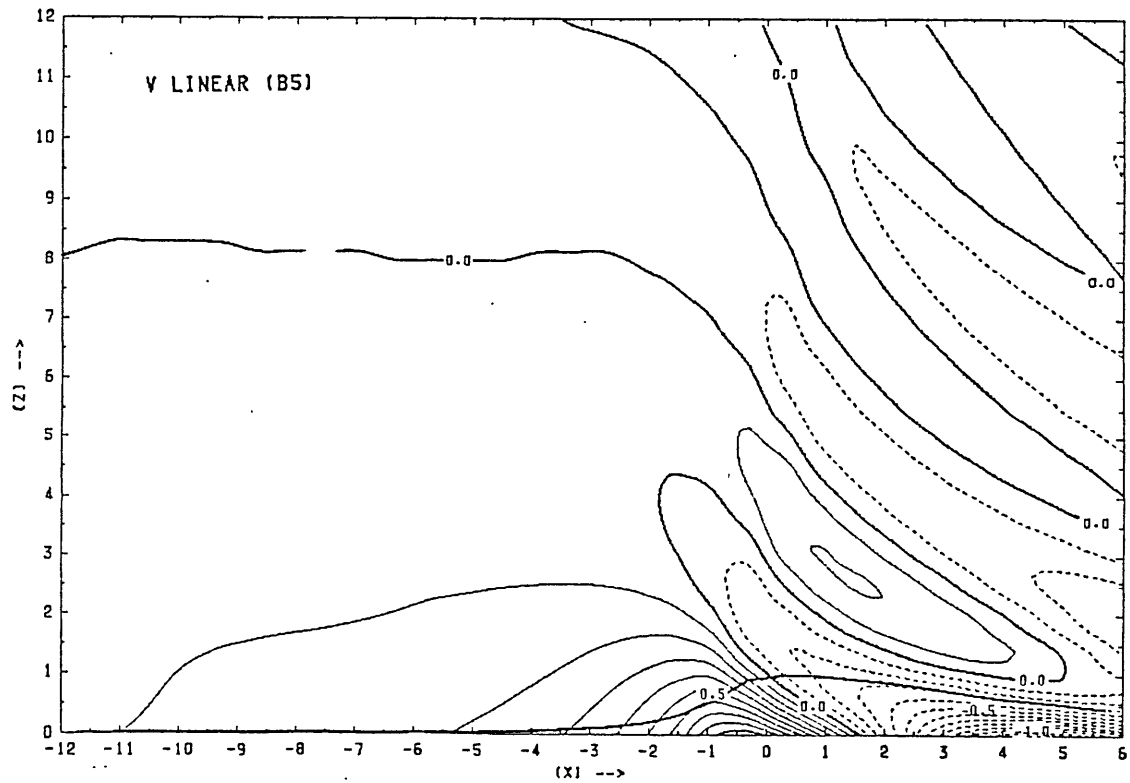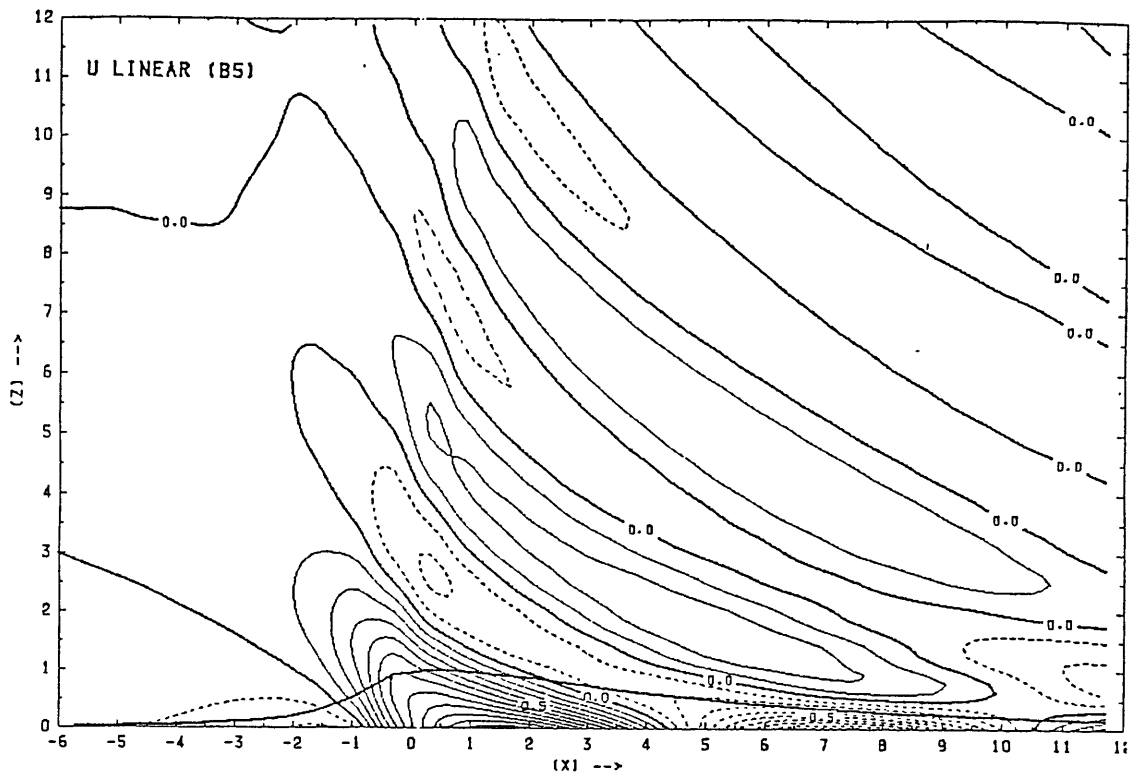
Fig. 4.9. Horizontal perturbation velocity components in steady (t = 50) linearized model solution for baroclinic (β = -0.6) flow past asymmetric bell mountain (B5). Mountain has windward slope of width Ro^{-1} = 1/2, and amplitude ten times the contour interval.

The inverse Rossby number is increased to $Ro^{-1} = 1$ in the final set of linear simulations, primarily to verify the scale and amplitude changes in the lee waves. The transform for the bell-shaped mountain has only a weak dependence on Ro near $k = Ro$. Hence much of the lee-wave activity is little affected beyond the changes in the normalized wavelengths. The cases shown in Figs. 4.10, 4.11 and 4.12 are for $\beta = 0$, -0.6 and 0.6, respectively. Recall that the condition $Ro = 1$ is a severe test of the radiative upper boundary condition, which assumes weak rotational effects (i.e., horizontal scales much shorter than U_0/f). The errors due to the upper boundary condition are more apparent in the parallel velocity component, which is more sensitive at large scales.

4.7 Nonlinear test simulations

The first nonlinear simulation imposes the simplest condition $Ro^{-1} = 0$. The amplitude of the bell-shaped mountain is set at $Fr = 0.4$, a value which is large enough to produce steepening but considerably below the overturning threshold, $Fr = 0.85$ (Lilly and Klemp, 1979). The small time interval is $\Delta t = 1/16$, while the "nonlinear" time step is $\Delta t_L = 1/4$. The two velocity components at $t = 20$ are plotted in Fig. 4.13. The solutions show the right kind of steepening, with <u>relative</u> enhancement of the velocities at all levels over the lee slope. However, at all but the lowest levels, the amplitudes fall short of the linear values, $u' = \pm Fr$ and $w = \pm 1$, which are lower bounds for the analytic nonlinear solutions.

The time sequence for the same simulation (Fig. 4.14) shows that energy is still converging at upper levels after $t = 20$, but that the amplitude of u' remains too low. The error is the result of the low

AR = 0.00   FR = 1.00   RO = 1.00   BX = 0.00   BY = 0.00   T = 40.0   U = 1.0   X = 39.5
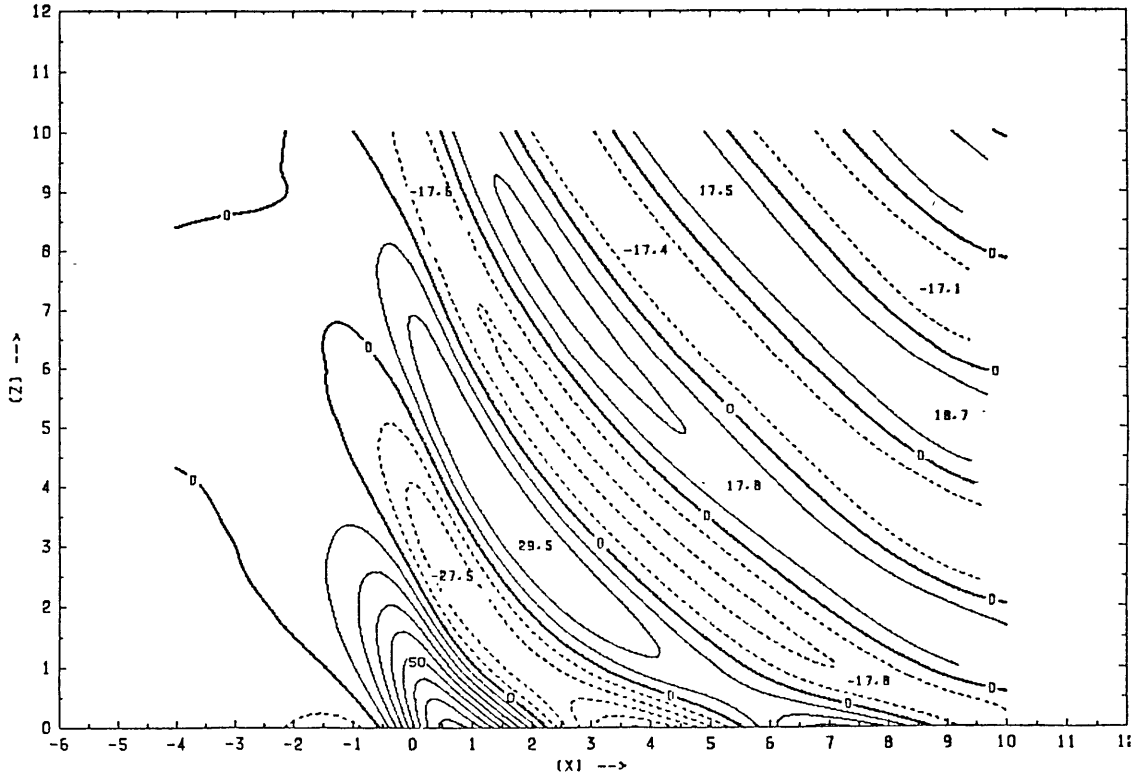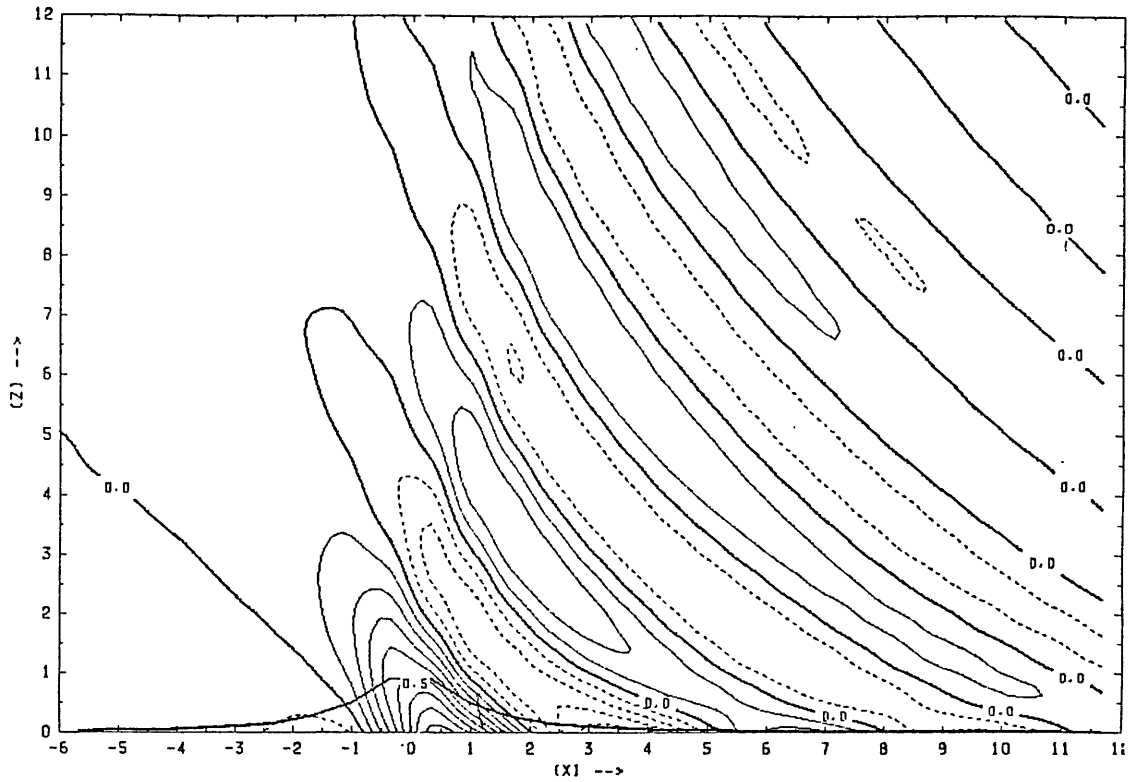
Fig. 4.10a. Comparison of linearized model solution at t = 40 (top) with steady-state analytic solution for u'. Mountain is bell shaped, with half-width of Ro^{-1} = 1 and amplitude ten times the contour interval.

1010A V LINEAR

AR = 0.00   FR = 1.00   RO = 1.00   BX = 0.00   BY = 0.00   T = 40.0   U = 1.0   X = 39.5
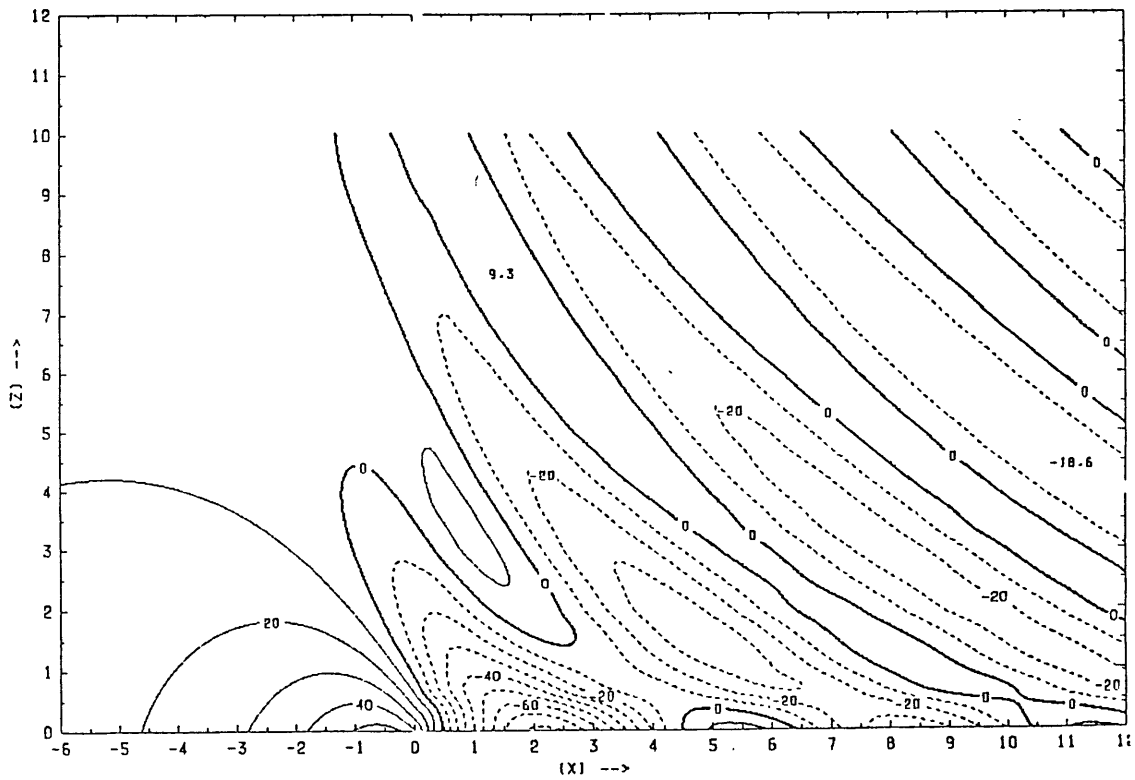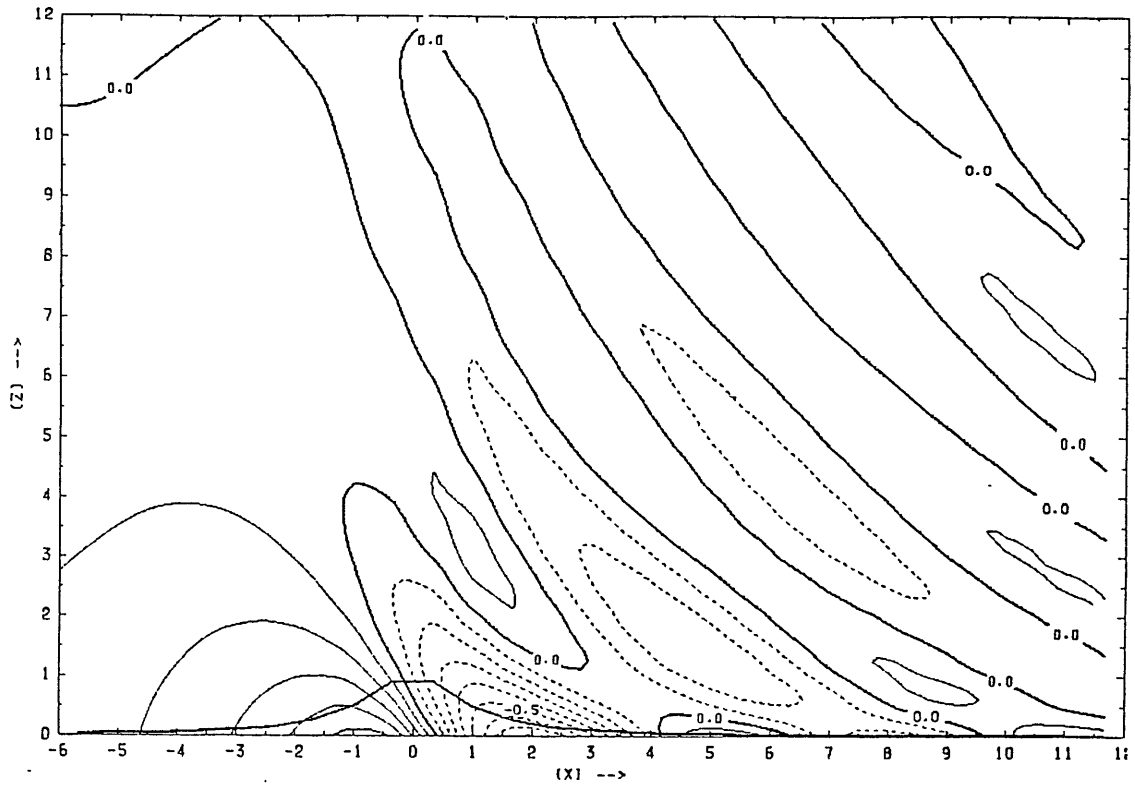
Fig. 4.10b. As in Fig. 4.10a, except model variable is v'.

1010L U LINEAR

AR = 0.00   FR = 1.00   RO = 1.00   BX = -0.60   BY = 0.0   T = 40.0   U = 1.0   X = 39.5

Fig. 4.11. As in Fig. 4.10a, except basic state is baroclinic, β = -0.6.
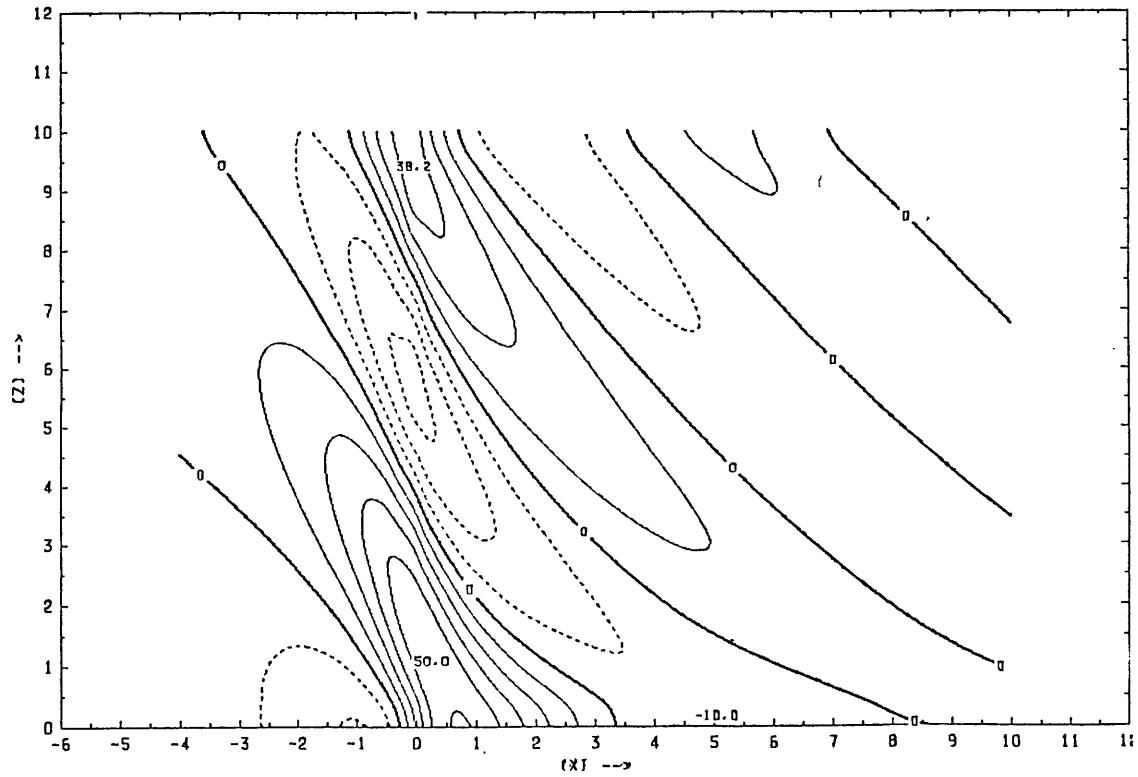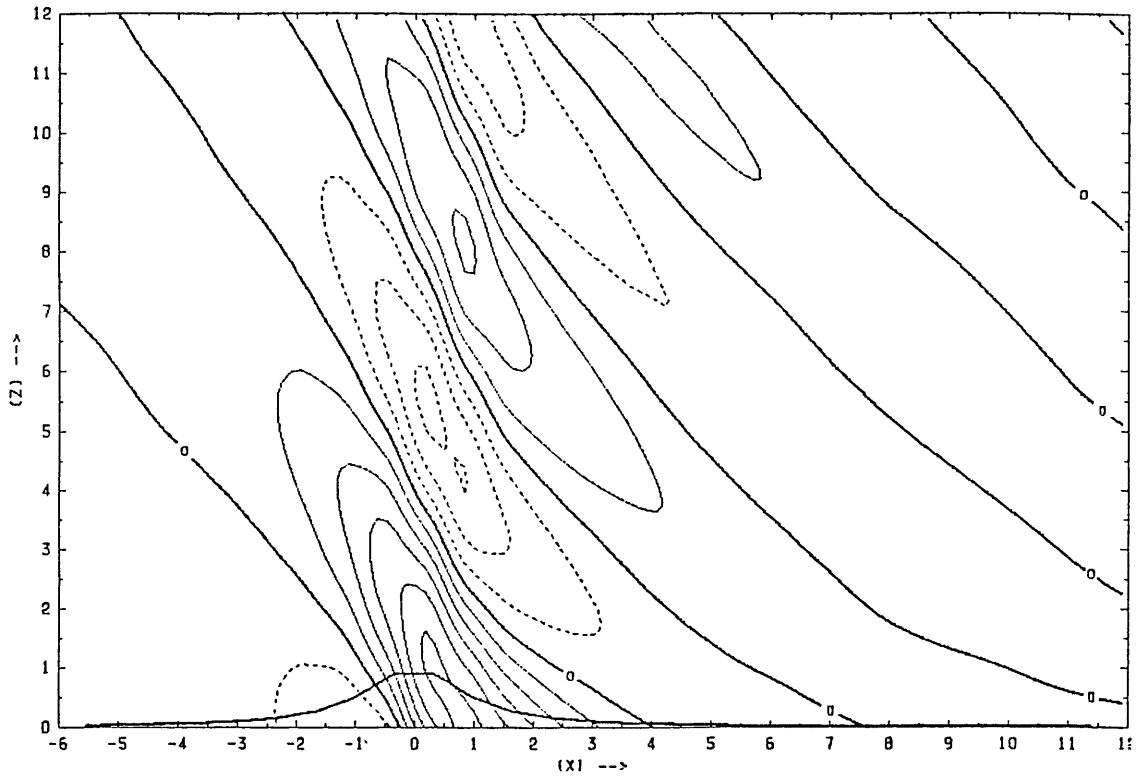
Fig. 4.12. As in Fig. 4.10a, except basic state is baroclinic, $\beta =$ +0.6.

AR = 0.04   FR = 0.40   RO = 0.00   BX = 0.00   BY = 0.00   T = 20.0   U = 1.0   X = 19.0
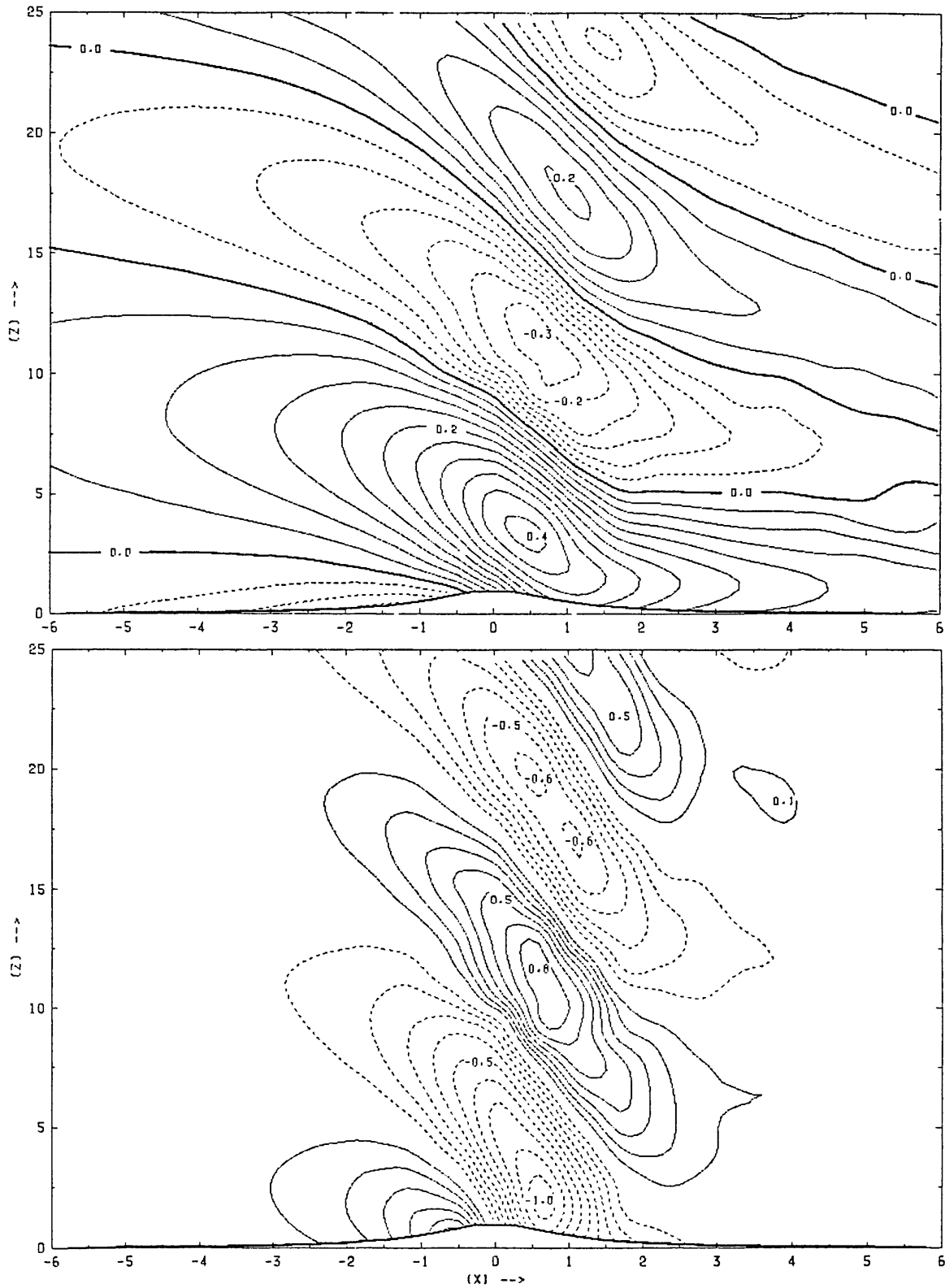
Fig. 4.13. Nonlinear model solution for u' (top, with contour interval 1/10 the mountain amplitude Fr = 0.4) and w (contour interval 0.1) at t = 20 in nonrotating flow past bell-shaped mountain ridge.

2000G U

AR = 0.04   FR = 0.40   RO = 0.00   BX = 0.00   BY = 0.00
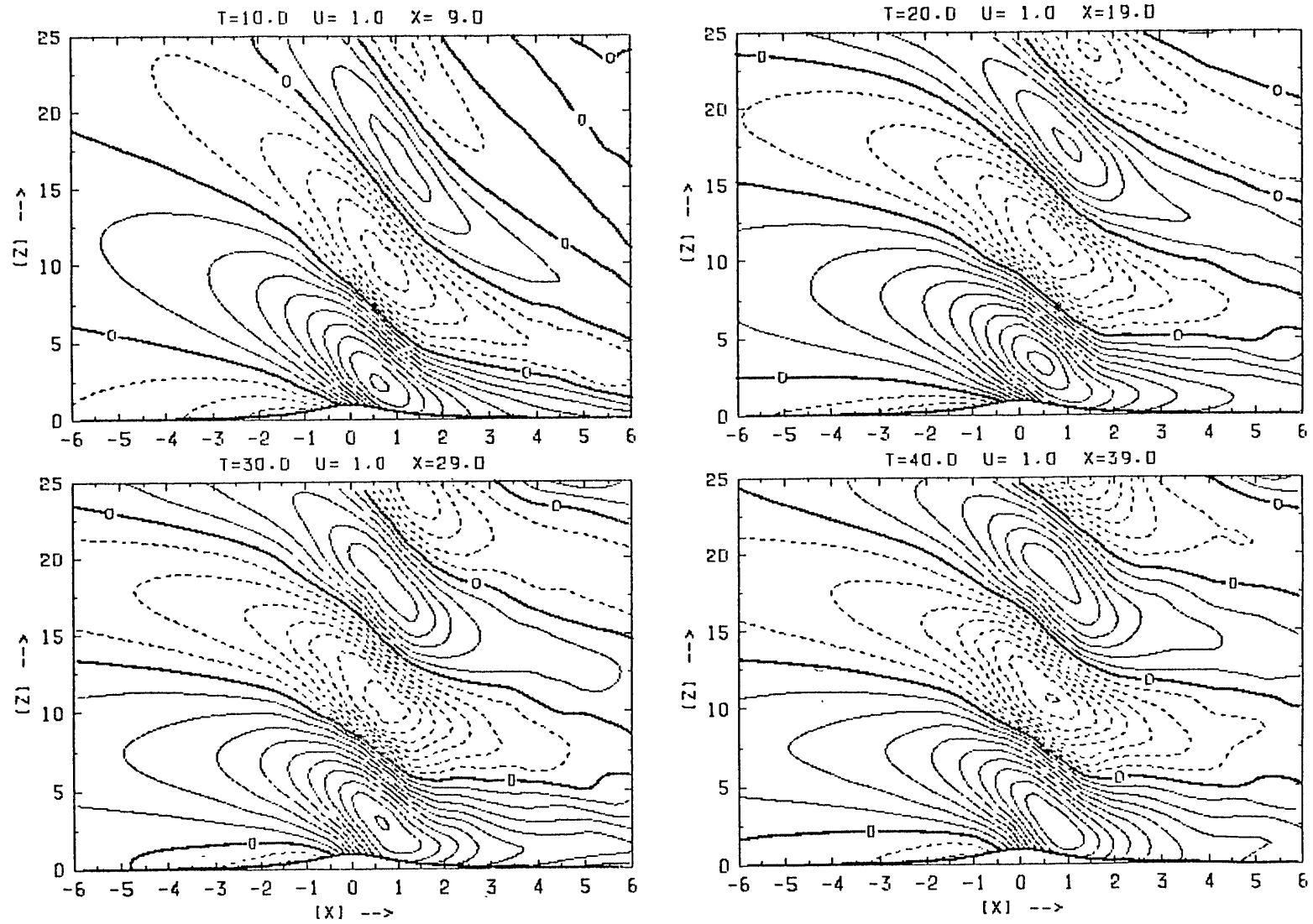
Fig. 4.14. Time sequence (Δt = 10) of u' in nonlinear simulation,
showing evidence of upward energy flux. Conditions are as in Fig. 4.13.

spatial resolution, the dual time scales and (to a lesser extent) the weak Rayleigh damping used for the sake of stabilizing the lateral boundaries. It should be borne in mind that the goal of the numerical modelling is to simulate steep temperature and velocity gradients, rather than high-frequency nonlinear oscillations.

Shown in Fig. 4.15 are the coordinate surfaces for the nonlinear simulation at t = 5, when the geostrophic flow has moved a distance of 4.5 units. The disturbance which persists near x = 4.5 reveals the initial deformation of the ζ-surfaces over the mountain. In order to expedite the data processing, all of the plotting in chapters 4 and 5, including Fig. 4.15, employs only half of the model data, namely the data defined on coordinate surfaces indexed with integer j and half-integer i (see Fig. 4.1).

The final simulation (Fig. 4.16) shows the result of adding a vertical shear to the mean flow in x. To balance the shear, the basic isentropes have a slope in the direction normal to the cross-section. Although there is temperature advection at the ground, the radiation upper boundary prevents global baroclinic instability. In order to avoid a critical layer below the model boundary, a weak shear was chosen by setting $\beta_y \equiv -U_z/N = 0.1$.

It can be seen in the plotted solution for u' and b (normalized by $N^2 h$) at t = 30, that the disturbance energy is being deflected to a shallower trajectory by the refractive effect of the shear. According to ray-tracing theory, steady modes with wavelengths of π or longer are confined below z = 5.5 (half the height of the critical level) because they have no vertical propagation in the weak, rotating flow at higher

COORD SURFACES

BX = 0.00   BY = 0.00   T = 5.0   U = 1.0   X = 4.5
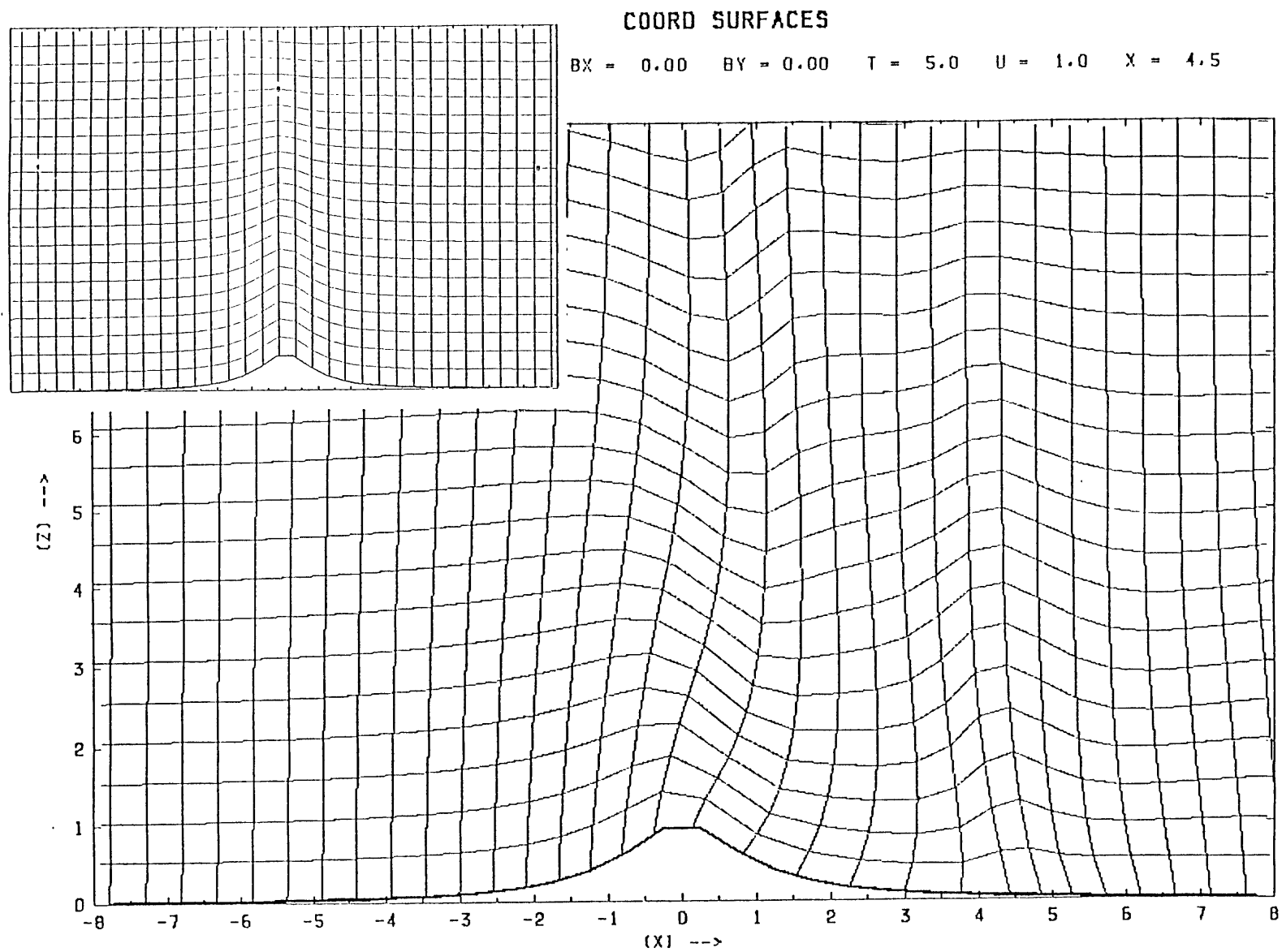
Fig. 4.15. Lagrangian coordinate surfaces in nonlinear (Fr = 0.4), nonrotating mountain-wave simulation at times t = 1 (inset) and t = 5.

1100A U (--) AND B

AR = 0.04   FR = 0.90   RO = 0.50   BX = 0.00   BY = 0.10   T = 30.0   U = 1.0   X = 29.5
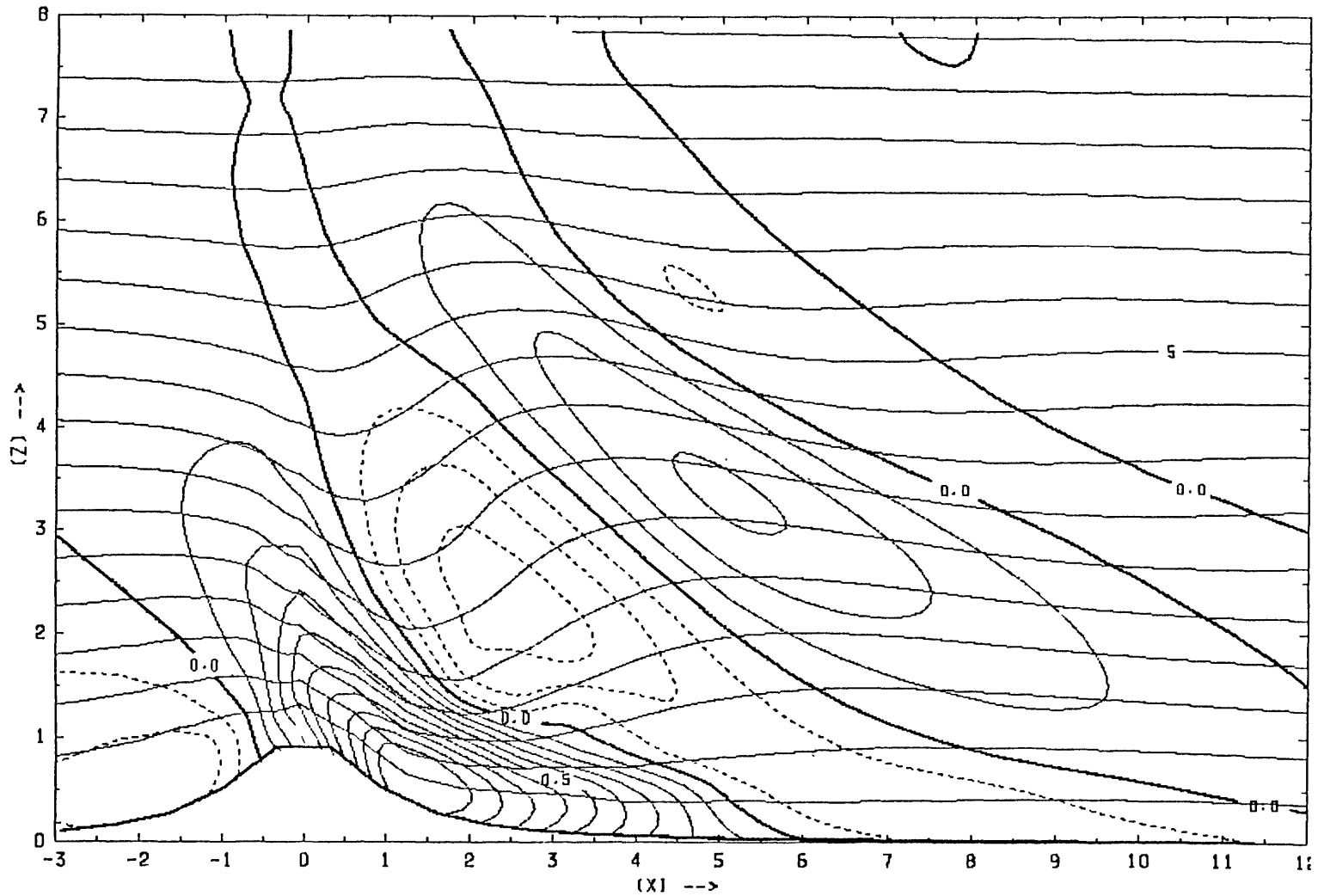
Fig. 4.16. Nonlinear (Fr = 0.9) model solution for potential buoyancy b (solid, contour interval 0.5) and u' (solid and dashed, contour interval 0.1) at t = 30. Mountain is bell-shaped, with half-width Ro^{-1} = 1/2. Basic state has zonal (y) temperature gradient, and negative vertical shear of meridional (x) velocity, determined by β_y = 0.1.

levels. The lack of energy above z = 5.5 shows that the mountain injects very little steady wave energy at shorter wavelengths than π half-widths.

4.8. Synopsis of Lagrangian model

• Governing system consists of two-dimensional, f-plane, non-hydrostatic, Boussinesq primitive equations.

• Average vorticity of each fluid element (cell) changes according to imbalances between solenoidal and Coriolis accelerations, determined by cell vertex configuration.

• Vertex configuration is obtained diagnostically, subject to mass conservation and finite-difference circulation theorem.

• Time-differencing is staggered, with vertex positions and velocities alternating.

• Positions needed in diagnostic calculation may be updated less frequently than velocities if separation of linear and nonlinear time scales is assumed.

• Lower boundary condition acts to keep lowest vertices in contact with uneven boundary; upper boundary condition enforces upward propagation of linear gravity-inertia wave groups (assuming weak rotation and shear).

• Lateral boundary condition on velocity is based on "phase advection", using time-variable phase speed estimates. Condition on conservative variables (absolute momentum and potential buoyancy) is "zero-normal-gradient" of perturbation.

• Lagrangian grid is replenished at regular time intervals with new points at upstream boundary. These are initialized in accordance with lateral boundary conditions.

• Viscosity parameterization assumes constant-coefficient, biharmonic mixing, and surface fluxes proportional to squared velocity (nonlinear drag law) or perturbation static stability.

• Lagrangian grid can be remapped in the vicinity of the forcing region by interpolating the perturbation variables to more regular points.

• Advection by sheared part of basic-state flow is treated as in an Eulerian model.

• Principal advantage: model requires fewer points to simulate systematic generation of steep gradients; principal disadvantage: requires more points to simulate rapid oscillations and/or large divergence along solid boundary.

CHAPTER 5.   NUMERICAL SIMULATIONS AND CONCLUSIONS

5.1 Review of previous modelling

Pierrehumbert and Wyman (1985) appear to be the first to theoretically and systematically investigate upstream influence by a two-dimensional barrier in a stratified flow. Their numerical model is a modification of the hydrostatic primitive-equation model of Orlanski and Ross (1977). PW retained the flow-dependent eddy-mixing parameterization and radiative lateral boundaries of the earlier model, and included topography and a wave-absorbing upper boundary layer. For the most part, these features seem to meet the exigencies of simulating mesoscale mountain-waves under conditions permitting convective overturning. PW chose a Gaussian mountain profile, which decays much more rapidly than the bell-shaped mountain at large distances from the summit. As indicated in chapter 3, the difference is slight in the near field.

The significant feature of the non-rotating simulations was a horizontal surge of long-wave energy coinciding with the onset of wave-breaking after an impulsive startup. For Froude numbers exceeding 1.5, or about twice the observed threshold for wave-breaking, the laterally-radiating energy was sufficient to permanently arrest a layer of fluid on the boundary upstream from the mountain. PW found a linear dependence of the depth of the stagnant layer on the Froude number, and therefore deduced that the flow underwent an "orographic adjustment", whose result was to keep the _effective_ Froude number from exceeding 1.5.

The rotating simulations also produced upstream surges, but the resulting low-level shear layers always retreated back toward the mountain

after roughly an inertial period. A diagram showing the dependence of the maximum upstream transient deceleration, $1-u_{min} \equiv -u'_{min}$, on the parameters Ro and Fr is reproduced in Fig. 5.1. The results demonstrate that u'_{min} is determined qualitatively by the steady-state theory; that is, u'_{min} is proportional to Fr and RoFr in the regions Ro > 1 and Ro < 1, respectively. However, the actual deceleration plotted in Fig. 5.1 for Ro < 1 exceeds the semi-geostrophic prediction by a factor of at least two. In the large Rossby number case, the departure from linear theory is smaller but the duration and width of the transient disturbance in the narrow-mountain simulations are large enough to make the steady solutions practically useless.

PW showed that the upstream penetration of the transients could be explained by assuming the disturbance was due to long-wave group propagation away from a vertical source distribution. On the basis of the same assumption, Emanuel (personal communication) has suggested that the strength of the upstream disturbance may depend physically on the ratio of the steady-state linear horizontal decay scale to the forcing width, presumed to be that of the mountain. It can be seen that constant values of this ratio, $\lambda/\ell = Ro\sqrt{(Fr^2-1)}$, closely follow the shape of the deceleration curves. The idea is consistent with the notion of the mountain as a vertical energy source which is well separated in space from the response. However, the nature and development of the vertical forcing are left unexplained.

The specific problem of coastal frontogenesis was investigated by Ballantine (1980) using a three-dimensional boundary-layer model similar to that of Pielke (1974). The model incorporates a sophisticated
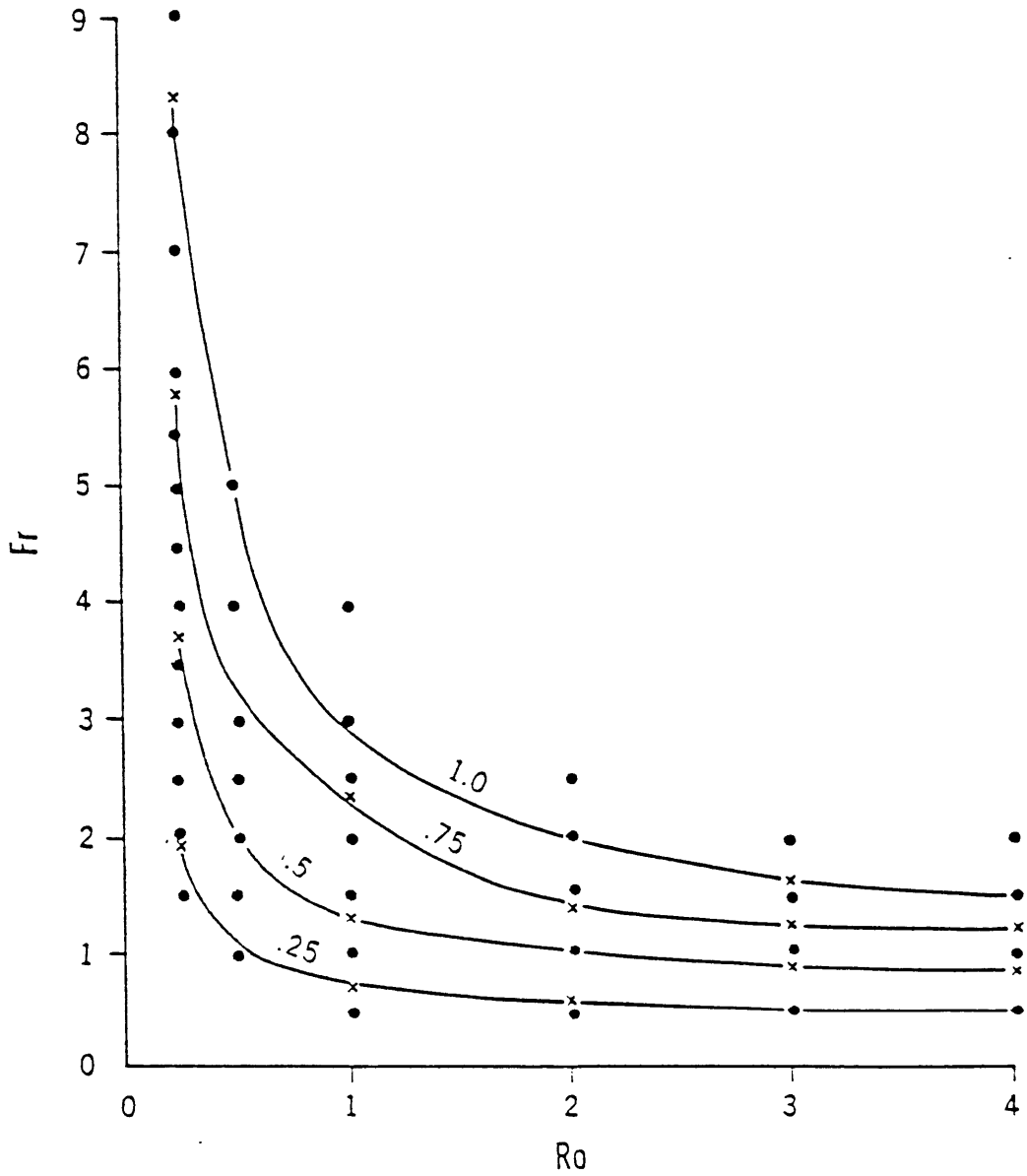
Fig. 5.1. Contours of maximum deceleration, $-u'_{min} = 1-u_{min}$, appearing upstream from a Gaussian mountain of amplitude Fr and half-width $1/Ro$, based on two-dimensional numerical simulation (from Pierrehumbert and Wyman, 1985).

eddy-flux parameterization as well as a 15-km-scale representation of the topography of southeastern New England. The potential technical limitations of the model arise from decisions to (1) place one of the lateral boundaries at the highest point of the terrain, (2) treat the upper boundary as a reflective free surface, and (3) allow no temperature advection across the lateral boundaries.

These features did not prevent the model from developing a realistic pattern of coastal convergence and frontogenesis over an equally realistic period of about a half day. A time sequence of potential temperature from Ballantine's case-study experiment is shown in Fig. 5.2. Notice that the sea-surface heating is strong enough to destroy most of the stratification in the heated layer during the first three hours. Hence, there is an implicit assumption that the air mass has been in contact with the water for considerably less than three hours before the initialization.

By repeating the experiment without orography or land-sea roughness contrast, Ballantine showed that both the coastal convergence and the backing of the low-level wind to northerly in the cold air can result entirely from an adjustment to the local heating. Such a mechanism probably does operate in the initiation of those coastal fronts which begin during large-scale cold advection. In the general case, it is hard to justify the initial temperature field over the warm water, without which the crucial isallobaric response identified by Ballantine is absent.

Ballantine's mechanism can be viewed from a flow-relative frame as a solenoidal circulation forced by a moving heat source on the boundary. It can then be seen that the best prospects for rapid frontogenesis are

EW Θ-SECTION (K = 15) AT 0 HRS

EW Θ-SECTION (K = 15) AT 3 HRS

EW Θ-SECTION (K = 15) AT 9 HRS

EW Θ-SECTION (K = 15) AT 15 HRS
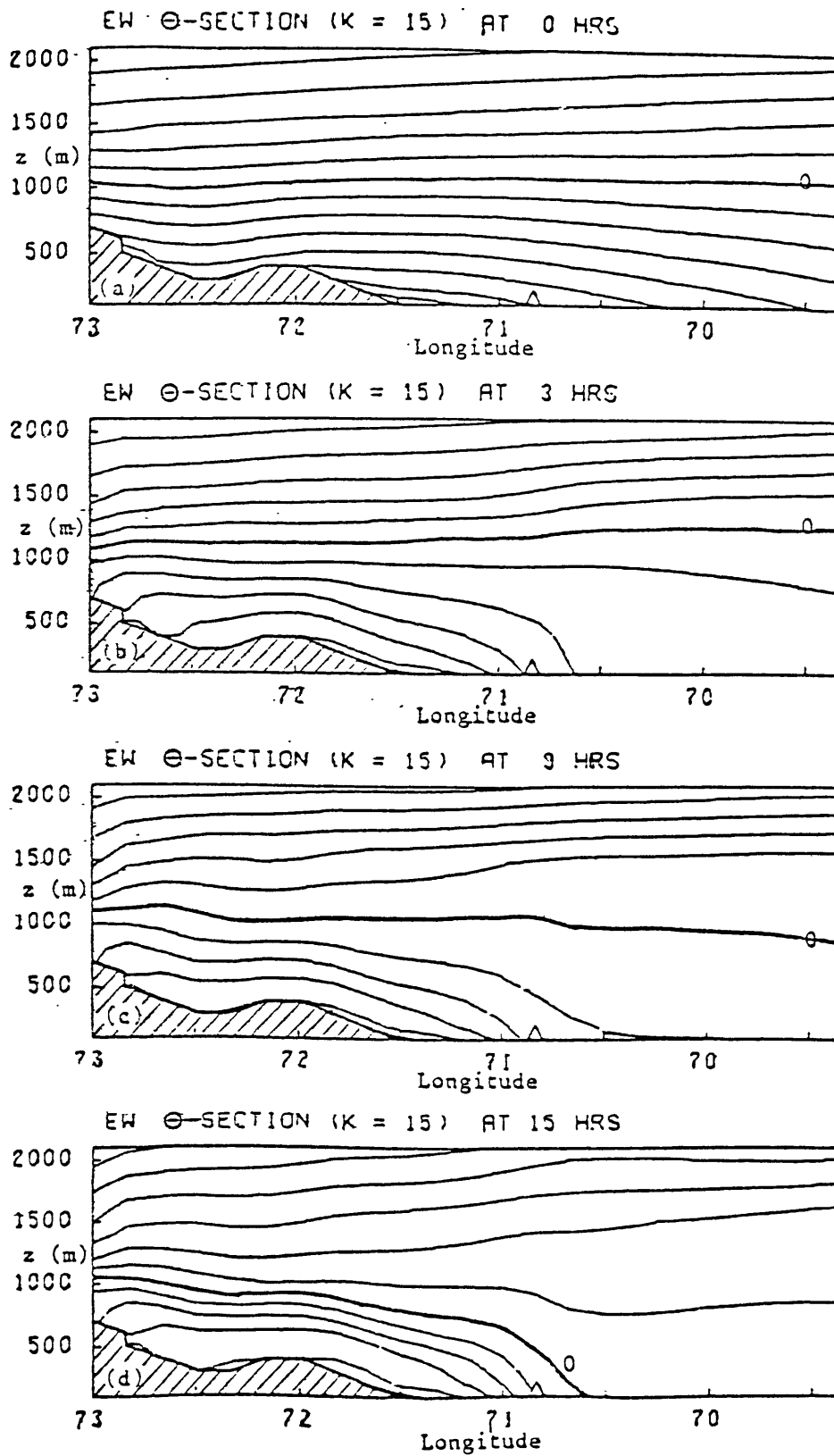
Fig. 5.2. Three-hourly sequence of potential temperature cross-sections from three-dimensional numerical simulation. Contour interval is 3 K. (From Ballantine, 1980)

realized when the induced flow of cold air stays even with the edge of the heat source. In that situation, the maximally heated air remains in contact with the unheated air, and moreover, recirculation is curtailed. To the extent that the initial surge of air toward the heating behaves as a density current, its speed depends on the density contrast as well as its own depth. There seems to be nothing in the heating mechanism to permit a dynamic adjustment of this depth, whence it would follow that the frontogenesis depends crucially on initial conditions and the speed of the heat source (mean flow).

The small-amplitude steady-state form of this problem was discussed at the end of chapter 3. It was found that a heating rate which neutralizes the stratification over the heating depth ia 3 h would produce a velocity perturbation comparable to the mean flow. Ballantine's solution suggests that a similar threshold for the heating rate applies in the time-dependent rigid-lid formulation of the problem.

What the heating mechanism lacks is a means of preventing a large-amplitude inertial oscillation of the type described by PW. Without further physical constraints, the Coriolis effect will eventually destroy the front, or convergence zone, by turning the cold air away from the heat source. The lifetime of the front beyond the time of approximate air-sea temperature equality is then limited to about half of an inertial period (9 h). It should be noted that Ballantine's frontogenesis is also the partial result of an apparent heat source, consisting of the shearing of the north-south gradient. The effect could be rendered more realistic, and more significant, by allowing temperature advection through the northern boundary.

The purpose of the numerical experiments in this chapter is to simulate _adiabatic_ frontogenesis appearing as a disturbance on an otherwise balanced, baroclinic basic state. Under these conditions, the orography is the only significant means of establishing the necessary vertical deformation. It is, however, noteworthy that the omission of boundary heating or cooling is still not the most conservative assumption, since in some cases, the large-scale air mass is slightly warmer than the sea surface.

The numerical model is described in detail in chapter 4, which includes a synopsis in section 4.8. The basic design is Lagrangian; that is, the grid points move with the flow. The advantage of such a model is that it provides more accurate conservation of tracer quantities such as potential vorticity, and improves the resolution of steep gradients. The chief disadvantage is that the flow in highly divergent regions, in particular at the mountaintop in the present application, must be remapped periodically onto more regularly spaced points. The remapping is performed after every two advection times (across the mountain half-width) in all of the experiments to follow.

To minimize the deformation of the Lagrangian grid without a crucial loss of realism, asymmetric mountain profiles will be used, in which the lee slope is broader than the windward slope. This type of asymmetry enhances the low-level deceleration in both the large Rossby number (Lilly and Klemp, 1979) and small Rossby number (Pierrehumbert, 1984) regimes. It was also found here to reduce the gradients in the lee of the mountain. A physical reason for such a choice of topography is that downward surface flow over complicated terrain, such as exists in New

England, is inhibited by strong vertical stratification in the valleys. This may well account for the absence of high winds in the valleys of New England in many easterly-flow regimes.

The parameter region of interest is roughly defined by $1 < Fr < 1.5$ and $Ro > 2$, in which blocking does not occur in a barotropic flow (PW). For reference, consider that a Froude number of 1.5 over terrain of height 500 m implies $U_0 \approx 7$ m/s when $N = .02$ s^{-1}. For the same flow speed, $Ro = 2$ requires a mountain half-width of $\ell \approx 35$ km. This distance may even be considered a large value for New England if "half-width" is strictly defined (as in chapter 1). All of the experiments are to be carried out under hydrostatic conditions, with $h/\ell \leq 1/20$.

Unless otherwise stated, the eddy mixing will used only for computational stability during startup. Thus, in the "inviscid" simulations, the Reynolds number, $Re = U_0h/K$ (with K the constant mixing coefficient), will be specified such that the dimensional mixing time, $\tau \equiv (Re\ h/\ell)\ \ell/U_0$, is at least $100\,\ell/U_0$. The surface flux coefficients (see section 4.5) are set at $C_d = 0.5Re^{-1}$ and $C_h = 0.5$ except in the surface drag experiments in section 5.4. The thermal mixing is shut off in section 5.2. Elsewhere it is determined (without great consequence) by $Pr = 2$.

The scaling of the variables will be as in chapter 2, except with $H = h$ and $L = \ell$ serving as the length scales. Thus, for example, the time scale is ℓ/U_0, and the potential buoyancy scale is N^2h. With only a few exceptions, the experiments are run in an initial domain measuring $z_T = 10$ units high and $2x_L = 20$ units wide, represented by $N_x = 40$ points by $N_z = 24$ points. The geostrophic wind starts up smoothly during

approximately the first advection time. The initial temperature

surfaces are distorted to follow the terrain, with the result that

upstream transients are suppressed early on, and a strong low-level

disturbance in the lee is avoided. The meridional velocity is initially

zero.

5.2 Blocking threshold for two asymmetric mountains

The first model experiments will attempt to identify the marginal

conditions for blocking of baroclinic flow past the mountain $g_0(x) =$

$x/(1+x^2)$. This choice is identified by Lilly and Klemp (1979, hereafter

LK) as an effective shape for "unsteepening" the density contours in

nonlinear hydrostatic solutions of Long's equation for steady,

two-dimensional nonrotating disturbances. The "LK" profile has the

further property that the minimum steady-state surface velocity occurs at

the ground at $x = 0$ in the linear solution, or slightly above and upstream

from this point in the nonlinear solutions.

LK's analysis indicates that the fully nonlinear solution has

$u_{min} \approx 0.3$. The non-rotating barotropic experiment shown at the top of

Fig. 5.3 produces a (nearly) steady-state u_{min} of 0.26 for the same

Froude number (the plotted values are of the perturbation, $u' = u-1$). The

discrepancy is mostly due to a combination of computational and explicit

dissipation. The linear solution, $u_G(x) = 1-Fr/(1+x^2)$ along $z = 0$,

gives $u_{min} = 0$ under the same conditions.

The second experiment in Fig. 5.3 was conducted with $Ro^{-1} = 0.2$

and $\beta = -0.4$. Recall that rotation in a barotropic flow reduces the

low-level upstream deceleration; in fact, for the LK profile, $u_{qg}(x) =$
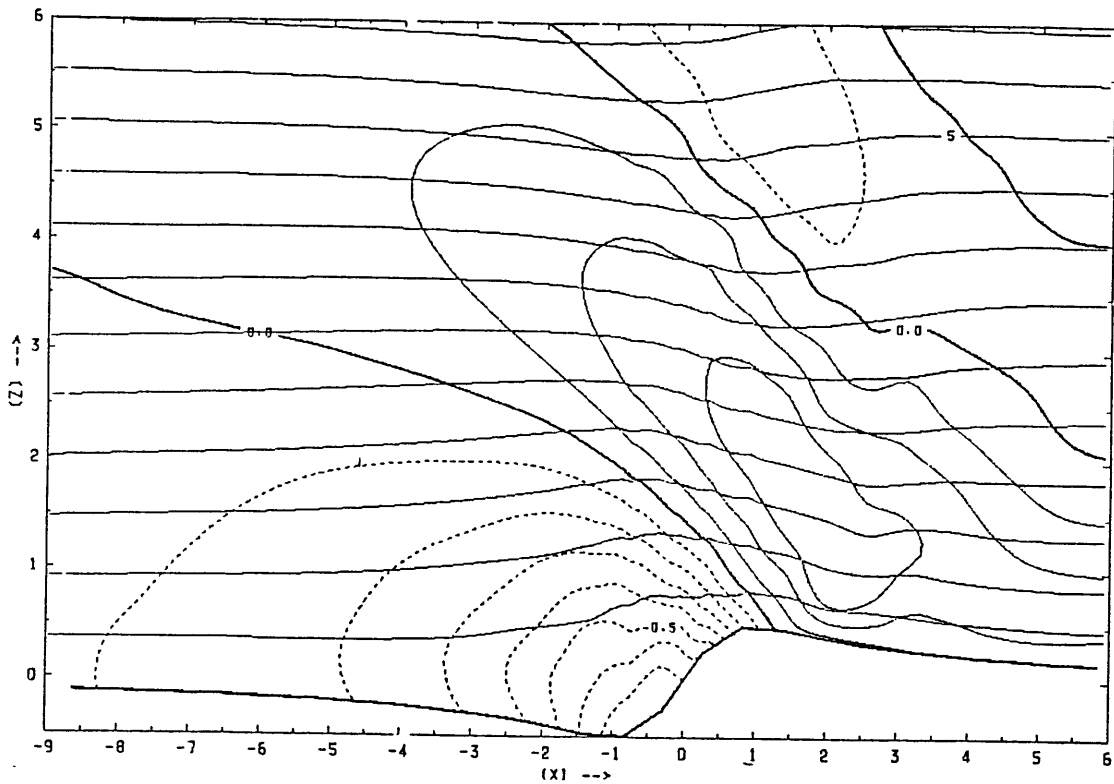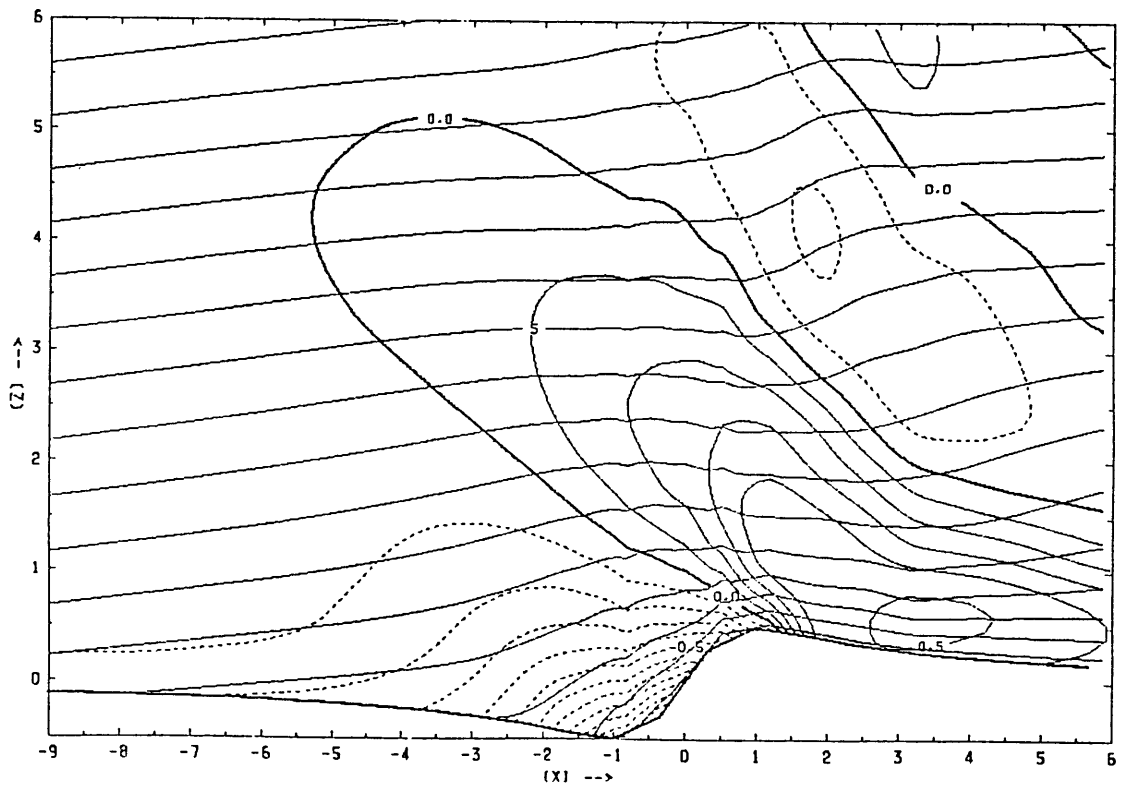
Fig. 5.3. Potential temperature (solid, contour interval 0.5) and perturbation velocity u' (solid and dashed, interval 0.1) in nonlinear (Fr = 1) flow past LK mountain at t = 20, assuming barotropic (top, Ro^{-1} = 0) and baroclinic (bottom, Ro^{-1} = 0.2, β = -0.4) basic state.

$1+2Frx/(1+x^2)^2$ is a significantly weaker response at $z = 0$ than $u_G(x)$.
Yet the nonlinearity and baroclinicity are sufficient to produce a small
volume of stagnant fluid at $x = 0$ in the figure. The flow at this point
comes to rest by $t = 16$ (roughly half the inertial period), and has u_{min}
$= -0.1$ at the time shown. Unlike PW's barotropic simulations using a
larger-amplitude Gaussian mountain, the solution here does not surge and
retreat. For the chosen marginal conditions, there is no significant
spreading of the stagnant fluid. On the other hand, because of the
gradual simultaneous increase in the low-level stratification and parallel
velocity, the baroclinic solution <u>cannot</u> be considered steady.

A second comparison between barotropic and baroclinic solutions
can be seen in Fig. 5.4 for the two-scale mountain profile defined by
(4.27). Each half of the mountain is bell-shaped, but the lee side is
made five times wider than the side facing the wind by setting $\ell_1 = 5$ in
(4.27). It should be borne in mind that the model slightly underestimates
the barrier effect for this profile (to be called "B5"), largely because
of the discrete representation of the topography. LK note that the
minimum steady-state surface wind in the linear solution is approximately
$u_{min} \approx 1 - Fr(1/4 + \pi^{-1}\log\ell_1)$ for large ℓ_1. It appears from
interpolating their finite-amplitude calculations that that the nonlinear
modification is small when $\ell_1 = 5$. Thus the model result, $u_{min} = 0.31$,
for the B5 profile shows less deceleration than the theoretical value of
about 0.25 for $Fr = 1$.

The marginal case of flow stagnation for $Fr = 1$ and $Ro^{-1} = 0.2$,
also shown in Fig. 5.4, is found at $\beta = -0.8$. The quasi-steady model
solution has $u_{min} = 0.1$, which represents a small recovery from a flow
reversal at $t = 16$. As with the LK profile, the vertical stratification
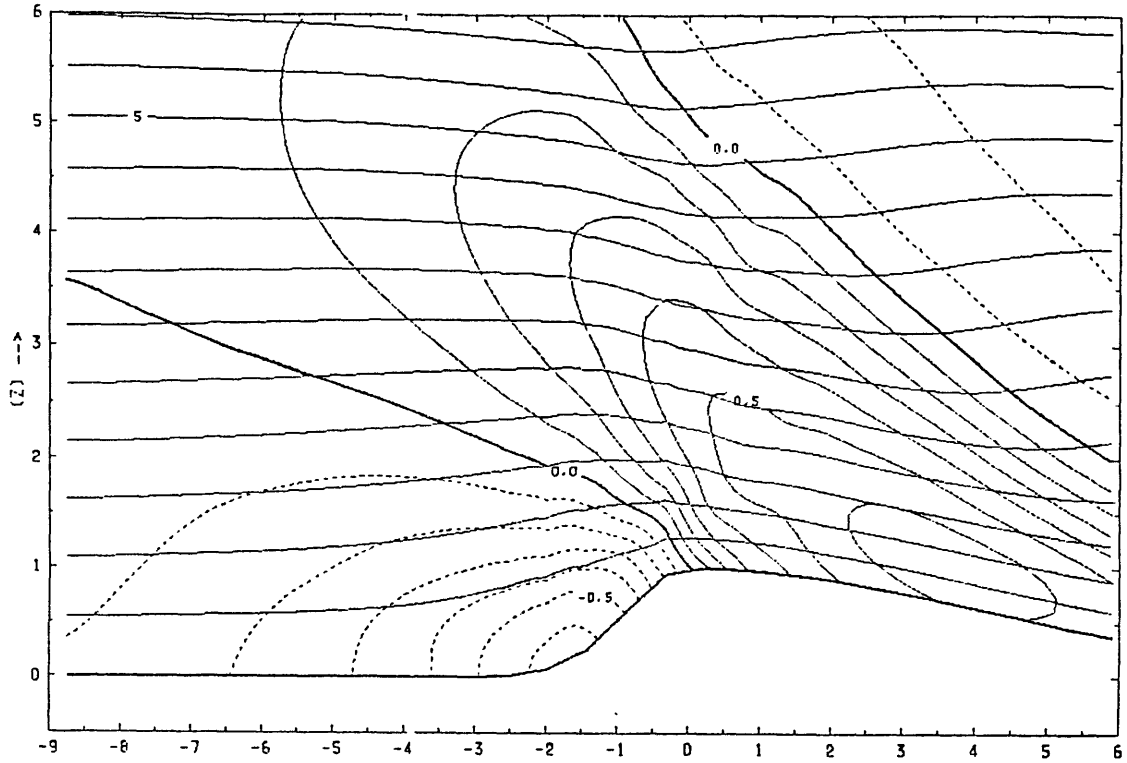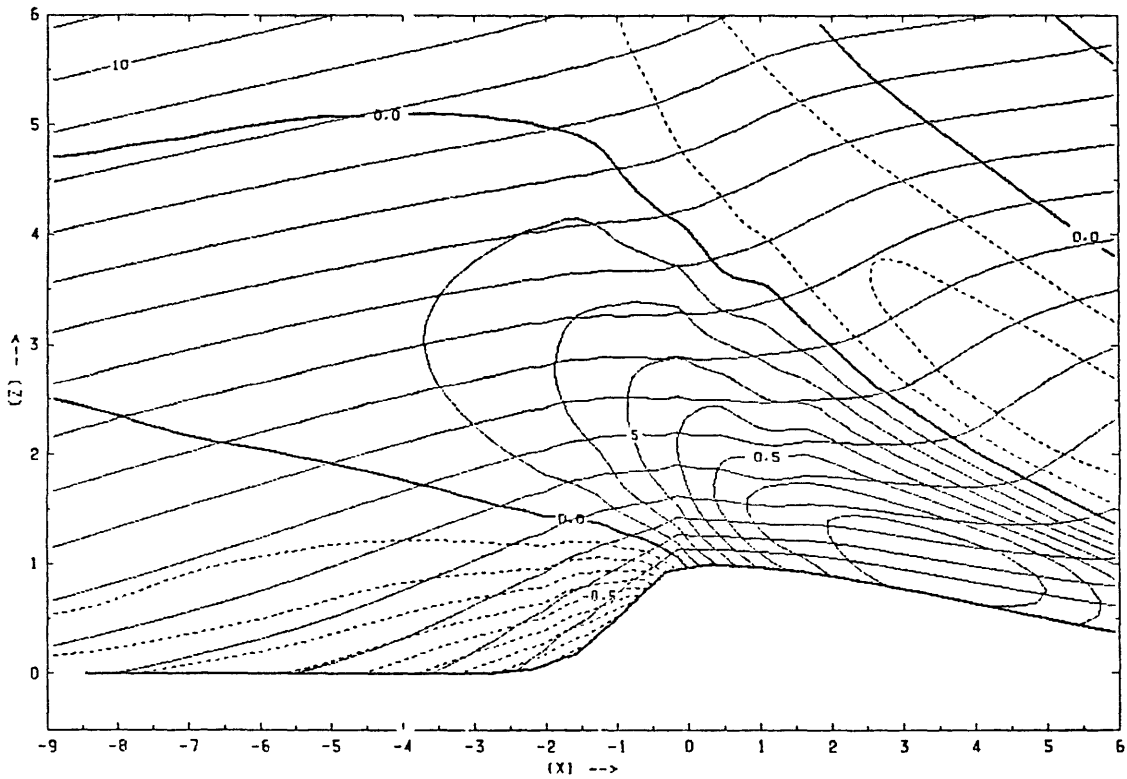
Fig. 5.4. As in Fig. 5.3, except for B5 mountain, and β = -0.8 in lower panel.

near the mountain in the marginally-blocked solution is roughly twice that of the steady barotropic solutions. It is probably only coincidental that the condition for stagnation in LK's solution of Long's equation is Fr = 2.0 for the LK profile (i.e., roughly the simulated _local_ Froude number at the mountaintop). Indeed, the analogous condition for the B5 mountain appears from their results to be somewhat weaker. Although an increased stratification is intuitively consistent with blocked flow, one cannot expect the theoretical critical Froude numbers to apply very accurately to subregions of a variably-stratified baroclinic fluid.

A more careful attempt to assess the consequences of local Froude number anomalies was made in chapter 3. It appeared that the secondary response to a weak modification of the temperature field by the mountain was controlled, in effect, by the nonlinear advection of parallel momentum. The general analysis indicated that the advection amplitude is independent of the Rossby number when that parameter is large, and that the strength of the response decreases slowly with Ro^{-1} until the inertial distance is several times the half-width of the forcing. It is emphasized that these conclusions follow from a number of assumptions, and from an idealization of the mountain and forcing shapes.

Fig. 5.5 summarizes a parametric study of blocking carried out for the LK and B5 profiles. Curves are drawn at the boundaries of the regions of the β-Ro^{-1} plane in which the horizontal temperature gradient was sufficient to reverse the flow for a particular value of Fr $\leq$ 1.4. A time limit of Δt = 20 was imposed as a further condition, since dissipative effects cannot be ignored much beyond this period. Notice that no blocking occurs in any case for $Ro^{-1} <$ 0.1. This range of Rossby
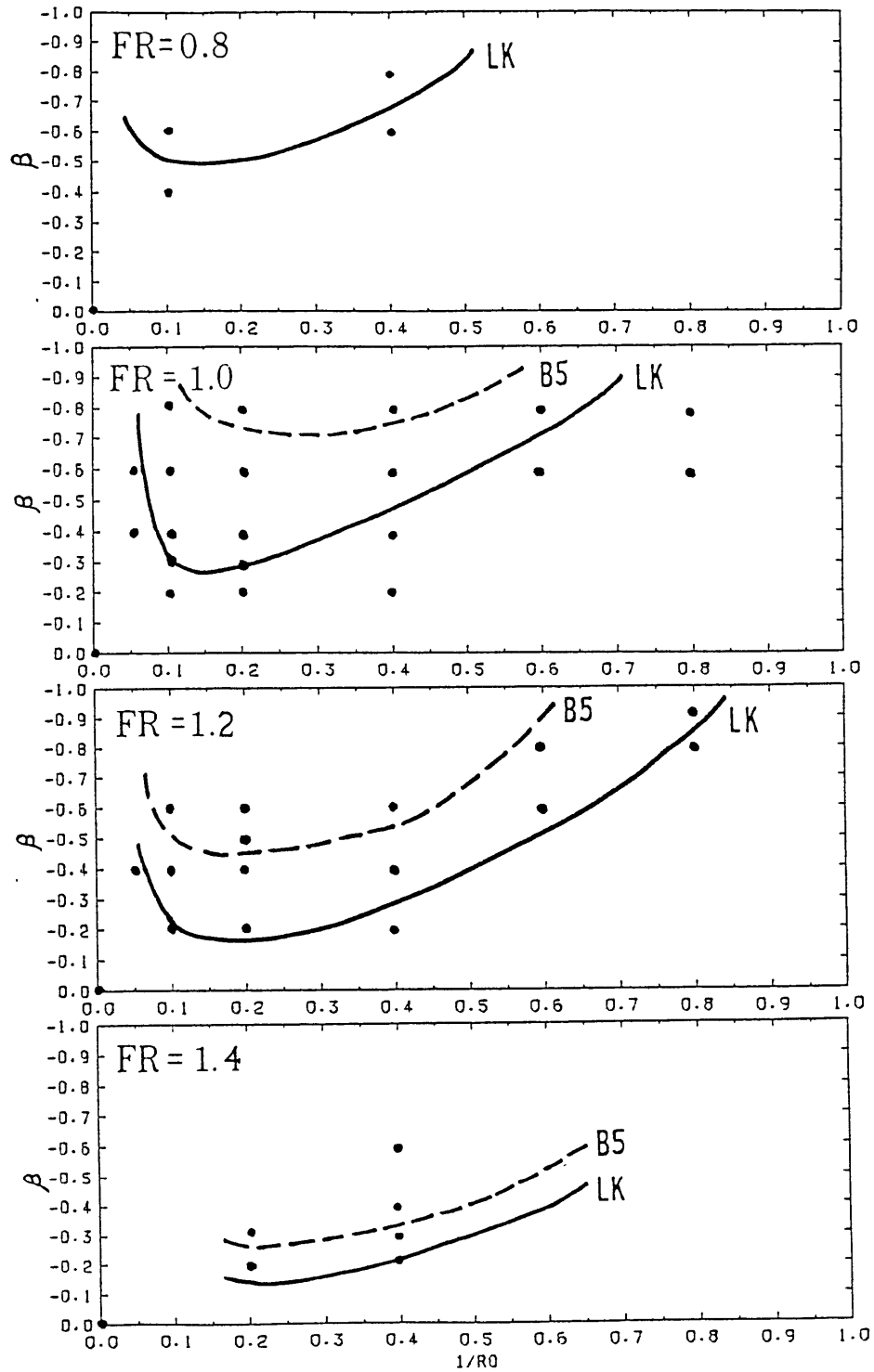
Fig. 5.5. Blocking boundaries in $Ro^{-1}-\beta$ parameter space for four values of Fr, and for two asymmetric mountains "LK" and "B5" defined in text. Flow reversal occurs by t = 20 when parameters are chosen from above the curves, which are interpolated from values of minimum upstream velocity observed in simulated cases marked by dots.

numbers yields the least reliable information because (1) the inertial half-period is considerably greater than $\Delta t = 20$, and (2) the model may not adequately resolve the horizontal temperature gradient. It is, however, necessary for the the curves to have a vertical asymptote at $Ro^{-1} = 0$, where Coriolis effects and the horizontal temperature gradient both disappear. No reliable simulations were achieved for Froude numbers large enough to cause blocking near this limit.

The Ro-dependence in the figure was not anticipated by the chapter 3 analysis, which indicated that the best prospects for blocking (without breaking lee waves) should occur near $Ro = 1$, the value for which the upstream response to dipole forcing of fixed strength is greatest. In fact, the analysis was made possible by the fact that the baroclinic feedback effect was relatively weak for large Ro. For a consistent explanation, it must be recalled that background rotation eliminates a long-wave singularity in the solution for steady flow over a step. Thus, it will be sufficient to show that the well-known large-amplitude non-rotating response at large ℓ_1 significantly offsets the effect of narrow forcing as Ro increases.

To this end, the advection of v at the ground was evaluated in several solutions of the linear topographic problem of flow past the LK and symmetric bell-shaped ("B1") mountains. Graphs of $J(\psi_0, v_0)$ versus x using LK profile solutions (via Fourier transforms) are shown in Fig. 5.6a for the cases $Ro^{-1} = 1$, $Ro^{-1} = 0.6$ and $Ro^{-1} = 0.2$. The horizontal distance is normalized by the mountain width, as in the model plots. Notice that negative values of the Jacobian become more important for narrow mountains, both in absolute terms and in relation to the
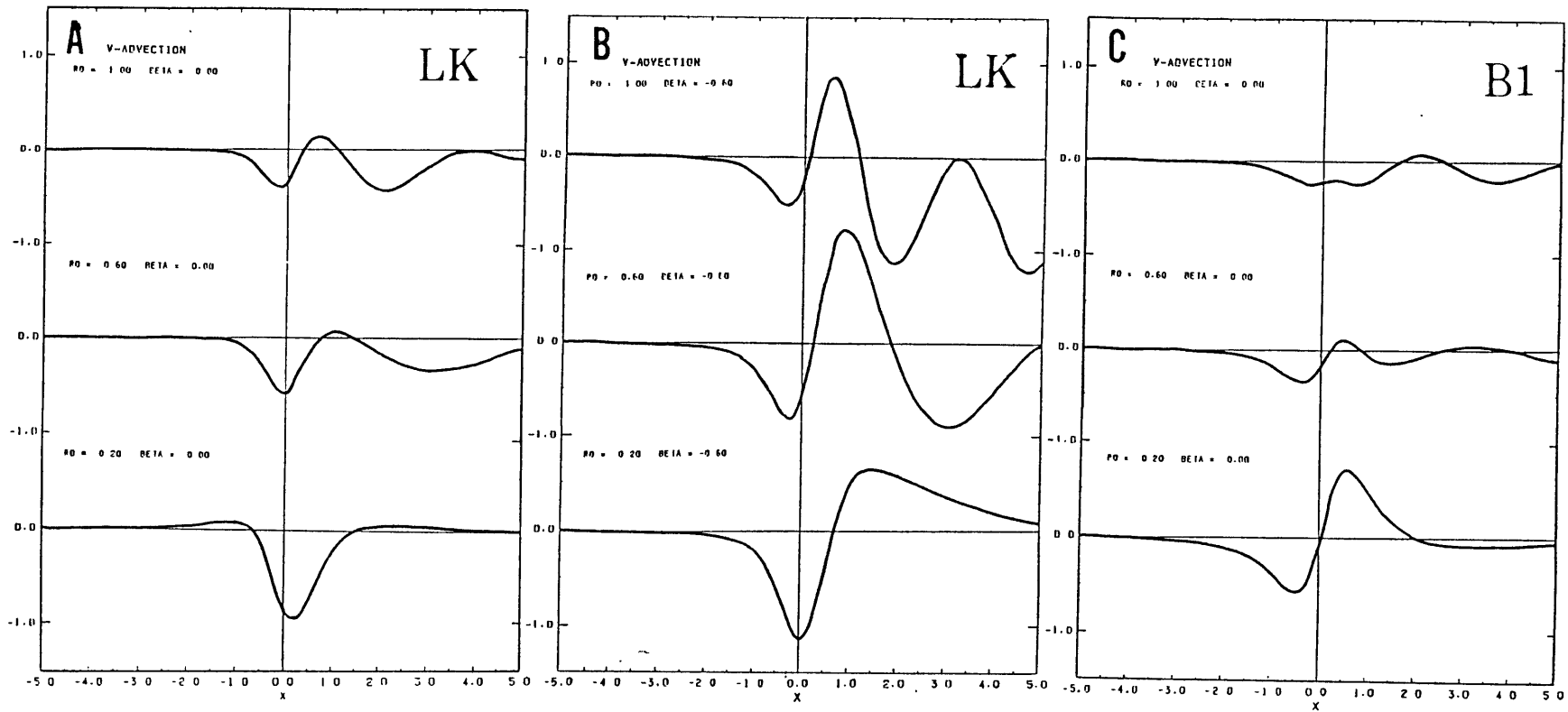
Fig. 5.6. Surface advection of v', in units of Fr^2, diagnosed in steady linear flow past (a and b) "LK" and (c) "Bl" mountains, with half-width Ro^{-1} = (top) 1, (middle) 0.6 and (bottom) 0.2. Basic state is barotropic in (a) and (c), but β = -0.6 in (b).

positive regions of the same distribution. It has already been shown that negative forcing is needed to feed back positively on the low-level convergence. Fig. 5.6b displays the same information for a highly baroclinic basic state. The growth of the negative source with increasing Ro is even more pronounced in this case.

The B1 profile produces a qualitatively different result, seen in Fig. 5.6c. While the amplitude of the v-advection still increases with Ro, the distribution is such that the negative region no longer dominates at large Ro. Because of the strong divergence at the mountaintop, the Lagrangian model could not complete a simulation of sufficiently large amplitude to produce an upstream flow reversal with the B1 mountain. However, it is suggested here that the Froude number condition is not greatly altered by the baroclinicity in the case of the symmetric mountain. The barotropic and baroclinic solutions can nevertheless be expected to differ drastically in the _duration_ of the period of blocked flow.

The chapter 3 analysis neglected to consider carefully a second possible sensitivity to the Rossby number. Namely, the effectiveness of a (sloping) mountain as a _vertical_ source may depend on the ratio of the horizontal response decay scale to its half-width. The sensitivity should be greatest when the two scales are comparable, as in the baroclinic experiments of Figs. 5.3 and 5.4. As observed by Emanuel (personal communication) in regard to PW's blocking summary (Fig. 5.1), the sensitivity is formally expressed by the ratio $\lambda/\ell = Ro\sqrt{(\sigma^2 Fr^2 - 1)}$ between the barotropic decay scale (corresponding to an effective mountain height, σFr) and the mountain half-width. Thus if σFr is supercritical (> 1) for

the baroclinic flow, the nonlinear "forcing" may remain sensitive to Ro somewhat beyond Ro = 1.

5.3 Basic frontogenesis experiments

The first long-term experiments are to test, by itself, the proposed mechanism of a streamwise temperature gradient in a primarily orographic disturbance. It will be seen that conditions which are supercritical for blocking can eventually lead to "partially" steady frontal structures in the baroclinic case. In addition to an initial flow reversal, frontogenesis requires a means of preventing the large-amplitude geostrophic adjustment oscillation which interferes with upstream influence in the barotropic case. The experiments should show how this works.

A successful frontogenesis simulation was achieved with the B5 profile for the strongly supercritical parameters $Fr = 1.2$, $Ro^{-1} = 0.2$ and $\beta = -0.8$. The contours of total potential buoyancy are plotted in Fig. 5.7a as a time sequence ending at $t = 30$. Notice that the discontinuity in the horizontal gradient moves upstream to about $x = -5.5$ by $t = 30$. At $t = 40$ (not shown) the gradient is somewhat stronger, but the frontal discontinuity remains near its final position in Fig. 5.7a. The gradient at the ground is ultimately limited by the continual remapping and the weak thermal diffusion being used for the sake of a smooth startup. These effects slowly heat the region of reversed fluid while new isentropes are being advected into the frontal zone.

The fields of <u>perturbation</u> velocity for the same four times can be seen in Fig. 5.7b and 5.7c. The maximum parallel component is $v' = 2.8$ at

AR = 0.05   FR = 1.20   RO = 0.20   BX = -0.80   BY = 0.00

T=12.0   U= 1.0   X=11.5

T=18.0   U= 1.0   X=17.5

T=24.0   U= 1.0   X=23.5

T=30.0   U= 1.0   X=29.5

[X] -->

[X] -->
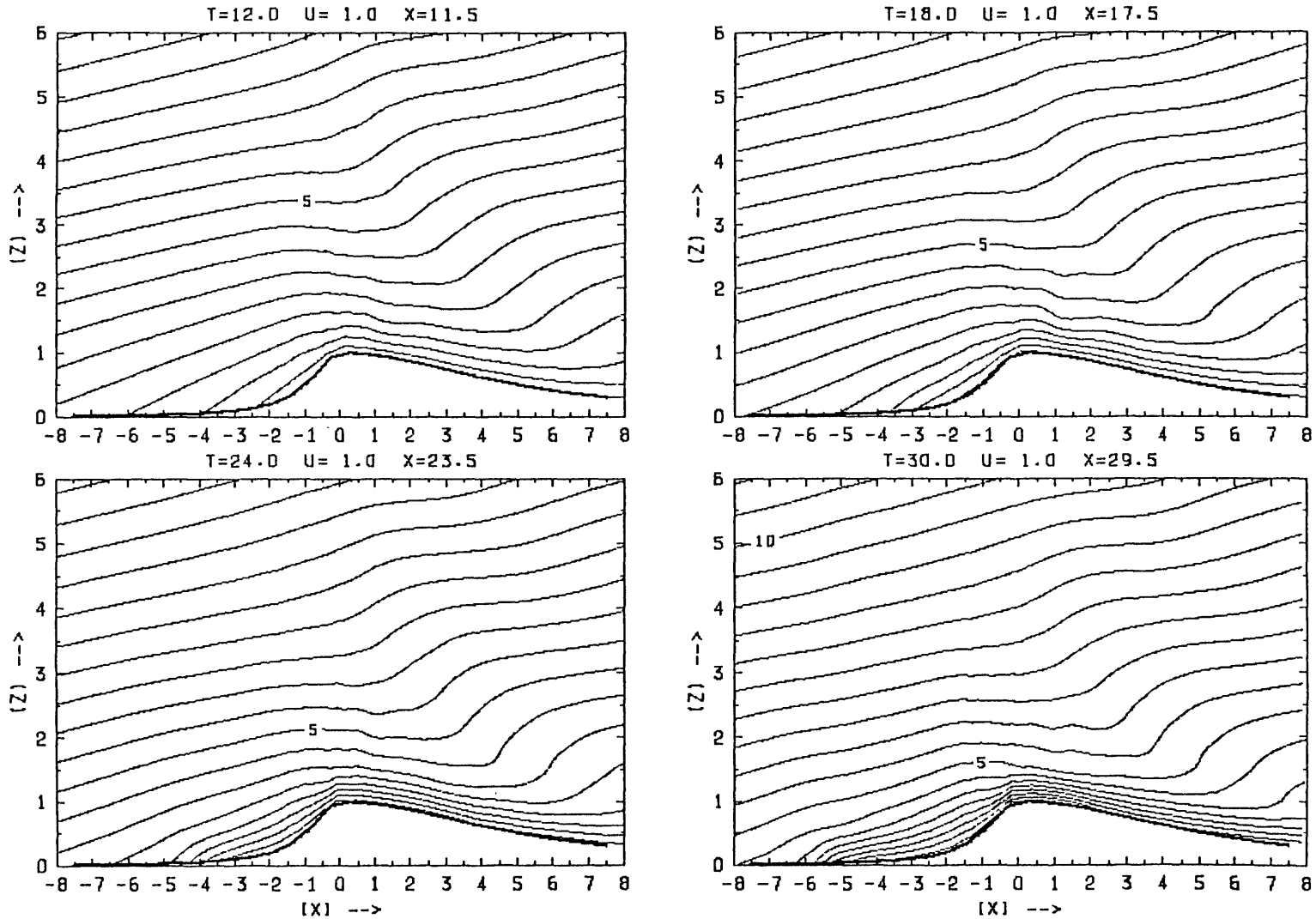
Fig. 5.7a.   Time sequence of total potential buoyancy (temperature) for nonlinear baroclinic flow past B5 mountain, ending at t = 30. Parameters are Fr = 1.2, Ro^{-1} = 0.2 and β = -0.8.   Time interval 6 (ℓ/U_0). Contour interval 0.5 ($N^2 h$).

0820A U

AR = 0.05   FR = 1.20   RO = 0.20   BX = -0.80   BY = 0.00

T=12.0   U= 1.0   X=11.5

T=18.0   U= 1.0   X=17.5

T=24.0   U= 1.0   X=23.5

T=30.0   U= 1.0   X=29.5
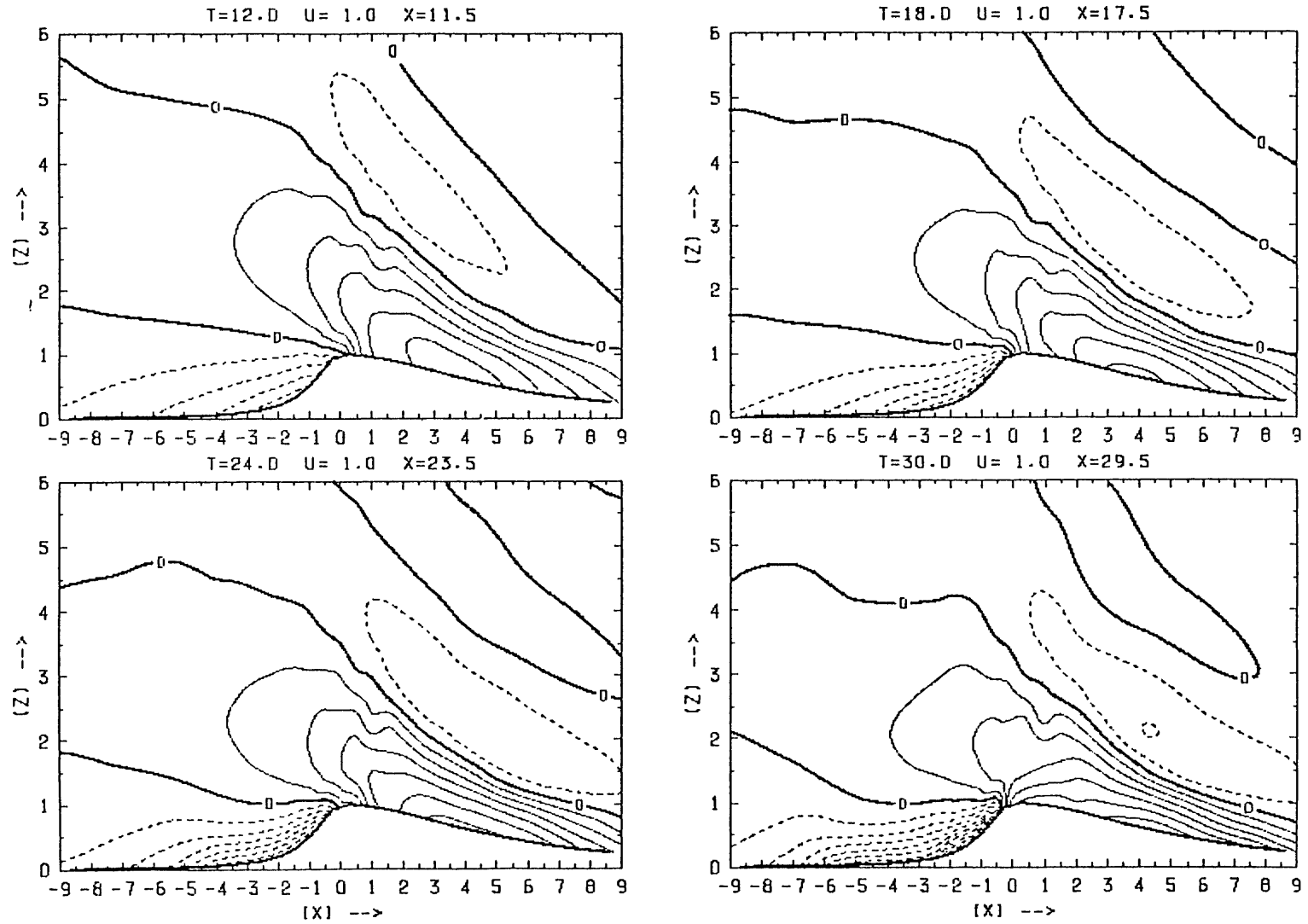
Fig. 5.7b. As in Fig. 5.7a, except model variable is perturbation streamwise velocity, u' and contour interval is 0.2.
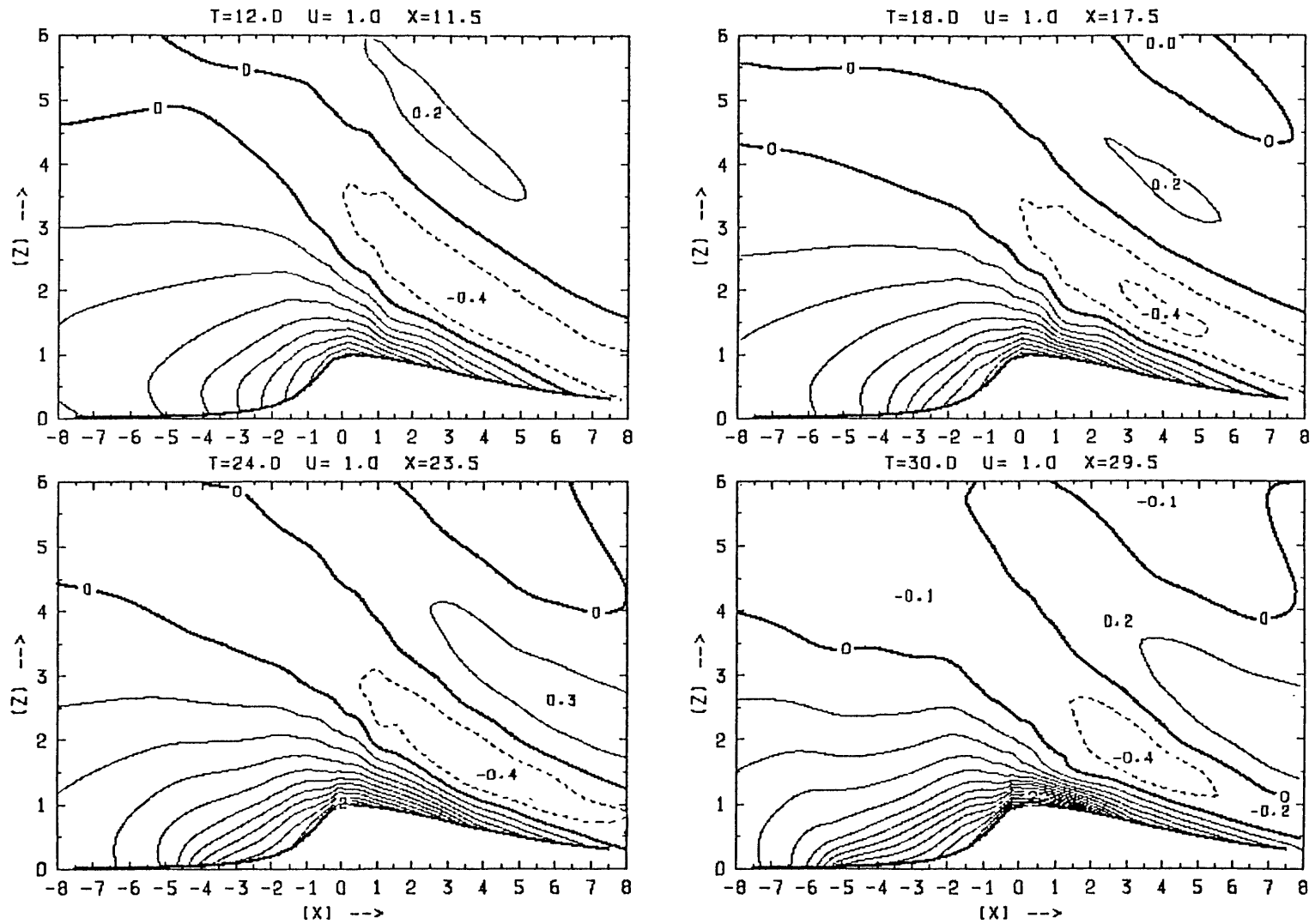
Fig. 5.7c. As in Fig. 5.7a, except model variable is perturbation
parallel velocity, v' and contour interval is 0.2.

the mountaintop in the last panel (in which the contours 2.2 and 2.6 are omitted). The total y-momentum at the same point is $v = v' + Fr\beta = 1.8$. Where the flow is stagnant, v' should increase by a unit amount in a nondimensional period $\Delta t = Ro$, or roughly the time between panels. However, the parallel velocity at the ground is increasing at about half this rate between $t = 24$ and $t = 30$ because of the vertical advection and mixing.

For $\beta = -0.8$, the angle between the basic b and m surfaces is unusually small, as is the potential vorticity. As the gradients of b and m increase, the corresponding contours must become even more nearly parallel to keep the potential vorticity constant. In the present solution, v' in the frontogenetical region is nearly parallel to basic-state M, and therefore to total m. Hence, the fields of b and v' become nearly indistinguishable when the gradients become large in the upstream region.

All three perturbation velocity components at $t = 30$ are shown in Fig. 5.8 for a closer examination. The reversed fluid extends to $x = -6$, but is very shallow compared to the mountain height. Notice that the total streamwise velocity is more than doubled on the lee side. Indeed, the absence of a realistic frictional boundary layer is evident in the excessive surface values of both u' and v' in $x \geq 0$. In the same connection, the vertical velocity field probably suffers from an underestimated frictional convergence in the cyclonic frontal circulation. The simulated vertical motion above $x = -5$ is only $w = 0.12$ $U_0 h/\ell$, or about $.003 U_0$ when $h = 500$ m and $\ell = 20$ km.

It should be noted from Figs. 5.7b and 5.7c that the formation of the cold pool on the windward side of the mountain has the side-effect of
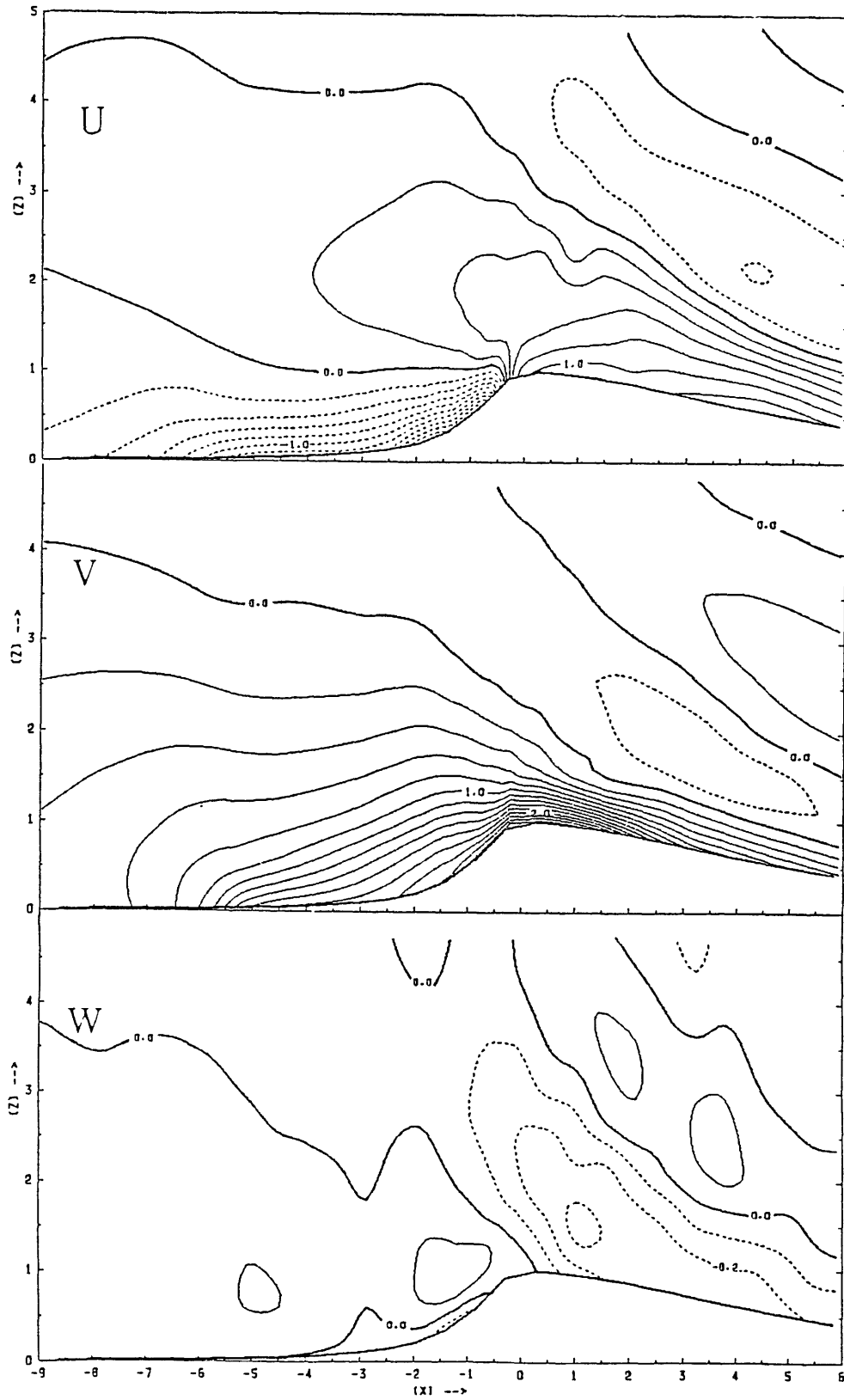
Fig. 5.8. Perturbation velocity components, u', v' (contour interval
0.2) and w (interval 0.1) at t = 30 in the experiment of Fig. 5.7.

slightly reducing the gravity-wave activity directly over the mountain.
This is the anticipated result of altering the effective breadth of the
obstacle. Note, too, that the limiting radius of the cold pool is close
to the Rossby deformation radius of RoFr = 6 units based on the mountain
height, or about 8 units based on the height of the frontal boundary over
the summit. An attempt to characterize the equilibrium which exists after
t = 30 in the experiment will lead to a slight improvement of this
estimate.

Fig. 5.9 shows a time sequence of potential temperature from an
experiment with Ro^{-1} = 0.4, i.e. twice the previous choice. The other
parameters are the same. The sequence is carried to t = 40 (48 h if 1/f =
3 h) to show the equilibration of the surface frontal position near x =
-3. The deformation radius determined by the mountain height is also 3
units (half-widths). The stagnant fluid at the ground is resolved by only
two grid points at t = 30, while at t = 40, the total streamwise velocity
is positive everywhere. The cold air is evidently too shallow to resist
erosion by mixing and inertial effects. The three velocity components at
t = 30 are shown together in Fig. 5.10. The v' field is larger by a
factor of 2 than in the previous experiment, in accordance with the
inverse dependence on Ro.

One of the reasons for the lack of inertial oscillations in
developing large-scale fronts is that the secondary circulation is itself
frontogenetical in the regions of strongest gradient, and continually
alters the conditions for equilibrium. The initial upstream surge in the
baroclinic barrier problem must also induce a secondary circulation. If
this circulation is frontogenetical, as when β < 0, it should reinforce

AR = 0.03   FR = 1.20   RO = 0.40   BX = -0.80   BY = 0.00
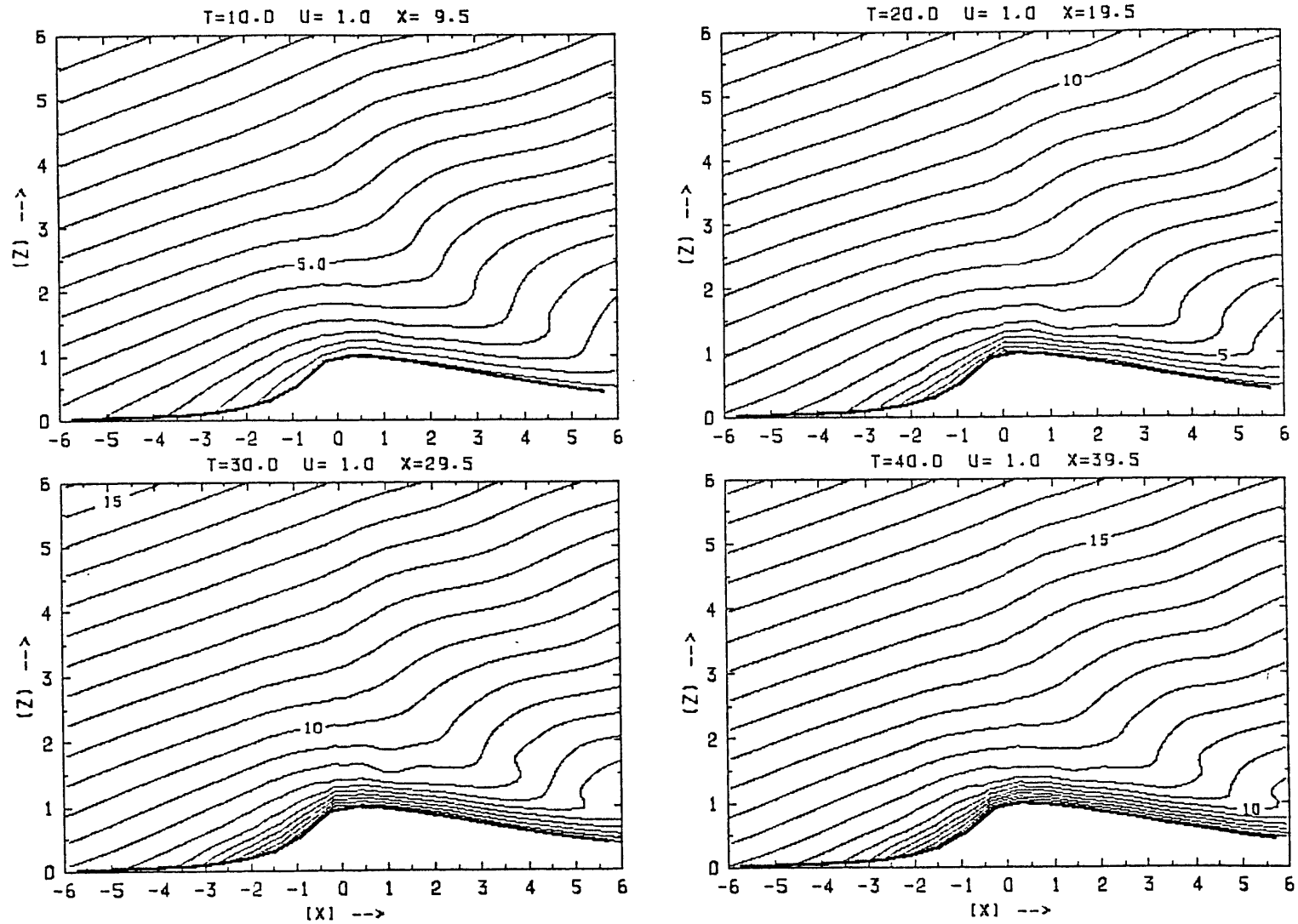
Fig. 5.9. Time sequence of total potential buoyancy (temperature) for nonlinear baroclinic flow past B5 mountain, ending at t = 40. Parameters are Fr = 1.2, Ro^{-1} = 0.4 and β = -0.8. Time interval 10 (ℓ/U_0). Contour interval 0.5 (N^2h).

AR = 0.03   FR = 1.20   RO = 0.40   BX = -0.80   BY = 0.00   T = 30.0   U = 1.0   X = 29.5
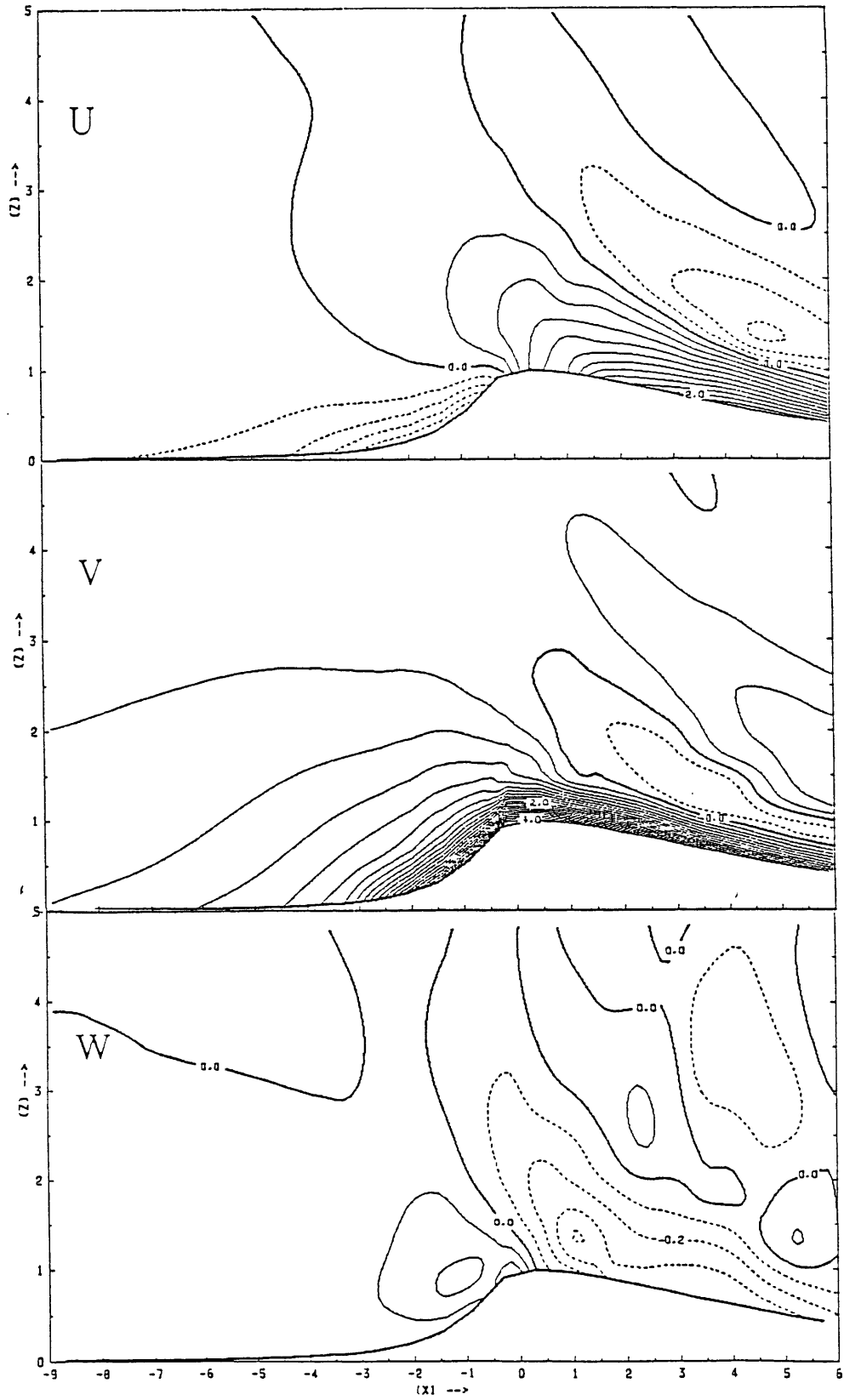
Fig. 5.10. Perturbation velocity components, u', v' (contour interval 0.2) and w (interval 0.1) at t = 30 in the experiment of Fig. 5.9.

the mass-momentum balance and at least partially damp the surge recovery. This argument is offered to explain the remarkably weak transient oscillations in the warm-advection model experiments. In contrast, the cold-advection simulation shown in Fig. 5.11 is notable for the comparative unsteadiness in the upstream velocity.

The fact that the upstream gradients increase indefinitely in the supercritical warm-advection case indicates that the feedback argument can be extended to explain the partial frontal equilibrium seen in the first two experiments. Namely, to prevent further acceleration of the vertical circulation, the temperature and parallel velocity at each point in the frontal zone must increase so as to preserve the existing proportion. The proportion is determined by the frontal slope according to Margules's principle.

The constraint may be expressed using $(\partial/\partial t)b_x \approx -u_x b_x$ and $(\partial/\partial t)m_z \approx -u_z m_x$ (neglecting vertical advection) as

$$\frac{u_x b_x}{f u_z m_x} = \frac{b_x}{f m_z} = 1. \qquad (5.1)$$

But this implies $\alpha_u = \alpha_m$, with $\alpha_u = -u_x/u_z$ and $\alpha_m = -m_x/m_z$ the slopes of the constant-u and constant-m surfaces. If the balance holds at the upstream edge of the region of steep gradient, then approximately $\alpha_u = \alpha_M$ as well. It has been shown by Hoskins and Bretherton (1972) that as the m and b surfaces coalesce in regions of steep gradient, their slopes must tend to a fixed limit, requiring in turn that u = const along the common surfaces. Thus, it follows from the various assumptions that the slope of the basic-state absolute momentum surfaces determines the limiting frontal slope in the barrier problem.

3000C U

AR = 0.05   FR = 1.20   RO = 0.20   BX = 0.80   BY = 0.00
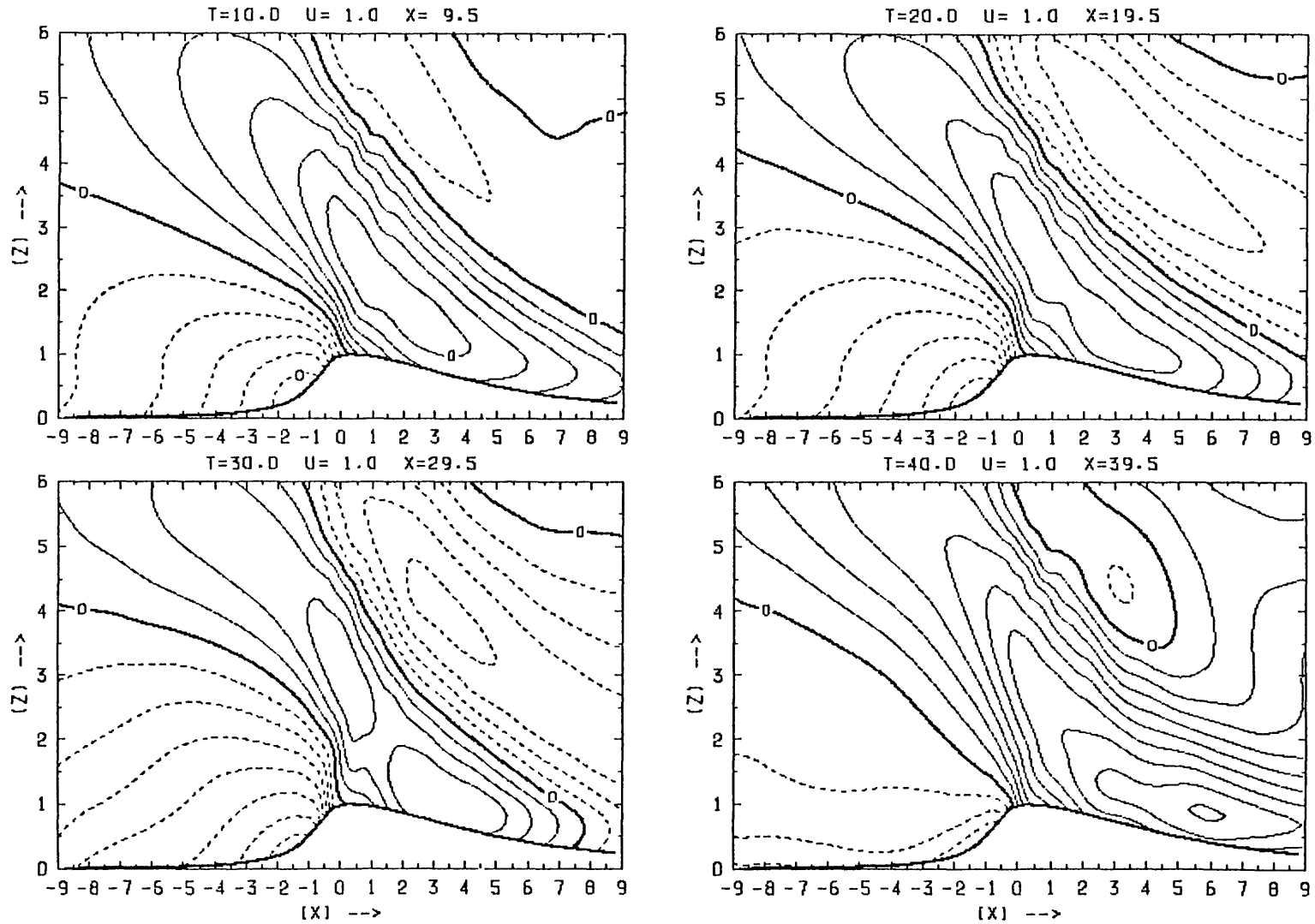
Fig. 5.11. Time sequence of perturbation streamwise velocity, u', for nonlinear baroclinic flow past B5 mountain, ending at t = 40. Parameters: Fr = 1.2, Ro^{-1} = 0.2, β = +0.8. Time interval 10; contour interval 0.1.

This particular chracterization of the partial equilibrium of

barrier fronts can be checked further by choosing smaller β in the

numerical model. Thus, the final experiment of this section uses a

narrower B5 mountain, with $Ro^{-1} = 0.1$ and $Fr = 1.2$. The choice $\beta = -0.6$

is slightly supercritical for these parameters. The ordinary deformation

radius is 12 units, which was also used as the distance from the mountain

to the model boundary. However, it can be seen in Fig. 5.12 that the

slope of the isentropes (and of the upstream u-surfaces by t = 60) is not

that determined by the deformation radius, but rather is close to that of

the basic M-surfaces, which determine a horizontal scale of only 7.2

half-widths. The vertical circulation in the experiment is essentially

steady by t = 60 (one inertial period), and further integration showed

that the sharp temperature gradient made no progress beyond x = -8.

For at least two reasons, the theoretically important M-surface

length scale, h/α_M, probably contains little practical predictive

value. First of all, the idealizations and assumptions may not stand up

to realistic complications such as diffusivity, three-dimensionality and

non-uniformity of the environment. Second, the difference between the two

scales identified in the analysis may be small in comparison to variations

in ambient conditions. Thus, the emphasis is to be placed on having

identified a consistent mechanism which uses the initial stratification of

the air mass to damp the inertial oscillations and fix the axis of

frontogenesis.

The most obvious alternative mechanisms for eliminating a surge

recovery are (1) three-dimensional perturbation pressure effects, and
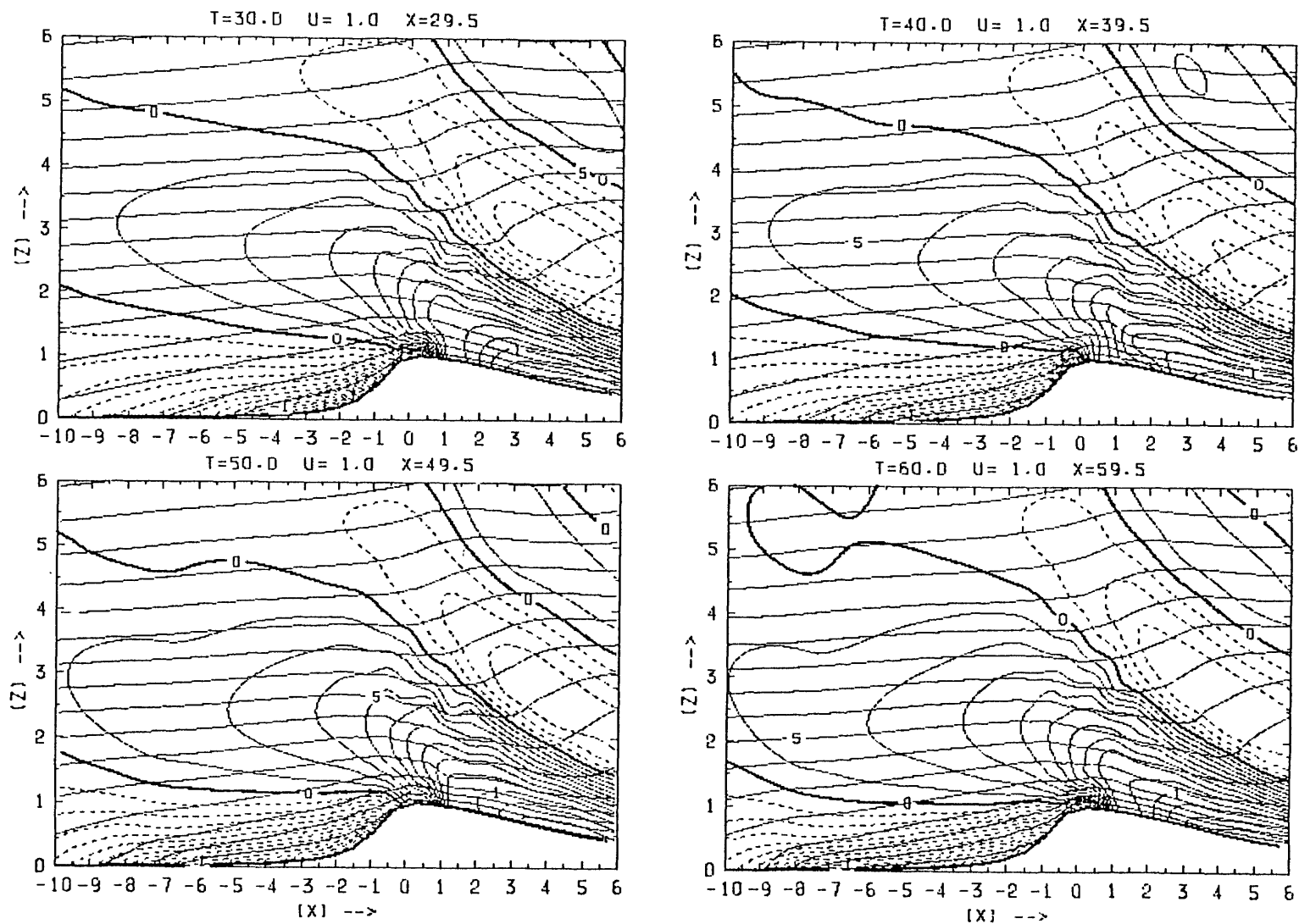
Fig. 5.12. Time sequence of total buoyancy (solid, contour interval 0.5) and u' (solid and dashed, interval 0.1) in flow past B5 mountain, ending at t = 60. Parameters are Fr = 1.2, Ro^{-1} = 0.1 and β = -0.6. Time interval 10 (ℓ/U_0).

(2) surface friction in y. However, if the basic modelling assumption of two-dimensional geography is accurate, a disturbance pressure gradient in y cannot be an overriding effect. The question of surface drag will be examined in the next section.

The last experiment of this section considers a slightly less asymmetric bell mountain, namely a "B3" profile ($\ell_1 = 3$). The fields of potential temperature and u' at $t = 20$ are shown in the lower half of Fig. 5.13, where they can be compared to the B5 solution seen before. There is a noticeable difference in the upstream progress of the reversed fluid between the two cases, but what is more significant is that the difference is small despite the great (factor of 2 at $t = 5$) disparity in the early response of the velocity fields. The comparison highlights the difference between the initial linear upstream disturbance, and the subsequent nonlinear evolution of the cold pool. Not unexpectedly in view of the foregoing analysis, the latter process seems less sensitive to the breadth of the mountain.

5.4 Experiments with shearing deformation and surface drag

The numerical model provides an opportunity to study the secondary effect of a transverse temperature gradient without neglecting the associated thermal wind. As noted in section 3.1, the prediction equations acquire advection terms due to the sheared part of the basic velocity $U_1(z) = -(B_y/f)z = -\beta_y Nz$, where β_y is dimensionless. As in section 4.7, the secondary gradient, β_y, is constant, and the advection by U_1 is evaluated explicitly in the model. In addition, the buoyancy equation has the second source $db/dt = -\beta_y v'$, which is the contribution
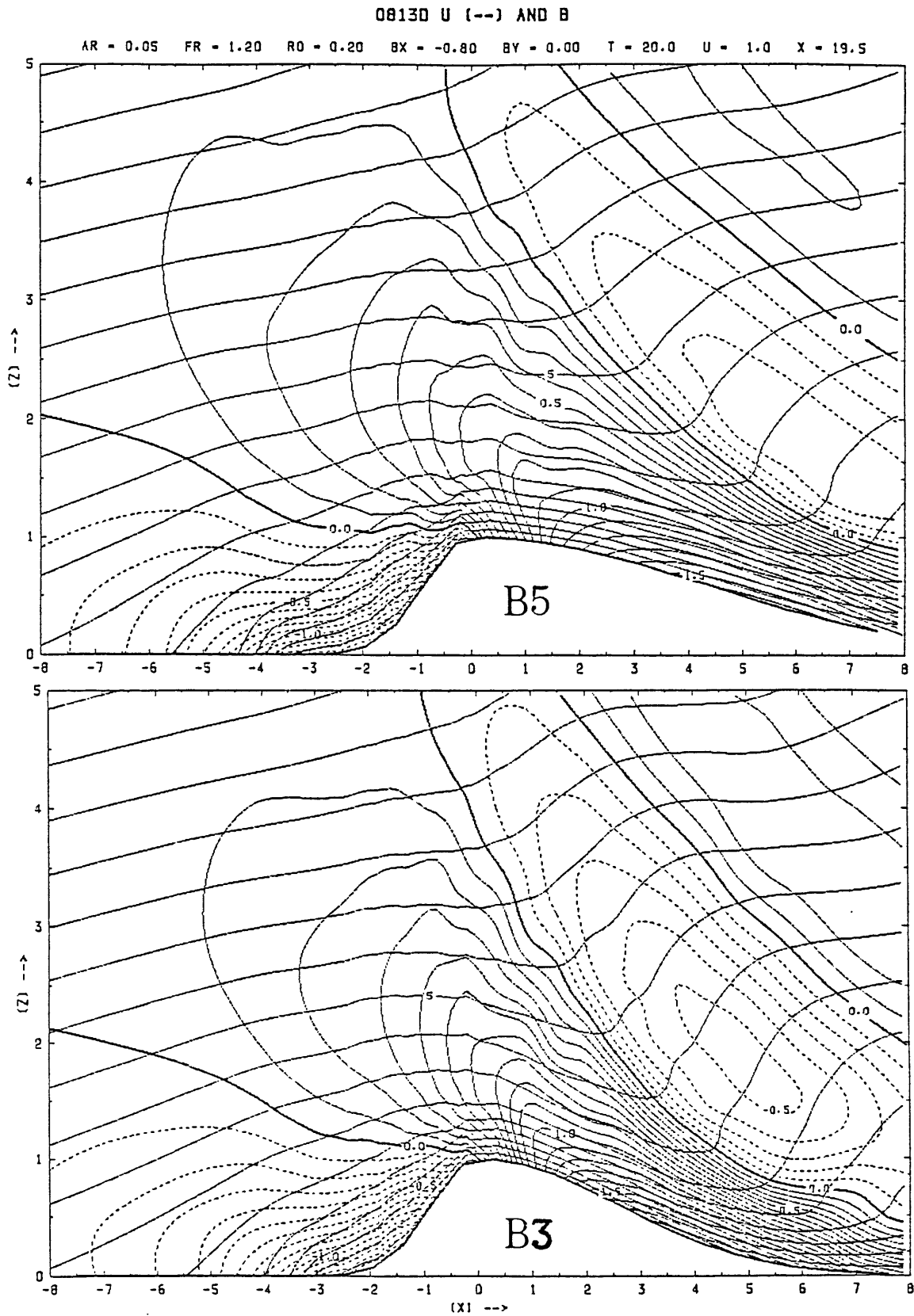
Fig. 5.13. Comparison of fields of total buoyancy (contour interval 0.5) and u' (interval 0.1) in flow past B5 (top) and B3 mountains, at t = 20. Parameters are Fr = 1.2, Ro^{-1} = 0.2 and β = -0.8.

from shearing deformation of the transverse gradient. (The basic-state

advection vanishes in the case of parallel shear.) The basic isotherms

and shear vector cross the mountain ridge at an angle $\tan^{-1}(\beta_y/\beta)$.

It was shown in chapter 3 that when $\beta_y > 0$, secondary cold

advection develops in decelerated regions of the flow, and feeds back

positively on the deceleration. A simulation performed with $\beta_y = 0.1$,

but Fr, Ro and β as in the first frontogenesis experiment, shows that the

vertical shear in x does not change the conclusions of chapter 3, i.e.,

the frontogenesis is indeed reinforced by the additional temperature

gradient. The cases $\beta_y = 0$ and $\beta_y = 0.1$ are compared at t = 20 in

Fig. 5.14. The lower figure, with the secondary gradient, exhibits a

slightly more advanced front and a deeper layer of convergence than in the

original case. The direct effect of cold advection is apparent in the

extra isentropes at the bottom of the cold pool in the lower panel.

Fig. 5.15 makes the same comparison for the B3 mountain. For this

more nearly symmetric obstacle, the upstream deceleration is less

extensive, and the secondary cold advection in the lower panel is rather

negligible. In fact, the vertical stratification in the cold pool is a

bit weaker in the case $\beta_y = 0.1$. The most striking difference between

the cases, however, is in the depth of the cold air at its upstream edge.

The horizontal convergence is also deeper, as in the B5 experiment.

The principle of potential vorticity conservation is the best tool

for understanding the effect of β_y, even though its value is primarily

diagnostic. If $q_2 \equiv J(m,b)/(fN^2)$ is the nondimensional "symmetric"

portion of the potential vorticity, then the total potential vorticity has

AR = 0.05   FR = 1.20   RO = 0.20   BX = -0.80   BY = 0.00   T = 20.0   U = 1.0   X = 19.5
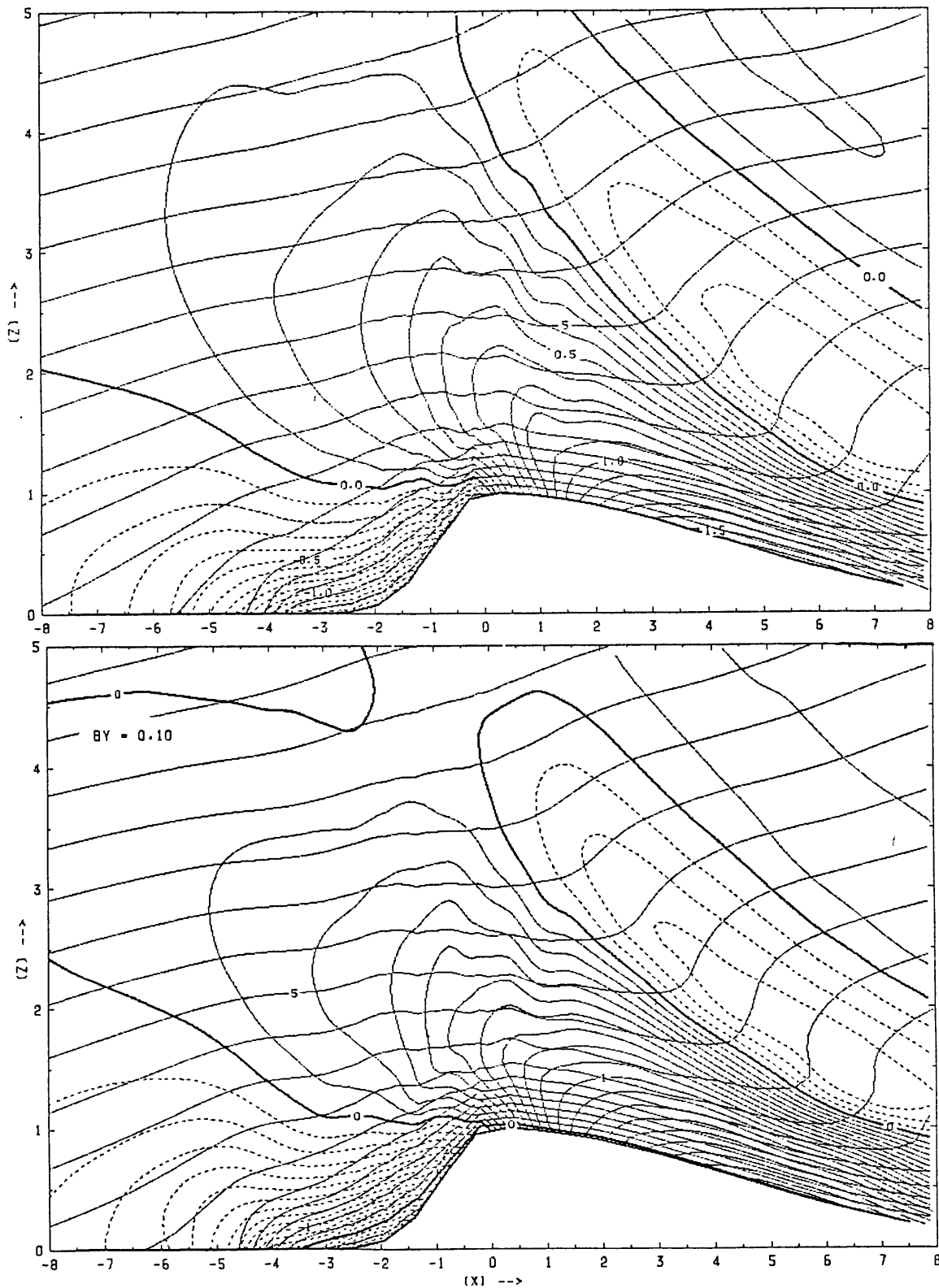
Fig. 5.14. Comparison of fields of total buoyancy and u' in flow past B5 mountain, at t = 20, with transverse buoyancy gradient β_y = 0 (top) and 0.1 (bottom). Other parameters: Fr = 1.2, Ro^{-1} = 0.2 and β = -0.8.
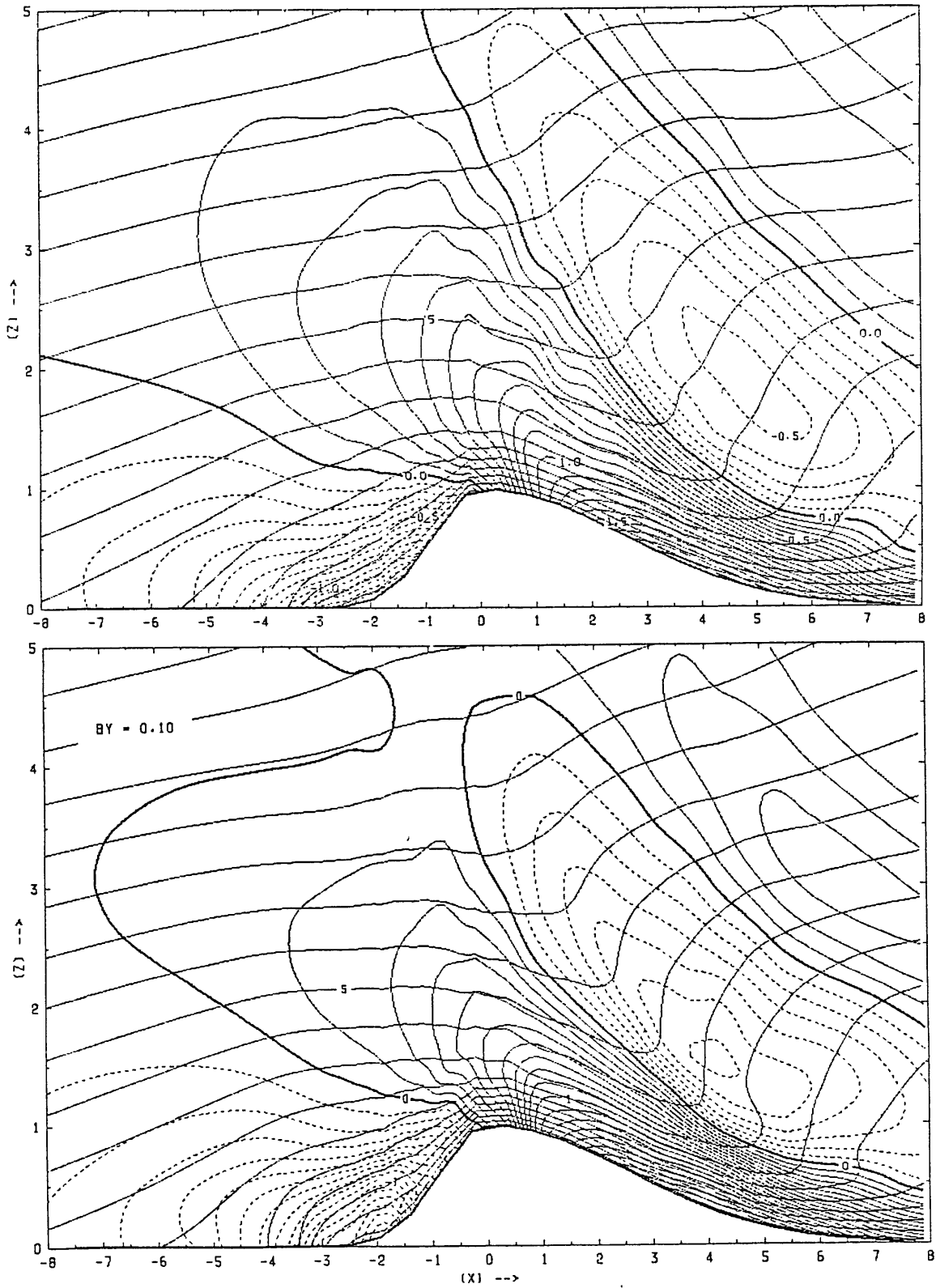
Fig. 5.15. As in Fig. 5.14, except for B3 mountain.

the form $q_3 = q_2 - \beta_y(\beta_y + \gamma/N)$, where $\gamma \equiv w_x - u'_z$ is the vorticity of the perturbation vertical circulation. Conservation of q_3 thus implies that q_2, which is also a measure of the symmetric stability, is reduced from its undisturbed value of $1-\beta^2$ in the frontogenetical region, because $\gamma < 0$.

It is convenient to view this alteration as a local increase in $|\beta|$. The diagnosis of q_2 does not reveal whether the change will be expressed as decreased vertical stratification or as increased (negative) vertical shear of the parallel wind. However, the simulations with $\beta_y > 0$ suggest that weaker cases of blocking may exhibit the former tendency, while the strongly supercritical cases, with large advective changes in N^2, will develop strong vertical shear. (Other ways to reduce q_2 are inconsistent with the basic properties of the frontal region.)

A more obvious consequence of reducing the symmetric potential vorticity is a more rapid coalescence of the m and b surfaces in the x-z plane. Recall that when these surfaces merge, semi-geostrophic balance requires that the u-contours also assume their common shape. Such a tendency can be seen in both of the experiments with $\beta_y > 0$, and may indicate a more complicated feedback than has heretofore been described. Namely, the coincidence of the u and b contours tends to prevent warm-air entrainment into the upper portion of the cold pool, thus leading progressively to a deeper layer of convergence.

The shearing deformation has essentially the same consequences for a slightly broader ($Ro^{-1} = 0.3$) B5 mountain, as seen in Fig. 5.16. Note, however, that the frontal surface at t = 20 has less curvature than in the previous simulation. This appears to be the result of a weaker

3000Q U (--) AND B

AR = 0.05   FR = 1.20   RO = 0.30   BX = -0.80   BY = 0.00   T = 20.0   U = 1.0   X = 19.5
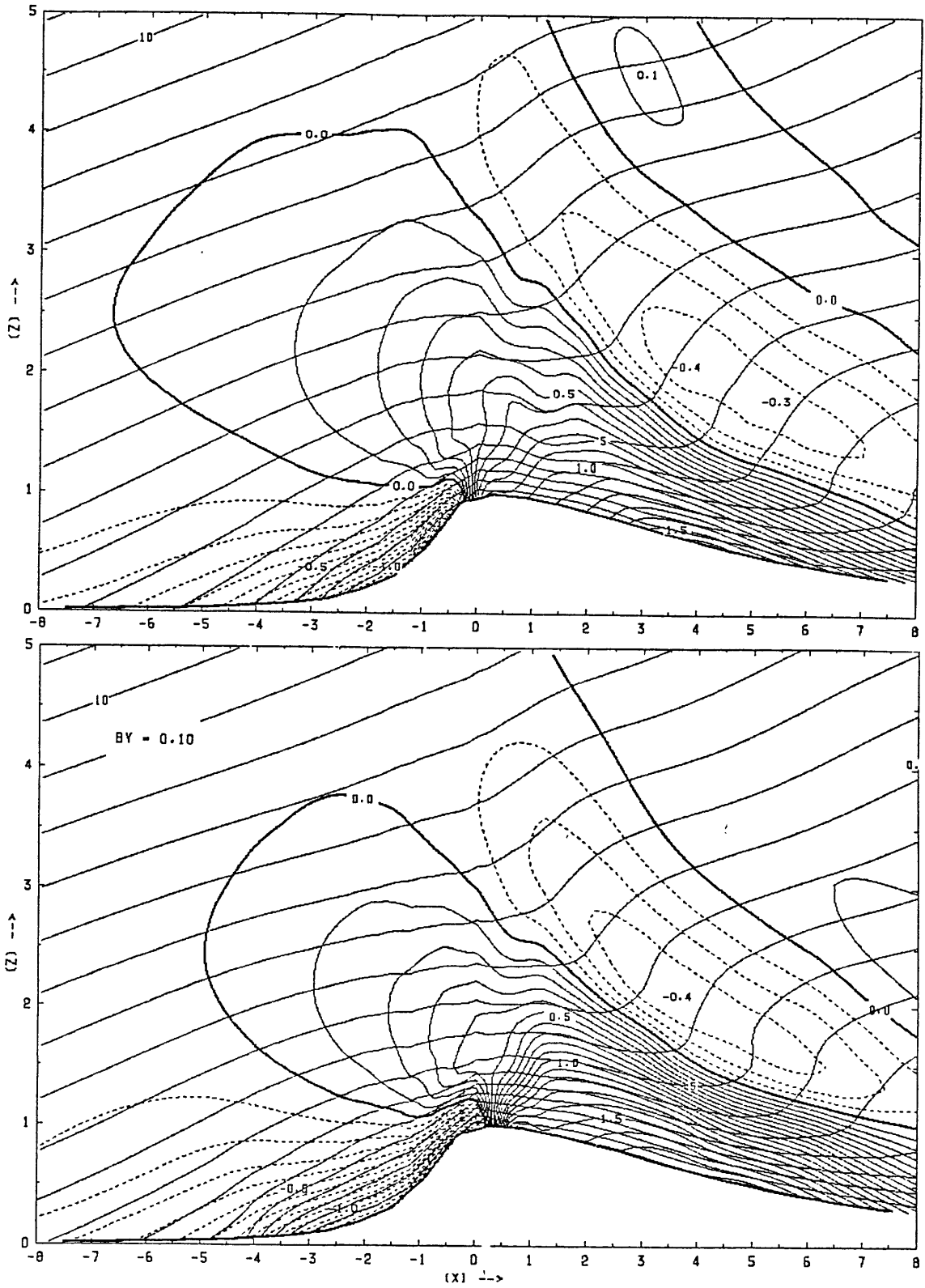
Fig. 5.16.   As in Fig. 5.14, except Ro^{-1} = 0.3.

startup surge and earlier geostrophic adjustment. It is useful to observe that the front in the $\beta_y = 0$ experiment settles near the point x = -3.5. This distance is comparable to both the (environmental) deformation radius, $L_D = 4$, and the M-surface radius, $h/\alpha_M = 3.2$. The $\beta_y > 0$ experiment became numerically unstable shortly after t = 30 because the advection of u' by $U_1(z)$ at the mountaintop was too strong for the time step. However, the cold pool at t = 30 still had not moved beyond x = -4.

The purpose of the surface drag experiment to be described next is to determine whether upstream rotational effects can be significantly reduced through the destruction of low-level parallel momentum, and whether more realistic surface velocities away from the front can be achieved. Since the model is equipped with only the simplest kind of drag and mixing parameterizations, only qualitative realism is expected.

The high-viscosity simulation is carried out with $Re^{-1} = 0.03h/\ell$, whence the mixing time (assuming a mixing depth of h) is $33\,\ell/U_0$. The surface drag coefficient (essentially the ratio between the squared velocity and the surface momentum flux) is $C_d = 1.5Re^{-1}$ instead of the control value of $0.5Re^{-1}$. The thermal mixing time is $67\,\ell/U_0$ since Pr = 2, but the assumption of small surface heat flux is retained with $C_h = 0.5$.

Fig. 5.7a compares the streamwise velocity perturbation for the "inviscid" control experiment, Fr = 1.2, $Ro^{-1} = 0.2$, $\beta = -0.6$, with that for the corresponding high-viscosity experiment. The friction moves the downstream region of high velocities off the ground to a height of about h/2, and considerably weakens of the anomaly. Also, the region of small and negative u inside the cold pool is broader and stronger as a result of
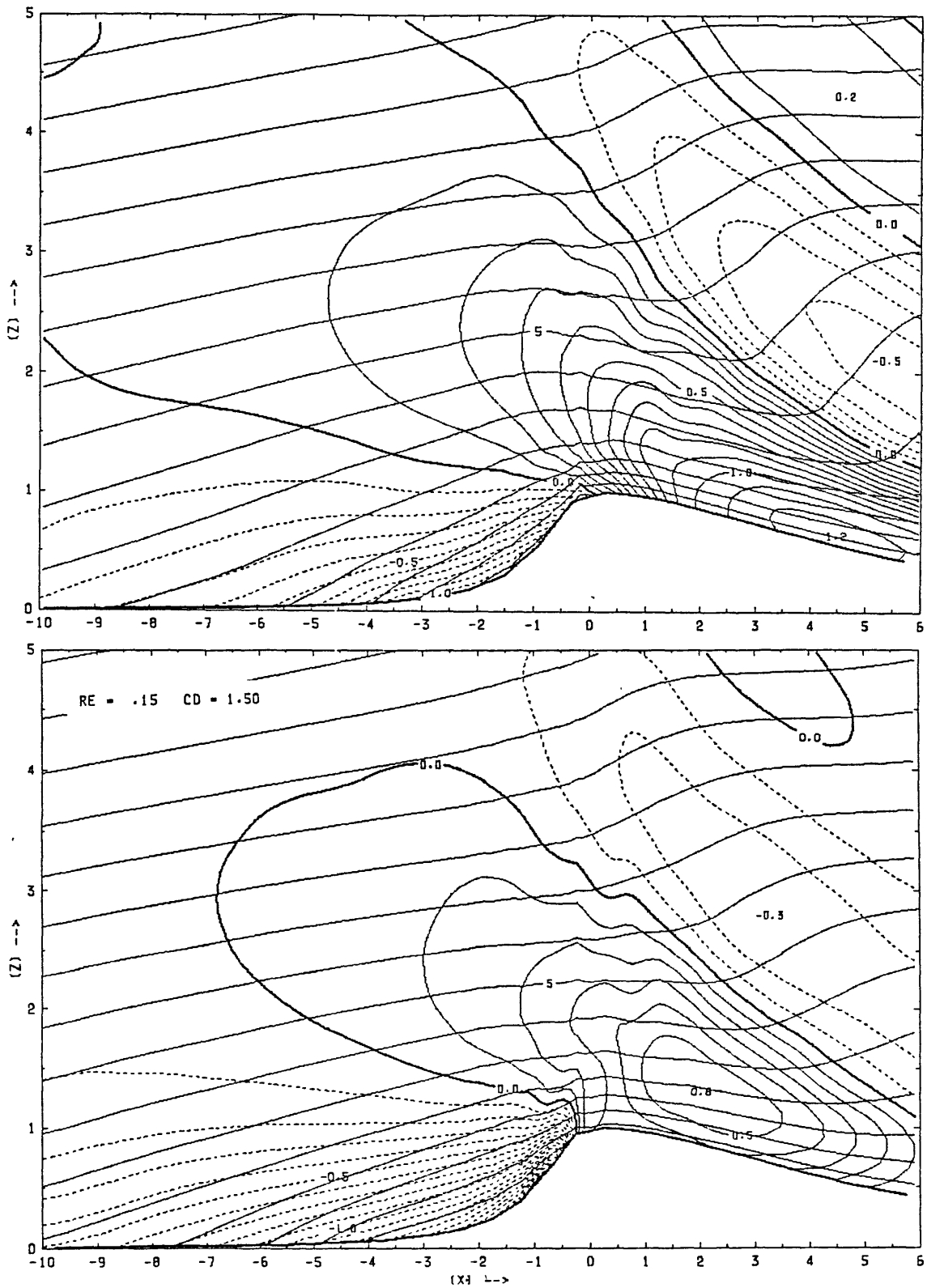
Fig. 5.17a. Comparison of perturbation streamwise velocity, u', in flow past B5 mountain, at t = 20, with strong surface drag and mixing (bottom) and without (top). Other parameters: Fr = 1.2, Ro^{-1} = 0.2 and β = -0.8. Contour intervals as in Fig. 5.12.

the friction. Although the chosen parameters are only slightly supercritical for blocking, the reversed fluid has already reached x = -5.5 by t = 20 in the second experiment, and continues to spread upstream well beyond the deformation radius at x = -5 (the distance $h/\omega_M = 3$ is even shorter). The frictionally-induced upstream penetration of low-momentum air is not accompanied by the same amount of convergence as in the more supercritical inviscid experiments. This circumstance combined with the strong horizontal mixing eliminates any semblance of a front at the ground.

The effect of the surface drag and mixing on the parallel velocity is even more dramatic (Fig. 5.17b). The largest value of v' no longer appears at the summit, but occurs in a relatively weak jet centered at a height of about h/2 above the windward slope. Similar structures are of course seen in more sophisticated frontogenesis simulations (e.g., Keyser and Anthes, 1982), as well as in the observations (e.g., Fig. 1.7).

Running the model with a simple viscosity parameterization demonstrates that the distribution of surface velocity away from the front can be made more realistic by including boundary-layer effects, and that upstream influence, per se, is enhanced by the friction. However, it is clear that the present assumption of uniform mixing length and surface roughness, and the particular choice of mixing parameters, are too restrictive to permit the baroclinic-orographic mechanism to generate a strong quasi-stationary front. Further modelling with a more realistic mixing scheme will probably show that a gradient of surface roughness (and boundary temperature) can cause a significant adjustment of the inviscid model prediction of the frontal position.

AR = 0.05   FR = 1.20   RO = 0.20   BX = -0.60   BY = 0.00   RE = -.05   CD = 0.50   T = 30.0   U = 1
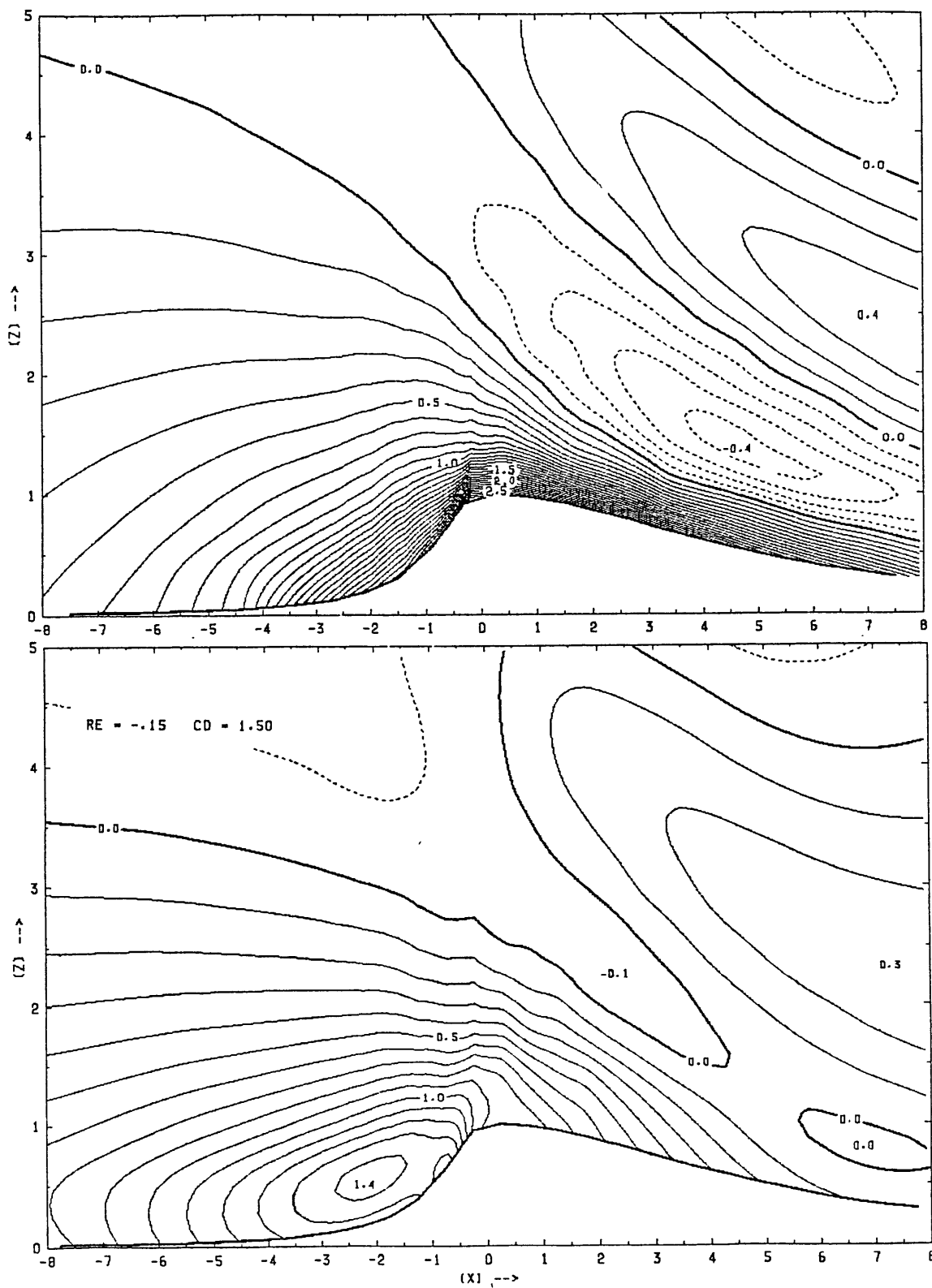
Fig. 5.17b. As in Fig. 5.17a, except model variable is v'.

5.5. Conclusions from the numerical modelling

The numerical experiments with the Lagrangian model confirm the basic hypothesis of this study that two-dimensional topography alone is sufficient to produce upstream flow stagnation and frontogenesis in an otherwise balanced, baroclinic flow. The original theory that the cold pool would evolve to a balanced size determined by the mountain height is also supported. Only a small theoretical refinement was needed to accommodate the unusual condition that the front "advects" with the mountain through the ambient flow. It is remarkable that the potential vorticity dynamics expounded for classical fronts by Hoskins and Bretherton (1972) are flexible enough to describe partially-equilibrated barrier fronts with so little adjustment.

The simulations reproduce some, but by no means all, of the characteristics of the New England coastal front. The model achieves realistic length and time scales, as well as reasonable horizontal shears and temperature contrasts. It also shows a significant response to a weak version of the north-south temperature gradient, a well-known concomitant of strong coastal frontogenesis. The principal unrealistic features are (1) the extreme uniformity of the stratification in the cold air, and (2) the excessive positive velocity perturbations at the ground. The first problem is clearly the result of periodically remapping the model data. Although the Lagrangian method was effective in economically generating large temperature contrasts, the remapping necessitated by the divergence over the mountain prevented a determination of true frontal "collapse".

The extreme positive velocity perturbations, on the other hand, are attributable to several factors. Most significant, of course, is the

absence of realistic mixing and drag, but the two-dimensionality assumption may also be responsible. To a lesser extent, the large lee velocities resulted from the large values of β (small values of the Richardson number). Although $\beta = -0.8$ is not an unrealistic respresentation of the surface temperature gradient, it may well overestimate the vertical shear and temperature gradient in the large-scale air mass.

The sensitivity of the upstream effects to the mountain shape must be carefully considered when judging the importance the orographic mechanism in New England. The choice of a lee-broadened mountain substantially enhances frontogenesis, and was rationalized as a kind of parameterization of complicated terrain under conditions of large static stability. This argument, and the proper dynamical definition of the mountain half-width, will require further investigation before the observed Rossby-number sensitivity can be fully understood.

Formal analysis using linear theory has provided rather persuasive evidence of an orographic adjustment process which is different from that for barotropic flows, the context in which the theory was originally proposed. The existence of an internal length scale absent from both the linear and nonlinear classical theories of mountain flow constitutes circumstantial evidence for such an adjustment. The process appears to operate through a positive feedback on the local Froude number below the mountaintop, as well as a negative feedback on the nonlinearity at higher levels. Even the latter process does not quite reproduce the barotropic scenario, which involves wave-breaking. The linear analysis falls short of specifying a relationship between the barotropic blocking condition and a suitably defined modified Froude number determined locally by baroclinic

effects. Such a result may require an analysis of the transient disturbance.

Modelling rapid frontogenesis as an adiabatic and inviscid alteration of a balanced, stratified flow altogether removes the role of the coastline. In this way, the present study adopts as extreme a view as the earlier numerical simulation of coastal frontogenesis, which assumes impulsive heating. As described above, the orographic hypothesis nevertheless has an advantage in explaining the persistence of the front, not to mention its occurrence when strong local heating cannot be demonstrated. In view of the shortcomings of both explanations, a likely inference is that the local heating often supplies the additional convergence and temperature contrast needed to generate the extraordinary small-scale features (i.e., gradients and vertical circulation) observed in some real events, especially when the present model identifies the large-scale environment as only marginally frontogenetical.

APPENDIX A.   COORDINATE TRANSFORMATION FOR BAROCLINIC SEMI-GEOSTROPHIC
             FLOW

When the nonlinear system (2.1) is rewritten using a Lagrangian vertical coordinate, the form of the mathematical problem becomes much simpler in certain limits. Let ξ and ζ be Lagrangian coordinates defined by $d\xi/dt = d\zeta/dt = 0$, with $\xi = x - U_0 t$ and $\zeta = z$ far upstream. Then the assumption of uniform wind shear and thermal stratification in a geostrophic basic state implies $b = fV_z \xi + N^2 \zeta$ and $m = fa^2 \xi + V_z \zeta$, where the potential buoyancy b and intrinsic absolute momentum m are individual constants.

If the formulae (4.3) are used to replace z with ζ as one of the independent variables [so that $z = Z(x, \zeta)$ becomes a dependent variable], the steady-state hydrostatic version of (2.1) reduces to a vorticity equation of the form

$$N^2 Z_x + (fa)^2 \xi_\zeta + fV_z\big(1 - J(\xi, Z)\big) = -U_0 \gamma_x, \qquad (A.1)$$

and a continuity equation of the form

$$Z_\zeta - \xi_x = 0. \qquad (A.2)$$

Here $\gamma \equiv -u_z\big|_x$ is the horizontal vorticity, and all partial derivatives are at constant x or ζ. The relation $u/U_0 = 1/Z_\zeta$ can be used to express the vorticity as $\gamma/U_0 = (u/U_0)^3 Z_{\zeta\zeta}$.

Now let x and ξ both be normalized by the horizontal scale ℓ, and z and ζ by the vertical scale $fa\ell/N$. If $\chi(x, \zeta)$ is defined by $\chi_x =$

$(z-\zeta)/(RoFr)$ and $\chi_\zeta = -(x-\xi)/(RoFr)$, then (A.2) is satisfied, and the vorticity equation becomes

$$\chi_{xx} + \chi_{\zeta\zeta} - 2\beta\chi_{x\zeta} + Ro^2\chi_{xx\zeta\zeta} = -\beta RoFr J(\chi_x, \chi_\zeta) - Ro^2\left((u^3-1)\chi_{\zeta\zeta x}\right)_x, \quad (A.3)$$

where u is now normalized by U_0, i.e., $u = (1+RoFr\chi_x)^{-1}$. The lower boundary condition is $\chi_x = g_0(x)$, where g_0 is an order-unity function specifying the terrain shape. The correct form of the radiation upper boundary condition when $Ro \neq 0$ is still not clear; however, Lilly and Klemp (1979) have obtained the appropriate condition for laminar solutions in the limit $Ro = \infty$.

The nonlinearity in the baroclinic problem is thus restricted to the two terms on the right side of (A.3). The quasi-geostrophic assumption, $Ro = 0$, eliminates the inertial nonlinearity, while the assumption of a barotropic basic state, $\beta = 0$, removes the Jacobian term. It is not strictly necessary to assume steady-state in the quasi- or semi-geostrophic problem; however, the restriction on the size of du/dt applies as well to accelerations of U_0. Note that since the inertial nonlinearity is unbounded when $RoFr = 0(1)$, and where $\chi_x < 0$ (accelerated regions), the semi-geostrophic approximation is not uniformly valid in space in the nonlinear regime, $RoFr > 1$.

APPENDIX B. APPARENT MASS SOURCES IN FINITE-DIFFERENCE EQUATIONS

In order to solve the diagnostic equations (4.5) for the velocity at time t_n without producing an $O(\Delta t)$ mass divergence, it is necessary to extrapolate the particle positions forward one-half time step from their standard values at $t_n-\Delta t/2$, using the velocities $\dot{X}_{ij}{}^{n-1}$ and $\dot{Z}_{ij}{}^{n-1}$ defined at time $t_n-\Delta t$. A convenient alternative to direct extrapolation is to write (4.5a) with the source term,

$$D_{ij}^n = -J_\Delta(\dot{X}_{ij}^{n-1}, \dot{Z}_{ij}^{n-1}), \tag{B.1}$$

which introduces errors of the same order (Δt^2). When the same short-cut is used for the vorticity equation, the apparent source vanishes identically.

A crucial modification of the divergence correction is needed where the atmosphere meets the uneven lower boundary. Here the appropriate definition of the cell volume is

$$A_i' = A_i + \frac{1}{2}(Z_{i-1/2}+Z_{i+1/2}) \, D_\xi X_i - \int_{X_{i-1/2}}^{X_{i+1/2}} g_0(x)dx, \tag{B.2}$$

in which A_i is the area of one of the quadrilaterals with three boundary vertices (and the index $j = 1$ is omitted). The correction $D_i{}^n$ in (B.1) must therefore be augmented by the time derivative of $2(A_i - A_i')$, which may be written

$$D_i'^n = \sum_i \{(\dot{X}_{i-1/2}^n + \dot{X}_{i+1/2}^n) \, D_\xi Z_i - (\dot{Z}_{i-1/2}^n + \dot{Z}_{i+1/2}^n) \, D_\xi X_i \}. \tag{B.3}$$

The indicated sum is taken over the two segments which terminate on the boundary.

The diagnostic (EVP) algorithm described in chapter 4 makes it possible to evaluate the velocities in (B.3) implicitly at time t_n rather than t_{n-1}. A forward time step can be used to obtain the positions at $t = t_n$, but errors of only the same order are introduced by using instead a third divergence correction, D_i''. D_i'' is defined in the same way as D_i', but with $\dot{X}^n$ and $\dot{Z}^n$ replaced by $\dot{X}^{n-1}$ and $\dot{Z}^{n-1}$, and X^n and Z^n replaced by $(1/2)\dot{X}^{n-1}$ and $(1/2)\dot{Z}^{n-1}$.

A computational separation of time scales governing the linear (Δt) and nonlinear (Δt_L) processes allows less frequent updating of the matrix used to solve the diagnostic system. To keep the time-differencing errors at $O(\Delta t^2)$, rather than $O(\Delta t_L{}^2)$, further correction terms are necessary in the velocity equations and lower boundary condition.

In general, each of the Jacobian terms in the diagnostic equations gives rise to a new inhomogeneity of the form $J(Q^n, P^n{}_0{}^{-1/2} - P^{n-1/2})$, where the index n corresponds to the time of the most recent calculation of the velocity, Q, and n_0 denotes the time of the last updating of the position variable, P, in the EVP routine. With the same index notation, the correction for the nonlinear part of the lower boundary condition can be written $(W_i{}^{n+1})' = -\big(g_0'(X^n{}_0)-g_0'(X^n)\big)\dot{X}^n$, which belongs on the right side of (4.12).

APPENDIX C. FIGURE CAPTIONS

Fig. 1.1. Profile of a warm front crossing a mountain range (from Bjerknes and Solberg, 1921).

p. 9

Fig. 1.2. Sequence of sea-level synoptic analyses showing the development of a sourtherly buster on a cold front (from Baines, 1984).

p. 11

Fig. 1.3. Composite analysis of sea-level pressure at onset of coastal frontogenesis (from McCarthy, 1977).

p. 23

Fig. 1.4. Mesoscale synoptic analyses of two coastal front events near time of onset. The cases differ in air-sea temperature contrast and geostrophic wind speed. (From Bosart et al., 1972).

p. 25

Fig. 1.5. Plan view and vertical cross-section of topography of sourthern New England. Cross-section is averaged over state of Massachusetts. (From Passarelli and Boehme, 1984).

p. 28

Fig. 1.6. Cross-sectional analysis of potential temperature (K) and water vapor mixing ratio (g/kg) between Chatham, MA, and Albany, NY, during coastal frontogenesis on 24 December 1970 (from McCarthy, 1977).

p. 30

Fig. 1.7. Analyzed cross-sections of aircraft-observed potential temperature and wind in mature coastal front (from Neilley, 1984).

p. 32

Fig. 2.1. Dispersion relation for gravity-inertia plane waves assuming baroclinic (solid) and barotropic (dashed) basic state. Limit points k = $\sqrt{(1-\beta^2)} \equiv$ r and μ = -r, and direction of group velocity, are indicated in baroclinic case.

p. 41

Fig. 2.2. Schematic showing type and location of propagating waves forced at (x_0, z_0), assuming baroclinic basic state ($\beta < 0$). Regions dominated by either buoyancy or rotational effects are shaded.

p. 60

REFERENCES

Ballentine, R.J., 1980: A numerical investigation of New England coastal
        frontogenesis. Mon. Wea. Rev., 108, 1479-1497.

Baines, P.G., 1980: The dynamics of the southerly buster. Aust. Meteorol.
        Mag., 28, 175-200.

_____ and P.A. Davies, 1980: Laboratory studies of topographic
        effects in rotating and/or stratified fluids. Orographic Effects
        in Planetary Flows, GARP Publ. Series, No. 23, WMO, ch. 8.

Baker, D.G., 1970: A study of high pressure ridges to the east of the
        Appalachian Mountains. Ph.D. thesis, Dept. Meteor., Mass. Inst.
        of Tech., 127 pp.

Bates, J.R. and A. McDonald, 1982: Multiply-upstream, semi-Lagrangian
        advective schemes: Analysis and application to a multi-level
        primitive equation model. Mon. Wea. Rev., 110, 1831-1842.

Bender, C.M. and S.A. Orszag, 1978: Advanced Mathematics for Scientists
        and Engineers. McGraw-Hill, New York, ch. 6.

Benjamin, T.B., 1968: Gravity currents and related phenomena. J. Fluid
        Mech., 31, 209-248.

Bennetts, D.A., and B.J. Hoskins, 1979: Conditional symmetric instability:
        A possible explanation for frontal rainbands. Quart. J. Roy.
        Meteor. Soc., 105, 945-962.

Bosart, L.F., 1975: New England coastal frontogenesis. Quart. J. Roy.
        Meteor. Soc., 101, 957-978.

_____, V. Pagnotti and B. Lettau, 1973: Climatological aspects of
        eastern United States backdoor frontal passages. Mon. Wea. Rev.,
        79, 627-635.

_____, C.J. Vaudo and J.H. Helsdon, Jr., 1972: Coastal
        frontogenesis. J. Appl. Meteor., 11, 1236-1258.

Bjerknes, J., and H. Solberg, 1921: Meteorological conditions for the
        formation of rain. Geofys. Publ., 2, 10-41.

Ching, J.K.S., 1975: Determining the drag coefficient from vorticity,
        momentum, and mass budget analyses. J. Atmos. Sci., 32,
        1898-1908.

Coulman, C.E., J.R. Colquhoun, R.K. Smith and K. McInnes, 1985:
        Orographically-forced cold fronts — mean structure and motion.
        Boundary-Layer Meteorol., 32, 57-83.

Durran, D.R. and J.B. Klemp, 1983: A compressible model for the simulation of moist mountain waves. J. Atmos. Sci., 111, 2341-2361.

Eliassen, A., 1962: On the vertical circulation in frontal zones. Geofys. Publik., 24, 147-160.

_____ and S. Thorsteinsson, 1984: Numerical studies of stratified air flow over a mountain ridge on the rotating earth. Tellus, 36, 172-186.

Emanuel, K.A., 1985: Frontal circulations in the presence of small moist symmetric stability. J. Atmos. Sci., 42, 1062-1071.

Garner, S., 1985: Modification of a computational upper boundary condition for f-plane applications. Mon. Wea. Rev. (in press).

Godske, C.L., T. Bergeron, J. Bjerknes and R.C. Bundgaard, 1957: Dynamic Meteorology and Weather Forecasting, American Meteorological Society, Boston, MA, ch. 16.

Harlow, F.H. and J.E. Welch, 1965: Numerical calculation of time-dependent viscous incompressible flow of fluid with free surface. Phys. Fluids, 8, 2182-2189.

Hirt, C.W., J.L. Cook and T.D. Butler, 1970: A Lagrangian model for calculating the dynamics of an incompressible fluid with free surface. J. Comp. Phys., 5, 103-124.

Hoskins, B.J., 1982: The mathematical theory of frontogenesis. Ann. Rev. Fluid Mech., 14, 131-151.

_____, 1975: The geostrophic momentum approximation and the semi-geostrophic equations. Quart. J. R. Met. Soc., 97, 139-153.

_____ and F.P. Bretherton, 1972: Atmospheric frontogenesis models: Mathematical formulation and solution. J. Atmos. Sci., 29, 11-37.

Keyser, D. and R.A. Anthes, 1982: The influence of planetary boundary layer physics on frontal structure in the Hoskins-Bretherton horizontal deformation model. J. Atmos. Sci., 39, 1783-1802.

Klemp, J.B., and D.R. Durran, 1983: An upper boundary condition permitting internal gravity wave radiation in numerical mesoscale models. Mon. Wea. Rev., 111, 430-444.

_____ and D.K. Lilly, 1980: Mountain waves and momentum flux, Orographic Effects in Planetary Flows, GARP Publ. Series, No. 23, WMO, ch. 4.

_____ and D.K. Lilly, 1977: Numerical simulation of hydrostatic mountain waves. J. Atmos. Sci., 35, 78-107.

Ley, B.E. and W.R. Peltier, 1979: Wave generation through frontal collapse. J. Atmos. Sci., 35, 3-17.

Lighthill, M.J., 1952: On sound generated aerodynamically I. General theory. Proc. Roy. Soc. London, 211A, 564-587.

Lilly, D.K., 1981: Doppler radar observations of upslope snowstorms. Preprint, 20th Conf. on Radar Meteorol., Boston (Nov.-Dec. 1981), Am. Met. Soc.

_____ and J.B. Klemp, 1979: The effects of terrain shape on nonlinear hydrostatic mountain waves. J. Fluid Mech., 95, 241-261.

Long, R.R., 1972: Finite amplitude disturbances in the flow of inviscid rotating and stratified fluids over obstacles. Ann. Rev. Fluid Mech., 4, 69-92.

_____, 1955: Some aspects of the flow of stratified fluids. Part III: Continuous density gradients. Tellus, 7, 341-357.

McCarthy, Dennis H., 1977: A study of the vertical structure of the New England coastal front. M.S. thesis, Dept. Atmos. Sci., Univ. of Wisconsin, 82 pp.

Merkine, L.O., 1975: Steady finite-amplitude baroclinic flow over long topography in a rotating stratified atmosphere. J. Atmos. Sci., 32, 1881-1893.

Neilley, P.P., 1984: Application of a density current model to aircraft obeservations of the New England Coastal Front. M.S. Thesis, Massachusetts Institute of Technology, Cambridge, Mass.

Orlanski, I., 1976: A simple boundary condition for unbounded hyperbolic flows. J. Comput. Phys., 21, 251.

_____ and B.B. Ross, 1977: The circulation associated with a cold front. Part I: Dry case. J. Atmos. Sci., 34, 1619-1633.

Passarelli, R.E. and H. Boehme, 1983: The orographic modulation of pre-warm-front precipitation in sourthern New England. Mon. Wea. Rev., 111, 1062-1070.

Pielke, R.A., 1974: A three-dimensional numerical model of the sea breezes over south Florida. Mon. Wea. Rev., 102, 115-139.

Pierrehumbert, R.T., 1984: Linear results on the barrier effect of mesoscale mountains. J. Atmos. Sci., 41, 1356-1367.

_____, 1985: Stratified semi-geostrophic flow over two-dimensional topography in an unbounded atmosphere, J. Atmos. Sci., 42, 523-526.

_____ and B. Wyman, 1985: Upstream effects of mesoscale
       mountains. J. Atmos. Sci., 42, 977-1003.

Plotkin, J., 1965: Detailed analysis of an intense surface cold front.
       M.S. Thesis, Dept. Meteor., Mass. Inst. of Tech., Cambridge, MA.

Queney, P., 1947: Theory of perturbations in stratified currents with
       application to airflow over mountain barriers. Dept. of
       Meteorology, Univ. of Chicago, Misc. Rep. No. 23, 67 pp.

_____, 1948: The problem of air flow over mountains: A summary of
       theoretical studies. Bull. Amer. Meteor. Soc., 29, 16-25.

Roache, P.J., 1976: Basic computational methods for incompressible flow.
       Computational Fluid Dynamics, Hermosa Publ., ch. 3.

Sanders, F., 1955: Investigation of the structure and dynamics of an
       intense surface frontal zone. J. Meteor., 12, 542-552.

Segur, H., 1973: The Korteweg-de Vries equation and water waves. Solutions
       of the equation. Part 1. J. Fluid Mech., 59, 721-736.

Smith, R.B., 1977: The steepening of hydrostatic mountain waves. J.
       Atmos. Sci., 34, 1634-1654.

_____, 1979: The influence of the earth's rotation on mountain wave
       drag. J. Atmos. Sci., 36, 177-180.

_____, 1982: Synoptic observations and theory of orographically
       disturbed wind and pressure. J. Atmos. Sci., 39, 60-70.

Stone, P.H., 1966: Frontogenesis by horizontal wind deformation fields.
       J. Atmos. Sci., 23, 455-465.

Williams, G.P., 1969: Numerical integration of the three-dimensional
       Navier-Stokes equations for incompressible flow. J. Fluid Mech.,
       37, 727-750.

Williams, R.T., 1967: Atmospheric frontogenesis: a numerical experiment.
       J. Atmos. Sci., 24, 627-641.

_____ and J. Plotkin, 1968: Quasi-geostrophic frontogenesis. J.
       Atmos. Sci., 25, 201-206.